

JOURNAL OF THE MYANMAR ACADEMY OF ARTS AND SCIENCE



Physics, Mathematics, Computer Studies

Vol. XXII, No.2, May, 2025

Myanmar Academy of Arts and Science

Journal of the Myanmar Academy of Arts and Science

Vol. XXII. No.2

Contents

Section (i) Physics

Sr.No	Title	Pages
1	Htaik Nandar Kyaw , *Detection of A Single- Λ Hypernucleus in J-Parc E07 Experiment	1
2	Noe Noe Honey , *Boost for Maintenance of Mini-Solar Modules Quality Due To Acid Rain	11
3	Kaung Kyaw Naing , *A Comprehensive Study on Synthesis, Characterization, and Electrochemical Performance of Pva and Pan-Derived Carbon Fibers for Energy Storage	15
4	Aung Zaw Myint , *An Innovative Design of an Electronic Data Acquisition Measurement System	23
5	Nwe Ni Hlaing , Conversion of Disposable Bamboo Chopsticks Waste to Adsorbents for Laboratory Wastewater and Dye Wastewater Treatment	31
6	Tay Zar Htein Win , Design and Implementation of Gamma Radiation Source Direction With Panoramic Sensor Coding Collimator (Psc) System	41
7	Mya Hnin Wai Wai , Temperatures Dependence of Zn-Ni-Mn Hierarchical Ternary Metal Oxide Films on Nickel Foam	53
8	Hlaing Darli Soe , Structural and Morphological Properties of Zinc Stannate Nanofibers	61
9	Than Min Khaing , Structural Characteristics of Sodium Calcium Silicate Glass Ceramics	69
10	Ami Soe , Growth And High Temperature Phase Characteristics of Pure and Doped (Kdp-Adp) Crystals	77
11	Myint Kalyar , Desalination and Water Quality Assessment Using Single-Slope Passive Solar Still	89
12	Htoo Nwe Nwe Aung , Analysis of The Concentration of Fe in Iron ore Sample by Irradiation with Am-Be Neutron Source	99
13	Wint Shwe War Hlaing , A Study on the Benefits of Living Things due to Physical Change in Myanmar Tea Leaves	109
14	Khin Htar Swe , Structural and Electrical Properties of Lithium Doped Zinc Oxide	119
15	Phyo Shwe Yi San , Fabrication and Characterization of $zn_{1-x}cu_xo$ Ceramics Compound	127

Sr.No	Title	Pages
16	Ye Htet Aung , Analysis of Wave Functions, Energy Levels and Cross-Section For (π^+ , K^+) Reactions Using Numerov's Method	135
17	Khin Moh Moh Tin , Cloud Based Real-Time Air Quality and Environmental Parameters Monitoring and Logging System	147
18	Sa Nanada Aung , Determination of Reflection Coefficients of the Parallel-Polarized and Perpendicularly-polarized Waves Incident on the Dielectric Materials	159
19	Bhone Pyae Linn , Fabrication and Characterization of Natural Dyes Based ZnOps Photoelectrode for Dye Sensitized Solar Cells (DSSCs)	167
20	Myo Nyunt , Determination of Energy Loss Characteristic in Different Density Materials by Alpha Spectroscopic System	177
21	Khin Sandar Lin , Mechanical Tensile Strength Analysis of Poly Vinyl Alcohol(PVA) Polymer Reinforced with Waste Scraped Tire Rubber Fibers	189
22	Kyaw Swar Min , Study on Physical and Chemical Properties of Soil at Kalay University Campus	197

Section (ii) Mathematics

Sr.No	Title	Pages
1	Hnin Ei Phyu , *Applying one Dimensional Differential Transform Method to Partial Differential Equations	209

Section (iii) Computer Studies

Sr.No	Title	Pages
1	Julie Marlar , * Analysis of Traffic Accident by Using Machine Learning	225
2	Ei Ei Thwe , Predicting Student Dropout System for Basic Education High School By K-Means Clustering	237

DETECTION OF A SINGLE- Λ HYPERNUCLEUS IN J-PARC E07 EXPERIMENT*

Htaik Nandar Kyaw¹, Chan Myae Aung²

Abstract

A single- Λ hypernucleus event which is detected in nuclear emulsion of J-PARC E07 experiment is analysed by applying relativistic kinematics. The ranges and position angles of charged particles tracks are calculated by using the position data supported by J-PARC E07 collaborators. The neutral particle emission at production point A and decay point B of single- Λ hypernucleus is checked by using the colinearity of two tracks and it is observed that, there is no neutral particle emission at point A but there is one or more neutral particles emission at point B. Charged particle track #4 is identified by its momentum and it is to be one of baryon families. The calculated results are compared with known experimental results. According to the analysis at point A, captured nucleus of Ξ^- hyperon is identified as ${}^{14}_7\text{N}$ and the charged particle track #2 is identified as ${}^4_2\text{He}$. At point B, single- Λ hypernucleus track #1 is identified as ${}^{10}_\Lambda\text{Be}$ and charged particle track #3 and #4 are identified as ${}^6_3\text{Li}$ and ${}^1_1\text{H}$. In addition to charged particles emission, neutral particles are contaminated at point B.

Keywords: J-PARC E07 experiment, position data, colinearity, single- Λ hypernucleus.

Introduction

Hypernuclear Physics is the study of nuclei in which one or more hyperons are involved in addition to nucleons (protons and neutrons). Hyperons possess a new property, strangeness quantum number. Due to strangeness contamination, a lambda hyperon is free from Pauli's exclusion principle. So it can explore the nuclear matter deeply and it may give various modifications of nuclear structure such as neutron star.

At present, a lot of data have been accumulated for nucleon-nucleon (NN) interaction. However, unified understanding the baryon-baryon interaction can be obtained by considering both nucleon and hyperons. But, hyperon-nucleon and hyperon-hyperon interactions data are very scarce. So, identification of observed hypernuclei is the most important work.

To develop the field of hypernuclear physics, both theoretical and experimental researches are performing with great effort. This research work is focused on the identification of single- Λ hypernucleus event by using the emulsion scanning data of J-PARC E07 experiment.

Experimental Procedure of J-PARC E07 Experiment

J-PARC E07 experiment, which stands for Japan Accelerator Research Complex, is aimed to improve the roles of material science, life science, nuclear physics and particle physics, especially in astrophysics. J-PARC E07 experiment was performed at K 1.8 beam line in J-PARC Hadron hall.

* First Prize(2023)

¹ Department of Physics, Kyaukse University

² Departments of Physics, Defence Services Academy

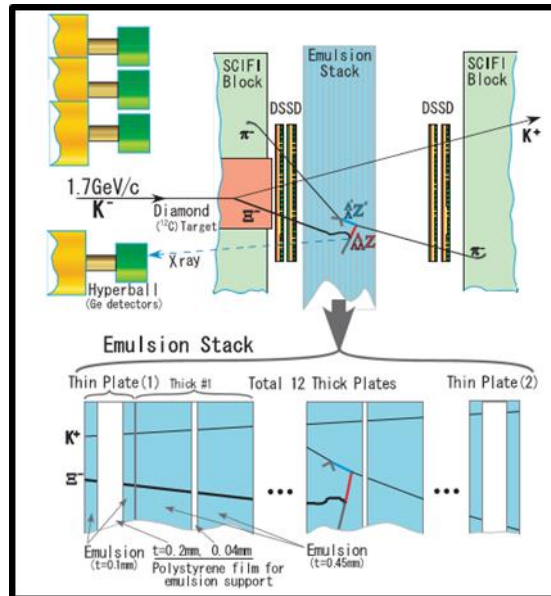


Figure1. Experimental set up of J-PARC E07 Experiment

This experiment is expected to detect approximately 100 double- Λ hypernuclear events among 10,000 Ξ^- stopping events by using hybrid emulsion method [Ekawa H, 2015]. In this experiment, the SSDs (Silicon micro-strip Detectors) and emulsion sheets are main detectors to detect hypernuclei which are the decay products of Ξ^- hyperons.

Beam exposure of J-PARC E07 was carried out in 2016 and 2017. The emulsion plates located between the two spectrometers are used to detect hypernuclei. There are 118 emulsion plates in J-PARC E07 experiment. Each emulsion plate consists of twelve thick emulsion sheets between two thin emulsion sheets. All of the thick and thin emulsion sheets are packed together in a stainless case and fixed tautly by vacuum pumping. Emulsion plates are stored in Kamioka mine located at Japan and surrounded by lead block.

In order to be able to get the exact measurement of ranges of charged particles in nuclear emulsion, it is important to know accurately the stopping power of emulsion for charged particles of various energies and thus establish the relationship between the energy of a charged particle and its range in the emulsion. The tracks of charged particles consist of a lot of silver grains with the size of about $1\mu\text{m}$. The photograph of a nuclear emulsion is shown in figure 3.

Nuclear emulsion is a three dimensional photographic film and a high sensitive particles detector. It is used to detect the trajectories [Morishima K, 2015] of charged particles in three dimensions with submicron resolution. These trajectories are recorded as tracks formed by the ionization process. Tracks of Ξ^- hyperons are searched in first emulsion sheet by the scanning system. Then, tracks are followed in the thick-type emulsion sheets with an automatic tracking system [Soe M K, 2017] by a series of microscopic images along a predicted track. Finally, a three vertices topology found at the end point of the followed track is performed by a detailed analysis.

The Ξ^- tracks are kinematically analyzed with the SSD detector by tagging (K^- , K^+) reaction. The Ξ^- candidate tracks which are consistent with the kinematical analysis are constructed. Only the Ξ^- candidate tracks with high energy deposit in SSD detector are chosen.

These Ξ^- tracks are high stopping probability. The emitted Ξ^- candidate tracks by the emulsion module without forming nuclear reactions are rejected by the downstream SSD detector.

The Ξ^- hyperons entering the emulsion module through the SSDs are traced by an automated scanning system. When the Ξ^- hyperons are predicted, the Ξ^- tracks are searched by scanning the most upstream sheets of emulsion modules within the area of $200\mu\text{m} \times 200\mu\text{m}$. After the human eyes check of the tracks images by the microscope system, we determine the kinematical analysis of decay daughters and identify the nuclear process from the image information. α -tracks decay chains within the thorium series isotopes with largest ranges and largest kinetic energy can be searched by an Overall Scanning Method. At present, the Overall Scanning Method is the appropriate technique to search hypernuclei and the J-PARC experiment is upgraded up to 30 GeV [Yamazaki Y, 2019] of beam energy.

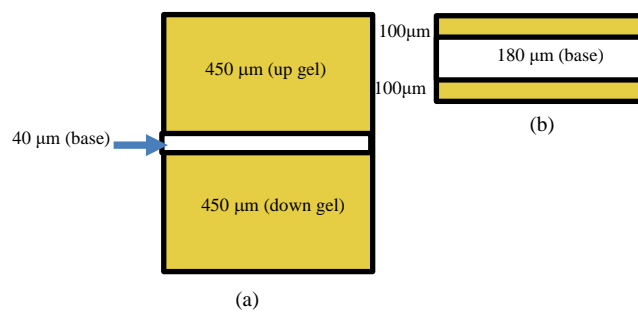


Figure 2. Schematic diagrams of nuclear emulsion in J-PARC E07 experiment; (a) thick emulsion plate and (b) thin emulsion plate

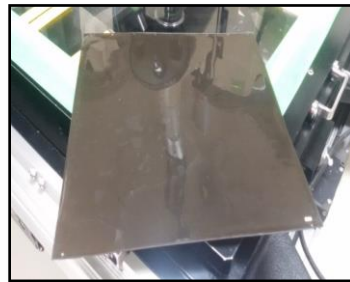


Figure 3. A photograph of a nuclear emulsion

Analysis of a Single- Λ Hypernucleus of J-PARC E07 Experiment

In this paper, a single- Λ hypernucleus event which is observed in J-PARC E07 experiment is kinematically analysed. The analysed event is detected in module #59, plate number #08 of J-PARC E07 experiment. The experimental data are provided by Professor Nakazawa and J-PARC E07 collaborators from Gifu University. Identification of hypernuclei events in nuclear emulsion has great physical interest. To perform this research work, kinematical analysis which is based on relativity theory is used. The detailed method of particles identification process will be presented in this section.

Event Description

In nuclear emulsion, a Ξ^- hyperon is captured by the emulsion nucleus at production point A from which two charged particles tracks #1 and #2 are emitted. At decay point B, track #1 decayed again into two charged particles tracks #3 and #4. This analysed event has two vertex points so that we identified as a single- Λ hypernucleus event. The photograph and schematic diagram of analyzed single- Λ hypernucleus event are presented in figure 4.

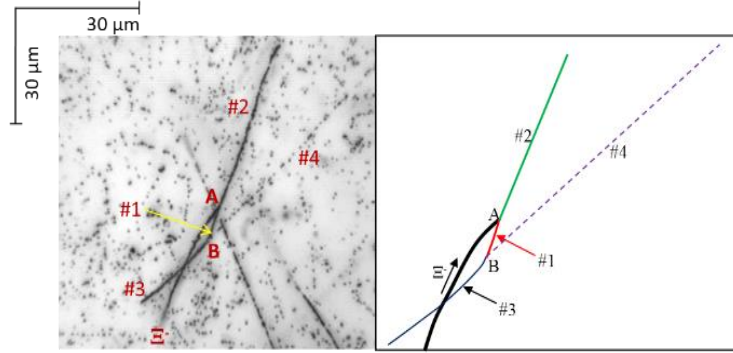


Figure 4. Photograph and schematic diagram of an analysed single- Λ hypernucleus event

Results and Discussions

Calculation of Ranges and Position Angles of Analysed Event

From experimental data, the positions (x, y, z) of tracks charged particles tracks (#1, #2, #3 and #4) were measured by three times. Using these measured data, the ranges formed by each click point for all charged particles tracks are calculated by equation (1).

Position angles of four charged particles tracks are calculated from calculated range values of these charged particles by using equation (2) and (3). The zenith angle θ is defined as the angle between a track of charged particle, range (R), and a verticle line, passing through z-direction. The azimuthal angle ϕ refers to the counter-clockwise angle from x-axis formed when the point is projected onto xy-plane. In equation (1), 'S' represents the shrinkage factor of emulsion plate.

$$R = \sqrt{\Delta x^2 + \Delta y^2 + (\Delta Z.S)^2} \quad (1)$$

$$\theta = \cos^{-1} \left[\frac{\Delta z}{\sqrt{\Delta x^2 + \Delta y^2 + (S.\Delta z)^2}} \right] \quad (2)$$

$$\Phi = \tan^{-1} \left[\frac{\Delta y}{\Delta x} \right] \quad (3)$$

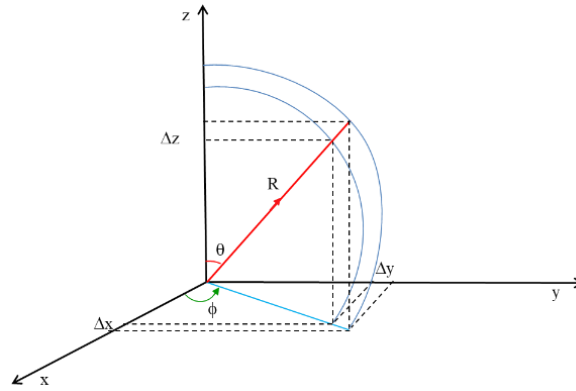


Figure 5. Schematic drawing for position angles θ and ϕ of the emitted charged particles tracks

For the first step of hypernuclei identification, ranges and position angles of four charged particles tracks are obtained from kinematical analysis as shown in table 1.

Table 1. Ranges and position angles of tracks #1, #2, #3 and #4

Vertex	Track	R (μm)	θ (degree)	ϕ (degree)
A	#1	8.33 ± 0.005	81.67 ± 0.59	109.53 ± 2.74
	#2	50.17 ± 0.006	97.35 ± 0.55	294.59 ± 2.45
B	#3	29.20 ± 0.003	65.12 ± 2.35	132.59 ± 0.90
	#4	$>13473.59 \pm 0.79$	109.81 ± 1.67	319.34 ± 0.87

In kinematical analysis, neutral particles emission at production and decay point is necessary to check. So, we performed that neutral particle emission is where or not for both vertices. There is no neutral particles emission at production point according to collinear checking. However, there'll be neutral particles emission at decay point. Thus, one or more neutral particles emission is considered in our analysis at decay point.

Analysis at Decay Point B

At point B, possibility of mesonic and non-mesonic decay is considered to identify track #4. Due to track formation and its range, track #4 may be π^- meson. However, possibility of π^- meson has a little chance according to momentum balance checking. At point B, π^0 meson emission is impossible due to comparison of total kinetic energy and Q-values for all possible decay modes. So, track #4 is identified as a baryon (i.e proton, deuteron, triton, helium and so on). Our analysis is continued as baryon decay and 161 decay modes are obtained. Some examples of non-mesonic decay modes are shown in table 2.

Table 2. Some examples of non-mesonic decay modes

No.	Single- Λ Hypernucleus (Track #1)	Decay Products		
		Track #3	Track #4	Neutral Particles
1	${}^4_{\Lambda}\text{He}$	${}^3_1\text{H}$	${}^1_1\text{H}$	
2		${}^2_1\text{H}$	${}^1_1\text{H}$	n
3		${}^1_1\text{H}$	${}^1_1\text{H}$	2n
4	${}^5_{\Lambda}\text{He}$	${}^3_1\text{H}$	${}^1_1\text{H}$	n
5		${}^2_1\text{H}$	${}^1_1\text{H}$	2n

Then, kinetic energy and momenta of decay products of single- Λ hypernuclei for all possible decay modes are calculated using range-energy software package. Total kinetic energy and Q-values are also calculated and compared using equations (4) and (5).

$$Q \text{ (MeV)} = [M_{\#1} - \{M_{\#3} + M_{\#4} + M_{\text{neutral}}\}]c^2 \times \text{MeV}/c^2 \quad (4)$$

$$KE_{\text{tot}} \text{ (MeV)} = KE_{\#3} + KE_{\#4} + KE_{\text{neutral}} \quad (5)$$

Decay modes with Q-values negative are rejected and 35 decay modes are chosen to continue our analysis. To identify a single- Λ hypernucleus and its decay species, invariant mass, initial mass and binding energy of single- Λ hypernuclei are calculated using equations (6) and (7).

$$M_{\text{invariant}} = M_{\#3} + M_{\#4} + M_{\text{neutral}} + KE_{\#3} + KE_{\#4} + KE_{\text{neutral}} \quad (6)$$

$$M_{\text{initial}} = M_{\Lambda X} + M_{\Lambda} \quad (7)$$

Negative binding energy values of single- Λ hypernucleus are rejected. The invariant masses and binding energies of single- Λ hypernuclei are compared with known experimental values [Bando H, 1990]. Finally, 19 single- Λ hypernuclei (${}^4_{\Lambda}\text{He}$, ${}^5_{\Lambda}\text{He}$, ${}^6_{\Lambda}\text{He}$, ${}^8_{\Lambda}\text{He}$, ${}^6_{\Lambda}\text{Li}$, ${}^7_{\Lambda}\text{Li}$, ${}^8_{\Lambda}\text{Li}$, ${}^9_{\Lambda}\text{Li}$, ${}^9_{\Lambda}\text{Be}$, ${}^{10}_{\Lambda}\text{Be}$, ${}^{11}_{\Lambda}\text{B}$, ${}^{12}_{\Lambda}\text{B}$, ${}^{13}_{\Lambda}\text{B}$, ${}^{12}_{\Lambda}\text{C}$, ${}^{13}_{\Lambda}\text{C}$, ${}^{14}_{\Lambda}\text{C}$, ${}^{14}_{\Lambda}\text{N}$, ${}^{15}_{\Lambda}\text{N}$ and ${}^{16}_{\Lambda}\text{O}$) can be accepted at decay point B from 27 decay modes.

Analysis at Production Point A

Our analysis is extended for production point A depending on 19 single- Λ hypernuclei from point B. At production point A, all possible production modes are considered. Ξ^- hyperon is captured by ${}^{12}_6\text{C}$ or ${}^{14}_7\text{N}$ or ${}^{16}_8\text{O}$ emulsion nucleus. Charged particles tracks #1 and #2 are emitted at point A and one free lambda hyperon is escaped at point A. Therefore, 53 possible production modes are obtained. Some examples of possible production modes with their decay modes are presented in table 3.

Table 3. Some examples of possible production modes

No.	Production Mode	Decay Mode
1	$\Xi^- + {}^{14}_7\text{N} \rightarrow {}^4_\Lambda\text{He} + {}^{10}_4\text{Be} + \Lambda$	${}^4_\Lambda\text{He} \rightarrow {}^2_1\text{H} + {}^1_1\text{H} + n$
2	$\Xi^- + {}^{12}_6\text{C} \rightarrow {}^5_\Lambda\text{He} + {}^7_3\text{Li} + \Lambda$	${}^5_\Lambda\text{He} \rightarrow {}^3_1\text{H} + {}^1_1\text{H} + n$
3	$\Xi^- + {}^{14}_7\text{N} \rightarrow {}^5_\Lambda\text{He} + {}^9_4\text{Be} + \Lambda$	
4	$\Xi^- + {}^{16}_8\text{O} \rightarrow {}^5_\Lambda\text{He} + {}^{11}_5\text{B} + \Lambda$	
5	$\Xi^- + {}^{12}_6\text{C} \rightarrow {}^5_\Lambda\text{He} + {}^7_3\text{Li} + \Lambda$	${}^5_\Lambda\text{He} \rightarrow {}^2_1\text{H} + {}^1_1\text{H} + 2n$
6	$\Xi^- + {}^{14}_7\text{N} \rightarrow {}^5_\Lambda\text{He} + {}^9_4\text{Be} + \Lambda$	

Q-value for all possible production modes is calculated. Furthermore, total kinetic energy of all emitted particles is calculated by using range-energy software package and kinetic energy of free lambda particle is calculated by using momentum conservation.

$$\Xi^- + {}^A_Z\text{X} \rightarrow \#1 + \#2 + \Lambda \tag{8}$$

$$Q \text{ (MeV)} = [M_{\Xi^-} + M_c] - [M_{\#1} + M_{\#2} + M_\Lambda] \tag{9}$$

$$KE_{\text{tot}} \text{ (MeV)} = KE_{\#1} + KE_{\#2} \tag{10}$$

$$B_{\Xi^-} = [M_{\Xi^-} + M_c] - [M_{\#1} + M_{\#2} + M_\Lambda + KE_{\#1} + KE_{\#2}] \tag{11}$$

Table 4. Q-value, (KE_{tot}) and (B_Ξ) for some possible production modes

Production Mode	Q-value (MeV)	KE _{tot} (MeV)	B _Ξ (MeV)
$\Xi^- + {}^{14}_7\text{N} \rightarrow {}^4_\Lambda\text{He} + {}^{10}_4\text{Be} + \Lambda$	22.06±0.25	29.14±0.00	-7.08±0.26
$\Xi^- + {}^{12}_6\text{C} \rightarrow {}^5_\Lambda\text{He} + {}^7_3\text{Li} + \Lambda$	6.50±0.25	18.71±0.00	-12.21±0.25
$\Xi^- + {}^{14}_7\text{N} \rightarrow {}^5_\Lambda\text{He} + {}^9_4\text{Be} + \Lambda$	12.93±0.25	28.24±0.00	-15.32±0.26
$\Xi^- + {}^{16}_8\text{O} \rightarrow {}^5_\Lambda\text{He} + {}^{11}_5\text{B} + \Lambda$	8.01±0.25	38.68±0.01	-30.67±0.26
$\Xi^- + {}^{12}_6\text{C} \rightarrow {}^5_\Lambda\text{He} + {}^7_3\text{Li} + \Lambda$	49.11±0.26	18.71±0.00	30.39±0.26
$\Xi^- + {}^{14}_7\text{N} \rightarrow {}^5_\Lambda\text{He} + {}^9_4\text{Be} + \Lambda$	55.53±0.26	28.24±0.00	27.29±0.26

At production point A, the nuclear process takes place energetically so that Q-values of this process should be positive. So, 15 possible production modes with negative Q-values and 6 production modes with negative B_Ξ are rejected and 32 possible production modes are accepted.

Range estimation of charged particle track #4 is continued by comparing with assigned particles. Charged particle track #4 passes through plate number #08 to #02. Therefore, it is not stopped in emulsion plate #02. Because of this fact, stopping point of track #4 is not seen between emulsion plate #02 and #08. That's why, its range must be longer than measured range.

So, estimated range of track #4 needs to be considered. If estimated range of track #4 is shorter than measured range, it is impossible to assign the charged particle track #4. If estimated range of track #4 is very longer than measured range of it, it is also impossible to assign the charged particle track #4. So, estimated range of track #4 should be comparable with measured range of it.

Moreover, it is assumed that track #3 and track #4 is back to back direction emission at decay point. The charged particle track #4 is assigned to be a pi-minus meson, proton, deuteron or triton. Charged particle track #3 is assigned to be ${}^1_1\text{H}$, ${}^2_1\text{H}$, ${}^3_1\text{H}$, ${}^3_2\text{He}$, ${}^4_2\text{He}$, ${}^6_3\text{Li}$, ${}^7_3\text{Li}$, ${}^9_4\text{Be}$, ${}^{10}_4\text{Be}$, ${}^{10}_5\text{B}$, ${}^{11}_5\text{B}$, ${}^{12}_6\text{C}$ or ${}^{12}_6\text{C}$. Range of track #3 is 29.20 μm . Using its range, kinetic energy of track #3 is calculated from range-energy relation. Using its kinetic energy, range of track #4 is estimated by energy-range relation software package.

$$\text{KE}_{\#4} = \frac{P_{\#4}^2}{2M_{\#4}} \quad (12)$$

The estimated ranges of charged particle track #4 are compared with calculated ranges of it. The calculated range of charged particle track #4 is 13479.59 μm . Only 5 production modes with their decay modes are acceptable as shown in table 4. That's why the estimated ranges of other 27 production modes are very smaller than the calculated ranges.

Table 5. The most acceptable possible production modes with their decay modes

Production Mode	Decay Mode	Estimated range of #4 (μm)
$\Xi^- + {}^{14}_7\text{N} \rightarrow {}^{10}_\Lambda\text{Be} + {}^4_2\text{He} + \Lambda$	${}^{10}_\Lambda\text{Be} \rightarrow {}^6_3\text{Li} + {}^1_1\text{H} + 3\text{n}$	17427
$\Xi^- + {}^{14}_7\text{N} \rightarrow {}^{11}_\Lambda\text{B} + {}^3_1\text{H} + \Lambda$	${}^{11}_\Lambda\text{B} \rightarrow {}^9_4\text{Be} + {}^2_1\text{H}$	13899
$\Xi^- + {}^{14}_7\text{N} \rightarrow {}^{12}_\Lambda\text{B} + {}^2_1\text{H} + \Lambda$	${}^{12}_\Lambda\text{B} \rightarrow {}^{10}_4\text{Be} + {}^2_1\text{H}$	17485
$\Xi^- + {}^{16}_8\text{O} \rightarrow {}^{12}_\Lambda\text{B} + {}^4_2\text{He} + \Lambda$	${}^{13}_\Lambda\text{C} \rightarrow {}^{11}_5\text{B} + {}^2_1\text{H}$	17485
$\Xi^- + {}^{16}_8\text{O} \rightarrow {}^{13}_\Lambda\text{C} + {}^3_1\text{H} + \Lambda$		34160

Results at Production Point A

Analysis at production point is performed to consistence at decay point B. According to our analysis at production point and decay point, the captured nuclei are accepted as ${}^{14}_7\text{N}$ or ${}^{16}_8\text{O}$. The single- Λ hypernucleus track #1 is accepted as ${}^{10}_\Lambda\text{Be}$ or ${}^{11}_\Lambda\text{Be}$ or ${}^{12}_\Lambda\text{Be}$ or ${}^{13}_\Lambda\text{C}$. The most acceptable production modes with their respective decay modes are presented in table 5.

Estimated ranges of acceptable production modes are longer than that of calculated and measured ranges and comparable with calculated range of charged particle track #4

Table 6. The calculated Q-value, total kinetic energy and binding energy for possible production modes

Production Mode	Q-value (MeV)	KE _{tot} (MeV)	B _Ξ (MeV)
$\Xi^- + {}^{14}_7\text{N} \rightarrow {}^{10}_\Lambda\text{Be} + {}^4_2\text{He} + \Lambda$	17.10 ± 0.21	9.64 ± 0.00	7.46 ± 0.21
$\Xi^- + {}^{14}_7\text{N} \rightarrow {}^{11}_\Lambda\text{B} + {}^3_1\text{H} + \Lambda$	69.41 ± 0.00	4.07 ± 0.00	65.34 ± 0.01
$\Xi^- + {}^{14}_7\text{N} \rightarrow {}^{12}_\Lambda\text{B} + {}^2_1\text{H} + \Lambda$	69.49 ± 0.16	3.61 ± 0.00	65.88 ± 0.17
$\Xi^- + {}^{16}_8\text{O} \rightarrow {}^{12}_\Lambda\text{B} + {}^4_2\text{He} + \Lambda$	72.60 ± 0.16	9.58 ± 0.00	63.02 ± 0.17
$\Xi^- + {}^{16}_8\text{O} \rightarrow {}^{13}_\Lambda\text{C} + {}^3_1\text{H} + \Lambda$	57.74 ± 0.00	4.01 ± 0.00	53.73 ± 0.01

The charged particle track #2 is accepted as ${}^2_1\text{H}$ or ${}^3_1\text{H}$ or ${}^4_2\text{He}$. The charged particle track #3 is accepted as ${}^6_3\text{Li}$ or ${}^9_4\text{Be}$ or ${}^{10}_4\text{Be}$ or ${}^{11}_5\text{B}$. The charged particle track #4 is accepted as ${}^1_1\text{H}$ or ${}^2_1\text{H}$. From the most acceptable 5 production modes with their respective decay modes, only one production mode is identified. Because only two charged particles are emitted at decay point B for the other 4 production modes. If only charged particle is emitted at the decay point, Q-value and KE_{tot} should be comparable. But, Q-values are greater than KE_{tot} at the other 4 decay modes. So, these decay modes are rejected. Finally, the captured nucleus is identified as ${}^{14}_7\text{N}$ at production point A. The charged particle track #2 is identified as ${}^4_2\text{He}$ at production point A.

Results at Decay Point B

At decay point B, we accepted four decay modes depending on five production modes. For those four decay modes, Q-value and total kinetic energy for decay species are compared. Furthermore, invariant mass and known experimental mass of single- Λ hypernucleus track #1 are compared. Moreover, binding energy of single- Λ hypernucleus is also calculated and compared with known experimental binding energy. At the end of our analysis, we can identify only one decay modes at point B as ${}^{10}_\Lambda\text{Be} \rightarrow {}^6_3\text{Li} + {}^1_1\text{H} + 3n$. So, the single- Λ hypernucleus track #1 is identified as ${}^{10}_\Lambda\text{Be}$ at point B and the charged particle track #3 is identified as ${}^6_3\text{Li}$ at that point. The charged particle track #4 is identified as proton (${}^1_1\text{H}$) from decay point. At decay point B, single- Λ hypernucleus ${}^{10}_\Lambda\text{Be}$ decay into two charged particles (${}^6_3\text{Li}$ and ${}^1_1\text{H}$) with contamination of three neutrons. Particles identification of this research is summarized in table 7.

Table 7. Particles identification at production point A and decay point B

Production point A			Decay point B		
Captured nucleus	Track #2	Track #1 (Single- Λ hypernucleus)	Track #3	Track #4	Neutral particles
$^{14}_7\text{N}$	^4_2He	$^{10}_{\Lambda}\text{Be}$	^6_3Li	^1_1H	3 n

Q-value is 138.78 ± 0.23 MeV, total kinetic energy of decay species is $>143.78 \pm 0.01$ MeV and, invariant mass, initial mass, known experimental mass, binding energy and known experimental binding energy of single- Λ hypernucleus $^{10}_{\Lambda}\text{Be}$ are $> 9504.31 \pm 0.21$ MeV/c², 9510.48 ± 0.00 MeV/c², 9499.33 ± 0.23 MeV/c², $< 6.71 \pm 0.21$ MeV and 9.11 ± 0.22 MeV.

Conclusion

The main purposes of strangeness hypernuclear physics are to extend the strangeness nuclear chart and to understand the structures of multi-strangeness systems. Therefore, the basic concepts of the hypernuclear physics are studied and collaborated in the hypernuclear experiments.

Present research work is focused on the identification of single- Λ hypernucleus event by using the emulsion scanning data of J-PARC E07 experiment. According to the decay topology of this event, a single- Λ hypernucleus event is firstly identified. But the kinematical analysis is inevitably needed to identify this event. That's why, present analysis is performed starting from range calculation to binding energy calculation of a single- Λ hypernucleus.

In this work, the ranges and position angles of the analysed event were calculated by using the experimental data from J-PARC E07 experiment. A single- Λ hypernucleus event can be identified by its decay topology and the decay daughters of a single- Λ hypernucleus have to be known. So, possible mesonic or non-mesonic decays are considered and checking the possibility of track #4 is the main analysis of particle identification.

From the present research, it can be obtained useful information for Λ -N interaction. Hypernuclear physics is now developing and it is necessary to get more and more information and data on hypernuclear production, decay, life time, mass and binding energy, etc. The present research can support those data to hypernuclear physics group.

Acknowledgements

I would like to thank Professor Nakazawa, Head of Physics Department, Gifu University, and all collaborators of J-PARC E07 experiment for their discussions, supports and valuable advices to carry out hypernuclear research.

References

- Bando H, Motoba T and Zofka J (1990), "Production, Structure and Decay of Hypernuclei", *International Journal of Modern Physics A*, Vol. 5, pp 4021-4198.
- Ekawa H et al., (2015), "Observation of a $_{\Lambda\Lambda}\text{Be}$ double- Λ hypernucleus in the J-PARC E07 experiment," *Prog. Theor. Exp. Phys.* DOI: 10.1093/ptep/0000000000.
- Morishima K (2015), "Latest Developments in Nuclear Emulsion Technology," 26th International Conference on Nuclear Tracks in Solids, 26ICNTS, *Physics Procedia* 80 pp 19-24.
- Soe M K, et al.(2017), *Nucl. Instrum. Methods Phys. Res. Sect. A* 848, pp 66-72.
- Yamazaki Y, J-PARC, KEK and JAEA, Japan (2020), "From KEK-PS To J-PARC."

BOOST FOR MAINTENANCE OF MINI-SOLAR MODULES QUALITY DUE TO ACID RAIN*

Noe Noe Honey¹, Saw Linn Oo², Yin Maung Maung³

Abstract

The impact of acid rain on the potential induced degradation (PID) and subsequent recovery of mini-solar modules was investigated over varying durations. The acid rain with a pH of 4 was prepared and immersed mini-solar modules (12.5 cm x 7.2 cm) in it for 2, 4, and 5 days. The initial degradation of the mini-solar modules was assessed through photocurrent measurements under different lighting conditions. Following this, we subjected the modules to a recovery process, annealing them for 30 minutes at 50°C, and reevaluated their performance through photocurrent measurements. Additionally, the surface characteristics of these modules were explored using electroluminescence images during different daytime settings. This entire procedure was repeated for double degradation and recovery. Our experimental findings suggest that a simple low-temperature method can effectively restore degraded mini-solar modules to their original state.

Keywords: potential induced degradation (PID), acid rain, solar modules, recovery

Introduction

High energy efficiency, a low rate of degradation, cost effectiveness, and a long lifespan of more than 30 years must be necessary for common solar cells. If the PV modules are not resisting degradation, the mechanism may result in losses of 20 % in less than a year [1]. PV modules have experienced degradation and failure in recent years, leading to PID and performance losses in a short amount of time[2-3]. It is remarkable for quality control in solar cells with regard to PID [4]. PID was generally described as a loss of power behavior that results from N-ion migration in solar modules [5-6]. In its most significant form, the shunting of solar modules in PID-affected regions caused an instantaneous reduction in solar modules [7]. A new and difficult credibility issue for solar modules has been identified as one of the degradation mechanisms, PID, which deteriorates the photovoltaic performance of crystalline Si-based solar cells over an extended period of time [8-10]. Actually, various factors such as high-temperature and high-humidity can cause the PID phenomenon to reduce the performance of PV modules and lead to their failure states [11-12]. This paper described the photocurrent and electroluminescence images of the acid rain-induced PID and recovery of mini-solar modules.

Preparation of acid rain

The artificial acid rain was prepared according to the ratio of sulfuric acid (H₂SO₄): nitric acid (HNO₃): hydrochloric acid (HCl) (5:1:1). The mixed solution was adjusted to pH-4 by pH meter. The mini-solar modules were kept in a glass jar filled with acid rain for 2 days (sample 1), 4 days (sample 2), and 5 days (sample 3) to be degraded. These degraded solar modules were recovered by annealing at a low temperature of 50 °C for 30 min. This above processes were done repeatedly for double degradation and double recovery. The artificial acid rain preparation was shown in Fig 1.

* Second Prize(2023)

¹ Department of Physics, University of Yangon

² Department of Physics, University of Yangon

³ Department of Physics, University of Yangon

Photocurrent and EL Measurements

The change in photocurrent as a function of light intensity was observed for the mini-module after degradation as well as recovery. Fig 2 (a-f) gave the variation of photocurrent and light intensity for all mini-modules under degradation-recovery and double degradation-double recovery were compared to those of mini-module at the initial state. From the characteristic curve, it was found that the photocurrent slightly increased with an increase in light intensity for all mini-modules. After degradation, the acid rain-induced affected a module, and the current nominally reached the initial state after recovery.

A high-resolution Electroluminescence (EL) camera was used for the characterization of the mini-solar modules. The EL images for degradation and recovery were described at Fig 3. The EL images for double degradation and double recovery were shown at Fig 4. As a result, no surface feature was found for all samples. The EL pictures of degraded mini-modules were changed a little on the module surface and the recovery nature could not be clearly shown by EL camera.

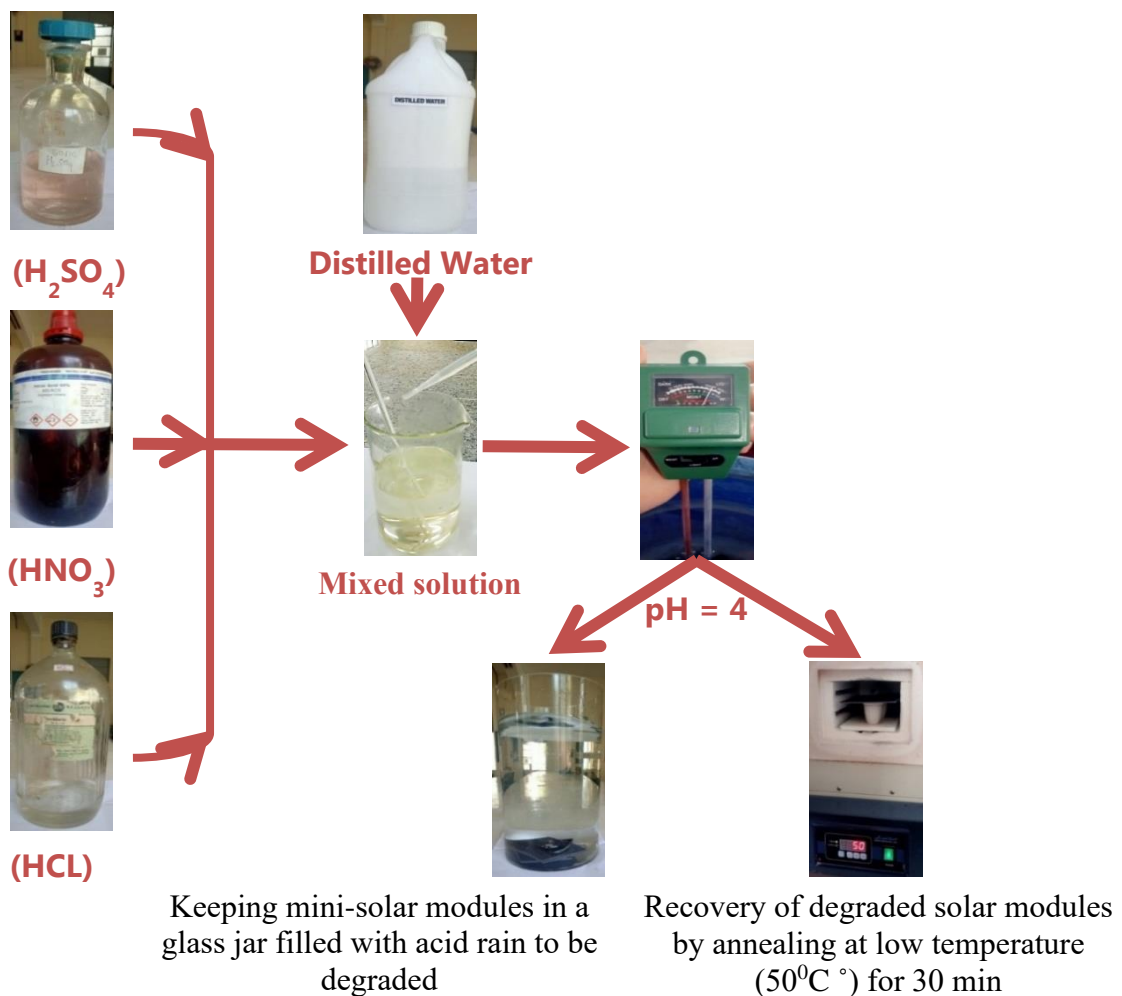
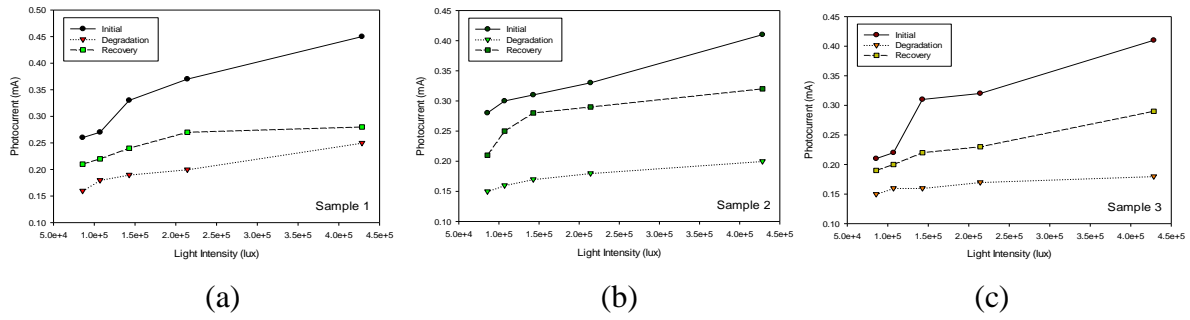


Figure 1 Acid rain preparation, Degradation, and Recovery

Degradation and Recovery



Double Degradation and Double Recovery

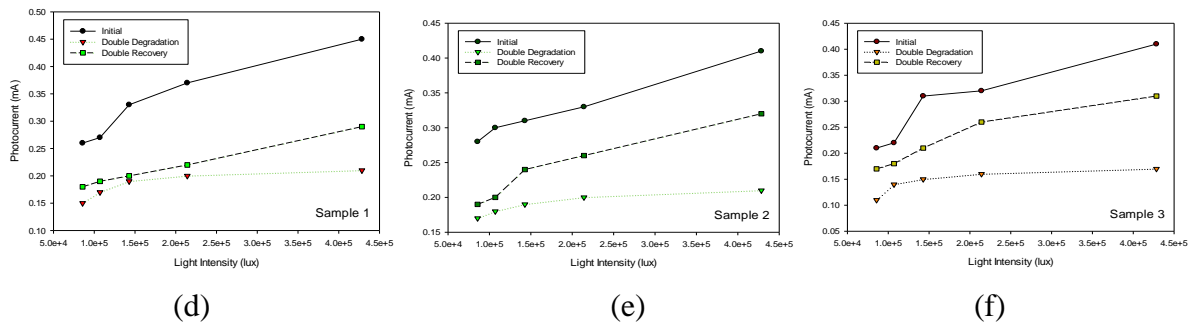


Figure 2 (a-f) Photo I-V characteristic curves corresponding to degradation-recovery and double degradation-double recovery of mini-solar modules

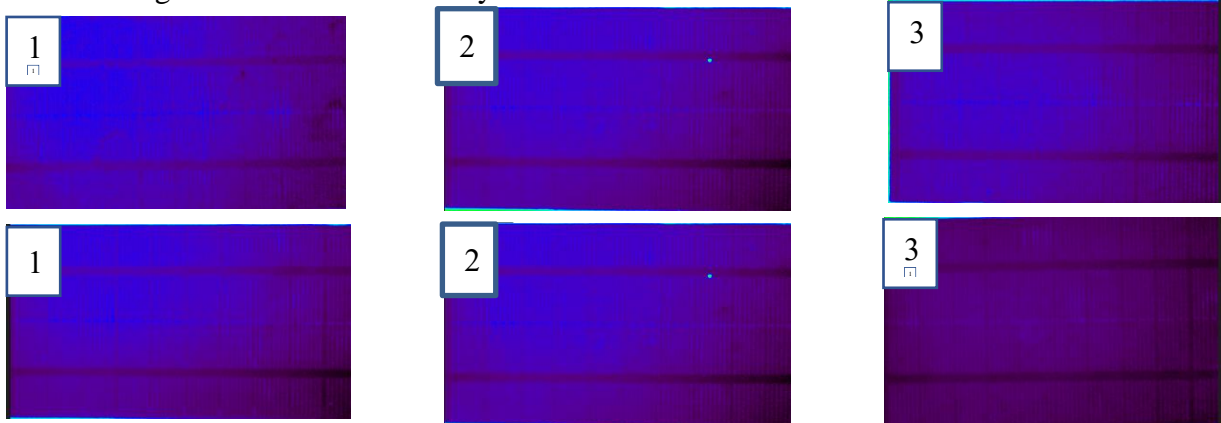


Figure 3 EL images before and after recovery of mini-solar modules

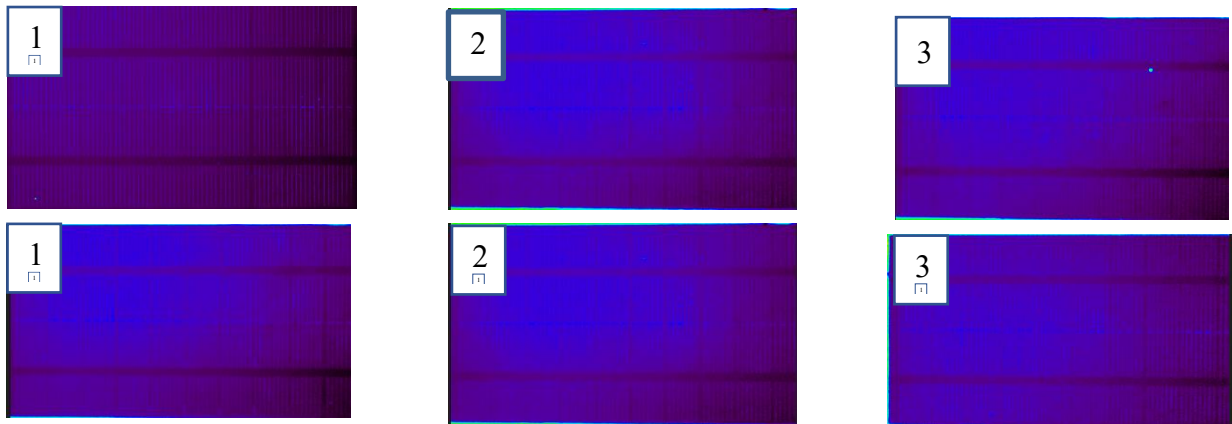


Figure 4 EL images for double degradation and double recovery of mini-solar modules

Conclusion

In contrast to this research, it is important to maintain solar cells over the extended period of time. The I-V characteristics were demonstrated under 1 sun illumination. However, surface damage may be the result of long term PID stress. Degradation must be prevented because acid rain caused damage to the mini-solar module. The purpose of this research was to explain the process of recovering from acid rain-induced solar cell degradation. In this study, photocurrent and EL images were used to analyze PID and recovery with regard to time enhancement under acid rain. The mini-module's photocurrent delivery was decreased due to degradation caused by acid rain. The degradation mechanism is shown by the losses evolution observed on the I-V curves. The findings of this research show that PID increases as the immersed in acid rain time increases. According to EL, the PV solar modules have been affected by the degradation mechanism. Degradation under I-V curves increased further as the amount of time immersed in acid rain increased. Using I-V curves and EL images, different characteristic states (initial, degradation, recovery, double degradation, and double recovery) of solar modules were defined and characterized in relation to acid rain immersion. The simple method under low-temperature treatment is straightforward for recovering damaged solar modules.

Acknowledgment

This research work was done at the Physics Department, University of Yangon, Myanmar (2022-23). Some measurements were performed at the Chemistry Department, University of Yangon, Myanmar

References

- Dhimish, M. (2022) 'Power loss and hotspot analysis for photovoltaic modules affected by potential induced degradation'. doi: 10.1038/s41529-022-00221-9
- Halm, A. *et al.* (2015) 'Potential-induced Degradation for Encapsulated n-type IBC Solar Cells with Front Floating Emitter', in *Energy Procedia*, pp. 356–363. doi: 10.1016/j.egypro.2015.07.050.
- Jang, E., Oh, K. S. and Ryu, S. (2022) 'Reduction of Potential-Induced-Degradation of p-Type PERC Solar Cell Modules by an Ion-Diffusion Barrier Layer Underneath the Front Glass', *Processes*, 10(2). doi: 10.3390/pr10020334.
- Lausch, D. *et al.* (2014) 'Sodium outdiffusion from stacking faults as root cause for the recovery process of potential-induced degradation (PID)', *Energy Procedia*, 55, pp. 486–493. doi: 10.1016/j.egypro.2014.08.013.
- Lee, S. *et al.* (2021) 'Characterization of potential-induced degradation and recovery in cigs solar cells', *Energies*, 14(15), pp. 1–12. doi: 10.3390/en14154628.
- Luo, W. *et al.* (2018) 'Investigation of the Impact of Illumination on the Polarization-Type Potential-Induced Degradation of Crystalline Silicon Photovoltaic Modules', *IEEE Journal of Photovoltaics*, 8(5), pp. 1168–1173. doi: 10.1109/JPHOTOV.2018.2843791.
- Ma, S. *et al.* (2022) 'Effective way to reduce rear-side potential-induced degradation of bifacial PERC solar cells', *Solar Energy Materials and Solar Cells*, 239(October 2021). doi: 10.1016/j.solmat.2022.111687.
- Naumann, V. *et al.* (2013) 'The role of stacking faults for the formation of shunts during potential-induced degradation of crystalline Si solar cells', *Physica Status Solidi - Rapid Research Letters*, 7(5), pp. 315–318. doi: 10.1002/pssr.201307090.
- Naumann, V. *et al.* (2014) 'Explanation of potential-induced degradation of the shunting type by Na decoration of stacking faults in Si solar cells', *Solar Energy Materials and Solar Cells*, 120(PART A), pp. 383–389. doi: 10.1016/j.solmat.2013.06.015.
- Sporleder, K. *et al.* (2021) 'Time-Resolved Investigation of Transient Field Effect Passivation States during Potential-Induced Degradation and Recovery of Bifacial Silicon Solar Cells', *Solar RRL*, 5(7). doi: 10.1002/solr.202100140.
- Xu, L. *et al.* (2022) 'Potential-induced degradation in perovskite/silicon tandem photovoltaic modules', *Cell Reports Physical Science*, 3(9), p. 101026. doi: 10.1016/j.xcrp.2022.101026.
- Yamaguchi, S. *et al.* (2020) 'Influence of emitter position of silicon heterojunction photovoltaic solar cell modules on their potential-induced degradation behaviors', *Solar Energy Materials and Solar Cells*, 216. doi: 10.1016/j.solmat.2020.110716.

A COMPREHENSIVE STUDY ON SYNTHESIS, CHARACTERIZATION, AND ELECTROCHEMICAL PERFORMANCE OF PVA AND PAN-DERIVED CARBON FIBERS FOR ENERGY STORAGE*

Kaung Kyaw Naing¹ and Ye Chan²

Abstract

This research investigates the synthesis, characterization, and electrochemical performance of electrospun carbon fibers derived from Polyvinyl Alcohol (PVA) and Polyacrylonitrile (PAN) precursors under a nitrogen atmosphere. The electrospinning process produces nanofiber mats, which are subsequently carbonized in a nitrogen environment to form carbon fibers. Comprehensive characterization using Raman spectroscopy, Energy Dispersive X-ray Fluorescence (EDXRF), X-ray Diffraction analysis (XRD), and Scanning Electron Microscopy (SEM) elucidates their structural and elemental properties. The synthesized carbon fibers are then prepared for electrodes, and their electrochemical properties, including specific capacitances and energy densities are evaluated. This research seeks to determine the suitability of PVA and PAN-based carbon fibers for advanced energy storage applications, potentially advancing the development of high-performance super capacitors and batteries for sustainable energy solutions

Keywords: Carbon fibers, electro spinning, cyclic voltammetry, energy storage.

Introduction

In an era marked by the ever-increasing demand for sustainable energy solutions, the exploration and development of advanced materials for energy storage applications have become paramount. Carbon fibers, owing to their exceptional properties, have emerged as promising candidates in this pursuit. This research proposal embarks on a comprehensive investigation into the synthesis, characterization, and electrochemical evaluation of electro spun carbon fibers derived from two distinct precursors: Polyvinyl Alcohol (PVA) and Polyacrylonitrile (PAN). These carbon fibers, synthesized under a nitrogen-rich environment, hold the potential to revolutionize the landscape of energy storage devices, such as super capacitors and batteries.

The process begins with the electro spinning of PVA and PAN solutions, yielding nanofiber mats that serve as the foundational materials for subsequent carbonization. Carbonization is executed in a nitrogen atmosphere, a critical step that imparts unique properties to the resulting carbon fibers. The structural and elemental properties of these fibers are meticulously investigated through advanced techniques, including Raman spectroscopy, X-ray Diffraction (XRD) analysis, and Scanning Electron Microscopy (SEM).

Furthermore, this research endeavors to bridge the gap between material synthesis and practical application by integrating these carbon fibers into electrodes. Through a thorough electrochemical evaluation, encompassing specific capacitance and impedance measurements, we aim to gain a deep understanding of their performance in real-world energy storage scenarios.

Ultimately, this research aspires to elucidate the potential of PVA-derived and PAN-derived carbon fibers as high-performance materials in the realm of energy storage. The insights garnered from this study hold the promise of propelling the development of sustainable and efficient energy storage solutions, contributing significantly to our collective journey towards a greener and more energy-conscious future.

* Third Prize(2023)

¹ Department of Physics, University of Yangon

² Universities, Research Center, University of Yangon

Materials and Methods

Materials

The chemical reagents used were polyvinyl alcohol (PVA) (Mw 80,000), polyacrylonitrile (PAN), dimethylformamide, iodine and distilled water in pure condition for preparing nanofibers. Potassium Chloride (KCL) (1 M) solution was used as electrolyte solution.

Characterization

The characterization of PVA-derived and PAN-derived carbon fibers were analyzed by X-ray diffractometer (Rigaku-RINT 2000). Raman spectra of PVA and PAN carbon fibers were also recorded with Horiba Lab RAM HR Evolution. The surface morphology of the PVA and PAN carbon fibers were examined with Scanning Electron Microscope (JEOL-JSM 5610LV). The cyclic voltammetry (CV) were measured using a three electrodes system to analyze the characteristics of the capacitance, impedance, electrical adsorption, and desorption of the fabricated PVA and PAN carbon fibers electrodes.

Experimental

Preparation of Electrospun Fibers

Polyvinyl Alcohol (PVA) 13 wt% solutions were prepared by dissolving PVA powder 13 g in 100 ml of distilled water. PVA powder was stirred into the distilled water at room temperature for 30 min. Then the temperature was gradually raised to 80°C while the mixture was constantly stirred for 5 hrs to obtain homogenize the solution. The transparent PVA solutions obtained were refrigerated overnight. Polyacrylonitrile (PAN) 6 wt% was dissolved in DMF solution. This mixture was continuously stirred at 60°C for 3 hrs until a homogeneous solution was obtained and then cooled down to room temperature.

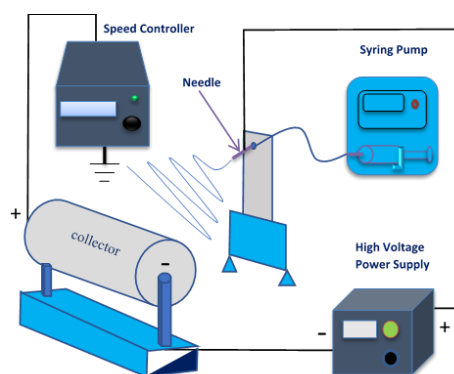
Electrospinning method was used for the preparation of nanofibers. PVA and PAN solutions were loaded into the syringe which is connected to a needle via a flexible tube. The needle was connected to a high-voltage DC power supply. The syringe was loaded to the syringe pump to control the flow rate of the solution. After switching on the power supply and syringe pump, PVA and PAN fibers were collected to the rotating collector which was covered by aluminum foils. The processing parameters were given in table 1. The fiber collection time was set to 3 hrs. Finally, PVA and PAN fibers were found on the aluminum foils.

Carbonization

Before carbonization process, firstly PVA fibers were heated ionization treatment. Electrospun PVA fibers were iodized by adding iodine crystals into a closed glass vessel for 24 hrs at 80°C. During the heating, the iodine was vaporized in that vessel. The color of the samples became dark brown due to complex formation of the sample with iodine. After that, OTF-1200X-S high temperature vacuum tube furnace was used for the carbonization process. Carbon fiber synthesis was performed into two-step calcination process. The softening point of PVA fibers were accepted at 215–224°C. Thus, to obtain a stable process, pre-heat treatment should be employed before the carbonization due to the fusion of the nanofibers at high temperatures. Firstly iodinated PVA fibers were calcinated for 1 hr at 180 °C under atmospheric conditions. Then, the second calcination step was carried out at 500°C for 6 hrs with 5°C min⁻¹ heating rate under nitrogen environment.

Table 1 Processing parameters for electrospinning

voltage	15 kV
flow rate	0.2 mL/hr
needle-to-collector distance	15 cm
collector geometry and velocity	Cylinder, 8 m/s
Needle diameter	0.2 mm
Temperature	31 °C
Humidity	42 %

**Figure 1.** Electrospinning system setup

The carbonization process plays a crucial role in the manufacture of carbon fibers derived from Polyacrylonitrile (PAN). Prior to carbonization, PAN precursor fibers undergo a critical stabilization phase. This involves subjecting the fibers to heat in an oxidizing environment, typically air, at a temperature of 280°C for a duration of 1 hour, using a heating rate of 5°C per minute. During stabilization, the PAN molecules undergo cross-linking and cyclization reactions, reinforcing the fibers and reducing their susceptibility to shrinking during the subsequent carbonization stage. Following stabilization, the PAN fibers are advanced to the carbonization step, conducted at even higher temperatures within an inert atmosphere. Specifically, carbonization is carried out at a temperature of 950°C for a duration of 1 hour, with a heating rate of 5°C per minute in a nitrogen environment. This process entails the pyrolysis of the PAN fibers, leading to the elimination of most non-carbon elements such as hydrogen, oxygen, and nitrogen in the form of volatile gases. Consequently, this transformation results in the PAN fibers evolving into a state of nearly pure carbon, characterized by a hexagonal graphite-like crystal structure.

Praperation of Electrodes

To prepare electrode materials, Copper tape was chosen to be used as a substrate because of its high electrical conductivity and low cost. The copper tape was cut into a 5 mm squares and then attached to acrylic sheets to make a flat and insulated surface on another side of electrode. The PVA-derived carbon fibers and PAN-derived carbon fibers were coated on the copper using spin coating method. The coated electrodes were dried at 70 °C in a drying oven for 30 mins to remove all organic solvents remaining in the micro pores of the electrode.

Results and Discussion

Morphology Analysis by Scanning Electron Microscope

The scanning electron microscope (SEM) images of carbon fibers reveal several important characteristics that are vital for understanding the material's structure and quality.

The average diameter of PVA-derived and PAN-derived carbon fibers are 339 ± 11 nm and 464 ± 13 nm respectively as shown in Fig 2. The size distribution of carbon fibers in the SEM images can be determined from σ values which are 138.9 ± 40.1 for PVA and 186.9 ± 33.7 PAN based carbon fibers respectively. Although PVA fibers have less diameter than PAN fibers they have wider range of size distribution. In the preparation of polymer solutions, PAN was dissolved in the DMF solution which has faster rate of evaporation than water that used in PVA solution. So, the fiber size of PAN is larger than that of PVA. This range indicates that the fibers in the sample are relatively uniform in size, with a slight variation around the mean. The narrow size distribution suggests a consistent manufacturing process or controlled growth conditions for the fibers.

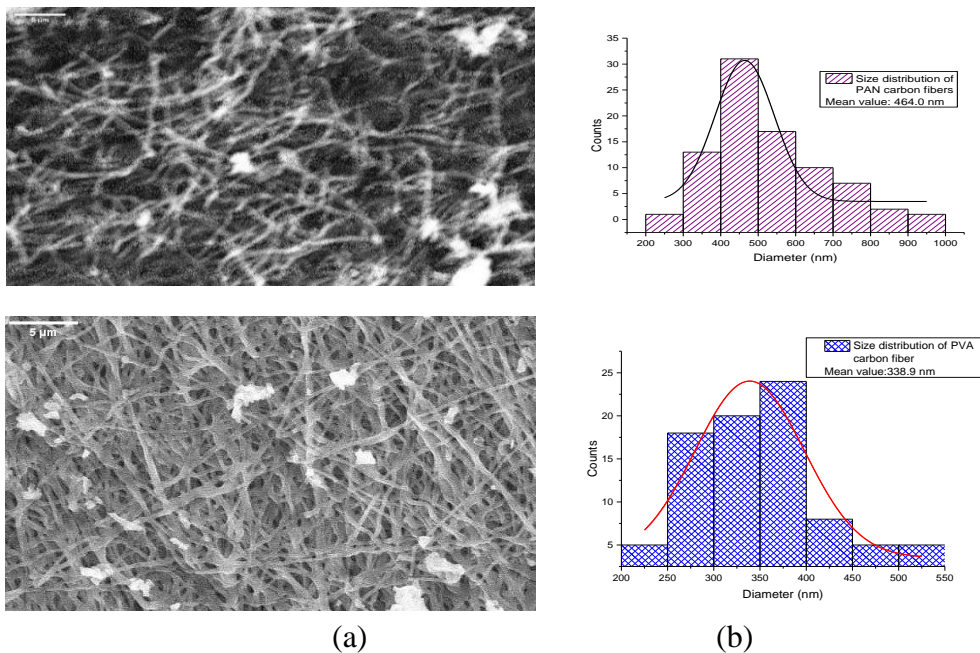


Figure 2. SEM images and fiber size distributions of (a) PVA-derived and (b) PAN-derived carbon fibers

The SEM images also reveal that the formation of the carbon fibers is irregular. This irregularity can manifest as variations in fiber diameter, branching, or twists and turns in the fiber structure. Irregular fiber formation can occur due to factors such as variations in growth conditions. Another noteworthy observation from the SEM analysis is the absence of significant residual materials or contaminants on the surface of the carbon fibers. This finding suggests that the manufacturing or preparation process effectively removes impurities or residues, ensuring the purity and quality of the carbon fibers. The SEM analysis of the carbon fiber sample provides valuable insights into its size distribution, irregular fiber formation, and the absence of significant residuals. These findings are essential for both quality control and optimizing the material for current research.

XRD Analysis

The XRD pattern of PVA-derived and PAN-derived carbon fibers shown in figure 3 were obtained from X-ray diffraction analysis. The sharp peaks of PVA-derived carbon fibers at 2θ values of $\approx 26.6^\circ$ corresponded to the reflection from the (002) plane was observed in XRD spectrum of carbon. The pattern revealed that the phase precipitated out in the sample was hexagonal structure. The observed characteristic diffraction peaks at $2\theta \approx 25.6^\circ$ was corresponded to (002) crystalline plane of the PAN-derived carbon fibers. The (002) diffraction peak between individual carbon layers was an indicator of the degree of carbonization. (Eluyemi *et al.*, 2016).

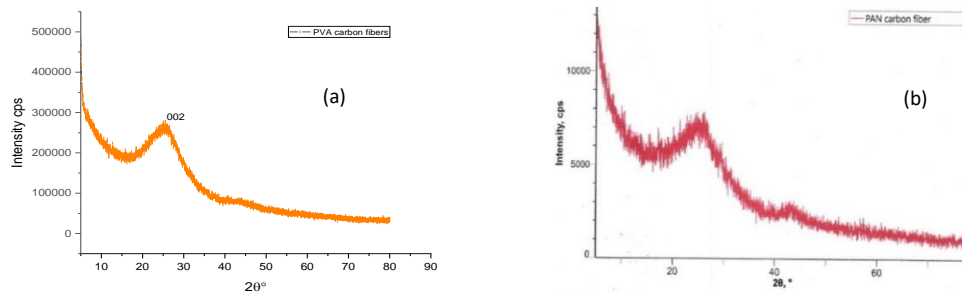


Figure 3. XRD patterns of (a) PVA-derived and (b) PAN-based carbon fibers

Raman Spectroscopy Analysis

Raman spectroscopy serves as an effective technique for assessing the proportions of structured and disordered regions within carbon-based structures (Choi, 2010). Fig. 3 displays Raman spectra for carbon fibers synthesized from PVA and PAN, highlighting distinctive characteristics. The carbon lattice for PVA-derived fibers appears at 1580.43 cm^{-1} , while PAN-based fibers exhibit it at 1559.21 cm^{-1} ; both correspond to C=C stretching vibrations inherent to sp^2 -bonded carbon atoms. Conversely, the D band at 1344.26 cm^{-1} (PVA-derived) and 1327.32 cm^{-1} (PAN-derived) arises from phonon modes originating from sp^2 -bonded carbon atoms situated near localized lattice distortions (defects) in the graphitic network. The ratio of D to G bands (I_D/I_G) serves as an indicator of graphene material defects, with PVA-based and PAN-based carbon fibers displaying intensity ratios of 0.84 and 0.85, respectively. Furthermore, the presence of a peak at 2796.09 cm^{-1} in the PAN-based carbon fiber's 2D band spectrum indicates C-H stretching within PAN.

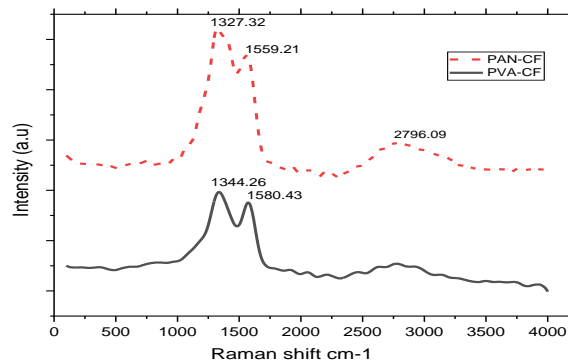


Figure 4. Raman spectra of PVA-based and PAN-based carbon fibers

Electrochemical Characterizations

The microstructural analysis and ion transport behavior of the electrospun carbon fibers materials were analyzed by cyclic voltammetry. The cyclic voltammetry (CV) prepared electrodes were carried out in KCl (1 M) electrolyte solution with three-electrode cell setup. The curves obtained in cyclic voltammetry for different scan rates: 0.1, 0.2, 0.4, 0.6, 0.8 and 1.0 Vs^{-1} are described in Fig.5(a) and (b), and the graphs show the battery nature rather than the pseudocapacitive behavior of the electrodes. By increasing scan rate, the cathodic peaks move towards lower potential whereas the anodic peaks shift towards higher voltage proposing an electrochemical reversibility. In the cyclic voltammograms of PVA-derived carbon electrode, there are double reduction and oxidation peaks. The main reason is electrochemical reactions of the iodine residuals in carbon fiber. PVA fibers were made by iodine treatment to enhance the stability during the carbonization process. The EDXRF analysis of PVA-derived carbon fibers gives the information of iodine and nitrogen residual in the sample. Iodine is known to undergo reversible redox reactions in the presence of various electrolytes. The presence of residual in the carbon fiber can lead to redox processes that appear as distinct peaks in the CV curve. Nitrogen doping can also introduce new redox-active sites on the carbon material. These nitrogen-containing functional groups can undergo redox reactions at specific potentials, resulting in additional peaks in the CV curve. There are extra reduction peaks in PAN-derived carbon fiber's voltammogram. Nitrogen doping can modify the electronic structure of carbon materials. Depending on the type and concentration of nitrogen dopants, it can change the conductivity and electron transfer kinetics of the electrode, leading to variations in the CV response.

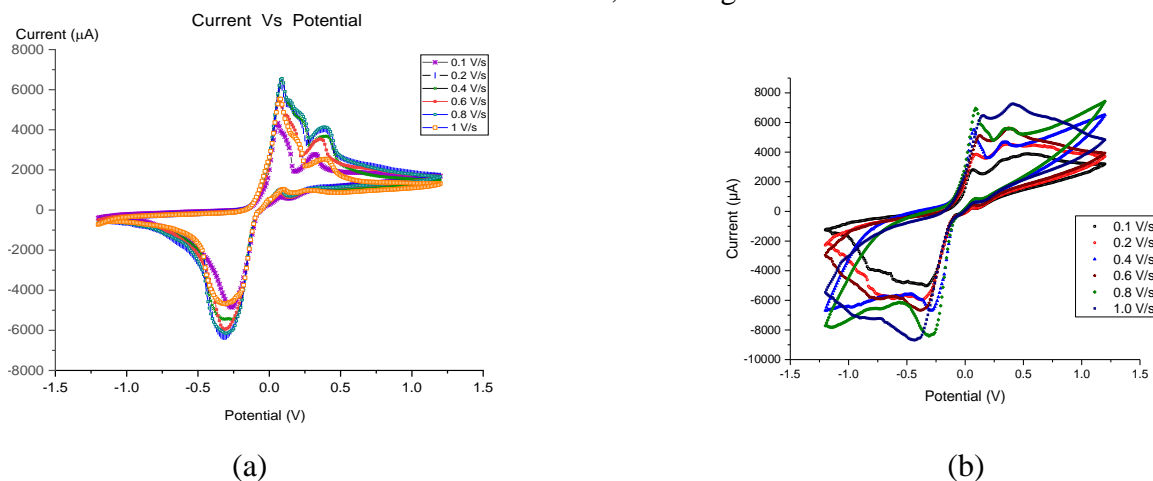


Figure 5. Cyclic voltammograms of (a) PVA-derived and (b) PAN-derived carbon fibers

The specific capacitance values of PVA-derived carbon fiber and PAN-derived carbon fiber electrodes were determined from the area enclosed by the CV curve of different scan rates using the following equation.

$$C_p = \frac{A}{2km\Delta V}$$

A is area enclosed by the CV curve, k is a scan rate, m is the mass of the active material and ΔV is the potential window. The results obtained are given in table 2 and Fig 6. At all scan rates, except 0.1V/s the PAN-derived carbon fiber electrodes consistently exhibit a higher specific capacitance (C_p) compared to the PVA-derived electrodes. This suggests that the PAN-

derived carbon fibers have a greater ability to store electrical charge per unit mass than PVA-derived fibers.

The differences in specific capacitance can be attributed to variations in the microstructure, surface area, and chemical properties of the two types of carbon fibers. It's evident that as the scan rate increases, both types of carbon fibers experience a decrease in specific capacitance. This behavior is typical for supercapacitor electrodes, where higher scan rates may limit the kinetics of charge storage, resulting in reduced capacitance. The PVA-derived fibers exhibit a more significant drop in specific capacitance with increasing scan rate compared to the PAN-derived fibers. This suggests that the PAN-derived fibers may have better charge kinetics or ion diffusion characteristics.

Energy density (E_g) is a crucial parameter as it quantifies the amount of energy a supercapacitor can store per unit mass. In terms of energy density, the PAN-derived carbon fibers consistently outperform the PVA-derived fibers across higher scan rates. This implies that for energy storage applications, the PAN-derived carbon fibers are more favorable due to their higher energy density. The data highlights that PVA-derived carbon fibers offer superior specific capacitance and energy density compared to PAN-derived fibers at lower scan rate. On the other hand, PAN based fibers have better performance than PVA ones. However, the choice of carbon fiber should consider other practical factors as well as specific application requirements.

Table 2. Specific capacitances and energy densities of the carbon fibers electrodes

Scan rate (V/s)	PVA-derived carbon fiber		PAN-derived carbon fiber	
	Cp (F/g)	E_g (J/g)	Cp (F/g)	E_g (J/g)
0.1	19.09	54.99	12.80	36.85
0.2	4.40	12.67	8.52	24.53
0.4	2.92	8.42	5.94	17.11
0.6	2.25	6.49	3.41	9.82
0.8	1.72	4.96	2.70	7.77
1.0	1.21	3.49	2.55	7.35
1.2	0.80	2.31	2.85	8.21

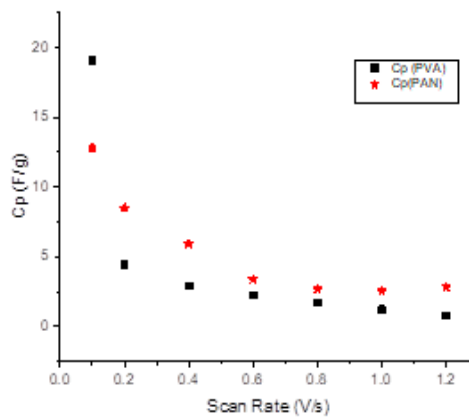


Figure 6. Dependence of specific capacitances of carbon fibers on scan rates

Conclusion

In this study, a comprehensive analysis of carbon fibers was conducted using various techniques, including scanning electron microscopy (SEM), X-ray diffraction (XRD), Raman spectroscopy, and electrochemical characterizations, providing valuable insights into their structural and performance characteristics. SEM images revealed that the carbon fibers exhibited a relatively uniform size distribution, indicating consistent manufacturing processes and high purity, as the absence of contaminants on their surfaces was observed. XRD analysis confirmed their crystalline nature and provided information on the degree of carbonization.

Raman spectroscopy indicated the presence of ordered and disordered regions within the carbon fibers, with both PVA-derived and PAN-derived fibers showing similar levels of disorder. Additionally, nitrogen doping was identified in PAN-derived fibers, influencing their electronic structure and electrochemical behavior. Electrochemical characterizations through cyclic voltammetry revealed battery-like behavior with redox reactions involving iodine residuals in PVA-derived fibers and nitrogen-containing functional groups in PAN-derived fibers. Specific capacitance and energy density varied with scan rates, with PVA-derived fibers excelling at lower rates and PAN-derived fibers outperforming at higher rates.

In summary, this research underscores the importance of tailoring carbon fiber selection to specific application requirements. PVA-derived fibers offer advantages in specific capacitance and energy density at lower scan rates, while PAN-derived fibers excel under high-rate conditions. These findings contribute to a better understanding of carbon fiber properties, guiding their utilization in diverse applications, such as energy storage and composites, with potential for further optimization.

Acknowledgement

This work was supported by the International Science Programme (ISP), Uppsala University (IPPS:MYA-02).

References

- Alwan, T. J., Z. A. Toma, M. A. Kudhier, and K. M. Ziadan, (2016). "Preparation and Characterization of the PVA Nanofibers produced by Electrospinning". *Madridge Journal Nanotechnology and Science*, vol.1(1), pp.1-3
- Andrijanto, E., S. Shoelarta, G. Subiyanto, and S. Rifki, (2016). "Facile synthesis of graphene from graphite using ascorbic acid as reducing agent," *AIP Conf. Proc.*, vol. (1725)
- Cao, N. and Y. Zhang, (2015). "Study of Reduced Graphene Oxide Preparation by Hummers' Method and Related Characterization". *J. Nanomater.*, pp.1155-168125
- Choo, K., Y. C. Ching, H. Chuah, S. Julai, and N. Liou, (2016) "Preparation and Characterization of Polyvinyl Alcohol-Chitosan Composite Films Reinforced with Cellulose Nanofiber". pp. 1-16
- Danni, N., T. Sasikumar, and A. Ahamed Fazil, (2016). "Mechanical Properties of Electrospun CNF/PVA Nanofiber Mats as Reinforcement in Polymer Matrix Composites". *International Journal of Applied Chemistry*, vol. 12(2), pp. 107-119
- Eluyemi, M. S., M. A. Eleruja, and A. V. Adedeji, (2016). "Synthesis and Characterization of Graphene Oxide and Reduced Graphene Oxide Thin Films Deposited by Spray Pyrolysis Method". Scientific Research Publishing, vol. (5), pp. 143-154
- Habte, A. T., D. W. Ayele, M. Hu, (2019). "Synthesis and Characterization of Reduced Graphene Oxide (rGO) Started from Graphene Oxide (GO) Using the Tour Method with Different Parameters," *Adv. Mater. Sci. Eng.*, vol. (10)
- Khan, Q. A., A. Shaur, A. Khan, Y. F. Joya and M. S. Awan, (2017). "Characterization of reduced graphene oxide produced through a modified Hoffman method". *Cogent Chem*, vol.3(1), pp.1080-1298980
- Tiwari *et al.*, A. P. (2021). "A Review of Electrospun Carbon Nanofiber-Based Negative Electrode Materials for Supercapacitors". pp. 236–250

AN INNOVATIVE DESIGN OF AN ELECTRONIC DATA ACQUISITION MEASUREMENT SYSTEM

Aung Zaw Myint¹, Nyunt Khat Khat Wai², Kyaw Soe Moe³

Abstract

In this research work, an innovative design of an electronic data acquisition measurement system is developed. The system consists of measuring voltage, resistance, capacitance and temperature. The unique feature of this system is that it can be measured three types of voltages simultaneously and display them on the liquid crystal display (LCD). The measurement result data are displayed on the LCD and stored in the micro secure digital (SD) card. The system is constructed using an Arduino mega 2560 development board, resistors, capacitors, temperature sensor and other electronic components. The system is innovatively designed to measure the electrical characteristics and electronic components.

Keywords: Data acquisition, Arduino ATmega2560, LM 35 sensor, micro SD card, measuring voltage, measuring resistance, measuring capacitance

Introduction

The process of collecting and measuring electrical data in a specific way is called data acquisition. To operate a control system or drive a prototype design for electronics studies, a data acquisition system is essential to obtain various parameters of electrical and physical properties. It is very important to develop or analyses an electronic circuit or to develop material science, thin film technology, developing solar cells and study of semiconductor researches. Data acquisition applications are usually controlled by software programs developed using various general-purpose programming languages such as Assembly, BASIC, C, C++, Fortran, Java, Lab VIEW, Pascal, etc. Data acquisition system is the process of sampling signals into digital numeric values to measure real world physical conditions. Data acquisition system convert analog waveforms into digital values for processing [Floyd, (2006)].

Materials and Method

Arduino Mega 2560 Microcontroller

Arduino microcontroller is a microcontroller built on a single printed circuit board. This board provides all the necessary circuitry for control work, including a microprocessor, I/O circuits; clock generator, random-access memory (RAM) that Stored program memory and required support ICs. The Arduino Mega 2560 includes multiple digital and analog I/O pins and selects the microcontroller used in the circuit for uploading of program code to larger program memory on Arduino developer boards. This code can be created in a high-level programming language. The Arduino mega is the heart of the circuit, a program code to operate the data acquisition system [John, (2013)]. Arduino mega includes 54 digital I/O pins and 16 analog input pins. The Arduino mega board works with a 16 MHz crystal oscillator.

* Special Award(2023)

¹ Department of Physics, Shwebo University

² Department of Physics, Shwebo University

³ Department of Physics, Pyay University

The Arduino mega board 2560 can be connected to a computer with a USB cable and powered via the USB connection or with a AC-to-DC adapter or battery to get started. The adapter can be connected by plugging a 2.1 mm center-positive plug into the board's power jack. The recommended range is 7 to 12 volts. If voltage supplied with less than 5 V, the board may become unstable. If using more than 12 V, the voltage regulator may overheat and damage the board. The whole circuit power supply can be obtained from the dc barrel jack by connecting with two lithium-ion batteries of 3.7 V rechargeable batteries. The component of Arduino mega microcontroller is shown in Figure 1.

Rotary Encoder Module

A rotary encoder-based menu is created to choose different measuring quantities by rotating the rotary encoder. A rotary encoder is a type of position sensor which is used for determining the angular position of a rotating shaft. It generates an electrical signal, either analog or digital, according to the rotational movement. Turning the rotor will change the menu and pressing the rotor will enter the selected menu and pressing again will return to start of the menu selection. Component of rotary encoder module is shown in Figure 2.

Micro SD Card Module

In some data acquisition, micro-SD card is required to log the measuring results [Jack, (2015)]. Logging data to the micro-SD card and exporting data to excel worksheet are at the time for measuring physical quantities. The terms SD card stands for "Secure Digital" Card, there are many types of SD cards. The SD cards can work in two operating modes, one is using the SD mode commands and the other is serial peripheral interface (SPI) mode. The SPI module consists of six pins and they are four SPI pins and two power pins. The data logging on SD memory card can be stored measuring data. While the data is logging on the micro-SD card, the data can be exported to the excel worksheet by connecting the circuit using USB cable [Harold, (2011)]. The Parallax Data Acquisitions (PLX-DAQ) tool software is an add-in tool for Microsoft excel. The component of micro-SD card module is as shown in Figure 3.

Temperature Sensor

Temperature is one of the most commonly measured parameters in the world. They are used in daily household devices from microwave, fridges, air conditional and all fields of engineering. The LM35 series are precision integrated-circuit temperature devices with an output voltage linearly-proportional to the centigrade temperature. The LM35 device has an advantage over linear temperature sensors calibrated in Kelvin, as the user is not required to subtract a large constant voltage from the output to obtain convenient Centigrade scaling. The LM35 device does not require any external calibration [10]. LM35 has very low self-heating of less than 0.1°C in still air. The LM35 device is rated to operate over a -55° C to 150° C temperature range. LM35 can be operated from a 5 V supply and the stand by current is less than 60 uA. The sensitivity of LM35 is 10 mV/degree Celsius. As temperature increases, output voltage also increases (E.g., 250 mV means 25°C). Temperature sensor LM35 is as shown in Figure 4.

The variable resistor 10k Ω was used to calibrate. The voltage divider ratio was the maximum input 50 V divided 10 times. Therefore, Arduino microcontroller input pins (A0, A1, A2) got maximum 5 V. Similarly, the other two pairs of volt meters were constructed using voltage divider circuits. In the program coding, the resolution of analog input was 10-bit resolution. Arduino microcontroller resolution value was 4.88 mV (5000mV/1024) on each digital reading because of reference voltage 5 V. The real input voltage was 10 times decreased by voltage divider circuit. Therefore, the voltage was again multiplied with 10 to obtain the real value. Then the value was printed on the LCD as volt meter 1 or volt meter 2 or volt meter 3 or three-volts meter. The voltage measuring was for higher voltage level 50 V.

The unknown resistor Rx was connected between the analog input pin and ground line. Therefore, one of the resistors on digital pin and unknown resistor become a voltage divider circuit. There was a specific voltage drop at the junction. The digital output 7 pins (pin 35,37,39,41, 43, 45, 49) and an analog input pin A3 pin were used to measure the resistance of an unknown resistor Rx. Seven different values of resistors are connected in parallel between each digital I/O pins and analog input pin. Arduino microcontroller read at analog input pin A3 pin. But the circuit was designed auto ranging, therefore, various resistors were added to achieve accurate reading in the program. But, switching diodes were added to protect reverse bias on the I/O pins, which would encounter incorrect reading of the unknown resistor value. Since the voltage divider output was a simple ratio of the input voltage. Simple ratio impedance through to the ADC input. If the relative impedance was low, unknown resistance could be measured in the low mega-ohm range. Then the unknown resistor could be obtained simple ratio of voltage divider calculation. To achieve measuring very high resistances, a buffer is required for the ADC through a voltage follower with a very high (tens or hundreds of tetra-ohms) impedance input.

The value of an unknown capacitor could be investigated by using resistor capacitor (RC) circuits, known as the time constant (TC). ($TC = R * C$) where TC was the time constant in seconds, R was the resistance in ohms, and C was the capacitance in farads. According to the RC time constant, charging and discharging resistors were connected. The charging pin was pin 31 and discharge pin was pin 33. The discharge pin is to prevent discharging the capacitor. The charging pin was HIGH for charging the capacitor. The junction of two resistor and capacitor was feed to analog A4 pin to check whether the voltage level of capacitor becomes 63.2% of the total voltage. The initial charging time was recorded by the Arduino. If charging voltage was under 63.2%, the charging, time counting and analog reading are looping again and again. If the analog reading is larger than 63.2%, time difference is made for current time and recorded start time. The charging voltage of 63.2% equals 1 TC. Using time constant equation, unknown capacitor value could be obtained. When the rotary encoder is selected to measure the unknown capacitor. Unknown capacitor value could be measured in micro farad, nano farad and pico farad range.

Temperature sensor basically measures heat or cold generated by an object. The semiconductor temperature sensor LM35 was used in the circuit. The power pin 1 of temperature sensor was connected with the 5 V power supply. The output pin 2 generated analog voltage according the variation of temperature. The 10-ohm resistor and 1 μ F capacitor were connected in series between the output of LM35 and ground line to protect the external interferences of electrical noises. The output voltage changed 10mV for 1 $^{\circ}$ C. The resolution of analog reading was 10bit value (0 to 1023), the reference voltage of LM35 is 5 V (5000 mV). Then the resolution was 5000 mV was divided by1024 and obtained 4.88mV. The program operation of the thermometer was chosen $^{\circ}$ C or $^{\circ}$ F by rotating the rotary encoder. Then the program jumps to temperature reading routine by reading the analog voltage on A5 pin and converted to temperature in degree Celsius.

Results and Discussion

For measuring voltage, rotary encoder could be chosen four categories which were “volt meter one”, “volt meter two”, “volt meter three” and “three volt meter”. The volt meter circuit was an application of analog to digital converter. The voltage divider circuit was used to measure high voltage level because Arduino microcontroller of reference analog input voltage was maximum 5 V. The measuring voltage range is 0 to 50 Vdc. Circuit operation for measuring voltage was shown in Figure 7.

For measuring unknown resistor R_x , the value of unknown resistor could be calculated using voltage divider circuit. Unknown resistor R_x was connected between the analog input pin and ground line. The voltage on the detection point was read to measure voltage using the ADC on the microcontroller. The circuit operation for measuring resistance was shown in Figure 8.

For measuring unknown capacitor C_x , known resistor and unknown capacitor were connected in series. The analog input A4 pin was repeatedly reading the voltage level of unknown capacitor C_x . If the charging was less than 63.2% of total charge, the time counting and analog reading were looping again and again. The unknown capacitance could be calculated using known resistor and time constant. The circuit operation for measuring of capacitance is as shown in Figure 9.

For measuring temperature circuit, output voltage of temperature sensor LM35 was connected to input A6 pin of microcontroller. The value was calculated by microcontroller and displayed on LCD in degree Celsius or Fahrenheit. To protect the external interferences of electrical noises, $10\ \Omega$ resistor and 1 μF capacitor were connected in series between the output of LM35 and ground line. The circuit operation for measuring temperature was shown in Figure 10.

Conclusion

The measurement of maximum dc voltage could be measured from 10 mV to 50 V. Each voltage divider circuit was connected adjusting small trimmer resistor to calibration. The measuring resistances results were nearly the same value of color code reading within tolerance. The maximum resistance value can be measured 20 M Ω . The capacitance values could be measured range from microfarad to picofarad. The measuring temperature range is from -55°C to 150°C .

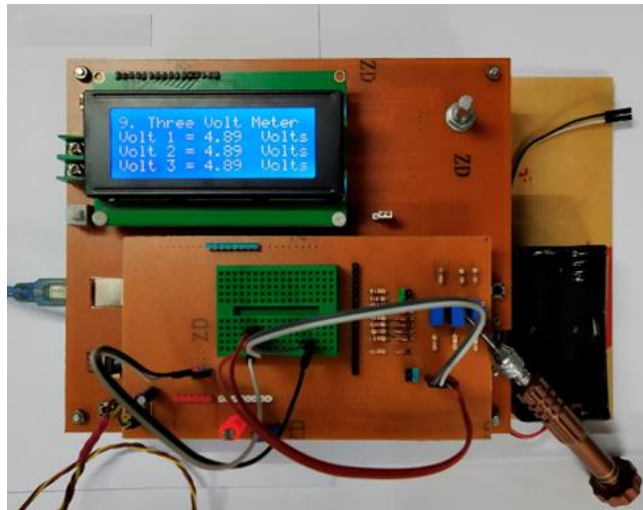


Figure 7: Photograph of measuring voltage results



Figure 8: Photograph of measuring results for resistance circuit

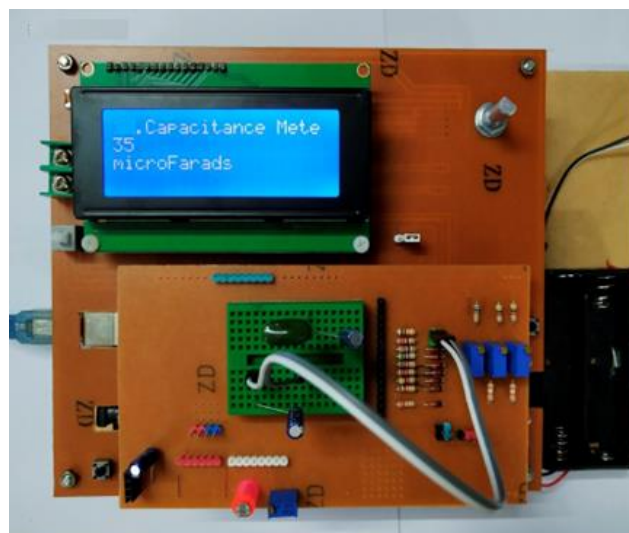


Figure 9: Photograph of measuring results for capacitance circuit



Figure 10: Photograph of measuring results for temperature

Acknowledgements

I would like to express special thanks to all the people who reviewed final results from laboratory tests, samples collection, literature studies, and research papers for the practical point of view to investigate at the laboratory of Department of Physics, Shwebo University.

References

- Bhattacharya, S. K. (2015). *Electrical measurement and control*, kindle ed, INDIA VIKAS.
- Eide, A.R., Jenison, R.D., Northup, L.L. and Mickelson, S. (2008). *Introduction to Engineering Problem Solving*, 5th ed, New York: McGraw-Hill.
- Floyd, T. L. (2006). *Digital Fundamental*, 9th ed, New Jersey: Prentice Hall.
- Harold, T. (2011). *Practical Arduino Engineering*, Paul Manning ed, (SBN-13: 978-1-4302-3886-7).
- John, B. (2013). *Arduino Workshop*, William Pollock (ISBN-13: 978-1-59327-448-1).
- Jack, J. Purdum. (2015). *Beginning C for Arduino: learn C programming for the Arduino*, 2nd ed, New York: (ISBN 9781484209400).
- Karvinen, T. and Karvinen, K. (2014). *Getting Started with Sensors: Measure the World with Electronics, Arduino, and Raspberry Pi*, Maker Media, Inc.
- Simon, M. (2010). *30 Arduino Projects for the Evil Genius*, New York: McGraw Hill.

CONVERSION OF DISPOSABLE BAMBOO CHOPSTICKS WASTE TO ADSORBENTS FOR LABORATORY WASTEWATER AND DYE WASTEWATER TREATMENT

Nwe Ni Hlaing¹, Htay Htay San², Thae Nu Aung³, Khin Aye Win⁴

Abstract

Laboratory wastewater and dye wastewater cause damage to the environment if released without proper treatment. According to the Sustainable Development Goal (SDG), water recovery from wastewater treatment has been emphasized for decades. In this study, ecofriendly adsorbents were prepared from disposable bamboo chopsticks waste to remove contaminants from laboratory and dye wastewater. Disposable bamboo chopsticks waste was collected from one of the restaurants around University of Magway. The adsorbents were prepared at 300 °C and 500 °C, respectively. For comparison, commercial activate carbon was used. The crystal structure of adsorbents was analyzed by X-ray diffractometer (XRD) and scanning electron microscopy (SEM) was used to observe morphology of the adsorbents. Energy dispersive X-ray fluorescence spectrometer (EDXRF) was used to study the elemental compositions of the adsorbents, initial and residual laboratory wastewater as well as dye wastewater. The dye removal percentages of prepared ecofriendly adsorbents were analyzed by ultraviolet-visible spectrophotometer (UV-vis). The results showed that the bamboo-based adsorbent prepared at 500 °C and commercial activated carbon performed higher removal in copper and zinc from laboratory wastewater, titanium, green and yellow colours from screen printing dye wastewater as well as methylene blue.

Keywords: adsorbent, bamboo, laboratory, dye, wastewater, adsorbent

Introduction

Laboratory wastewater derived from different types of laboratories including research, education, industrial, and agricultural institutions. The wastewater from laboratories was discharged from various laboratory activities such as washing of glass ware, chemical waste from research and student's practicum as well as educational experimental activities. Although the quantity of wastewater produced by the laboratory is relatively small, it has a real impact on the living organism and environment around the laboratory because the discharged wastewater contains toxic chemicals, organic compounds and heavy metals (such as copper, zinc, cadmium, mercury, lead, chromium, iron, nickel, tin, arsenic, etc) depending on the research and module of the practicum. Therefore, the laboratory wastewater must be prevented from reaching directly to the environment (Susila Arita et al., 2022; Tamirat Dula Chaemiso and Tariku Nefo, 2019).

Methylene blue (MB) is a cationic dye that is used in paper colouring, cottons and wool dyeing, solar cells and as temporary hair colour. As result, it leads to the obtaining of large amounts of residual water (Bingbing Mi et al., 2019). Recent years, dye wastewater from screen printing services or industries is potential to pollute the environment since it flows into drainage channel without prior treatment. The most visible parameter is colour due to dye usage. Waste dyes are difficult to decompose, non-biodegradable, and toxic organic compounds. Untreated dye wastewater can be harmful to both aquatic and terrestrial life. Hence, it is necessary to treat dye wastewater before discharging to the environment (Nguyen Ngoc Tue et al., 2020).

¹ Department of Physics, University of Magway

² Department of Physics, University of Magway

³ Department of Physics, University of Magway

⁴ Department of Physics, Sittway University

In order to remove toxic heavy metals and contaminants from wastewater, several techniques have been applied by advanced physical and chemical treatment. Some of these techniques include membrane separation, ion exchange, oxidation precipitation filtration process, advanced oxidation method, ultrafiltration, electrolysis. However, the major disadvantages of such techniques are a higher cost of production, high-cost equipment, expensive chemical requirements, and large-scale operation (Susila Arita et al., 2022; Junidah Lamaming et al., 2022).

Adsorption technique is widely used for the removal of various pollutants such as textile dyes, organic contaminants, inorganic anions, pesticides, and heavy metals. For adsorption technique, commercial activated carbon, a high surface area and a highly porous material, is a preferred adsorbent to remove impurities from liquid solutions. However, the high cost of activated carbon has inspired the researchers to search for suitable low-cost adsorbents. The alternative low-cost adsorbents have been investigated using various natural sources, agricultural wastes, forest wastes, municipal wastes and industrial wastes (S Fitriana et al., 2021; Kung-Yuh Chiang et al., 2012).

Nowadays, the managing disposable bamboo chopsticks waste is challenging. Because bamboo chopsticks are widely used not only in Asian countries but also throughout the world as Asian cuisine is popular around the world and an essential component of Asian cuisine culture is the use of chopsticks. Disposable bamboo chopsticks are discharged daily from street food, trunks, canteens, food deliveries, and restaurants. The service life of one pair of chopsticks is just one meal, and most end up in a landfill (Saowanee Wjitkosum, 2023; Jian Jiang et al., 2014). Uncontrollable amounts of bamboo chopsticks waste contribute to the environmental problem. Thus, more research is required to be carried out to investigate other potential uses of bamboo chopsticks waste.

Therefore, this research aims to convert disposable bamboo chopsticks waste (low-value waste materials) to high-value ecofriendly adsorbents for laboratory and dye wastewater treatment do develop the circular economy. For this purpose, firstly, disposable bamboo chopsticks waste was collected from one of the restaurants around University of Magway. Then, the collected disposable bamboo chopsticks waste was prepared as adsorbents by carbonization at 300 °C and 500 °C and the prepared adsorbents were characterized by XRD, SEM and EDXRF, respectively. Finally, the laboratory and dye wastewater as well as methylene blue removal percentage of prepared ecofriendly adsorbents were investigated by EDXRF and UV-vis, respectively.

Materials and Method

In order to prepare ecofriendly adsorbent, disposable bamboo chopsticks waste was used as raw materials. Laboratory wastewater was collected from sample preparation laboratory, University Research Center, University of Magway. Dye wastewater (yellow and green) was collected from a screen-printing service from Taunggyi city. Methylene blue ($C_{16}H_{18}ClN_3S$, MB) was also used as dye. Distilled water was used as solvent.

First, disposable bamboo chopsticks waste was collected from one of the restaurants around University of Magway. Second, the collected bamboo chopsticks waste was washed thoroughly with the boiled water for three times to remove impurities. Then, the washed bamboo chopsticks

waste was cut into small pieces and dried under sunlight for two days. Finally, the dried bamboo chopsticks waste was carbonized in muffle furnace at 300 °C and 500 °C to obtain the desired ecofriendly adsorbents. The flow chart and the photographic illustration of preparation of adsorbents are shown in Figure 1 and Figure 2. X-ray diffractometer (XRD) and scanning electron microscope (SEM) were used to study the crystal structure and morphology of the adsorbents. The elemental compositions of prepared adsorbents were analyzed by energy dispersive x-ray fluorescence spectrometer (EDXRF).

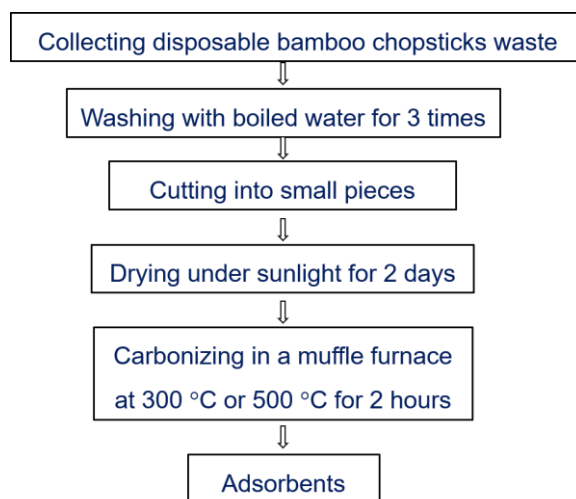


Figure 1. Flow chart of the preparation of adsorbents derived from disposable bamboo chopsticks waste

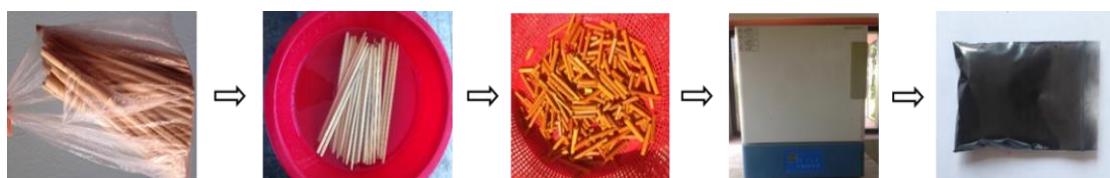


Figure 2. Photographic illustration of the preparation of adsorbents derived from disposable bamboo chopsticks waste

The ecofriendly adsorbents derived from disposable bamboo chopsticks waste prepared at 300 °C and 500 °C as well as commercial activated carbon were denoted as B-300, B-500 and CAC, respectively. For adsorption processes, 0.5 g of B-300, B-500 and CAC adsorbents were separately added to the 50 ml of laboratory wastewater, 50 ml of methylene blue (MB), 50 ml of yellow and green dye wastewater in 250 ml conical flasks. As shown in Figure 3, the adsorption process was carried out by shaking with 110 rpm in the water bath shaker (BT-150RD) for 1 hour. Then, the adsorbed laboratory wastewater, methylene blue, yellow and green dye wastewater solutions were filtered by filtered paper and the residual solutions were kept in laboratory glass bottles.

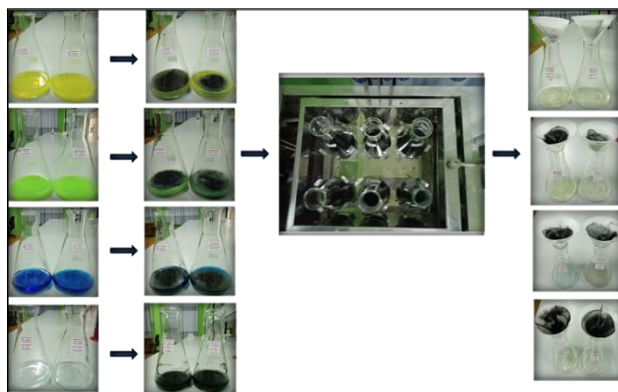


Figure 3. Photographic illustration of laboratory wastewater, methylene blue as well as yellow and green dye wastewater adsorption process using B-300 and B-500 adsorbents

In practical applications, the adsorption process is dealt with the regeneration of the spent adsorbents. Therefore, the regeneration process was conducted in this study. The Laboratory wastewater, MB, yellow and green dye wastewater loaded B-500 adsorbents were mixed with 1 M of hydrochloric acid (HCl). The mixed solution was stirred with 150 rpm at 60 °C for 1 hour followed by filtering and drying in oven at 80°C for 2 hours. Then, 0.5 g of regenerated B-500 adsorbent denoted as 2B and 50 ml of MB were used to conduct second time adsorption. The adsorption process was the same procedure as mention above.

Energy dispersive x-ray fluorescence spectrometer (Xenometrix, EDXRF spectrometer X-Calibur) and UV-visible spectrophotometer (UV-2600) were used to study the removal efficiency of prepared adsorbents. The removal percentages of the prepared adsorbents were calculated from the following equation:

$$\text{Removal \%} = \frac{C_i - C_f}{C_i} \times 100\% \quad (1)$$

where C_i and C_f are the initial and final (residual) concentration of wastewater (or MB).

Results and Discussion

Figure 4(a) shows XRD patterns of B-300 and B-500 adsorbents while Figure 4(b) expresses the XRD pattern of CAC adsorbent. The broad peak between 15° and 30° showed the amorphous structure of the adsorbents due to the conversion of hemicellulose and lignin to a more carbonaceous structure during carbonization. XRD patterns in this study match well to previously reported pattern (Qian Liu et al., 2023). In Figure 4(b), the sharp peak at around 43° implied the existence of graphite in CAC adsorbent.

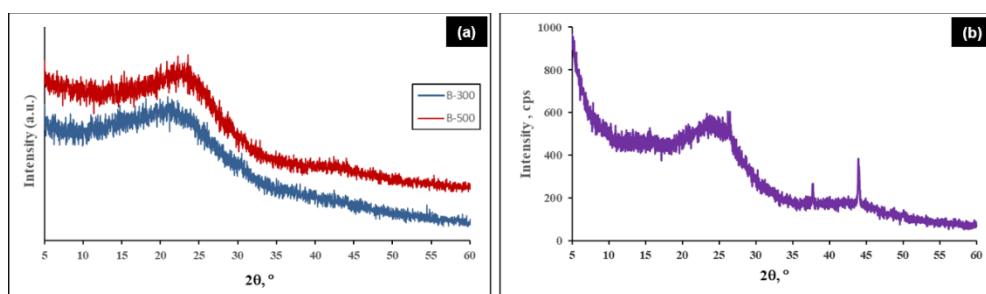


Figure 4. XRD patterns of (a) B-300, B-500 and (b) CAC adsorbents

Figure 5(a-c) shows SEM images of B-300, B-500 and CAC adsorbents. Bamboo is composed of vascular bundles and these are the origin of the large pores (Arachaporn Wilamas et al., 2023). Porous structure was observed in SEM images of B-300 and B-500 adsorbents (Figure 5(a-b)). In comparison with B-300 adsorbent, B-500 adsorbent possessed larger longitudinal pores which were suitable for removal of pollutants in liquid phase. The irregular shape and size of CAC adsorbent was seen in the SEM image shown in Figure 5(c).

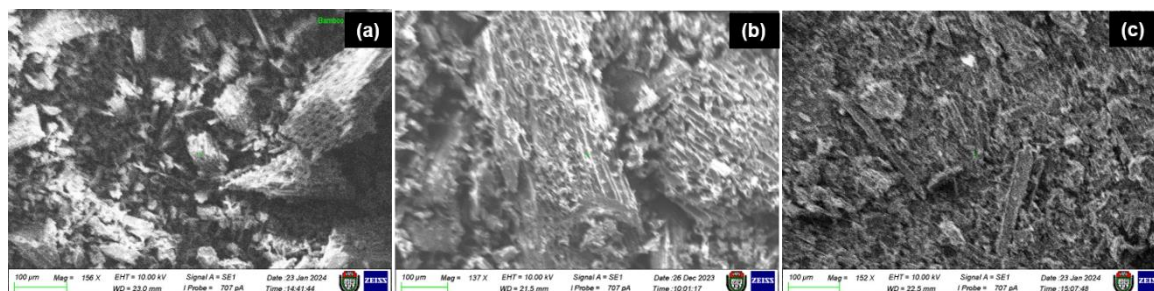


Figure 5. SEM images of (a) B-300, (b) B-500 and (b) CAC adsorbents

Figure 6(a-b) shows the elemental composition of B-300 and B-500 as well as CAC adsorbents studied by EDXRF. Generally, 9 elements such as Al (aluminum), Si (silicon), P (phosphate), S (sulphur), K (potassium), Mn (manganese), Fe (iron), Cu (copper), Zn (zinc) were found in B-300 and B-500 adsorbents (Figure 6(a)). In the B-500 adsorbent, Ca (calcium), and Pb (lead) were observed whereas Ca and Pb were not detected in the B-300 adsorbent. K was the main component of B-300 and B-500. B-500 had higher content of K (63.34%), and Ca (10.24%), and the results were comparable to the reported values of K (64.5%) and Ca (7.78%) (Arachaporn Wilamas et al., 2023). In the EDXRF result shown in Figure 6(b), 12 elements including Al, Si, P, S, K, Ca, Ti (titanium), Cr (chromium), Mn, Fe, Cu and Zn were observed. The higher levels of metals (Ca, Fe, Cu, Zn, Ti) and S were present in the CAC adsorbent compared to B-300 and B-500 adsorbents.

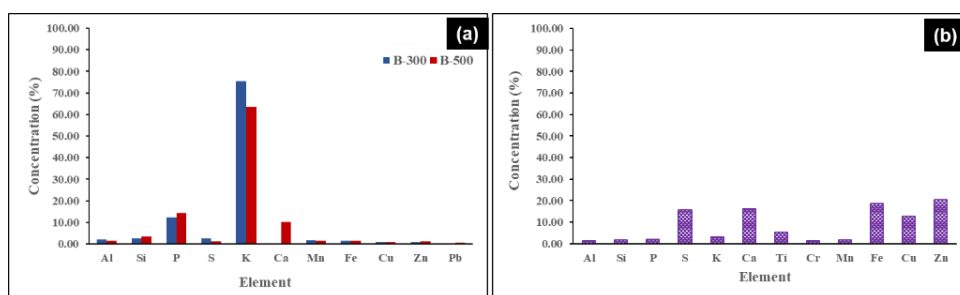


Figure 6. EDXRF results of (a) B-300 and B-500 and (b) CAC adsorbents

EDXRF analysis was also conducted to observe the elemental contents in the laboratory and dye wastewater and to study the removal percentages of B-300 and B-500 adsorbents. Figure 7 shows the elemental compositions of the initial laboratory wastewater. Al, Si, Ca, Cu and Zn were observed in the laboratory wastewater. The laboratory wastewater was collected during the synthesis of copper oxide and zinc oxide nanoparticles. As a result, the presence of higher amount of copper (50.58 wt%) and zinc (39.90 wt%) were observed.

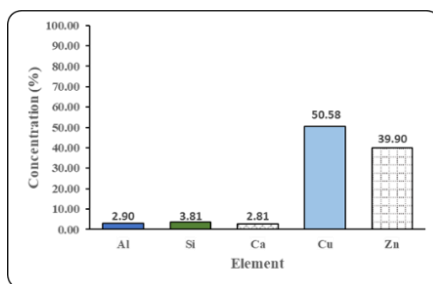


Figure 7. Elemental compositions of initial laboratory wastewater

After adsorption with B-300, B-500 and CAC adsorbents, the decrease in Cu and Zn concentration in comparison with the initial laboratory wastewater were observed obviously in Figure 8(a-c). Figure 9(a-b) show Cu and Zn removal percentages of B-300, B-500 and CAC adsorbents. As seen, Zn removal percentages of B-300, B-500 and CAC adsorbents were about 93%, 97% and 98%, respectively which were higher than the Cu removal percentages, about 71%, 77% and 82%, respectively.

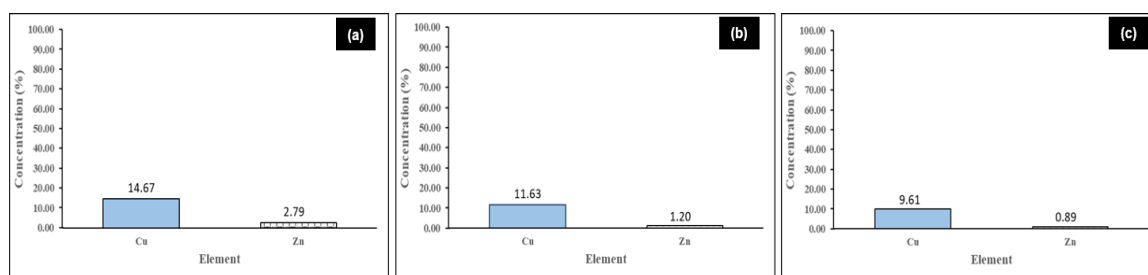


Figure 8. Cu and Zn concentration of residual laboratory wastewater after adsorption with (a) B-300, (b) B-500 and (c) CAC adsorbents

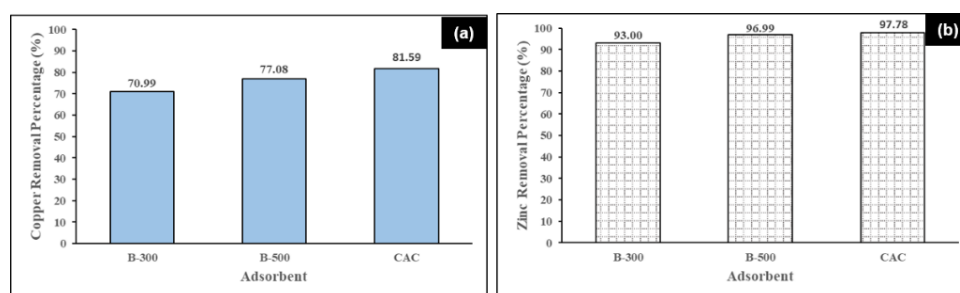


Figure 9. (a) Cu and (b) Zn removal percentages of B-300, B-500 and CAC adsorbents

Figure 10(a) shows Ti concentration in initial and residual yellow and green dye wastewater solutions (adsorbed by B-300, B-500, and CAC adsorbents). Before the adsorption process, the higher concentration Ti about 61% and 80% were found in the EDXRF results of yellow and green dye wastewater. After adsorption with B-300 adsorbent, about 5% and 8% of the Ti concentration were left. When initial yellow and green dye wastewater were adsorbed by B-500 and CAC adsorbents, the presence of Ti was not observed in the EDXRF results of residual yellow and green dye wastewater. Figure 10(b) shows the Ti removal percentages of B-300, B-500, and CAC adsorbents. The results proved that the highest Ti removal percentage of B-500 adsorbent was comparable with the CAC adsorbent.

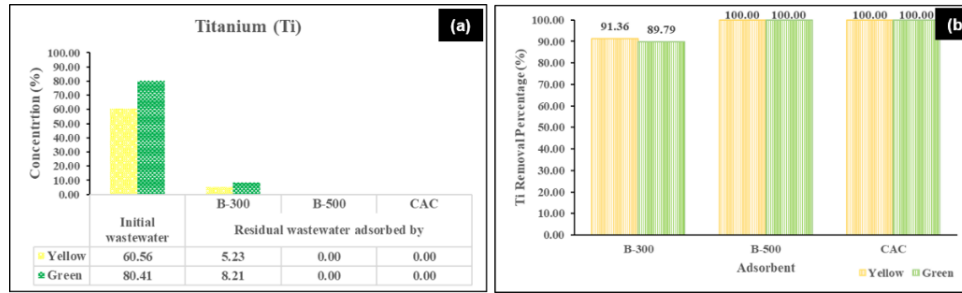


Figure 10. (a) Ti concentration in initial and residual yellow and green dye wastewater solutions (adsorbed by B-300, B-500, and CAC adsorbents) and (b) Ti removal percentages of B-300, B-500, and CAC adsorbents

Figure 11(a-c) and Figure 12(a-c) show the photographic illustration of the comparison of initial and residual MB, yellow and green dye wastewater solutions. As seen in Figure 11(a-c) and Figure 12(a-c), the significant decrease in MB, yellow and green colours were observed after adsorption with B-300, B-500 and CAC adsorbents for 1 hour, indicating that bamboo-based adsorbents were comparable with the commercial activated carbon.

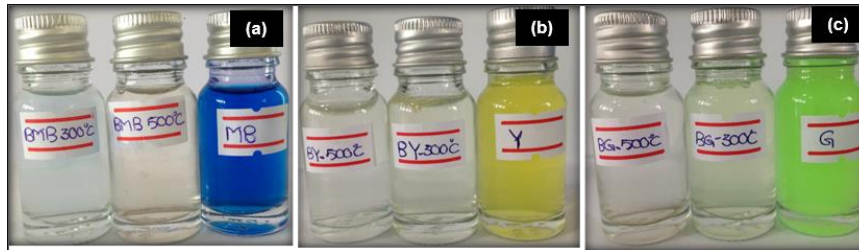


Figure 11. Initial and residual (a) MB, (b) yellow and (c) green dye wastewater solutions (B-300 and B-500 adsorbents were used for the adsorption process)

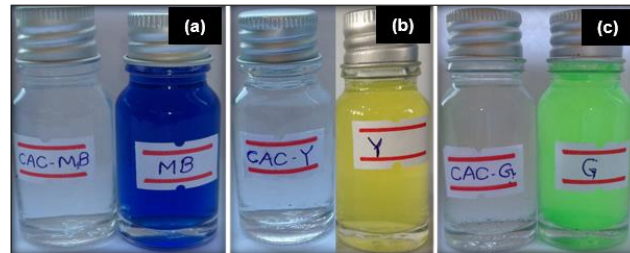


Figure 12. Initial and residual (a) MB, (b) yellow and (c) green dye wastewater solutions (CAC adsorbent was used for the adsorption process)

UV-vis analysis was conducted to study the MB, yellow and green dye wastewater removal percentages of B-300, B-500 and CAC adsorbents. As shown in Figure 13, MB, yellow and green dye removal percentages of B-500 adsorbent (about 97%, 95% and 94%) and CAC adsorbent (about 100%, 99% and 99%) were higher when compared to those of B-300 adsorbent (about 67%, 82% and 61%). The results proved that removal efficiency of B-500 adsorbent was greater than that of B-300 adsorbent due to the larger longitudinal porous structure.

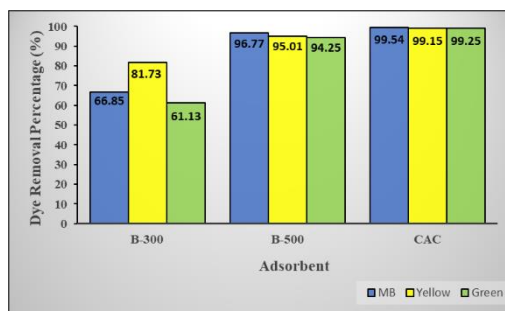


Figure 13. Methylene blue, yellow and green dye removal percentages of B-300, B-500 and CAC adsorbents

From economy and environmental point of view, the reuse of adsorbent is important. Therefore, the regeneration of wastewater loaded B-500 adsorbents was carried out. The regenerated B-500 adsorbent (denoted as 2B) was conducted for MB adsorption to test the reusability of 2B. UV-vis spectra were detected the wavelength range between 500 nm and 750 nm. As reported, the UV-vis spectrum of the initial MB solution exhibited a characteristic absorption peak at 664 nm (Idrees Khan et al., 2022). Figure 14(a-b) shows the photographic illustration and UV-vis spectra of initial and residual MB solution. The absorbance values obtained from the highest peaks in UV-vis spectra of initial and residual MB solution were 2.75 and 0.25, respectively. The calculated removal percentage about 91% showed that 2B adsorbent had a strong potential to adsorb significant amount of MB molecules, implying the reusability of the prepared adsorbent.

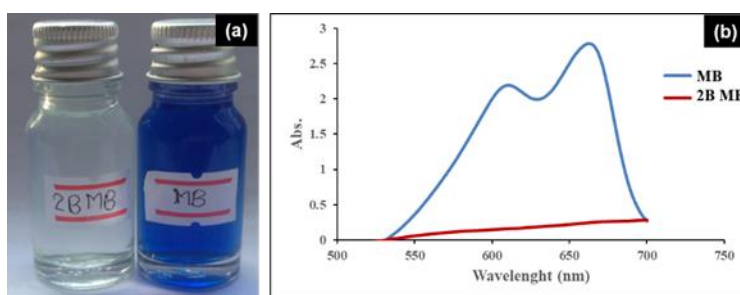


Figure 14. (a) Photographic illustration and (b) UV-vis spectra of initial and residual MB solution

Conclusion

In this study, disposable bamboo chopsticks waste, a widespread and easily available raw material was used to convert ecofriendly adsorbents at 300 °C and 500 °C, respectively. The obtained adsorbents and commercial activated carbon were analyzed by XRD, SEM, EDXRF and UV-vis. The EDXRF and UV-vis results showed that B-500 adsorbent possessed high removal percentages for Laboratory wastewater (about 77 % of Cu and 97 % of Zn) as well as for methylene blue, MB (about 97 %), for screen printing dye wastewater (about 100% of Ti, 94 % of green and 95 % of yellow colours). These removal percentages of B-500 adsorbent were comparable with the removal percentages of commercial activated carbon (about 82% of Cu, 98% of Zn, 100% of MB, 100% of Ti, 99% of green and 99% of yellow colours). The reusability study of the B-500 adsorbent showed higher removal percentage about 91%. The results

indicated that the conversion of bamboo waste as a local adsorbent might be an alternative choice for the adsorption process to remove the contaminants from Laboratory and dye wastewater.

Acknowledgements

The financial support (2023-204 fiscal year) received from Department of Higher Education, Ministry of Education, Myanmar is gratefully acknowledged. Special thanks are addressed to Dr Khin Maung Oo, Rector, University of Magway, Dr Than Aung Htwe, Pro-Rector and , Dr Cho Cho Lwin Pro-Rector, University of Magway, Dr Kyaw Kywe Kywe Aung, Professor and Head, Department of Physics and Dr Kyaw Soe Moe, Professor, Department of physics, University of Magway for their permission to submit this research.

References

- Bingbing Mi, Jingxin Wang, Hongzhong Xiang, Fang Liang, Jianfei Yang, Zixing Feng, Tao Zhang, Wanhe Hu, Xianmiao Liu, Zhijia Liu 1, and Benhua Fei, (2019), “Nitrogen Self-Doped Activated Carbons Derived from Bamboo Shoots as Adsorbent for Methylene Blue Adsorption”, *Molecules*, vol 24, pp. 1-13.
- Idrees Khan, Khalid Saeed, Ivar Zekker, Baoliang Zhang, Abdulmajeed H. Hendi, Ashfaq Ahmad, Shujaat Ahmad, Noor Zada, Hanif Ahmad, Luqman Ali Shah, Tariq Shah and Ibrahim Khan, (2022), “Review on Methylene Blue: Its Properties, Uses, Toxicity and Photodegradation”, *Water*, vol 14, 242, pp. 1-30.
- Jian Jiang, Jianhui Zhu, Wei Ai, Zhanxi Fan, Xiaonan Shen, Chenji Zou, Jinping Liu Hua Zhangb and Ting Yu, (2014), “Evolution of Disposable Bamboo Chopsticks into Uniform Carbon Fibers: A Smart Strategy to Fabricate Sustainable Anodes for Li-Ion Batteries”, *Energy Environ. Sci.*, vol 7, pp. 2670-2679.
- Junidah Lamaming, Sariah Saalah, Mariani Rajin, Noor Maizura Ismail, and Abu Zahrim Yaser, (2022), “A Review on Bamboo as an Adsorbent for Removal of Pollutants for Wastewater Treatment”, *Hindawi, International Journal of Chemical Engineering*, pp. 1-14.
- Kung-Yuh Chiang, Ya-Sing Chen, Wei-Sin Tsai, Cheng-Han Lu, Kuang-Li Chien, (2012), “Effect of Calcium Based Catalyst on Production of Synthesis Gas in Gasification of Waste Bamboo Chopsticks”, *International Journal of Hydrogen Energy*, vol 37, pp. 13737-13745.
- Nguyen Ngoc Tue, Nguyen Trong Nghia, Nghiem Thi Thuong, Tran Thuong Quang, Nguyen Duc Trung, (2020), “Study on Printing Wastewater Treatment by Decomposition Reaction H_2O_2 Catalyzed of Complex Between Ion Ni^{2+} and Citric Acid”, *Vietnam Journal of Catalysis and Adsorption*, vol 9, pp. 106-110.
- Qian Liu, Wen-Yong Deng, Lie-Yuan Zhang, Chang-Xiang Liu, Wei-Wei Jie, Rui-Xuan Su, Bin Zhou, Li-Min Lu, Shu-Wu Liu and Xi-Gen Huang, (2023), “Modified Bamboo Charcoal as a Bifunctional Material for Methylene Blue Removal”, *Materials*, vol 16, 1528, pp. 1-20.
- S Fitriana, A Wijayanti and R Hadisoebroto, “Utilization of Coconut Coir as Adsorbent for Dye Removal in Wastewater: The Effect of Mixing Speed”, *IOP Conf. Series: Earth and Environmental Science*, vol 737, pp. 1-6.
- Saowanee Wijitkosum, (2023), “Repurposing Disposable Bamboo Chopsticks Waste as Biochar for Agronomical Application”, *Energies*, vol 16, pp. 1-16.
- Susila Arita, Tuty Emilia Agustina, Nurul Ilmi, Violanda Dwi Wulandari Pranajaya, Rianzya Gayatri, (2022), “Treatment of Laboratory Wastewater by Using Fenton Reagent and Combination of Coagulation-Adsorption as Pretreatment”, *Journal of Ecological Engineering*, vol 23, pp. 211-221.
- Tamirat Dula Chaemiso and Tariku Nefo, (2019), “Removal Methods of Heavy Metals from Laboratory Wastewater”, *Journal of Natural Sciences Research*, vol 9, pp. 36-42.

DESIGN AND IMPLEMENTATION OF GAMMA RADIATION SOURCE DIRECTION WITH PANORAMIC SENSOR CODING COLLIMATOR (PSCC) SYSTEM

Tay Zar Htein Win¹, Naing Win², Myo Zaw Htut³, Zaw Htun Aung⁴, Myo Nyunt⁵

Abstract

This research work concerns with Panoramic Sensor with Coding Collimator to investigate the direction of the gamma radiation sources by using spectroscopic method. In this research work Gamma Radiation Source Investigation with Panoramic Sensor Coding Collimator (PSCC) system is constructed and the apply program for this system in MATLAB software package is created. NaI(Tl) 3x3 inches scintillation detector has been used for measurement of different gamma radiation sources with some kBq activities: Americium-241, Cesium-137 and Cobalt-60 sources in different distances and directions. By using this system, the unknown direction and the distance of radiation source have been identified. According to the result from measurements, PSCC system can be applied for multi-dimensional measurements and used as device for radiation monitoring and safety.

Keywords: *Direction Identification, Gamma Radiation Sources, Panoramic Sensor Coding Collimator, Radiation Monitoring, Radiation Safety, Scintillation Detector NaI (Tl).*

Introduction

In recent years, radiation and nuclear technologies have been deployed rapidly and broadly in various industrial, economic sectors, society. However, the management, transportation, storage and usage of radioactive sources are complicated by many challenges. Radioactive materials are especially dangerous substances. Any negligent, inaccurate or ignorant manipulation with them can lead to radioactive pollution [1, 3]. In radiation monitoring of the limited or remote areas, it is necessary to determine correctly spatial distribution of a field of radiation and location of the sources [5].

One of the major technical problems is instrumentation of the control over migrations of radioactive materials. Detectors of nuclear radiation with various configurations are applied to solve these problems [1, 5]. Identification of ionizing radiation source is physically limited in the areas (buildings, warehouses, etc.), as well as in mines and wells, therefore highly efficient detection system is necessary to investigate the direction of the source. For these purposes, the most appropriate instrument based on the principle of multiplexed detection of radiation is considered [6, 9]. The panoramic sensor concerns to radiation detection system with coding collimator, which allows the identification of gamma radiation source direction.

AIM

The aim of current research work is to implement the design for investigation of the gamma radiation source's direction by using panoramic sensor with coding collimator system and created application program.

Materials and Method

A. Design Layout of Panoramic Sensor with Coding Collimator (PSCC)

Design layout of Panoramic Sensor with Coding Collimator (PSCC) is intended to solve the coding with collimator, rotation collimation system and the blocking of the radiation measurement [5].

¹ Department of Physics, Defence Services Academy, Pyin Oo Lwin

² Department of Physics, Defence Services Academy, Pyin Oo Lwin

³ Department of Nuclear Physics, Defence Services Academy, Pyin Oo Lwin

⁴ Department of Nuclear Physics, Defence Services Academy, Pyin Oo Lwin

⁵ Department of Nuclear Physics, Defence Services Academy, Pyin Oo Lwin

Three-dimensional model describes the collimator created by Auto Desk 3D modelling software. Figure 1(a) and (b) show the 3D view of PSCC design and dimensions of this collimator.

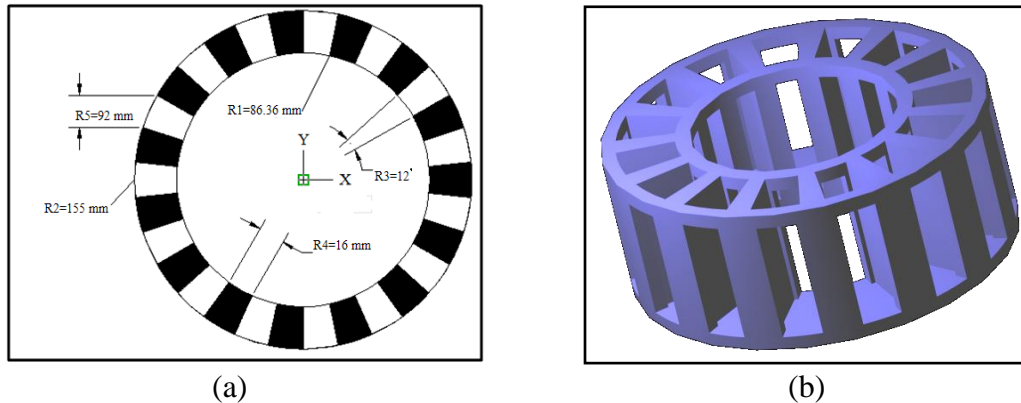


Figure 1(a) Top View with Dimensions of PSCC and **(b)** 3D View of PSCC

B. Main Characteristics of PSCC

Panoramic sensor with coding collimator is a complete measuring system based on cylindrical geometry with open and close blocks. The dimensions and parameters of the PSCC is shown in table 1 [1]:

Table 1 Typical parameters of PSCC

Overall dimension of PSCC	Dimension
Diameter (Outer)	330 mm
Diameter (Inner)	155 mm
Size of collimator	
Height	145 mm
External diameter	155 mm
Internal diameter	86.4 mm
Height of a slot-hole aperture	92 mm
Width of a slot-hole aperture	16 mm
Weight of PSCC	21 kg

C. Determination Methods for Direction of Gamma Radiation Source

Method for investigation of the direction of gamma radiation source (GRSI) is an integrated part of the created design layout of PSCC. The proposed method with more reliability and the shortest time interval will determine the direction and position of the source.

The device is designed to improve the detection of radiation and determine the direction of the source, by using the principle of the multiplex measurements. The measuring data count rate is recorded in several sectors. The result data received from the detector can be represented as follow; [2, 4]

$$y_i = c_i + \beta_0 x_i^0 + \beta_1 x_i^1 + \dots + \beta_N x_i^N \quad (1)$$

where,

y_i = the count rate of the number of pulses recorded by the detector in the i^{th} direction

$x_i^0, x_i^1, \dots, x_i^N$ = the count rate of the number of pulses in discrete sectors of decomposing in the i^{th} direction

c_i = the background count rate

$\beta_0, \beta_1, \dots, \beta_N$ = coefficient of an integral code transformation for experimental design

The expectation of equation (1) can be expressed in matrix form:

$$\hat{y} = \hat{B} \times \hat{x} + \bar{c} \tag{2}$$

Matrix can be conveniently represented as a product of two matrices, one of which is matrix of experimental resulted data, and the second is matrix of the collimator system. Therefore, the measurement result is as follow;

$$\hat{y} = \hat{A}\hat{T} \times \hat{x} + \bar{c} \tag{3}$$

where,

\hat{A} = representation of matrix

\hat{T} = unit diagonal matrix taking account of the collimator system

Assessment of the desired parameters and their variances can produce using the least square method in either case, if the number of dimension equal to the number of unknown parameters (the square matrix) may use the formula;

$$\hat{x} = \hat{A}^{-1} \hat{y} \tag{4}$$

$$\hat{D}(\hat{x}) = [\hat{A}^T \hat{D}^{-1}(y) \hat{A}]^{-1} \tag{5}$$

The implementation of these methods was used Circulant-Matrix, built on the basis of sequences which are a set of “0” and “1” located pseudo random order. Rotational shifting the sequence in a particular direction by current position forms rows of the matrix. Thus, Circulant-matrix can be represented as follow;

$$\hat{A} = \begin{pmatrix} a_0 & a_{n-1} & a_{n-2} & \dots & a_1 \\ a_1 & a_0 & a_{n-1} & \dots & a_2 \\ a_2 & a_1 & a_0 & \dots & a_3 \\ \cdot & \cdot & \cdot & \dots & \cdot \\ \cdot & \cdot & \cdot & \dots & \cdot \\ \cdot & \cdot & \cdot & \dots & \cdot \\ a_{n-1} & a_{n-2} & a_{n-3} & \dots & a_0 \end{pmatrix}$$

where,

a_0, a_1, \dots, a_n = elements of the pseudo-random sequence takes the value “0” or “1” [2, 4]

D. Data Processing using Circulant-Matrix Method

To identify the direction for maximum level of radiation, it is necessary to measure the radiation intensity in a given point of the location area along the radial directions (See Fig. 2). The figure 2 shows the geometry of the measurements to identify the direction of improving radiation emission. Firstly, we need to collect the data about the distribution of the flux of gamma radiation in the current location of the detector, and then these data are processed and finally result data from processing is obtained in a convenient form for analysis [4].

The measurements are performed in the radial direction and the count rates are N_1, N_2, N_3 and so on. A dashed line shows the conditional partition of full azimuth angle on the sector and the maximum rotation angle $\Delta\phi$ is equal to the all sectors [6, 7, 8].

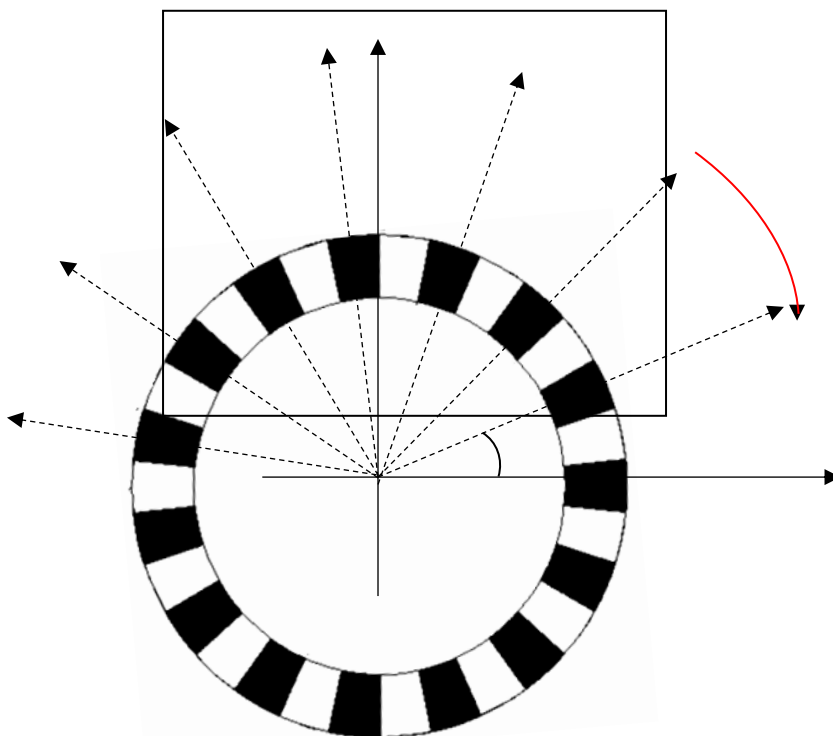


Figure 2 The geometry of the experiment with PSCC System

E. Program of Gamma Radiation Source Investigation with Panoramic Sensor Coding Collimator (PSCC) System

In this research, program for identification of the directions of gamma radiation source was created based on the detection of gamma radiation by CASSY-modules and MATLAB software package. [9]

By using this program, the unknown directions of gamma radiation sources can be determined. After carried out the experiments with program calculated not only the unknown directions, but also distance of radiation source and collimator. The lab-scaled experimental design of the PSCC system is represented in figure 3.

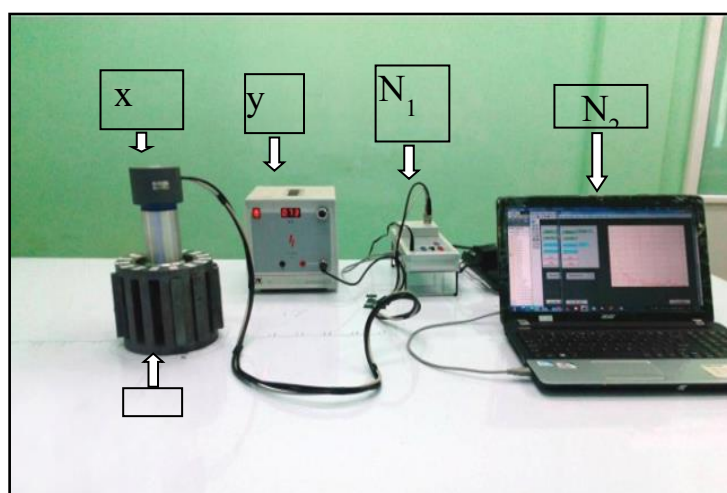


Figure 3 Lab-scaled experimental design of the PSCC system

Program “PSCC” is created in MATLAB-GUI with CASSY-modules. This program controls the measurement of gamma radiation and analyzes the measured data [9]. The program “PSCC” consists of two sub-programs;

- (a) Measurement program and
- (b) Identification program.

This program can perform the various conditions, such as single- and multi-sources measurements in different directions and distances of gamma radiation sources with different energies and activities. The interface for identification sub-program of PSCC was shown in figure 4.

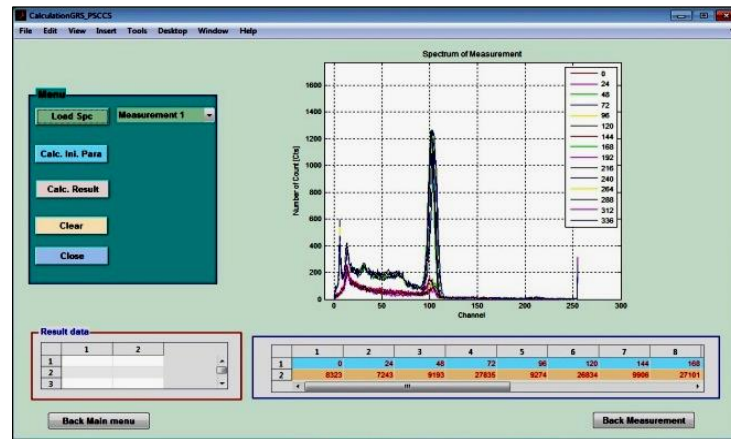


Figure 4 Interface for identification sub-program of “PSCC”

EXPERIMENT

The measurement of gamma radiation was performed by the following procedure:

- (1) The detector is placed a position and guided the first slotted-hole aperture to the north.
- (2) Then, the set of spectrum data is recorded during the measuring time with 60 sec.
- (3) After the measurement, collimator is turned about 24° clockwise on its own axis.
- (4) Measurement is repeated 15 times by rotating collimator clockwise-direction for the whole collimation system.

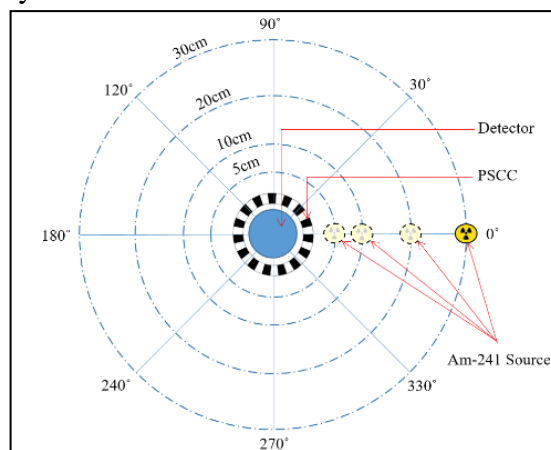


Figure 5 Scheme of Single-Source Measurement with PSCC System

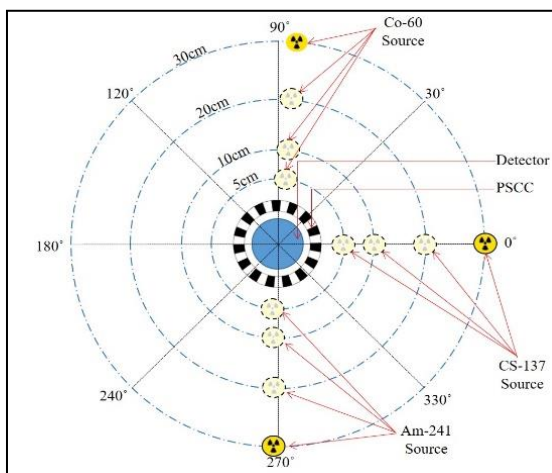


Figure 6 Scheme of Multi-Sources Measurement with PSCC System

By performing above procedure of measurement, Spectra display after 15 times and subsequent matrix can be analysed by the methods. The certain energy range can occur in the result data from the measured spectra. Energy range and the source type from measured spectra can be known in advance by energy calibration with standard gamma radiation sources. The specific energy range can also significantly improve by taking the ratio of the background counts, which in turn improves a certain direction of the source [3].

In this research work, the two types of measurements: single- and multi-gamma radiation sources with various directions and locations have been performed (See Figure 5 and 6).

Result and Discussion

A. Result of Single-Gamma Radiation Source Measurement

For measurement with single-gamma radiation source, ²⁴¹Am with current activity 370 kBq was chosen. In this measurement, the gamma radiation source was placed in various distances about 5cm, 10cm, 20cm and 30 cm respectively.

The measured result data of gamma radiation source ²⁴¹Am with various distances from 5 to 30 cm with 60 sec measuring time for horizontal geometric system are expressed in table 2.

Table 2 Results of identification with ²⁴¹Am in distance from 5 to 30 cm

Meas. No.	No. of Collimator	Rot. Angle	5cm		10cm		20 cm		30cm	
			Intensity	Weight Function (×10 ³)	Intensity	Weight Function (×10 ³)	Intensity	Weight Function (×10 ³)	Intensity	Weight Function (×10 ³)
1	1	0	15131	105.5	9940	68.7	7127	49.1	6388	41.5
2	0	24	5741	58.1	5780	47.6	5794	42.1	5605	39.8
3	0	48	5762	76.5	5777	56.2	5689	44.9	5796	42.3
4	1	72	15226	58.6	9683	47.8	7149	42.2	6342	40.3
5	0	96	5618	86.9	5763	60.7	5667	46.6	5541	42.9
6	0	120	5819	58.7	5867	47.8	5674	42.5	5879	40.5
7	0	144	5709	67.8	5852	52.7	5786	43.8	5694	41.6
8	1	168	15770	68.9	10425	52.8	7179	43.9	6976	44.0
9	0	192	5458	67.7	5403	52.5	5732	43.9	5605	41.6
10	1	216	14630	68.1	9722	52.4	6859	43.8	6130	41.2
11	0	240	5305	57.6	5463	47.8	5388	42.1	5350	40.4
12	1	264	14273	86.4	9375	60.2	6815	46.0	6345	42.7
13	0	288	5524	57.0	5590	47.3	5508	42.0	5264	40.0
14	1	316	15154	76.9	9825	56.5	7010	44.8	6320	41.9
15	1	336	15379	58.2	9733	47.6	6976	42.0	6267	40.2

From these experimental data, we have found that the dependence of the intensity of ²⁴¹Am source on measuring distance. Maximum average intensities in open collimator are 15770 counts in 5cm, 10425 counts in 10 cm, 7179 counts in 20 cm and 6976 counts in 30 cm. In close collimator the maximum average intensities 5819 counts in 5cm, 5867 counts in 10 cm, 5794 counts in 20 cm and 5879 counts in 30 cm.

According to the analysis of experimental data with PSCC system, the amount of gamma radiation intensity is decreased about 30-34%. When increasing the distance between the source and detector, the data show that the intensity of ²⁴¹Am source is remained 66% shown in figure 7(a, b, c, d).

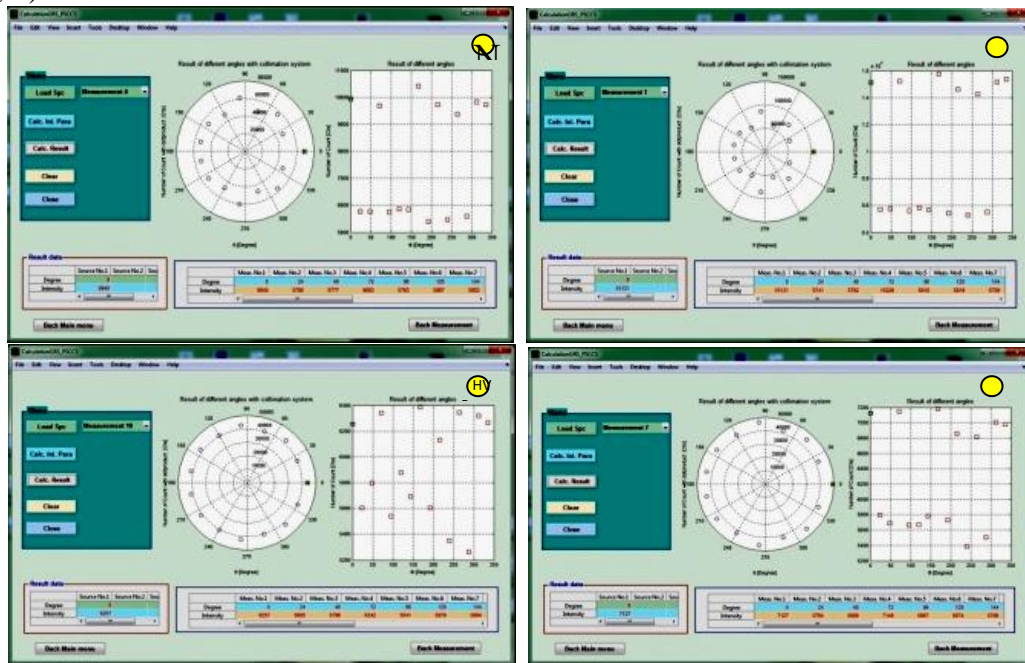


Figure 7(a, b, c, d) Results of identification of ²⁴¹Am source in distance from 5 to 30 cm and 0 degree location

According to the result of experimental data from table 2, we can determine the direction of ²⁴¹Am source by the weight function value. Therefore, the directions of ²⁴¹Am gamma radiation source are located in '0' degree at various distance 5 cm, 10 cm, 20 cm and 30 cm respectively. Maximum weight function values are 105.5x10³ counts in 5cm, 68.7x 10³ counts in 10 cm, 49.1x10³ counts in 20 cm and 44.0x10³ counts in 30 cm (See Figure 8).

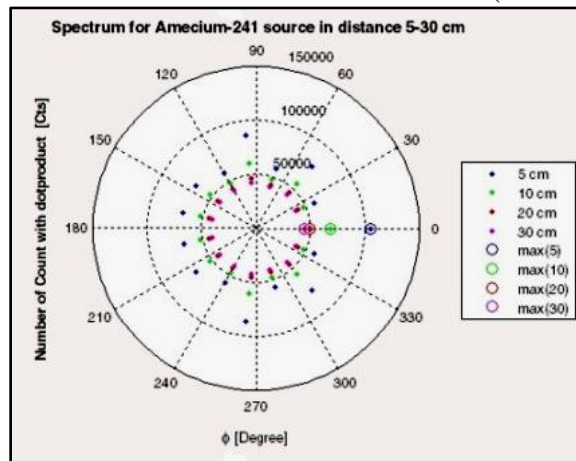


Figure 8 Result of identification to determine the direction of ²⁴¹Am source by using Circulant-Matrix method

B. Results from Measurement of Multi-Gamma Radiation Sources

In measuring with multi-gamma radiation source, a set of ²⁴¹Am, ⁶⁰Co, ¹³⁷Cs gamma radiation sources with some activity 370 kBq was chosen. In this measurement, the gamma radiation sources are placed in various distances with 5cm, 10cm, 20cm and 30 cm respectively. The measured data of research gamma radiation source ¹³⁷Cs and ⁶⁰Co with various distances from 5-30 cm and direction with ¹³⁷Cs at 0°(or) 360° and ⁶⁰Co at 270° are expressed in table 3.

Table 3 Results of identification with ¹³⁷Cs and ⁶⁰Co in distance from 5 to 30 cm

Meas. No.	No. of Collimator	Rot. Angle	5cm		10cm		20 cm		30cm	
			Intensity	Weight Function (×10 ³)						
1	1	0	64437	413.9	35692	231.4	17947	117.6	12234	81.7
2	0	24	30059	273.5	21529	175.9	13474	100.9	9976	74.2
3	0	48	50933	336.5	29247	195.2	16194	105.1	11407	75.1
4	1	72	67908	285.2	38268	182.0	19282	104.4	13067	75.6
5	0	96	45148	417.3	27565	233.1	14939	118.8	11066	82.5
6	0	120	24253	272.5	16599	174.3	10769	100.4	8504	73.9
7	0	144	26463	315.9	19718	187.5	12361	102.4	9289	74.0
8	1	168	63129	292.0	34508	182.1	16569	102.1	11558	74.1
9	0	192	23988	336.2	17944	198.1	11516	106.0	9096	75.9
10	1	216	41059	280.0	24294	174.8	12865	97.9	9662	72.0
11	0	240	28707	279.9	20756	173.9	12646	97.9	9702	72.1
12	1	264	62146	338.7	33444	198.6	16568	105.7	11344	75.8
13	0	288	29616	280.5	21681	176.8	13444	99.4	10009	72.9
14	1	316	63665	313.9	34402	186.4	17380	101.0	11920	73.1
15	1	336	51565	274.9	30811	174.5	17002	100.5	12014	73.6

From these experimental data, the variation intensities of ¹³⁷Cs and ⁶⁰Co sources were found. Maximum average intensities in open collimator are 67908 counts in 5cm, 38268 counts in 10 cm, 19282 counts in 20 cm and 13067 counts in 30 cm. In close collimator the maximum averaged intensities 50933 counts in 5cm, 29247 counts in 10 cm, 16194 counts in 20 cm and 11407 counts in 30 cm. According to the analysis experimental data with the amount of gamma radiation intensity is decreased about 45%. Increasing the distance between the source and detector shows that the intensity of ¹³⁷Cs and ⁶⁰Co source is remained about 55% which are shown in figure 9 (a, b, c, d).

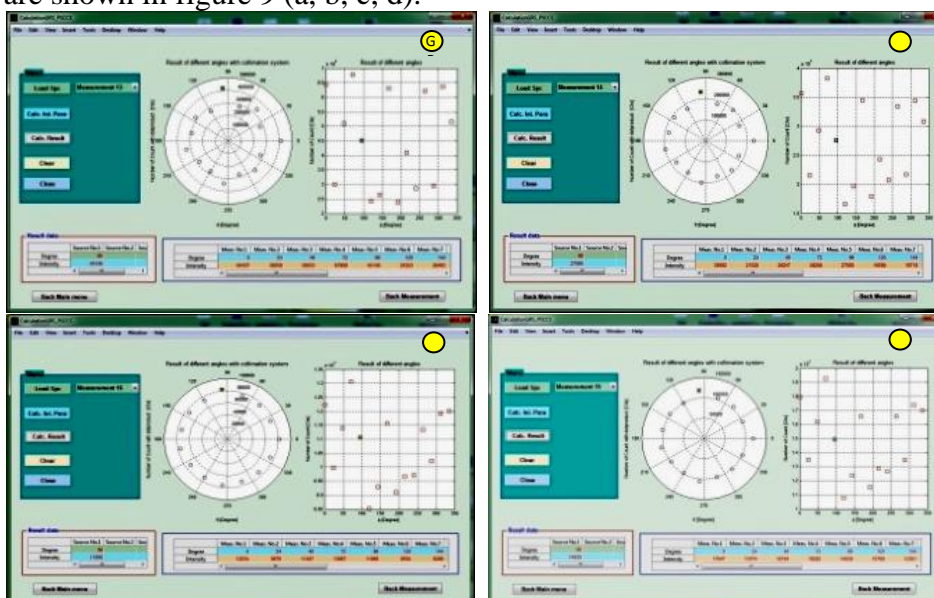


Figure 9(a, b, c, d) Results of identification of ¹³⁷Cs and ⁶⁰Co sources in distance from 5cm, 10 cm, 20 cm, 30 cm

The measured data of research gamma radiation source ^{137}Cs and ^{60}Co with various distances from 5-30 cm with 60 sec measuring time are shown in table 3.

According to the result of experimental data from table 3, the direction of ^{137}Cs and ^{241}Co source can be determined by the weight function value. The directions of ^{137}Cs and ^{241}Co gamma radiation source are located in '0' degree at various distance 5 cm, 10 cm, 20 cm and 30 cm respectively. Maximum weight function values are 413.9×10^3 and 417.3×10^3 counts in 5cm, 231.4×10^3 and 233.1×10^3 counts in 10 cm, 117.6×10^3 and 118.8×10^3 counts in 20 cm and 81.7×10^3 and 82.5×10^3 counts in 30 cm (see Figure 10).

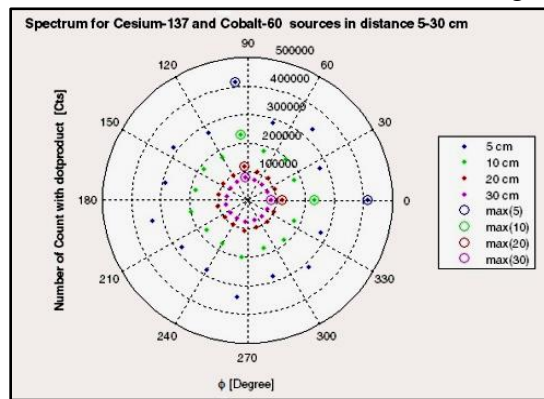


Figure 10 Result of identification to determine the direction of ^{137}Cs and ^{60}Co sources obtained by using Circulant-Matrix method

In table 4, the measured data of research gamma radiation source ^{137}Cs , ^{60}Co and ^{241}Am with various distances from 5-30 cm for horizontal direction with ^{137}Cs at 0° (or) 360° , ^{60}Co at 90° and ^{241}Am at 270° are presented.

Table 4 Result of identification with ^{137}Cs , ^{60}Co and ^{241}Am in distance from 5 to 30 cm

Meas. No.	No. of Collimator	Rot. Angle	5cm		10cm		20 cm		30cm	
			Inten-sity	Weight Function ($\times 10^3$)	Inten-sity	Weight Function ($\times 10^3$)	Inten-sity	Weight Function ($\times 10^3$)	Inten-sity	Weight Function ($\times 10^3$)
1	1	0	64891	447.2	35057	247.5	17705	123.0	12154	84.5
2	0	24	30268	284.1	21350	180.4	13417	102.8	10126	76.3
3	0	48	50922	359.9	29259	204.7	16194	107.9	11753	77.4
4	1	72	73434	303.1	41601	191.6	20511	107.8	13345	78.4
5	0	96	43876	437.5	26514	241.6	14976	122.2	10938	84.3
6	0	120	30351	289.9	20051	183.4	11795	103.7	9979	76.1
7	0	144	27661	335.5	19861	192.2	12632	104.5	9998	75.5
8	1	168	67918	320.2	37441	198.3	18191	108.1	12144	77.5
9	0	192	24224	345.1	17957	203.6	11641	108.9	9981	78.0
10	1	216	46979	303.4	27264	187.1	14164	103.3	10155	74.7
11	0	240	33077	297.6	23620	178.6	13733	100.3	10562	74.1
12	1	264	65614	374.8	37525	221.9	17583	113.7	12133	80.2
13	0	288	30273	289.6	21517	182.1	13582	101.8	10447	75.1
14	1	316	70879	342.2	34223	199.3	17044	105.7	11902	76.0
15	1	336	57499	294.5	34449	180.8	17822	102.6	12730	76.2

From these experimental data, the variation intensity of ^{137}Cs , ^{60}Co and ^{241}Am sources from 5-30 cm are found. According to the analysis of result data with collimation system, the amount of gamma radiation intensity is decreased about 46%. Increasing the distance between

the source and detector shows the intensity of ^{137}Cs source is remained 54% which is shown in figure 11(a, b, c, d).

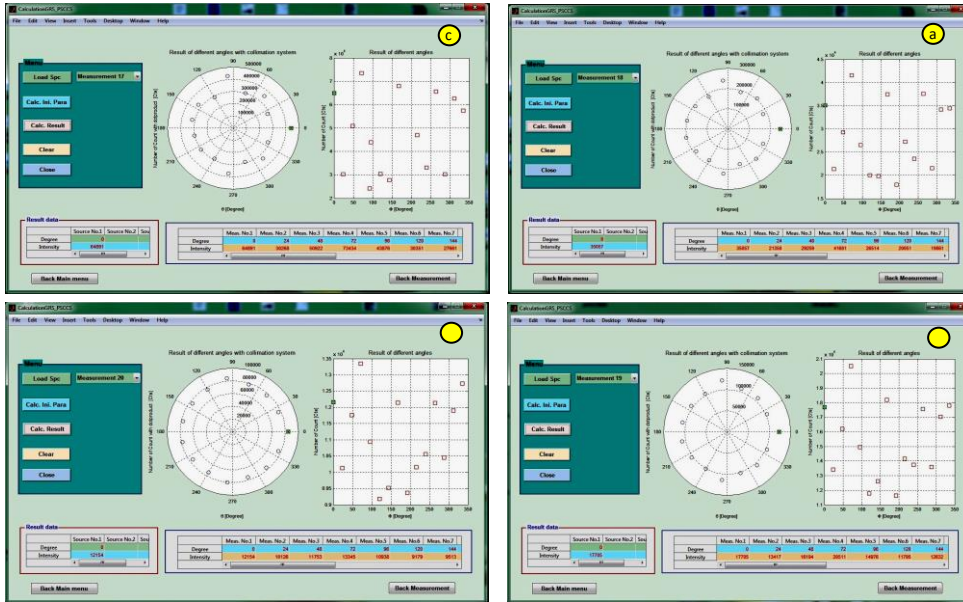


Figure 11(a, b, c, d) Results of identification of ^{137}Cs and ^{60}Co sources in distance from 5cm to 30 cm

According to the result of experimental data from table 4, we can be determined the direction of ^{137}Cs , ^{241}Co and ^{241}Am sources by the weight function value. Therefore, the directions of ^{137}Cs , ^{241}Co and ^{241}Am gamma radiation sources are located in ‘0’ degree at various distance 5 cm, 10 cm, 20 cm and 30 cm respectively. Maximum weight function values are 447.2×10^3 , 437.5×10^3 and $374.8.5 \times 10^3$ counts in 5cm, 247.5×10^3 , 241.6×10^3 and 221.9×10^3 counts in 10 cm, 123.0×10^3 , 122.2×10^3 and 113.7×10^3 counts in 20 cm and 84.5×10^3 , 84.3×10^3 and 80.2×10^3 counts in 30 cm (see Figure 12).

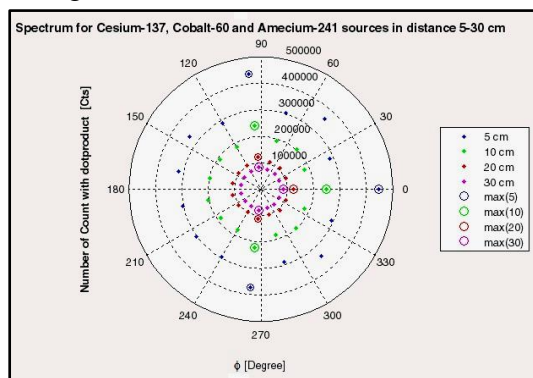


Figure 12 Result of identification to determine the direction of ^{137}Cs , ^{60}Co and ^{241}Am sources obtained by using Circulant-Matrix method

C. Discussion on Overall Results

The design and model for identification the direction of gamma radiation source by Panoramic Sensor with Coding Collimator (PSCC) was constructed. The various measurements with single and multi-gamma radiation sources in different directions and distances are performed.

According to the analysis of result data with different gamma radiation sources in various distances, the amount of gamma radiation intensity is mainly dependent on the energy of gamma

radiation source and distance from detector. In addition, the count rate depends on the activity of gamma radiation sources in the same distance of location area, which is detectable range and dependent on detector sensitivity.

The current system can be used in the horizontal measurement with 360° field of view and the vertical measurement with 180° field of view. In addition, the created PSCC program was operated in the detection system of current design and the directions of researched gamma radiation sources with the result data are obtained. The data of current experimental setup design are good in agreement with theoretical data.

Conclusion

In this research work, the design and model of PSCC system based on single detector system for multi-dimensional measurements is presented. Moreover, MATLAB program is applied to the operation of various measurements with current detection assembly and data acquisition system.

The investigation of the direction of gamma radiation source was used classical mathematical method of Circulant-Matrix, which based on design idea of panoramic sensor with coding collimator system. In addition, program of PSCC is operated in the detection system of current design to identify the directions of researched gamma radiation sources. The proposed design of PSCC can perform the horizontal measurement (transverse arrangement) with 360° field of view and the vertical measurement (longitudinal arrangement) with 180° field of view.

The results show that the current propose design can clearly identify the unknown direction of single- and multi-radiation sources. Moreover, the activity and radioisotope of single- and multi-radiation sources can also be identified for my further study. Therefore, the propose PSCC system can help to solve the problems related with radiation monitoring, safety and protection.

Acknowledgement

The current study was carried out at the Nuclear Physics Laboratory, Faculty of Physics, D.S.A. The authors gratefully acknowledge to Commandant and Rector of D.S.A for their kind permission and encouragement for this research work. Moreover, authors express their great thanks to Heads of Physics and Nuclear Physics departments for allowing to do this research work and all persons who directly and indirectly contributed towards the success of this work.

References

- Aung Myint, "Panoramic sensor coding with collimator based on scintillation detector for detection of gamma radiation sources", 2016.
- Hadamard J., "Resolution d'une question relative aux determinants" // Bull. Scientific math, 1983, Volume.2, page 240-248.
- Isakov S.V., Kadilin V.V., Modjaev A.D., Samosadnyj V.T. "Procedure of carrying out of radiating monitoring with application of a panoramic detecting arrangement. 2000. №1. page.9-10.
- Medyanik A.I., "Inscribed into a cube regular simplex and half-circulant Hadamard matrix type", page 458-471, 1997.
- Naing Win, Kolesnikov S. V., Novikov D.V and others. "The panoramic sensor coding collimator for detection of radioactive source" // 4th Kurchatov. Youth Scientific School. Russian Research Center "Kurchatov Institute", Moscow, 2006, page – 23.
- Sorokoo. L. M., "Multiplex particle detection system". 1973, №.5, page 7.
- Sorokoo. L. M., "Multiplexed measurement system in Physics", page 120, 1980.
- Volkov D. V., V.I. Mukhin, Fedorov G.A., "Optimal factorial design of experiments to determine the spatial characteristics of the measuring field". Applied nuclear spectroscopy. Page.250-256, 1977.
- "MATLAB user Guide", <http://www.mathworks.com>

TEMPERATURES DEPENDENCE OF Zn-Ni-Mn HIERARCHICAL TERNARY METAL OXIDE FILMS ON NICKEL FOAM

Mya Hnin Wai Wai¹, Zin Min Tun², Zin Min Myat³, Yin Maung Maung⁴

Abstract

Supercapacitors have been widely distributed in recent years and are becoming one of the promising energy storage systems. In this work, hierarchical mesoporous Zn-Ni-Mn ternary oxide (ZNMO) films were firstly prepared to ongoing the supercapacitors by a simple hydrothermal method at different annealing temperatures. Hydrothermal treatment is conducted to prepare unusual ternary metal oxide nanostructures (nanocubes and hollow spheres). The structural and morphological properties of Zn-Ni-Mn ternary metal oxide films onto the nickel foam were characterized by some analytical methods such as X-ray powder diffraction (XRD), Scanning Electron Microscopy (SEM). The XRD analysis confirmed that the crystallographic phases of samples were in good agreement with the tetragonal structure for Zn-Ni-Mn ternary metal oxide film. SEM can be shown that the presence of non-homogeneous grains and having different grain sizes were found the surface morphology of Zn-Ni-Mn ternary metal oxide film.

Keywords: Hierarchical, Zn-Ni-Mn ternary oxides, hydrothermal, XRD, SEM

Introduction

Supercapacitors have been extensively used in recent years because of their advanced properties including long cycle stability, fast charging/discharging rate, high power density and eco-friendly and is becoming one of the promising energy storage systems [S. Li, S. J. Silvers, et al, 1997]. Recently, the transition metal oxides, such as MnO₂, NiO, et al. have been widely explored due to the advantages including easy large-scale fabrication and brilliant flexibility in morphology and structures [A. Kolodziejczak-Radzimska and T. Jesionowski, 2014]. A number of electrode materials have been examined for enhancing the capacitive performance of the SC devices including carbonaceous nanostructures, metallic species, metal/carbon hybrids, etc [G. Oxide and E. Suvaci, 2020]. Supercapacitors (SCs) have induced enormous interest due to high power density, fast charging/discharging and long service life and have found extensive scale applications from portable electronic devices to large road market [S. Komarneni, et al, 1998]. However, the SCs generally display to lower energy densities (0-10 Wh Kg⁻¹) which limit their applications at commercial scale [Y.-L. Cheng, et al, 2016]. The issue of relatively lower energy density has been approached by increasing either the capacitive performance i.e., increasing specific capacitance or by broadening the operating voltage window [C. Abinaya ,et al.,2017]. The specific capacitance and operating window are dependent upon the properties and structure of the constituent materials along with several other factors. Nanotechnology has opened up new horizons with the development of novel materials and Nanostructures [C. Abinaya ,et al., 2017]. Among various electrode materials, the metal based materials have exposed promising results due to reversible Faradaic reactions happening on the metal electrode surface reporting for higher charge storage capability [G. Z. Gayda ,et al.,2019]. Most of research induced to use hydrothermal and sol gel processes because the shape of materials that can be easily controlled, while others better precipitation method since it offers simplicity, low cost, quick preparative method, finally easily controlled of both particle size and composition [J. N. Hasnidawani, et al, 2016]. The search for nanostructured ceramic materials that result in high-performance materials has led to the development of several chemical methods on a laboratory scale [G. Vijayaprasath ,et al., 2016]. Among the various methods of chemical synthesis, the effective and simple method

¹ Department of Physics, Sittway University

² Department of Physics, Sagaing University

³ Department of Physics, Sagaing University

⁴ Department of Physics, University of Yangon

is hydrothermal method [X. Wang, C. Yan, et al, 2013]. In this work, Nickel foam supported hierarchical mesoporous Zn-Ni-Mn ternary oxide (ZNMO) films will be firstly prepared by a hydrothermal method. The hydrothermal method is a useful and attractive technique for the preparation of nanosized particles because of its benefits: it's good to control chemical rate and the production of excellent particles with a narrow size distribution in a relatively short processing time at lower temperatures [A. R. Nanakkal and L. K. Alexander, 2017].

Materials and Method

Experimental Procedure of Zn-Ni-Mn Ternary Metal Oxide Film Materials

In this work, analytical grade of zinc chloride (ZnCl_2), nickel chloride ($\text{NiCl}_2 \cdot 6\text{H}_2\text{O}$) and manganese chloride ($\text{MnCl}_2 \cdot 4\text{H}_2\text{O}$) mixture were used as the starting materials to produce hierarchical ternary oxide by hydrothermal method. Ammonium fluoride and distilled water were used as the dissolving and cleaning factors. All chemicals and solvents were purchased from Academy chemical shop in Yangon. All reagents were commercial grade and were used without further purification.

Method

Hydrothermal synthesis relies on the forced hydrolysis of the reactants in order to produce the oxide ceramics. This is achieved at moderate temperatures ($<200\text{ }^\circ\text{C}$) and high pressures by placing the reagents in a sealed container and heating the system to the reaction temperatures. Hydrothermal synthesis can generate nanomaterials which are not stable at elevated temperatures and thus that combines results of first principal calculations, elements of aqueous thermochemistry, and experimental free energies of formation.

Experimental Procedure of Zn-Ni-Mn Ternary Metal Oxide Film

ZNMO ternary metal oxide film is prepared by a simple hydrothermal treatment. In first step, 0.1 mol of zinc chloride (ZnCl_2), 0.1 mol of nickel chloride ($\text{NiCl}_2 \cdot 6\text{H}_2\text{O}$), 0.1 mol of manganese chloride ($\text{MnCl}_2 \cdot 4\text{H}_2\text{O}$), 0.3 mol of urea ($\text{CO}(\text{NH}_2)_2$) and 0.1 mol of ammonium fluoride (NH_4F) were added to the 50 ml of distilled water with continuous stirring by using magnetic stirrer for 2 h. The 1 cmx1 cm sizes of nickel foams were immersed into the precursor solution. The homogeneous mixture was kept at $130\text{ }^\circ\text{C}$ for 8 h after transferred into 100 mL Teflon-lined stainless -steel vessel. Then nickel foams were took out and washed several times with distilled water. Afterwards, the sample was dried at room temperature for 24 h. And then annealed at $300\text{ }^\circ\text{C}$, $350\text{ }^\circ\text{C}$, $400\text{ }^\circ\text{C}$, $450\text{ }^\circ\text{C}$ and $500\text{ }^\circ\text{C}$ in a muffle furnace for 3 h to obtain the Zn-Ni-Mn ternary metal oxide film onto the nickel foam. The block diagram of the experimental procedure of Zn-Ni-Mn ternary metal oxide film was shown in figure 1.

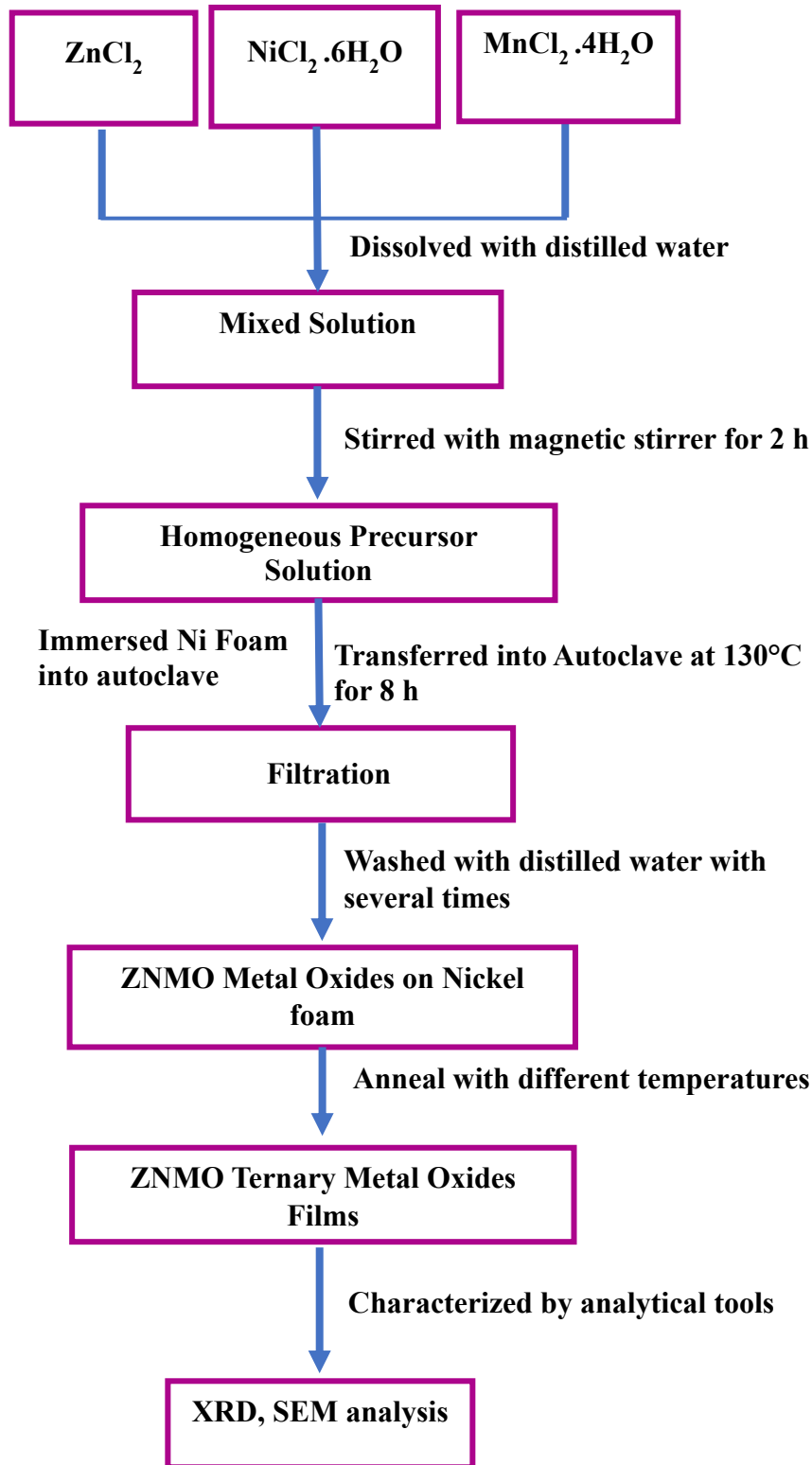


Figure 1 Block diagram of the experimental procedure of Zn-Ni-Mn ternary metal oxide films on nickel foam

Results and Discussions

Characterization of Materials

The prepared Zn-Ni-Mn hierarchical ternary metal oxide film were characterized for structural and crystal structures with X-ray Diffraction (XRD) technique (Rigaku D/max 220 i.e., X-ray Diffractometer System D/max Japan) and the grain sizes and surface morphology of prepared oxides were examined using Scanning Electron Microscopy (SEM) (Phenom Pro X).

XRD Analysis of Zn-Ni-Mn Ternary Metal Oxide Films on Nickel Foam Substrate

Structural properties of Zn-Ni-Mn ternary metal oxide films on nickel foam were examined by XRD technique. It was performed using monochromatic Cu K α radiation ($\lambda = 1.54056 \text{ \AA}$) operated at 40 kV (tube voltage) and 30 mA (tube current). Sample was scanned from 20° to 70° in diffraction angle 2θ with a step-size of 0.01°. All diffracted peak of observed spectrum well match with those of standard peaks. The most dominant peaks were also occurred at (220), (222) and (151) planes for all temperature. According to the observed XRD, the Zn-Ni-Mn ternary metal oxides have tetragonal structure. The crystallographic phases of samples were in good agreement with the typical tetragonal structure. The crystallite sizes of the prepared ternary oxide were calculated using the Debye Scherrer's formula.

$$D = \frac{0.9 \lambda}{\beta \cos \theta} \quad (1)$$

where λ , θ and β are the X-ray wavelength (1.54056 Å), Bragg diffraction angle and full width at half maximum (FWHM) respectively. Table 1 described the average crystallite sizes and crystal structure of Zn-Ni-Mn ternary metal oxide films on nickel foam for different temperatures. Table 2 showed the calculated dislocation density and microstrain of Zn-Ni-Mn ternary metal oxide films. From the XRD results, when the temperature increased, the crystallized size also increased. Figure 2 showed the comparison of ZNMO/nickel foam at different temperatures.

Table 1 The average crystallite sizes and crystal structure of ZNMO/nickel foam at different temperatures

ZNMO/nickel foam					
Temperatures	300 °C	350 °C	400 °C	450 °C	500 °C
Average Crystallite sizes	44.68 nm	48.62 nm	49.27 nm	53.57 nm	57.24 nm
Crystal structure	Tetragonal structure				

Table 2 Dislocation Density and Microstrain of ZNMO/nickel foam at different temperatures

Temperature	300 °C	350 °C	400 °C	450 °C	500 °C
Average Dislocation Density	0.00050	0.00042	0.00041	0.00035	0.00031
Average Microstrain	0.2134	0.1849	0.2978	0.1855	0.1783

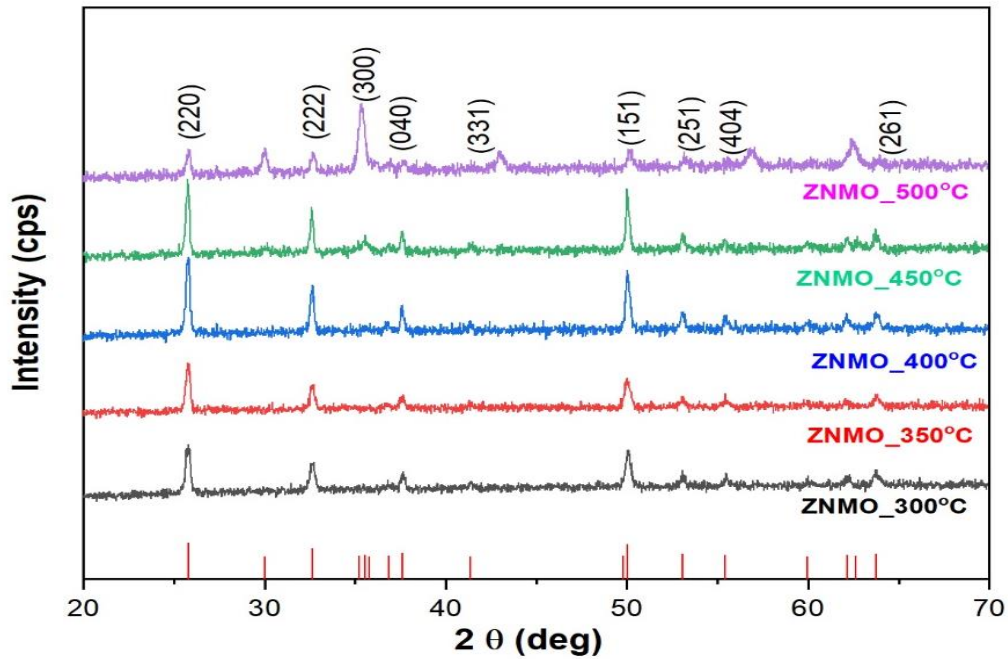


Figure 2 The XRD patterns for Zn-Ni-Mn ternary metal oxide film on nickel foam at different temperatures

SEM Analysis of Zn-Ni-Mn Ternary Metal Oxide Films on Nickel Foam

The surface morphology, microstructural properties of fabricated Zn-Ni-Mn ternary metal oxide films on nickel foam at different temperature were carried out by using the Scanning Electron Microscope (SEM) as shown in Figure 4 (a-e). From the SEM images, the Zn-Ni-Mn ternary metal oxide was well deposited on nickel foam and it has good morphology. According to SEM analysis, the morphologies ZNMO/nickel foam films were absolutely rod shapes and approach to wires phase. The well-defined nanorod shapes samples were found in Figure 6(a,b,d) and in Figure 6 (c,e), it look liked mixtures of nanorod and nanocube shapes. The diameters of these Zn-Ni-Mn ternary metal oxide films onto nickel foam were $0.170\ \mu\text{m}$ (~170 nm) at 300 °C, $0.140\ \mu\text{m}$ (~140 nm) at 350 °C, $0.13\ \mu\text{m}$ (~130 nm) at 400 °C, $0.125\ \mu\text{m}$ (~125 nm) at 450 °C and $0.113\ \mu\text{m}$ (~113 nm) at 500 °C.

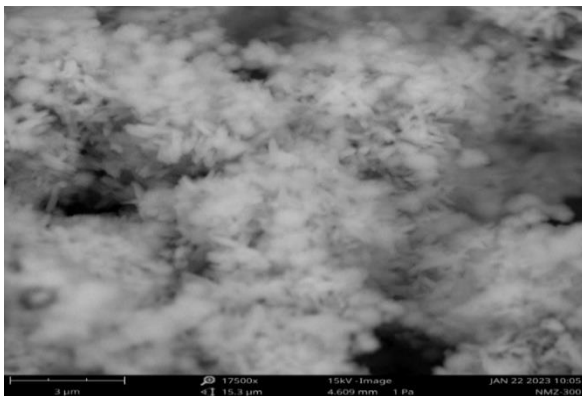


Figure 3 (a) SEM micrograph of Zn-Ni-Mn ternary metal oxide film at 300 °C

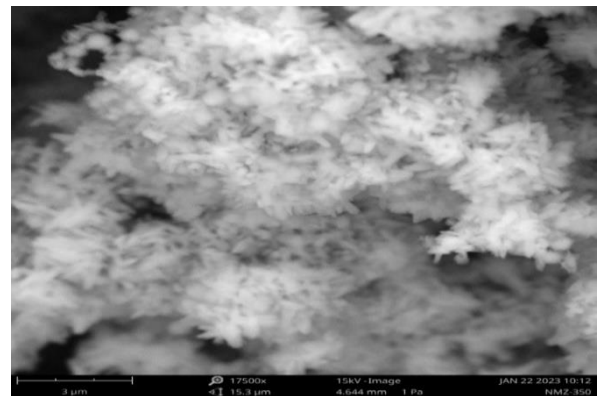


Figure 3 (b) SEM micrograph of Zn-Ni-Mn ternary metal oxide film at 350 °C

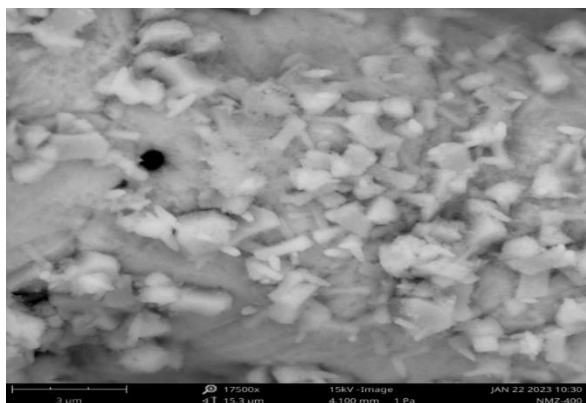


Figure 3 (c) SEM micrograph of Zn-Ni-Mn ternary metal oxide film at 400 °C

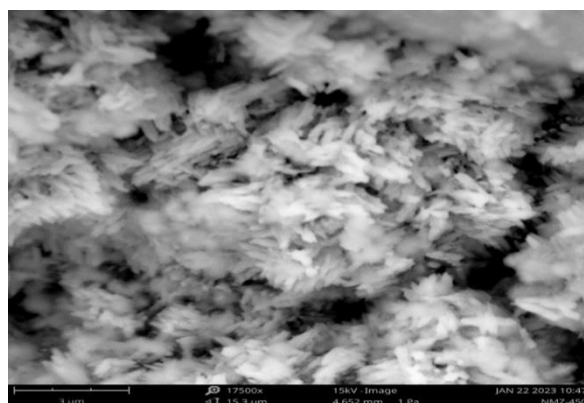


Figure 3 (d) SEM micrograph of Zn-Ni-Mn ternary metal oxide film at 450 °C

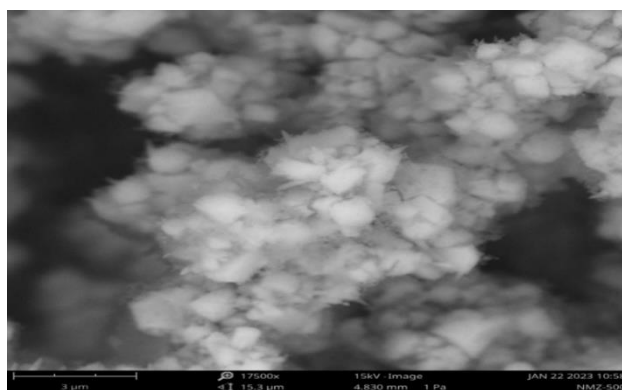


Figure 3 (e) SEM micrograph of Zn-Ni-Mn ternary metal oxide film at 500 °C

Conclusion

In this research, the controllable fabrication of highly ordered nanostructure on nickel foam substrate will be widely studied by using hydrothermal method. In his research work, hierarchical ternary metal oxide films of Zn-Ni-Mn array onto nickel foam were synthesized by a hydrothermal method. According to literature research papers, the hydrothermal routes are much more easily controlled and can produce nano arrays in a designed structure and morphology. Several general strategies for making advanced materials for supercapacitors have been developed, such as nanostructuring, nano-/microcombination, pore structure control, hierarchical design. According to XRD analysis, all the peak heights and peak positions of different temperatures were in good agreement of tetragonal structure with library file of XRD machine. According to the observed XRD, the average crystallite sizes of the Zn-Ni-Mn ternary metal oxide films were 44.68 nm, 48.62 nm, 49.27 nm, 53.57 nm and 57.24 nm at 300 °C, 350 °C, 400 °C, 450 °C and 500 °C which indicates that the crystallite size increases with the increasing temperature. From SEM images, some pores and crack growth pattern nano flowers and tube like structures were formed and it might not be cleared in shapes due to some impurity's formation during thermal treatment. It was also found to be look liked mixtures of nanorod and nanocube shapes. This suggests that the diameter of agglomerated grain size decrease with increasing thermal decomposition temperature. The experimental finding resulted from this research work indicated that the crystal structure, phase formation and morphology of Zn-Ni-Mn ternary metal

oxide films were influenced by different annealing temperatures. The resulting values were successfully represented significant progress in the development of supercapacitors.

Acknowledgements

I would like to express my sincere thanks to Professor Dr Soe Myat, Head of the Department of Physics, Sittway University for his kind encouragement, guidance and permission to perform this research work. I would like to thank to Professor Dr Nu Nu, Department of Physics, Sittway University, for her kind advice for this research.

References

- A. Kolodziejczak-Radzimska and T. Jesionowski, "Zinc oxide—from synthesis to application: A review," *Materials (Basel)*, vol. 7, no. 4, pp. 2833–2881, 2014, doi: 10.3390/ma7042833.
- A. R. Nanakkal and L. K. Alexander, "Photocatalytic Activity of Graphene/ZnO Nanocomposite Fabricated by Two-step Electrochemical Route," *J. Chem. Sci.*, vol. 129, no. 1, pp. 95–102, 2017, doi: 10.1007/s12039-016-1206-x
- C. Abinaya *et al.*, "Synthetic Method Dependent Physicochemical Properties and Electrochemical Performance of Ni-Doped ZnO," *ChemistrySelect*, vol. 2, no. 28, pp. 9014–9023, 2017, doi: 10.1002/slct.201701584.
- G. Oxide and E. Suvaci, "Hydrothermal Method Hydrothermal Synthesis Hydrothermal and Solvothermal Syntheses," *J. Power Sources*, 2020.
- G. Z. Gayda *et al.*, "Metallic nanoparticles obtained via 'green' synthesis as a platform for biosensor construction," *Appl. Sci.*, vol. 9, no. 4, 2019, doi: 10.3390/app9040720.
- G. Vijayaprasath *et al.*, "Structural and magnetic behavior of Ni/Mn co-doped ZnO nanoparticles prepared by co-precipitation method," *Ceram. Int.*, vol. 42, no. 2, pp. 2836–2845, 2016, doi: 10.1016/j.ceramint.2015.11.019
- J. N. Hasnidawani, H. N. Azlina, H. Norita, N. N. Bonnia, S. Ratim, and E. S. Ali, "Synthesis of ZnO Nanostructures Using Sol-Gel Method," *Procedia Chem.*, vol. 19, pp. 211–216, 2016, doi: 10.1016/j.proche.2016.03.095.
- Q. Yang *et al.*, "Metal oxide and hydroxide nanoarrays: Hydrothermal synthesis and applications as supercapacitors and nanocatalysts," *Prog. Nat. Sci. Mater. Int.*, vol. 23, no. 4, pp. 351–366, 2013, doi: 10.1016/j.pnsc.2013.06.015.
- S. Li, S. J. Silvers, and M. S. El-Shall, "Preparation, characterization and optical properties of zinc oxide nanoparticles," *Mater. Res. Soc. Symp. - Proc.*, vol. 452, pp. 389–394, 1997, doi: 10.1557/proc-452-389.
- S. Komarneni, M. C. D'Arrigo, C. Leonelli, G. C. Pellacani, and H. Katsuki, "Microwave-hydrothermal synthesis of nanophase ferrites," *J. Am. Ceram. Soc.*, vol. 81, no. 11, pp. 3041–3043, 1998, doi: 10.1111/j.1151-2916.1998.tb02738.x.
- X. Wang, C. Yan, A. Sumboja, and P. S. Lee, "High performance porous nickel cobalt oxide nanowires for asymmetric supercapacitor," *Nano Energy*, vol. 3, pp. 119–126, 2014, doi: 10.1016/j.nanoen.2013.11.001.
- Y.-L. Cheng *et al.*, "We are IntechOpen , the world ' s leading publisher of Open Access books Built by scientists , for scientists TOP 1 %," *Intech*, vol. 11, no. tourism, p. 13, 2016, [Online]. Available: <https://www.intechopen.com/books/advanced-biometric-technologies/liveness-detection-in-biometrics>

STRUCTURAL AND MORPHOLOGICAL PROPERTIES OF ZINC STANNATE NANOFIBERS

Hlaing Darli Soe¹, Zin Min Myat², Zin Min Tun³, Yin Maung Maung⁴

Abstract

Zinc stannate nanofibers have unique properties due to their size, distribution, and morphology and are a very important component in the rapidly developing fields of nanotechnology. In this research, zinc stannate nanopowders using zinc chloride and tin chloride were used as the starting materials of the zinc and tin sources. Zinc stannate nanofibers are grown onto fluorine-doped tin oxide (FTO) glass substrates from an aqueous solution of zinc stannate and polyvinyl alcohol (PVA) is used to produce zinc stannate nanofibers. Firstly, zinc stannate nanopowders were prepared by using the sol-gel technique. Then, zinc stannate nanofibers were fabricated by using the electrospinning method. The structural properties of zinc stannate nanopowders were characterized by instrumental analysis such as X-ray Diffraction (XRD). The morphological properties of zinc stannate nanofibers were examined by Scanning Electron Microscopy (SEM). Generated zinc stannate nanomaterials were investigated to different degrees due to their environmental friendliness, and low cost, especially in the context of enhancing their efficiency and durability, zinc stannate nanofibers are a promising class of photovoltaic cells with the capability of generating energy and have attracted numerous kinds of research.

Keywords: Zinc Stannate Nanofibers, Sol-gel Method, Electrospinning Method, XRD, and SEM

Introduction

Nanofibers offer small pore sizes and large surface areas with novel and significantly improved physical, chemical, and biological properties as the fiber diameter decreases to the nano level [Ondarcuhu, T. et al, 1998]. Fiber with a diameter in the nanometer range. Many types of polymers were processed into nanofibers of 50 to 1000 nanometers in diameter, several orders of magnitude smaller than conventional fiber spinning. Polymer nanofibers possess many unique properties since these fibers have a very large surface area per unit mass, as well as a small pore size [Q. WEI, et al, 2012]. Polymer nanofibers with specific surface properties are of importance in many technical applications as the surface features affect wettability, adsorption, electrical conductivity, optical properties, and biocompatibility. Modification of polymer nanofibers improves the surface properties of these materials to meet some special applications [F. Huang, et al, 2012]. Nanofibers can be produced from almost all polymers. However, their properties and applications are different. The diameters of nanofibers depend on the type of polymers used and their production method. They can be produced using various techniques [W.S. Khan, 2010].

There are various processes available to generate nanofibers. These processes include template synthesis, phase separation, and self-assembly. However, electrospinning is the simplest, most straightforward, and cheapest process of producing nano- and micro-sized fibers in a very short period with minimum investment [W.S. Khan, et al, 2010]. Generally, electrospinning is used to produce high-surface-area submicron and nanosized fibers. These fibers possess more exceptional physical properties (e.g., mechanical, magnetic, electrical, optical, and thermal) than their bulk-size fibers. Electrospinning is related to the principle of spinning polymeric solutions or melting at elevated temperatures in a high DC electric field

¹ Department of Physics, Patheingyi University

² Department of Physics, Sagaing University

³ Department of Physics, Sagaing University

⁴ Department of Physics, University of Yangon

[W.S. Khan, et al, 2012.]. Electrospinning is a process in which a high voltage, and consequently a high electrostatic field, is applied to a polymeric solution or melt to generate nanofibers in a very quick time. The term “electrospinning” was derived from “electrostatic spinning” because of the electrostatic field utilized during the fabrication process [J.H. He, et al, 2008]. Electrospinning is a relatively simpler, easier, and more direct process of fabricating a nonwoven mat of polymer fibers compared to conventional methods, such as melt spinning, wet spinning, and extrusion molding with the minimum initial investment and in the shortest possible time. Electrospinning generally produces fibers with diameters in the range of 40-2000 nm. Several different shapes and sizes of micron and nanoscale fibers can be fabricated from various classes of polymers [D.H. Reneker, et al, 1996].

Polymer nanofibers can be fabricated using several different methods such as self-assembly, template synthesis, drawing, phase separation, melt blowing, solvent casting, and electrospinning. Among these, electrospinning appears to be one of the most convenient and cost-effective methods because it can fabricate long and continuous nanofibers with adjustable diameters and is widely used to produce polymer nanofibers [S. S. Dissanayake, et al, 2015]. Electrospinning is the technique that uses a strong electric field to produce polymer nanofibers from a polymer solution or polymer melt. If electrostatic forces overcome the surface tension of a polymer solution a charged jet is ejected and moves toward a grounded electrode. The electrospun nanofibers can be collected on a substrate located on the counter electrode [Baumgarten, P. K, et al, 1971]. An electrospinning apparatus consists of the following four major components: High-voltage power supply, Flow control pump, and Spinneret, Collector. The apparatus as well as the components can be set up and adjusted by the actual needs. With high-voltage potential applied, the polymer solution or melt inside the spinneret is forced through a flow control pump to form a pendant drop at the tip of the spinneret. Free charges are induced into the polymer solution as a result of the applied high-voltage potential. In response to the applied electric field, these charged ions move toward the electrode of opposite polarity, transferring stretching forces generated by the electrical field to the polymer liquid. As the applied electric field increases, the hemispherical surface of the fluid at the tip of the spinneret is stretched and a conic shape called a Taylor cone is formed. When the applied high-voltage potential reaches a critical value, the electrostatic forces overcome the surface tension, and a charged jet of the solution ejected from the tip of the Taylor cone is rapidly accelerated to the grounded collecting target. Due to instabilities in the jet, the charged jet undergoes violent whipping and elongation, allowing the evaporation of solvent or cooling of melts to form solid fibers on the collector [Huang, Z. M, et al, 2003].

Materials and Methods

Sample Preparation of zinc stannate nanopowders

Materials

In this research work, analytical standard grades of zinc chloride, tin chloride, potassium hydroxide (KOH), and hydrochloric acid (HCl) were used as the starting materials to synthesize zinc stannate nanopowders. Distilled water was used as the dissolving solvent. All chemicals and solvents were purchased from the Academy chemical shop in Yangon. All reagents were commercial grade and were used without further purification.

Methods

The synthesis method consisted of two steps (1) The preparation of zinc stannate nanopowders was synthesized by the sol-gel technique and (2) zinc stannate nanofibers were fabricated by using the electrospinning method.

Sample Preparation of zinc stannate nanopowders

In this recent research work, Zinc Stannate samples were prepared by a wet chemical sol-gel method. Zinc Chloride and Tin Chloride were used as the zinc and tin sources respectively. 0.2 M of both materials were mixed with 200 ml of distilled water in beakers respectively. After that, the beaker was put over the magnetic stirrer and stirred at 400 rpm for 30 minutes. Both precursors were first dissolved in distilled water to form two transparent solutions and then mixed. The solutions were prepared by thoroughly mixing both solutions in a beaker. The solution was precipitated at room temperature by adding dropwise 0.5M KOH until a pH value in the system of 14 was reached and stirred at 1000 rpm for 4 hours. To get the anticipated pH level range (7~8), dilute HCL was added drop by drop until the mixture solution and stirred at 1000 rpm for 3 hours. The white gelatinous precipitate formed was filtered using filter paper. The precipitate was washed with distilled water several times until the pH value was approximately equal to 7 and then dried at 100 °C for 24 hours. Finally, dried powders were calcined at 100 °C intervals from 500 °C to 900 °C from room temperature in air for 6 hours to obtain spinal structure. The final samples were kept in a dry place to avoid moisture. The structural properties of all samples were characterized by XRD. Figure 1 shows the block diagram of the preparation of zinc stannate nanopowders and fibers.

Fabrication of Electrospun Zinc Stannate Nanofibers

Firstly, the polymer solution is made to obtain the nanofibers. The solution used to produce nanofibers was prepared with PVA. Fibers were produced using five types of Zinc Stannate nanopowder at different temperatures. Zinc Stannate nanopowder and solution are mixed and added to the beaker and then stirred with a magnetic stirrer. The mixture was first heated at 100 with constant stirring until a transparent homogeneous polymer solution was formed. The electrospun Zn_2SnO_4 /PVA nanofiber membranes were prepared using the electrospinning system. Then it was allowed to cool down to room temperature and was transferred to a syringe pump connected to a needle. A high voltage of 2.5 kV was applied between the tip of the needle and the grounded drum collector which were fixed to be 4 cm apart. The PVA nanofibers were deposited onto a glass substrate which was attached to the drum collector by an aluminum foil. The nanofiber membrane deposited on the glass substrate, whether or not it is a fiber was examined with SEM.

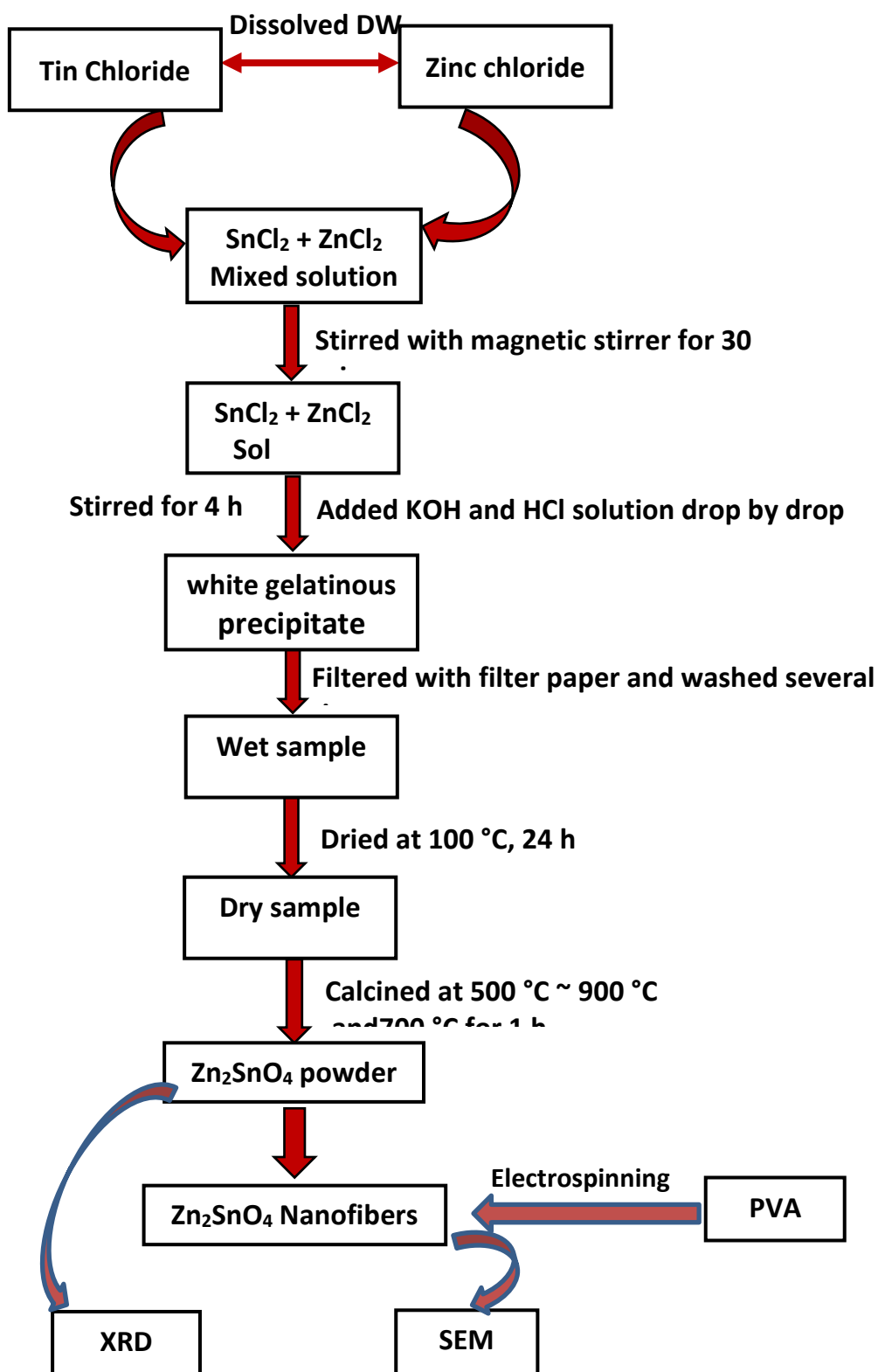


Figure 1 The Block Diagram of Preparation of Zinc Stannate Nanofibers

Results and Discussions

Characterization Techniques

The nanopowder and nanofiber synthesis of zinc stannate was characterized by XRD and SEM for structural, and morphological properties.

XRD Analysis of Zinc Stannate Nanopowder

X-ray diffraction is a powerful technique for investigating the structure of crystalline materials. To examine the crystal structure and phase formation of zinc stannate (Zn_2SnO_4) nanopowders at 500 °C, 600 °C, 700 °C, 800 °C, and 900 °C was performed using monochromatic CuK_{α} radiation ($\lambda = 1.54056 \text{ \AA}$) operated at 40 kV (tube voltage) and 30 mA (tube current). The sample was scanned from 10° to 80° in diffraction angle, 2θ with a step-size of 0.01°. Figure 2 shows the comparison of the XRD spectrum of zinc stannate (Zn_2SnO_4) nanopowders with tin chloride ($SnCl_2$) and zinc chloride ($ZnCl_2$) at five different temperatures of zinc stannate nanopowders. On the XRD spectrum, the (110), (311), and (440) peaks were sharply observed. The upper side of the XRD profile represented the observed profile while the lower side indicated the standard JCPDS (Joint Committee on Powder Diffraction Standards) library file. The dominant peaks were compared to the data from the library (or) standard file (pdf card no. 00-024-1470 Zn_2SnO_4). They were well-matched with the standard library profiles. The dominant peaks were well matched with the library (or) standard file of zinc stannate (Zn_2SnO_4). X-ray diffraction (XRD) demonstrated the cubic perovskite structure of the zinc stannate (Zn_2SnO_4) nanopowders. The average crystallite size of zinc stannate (Zn_2SnO_4) nanopowders at 500 °C, 600 °C, 700 °C, 800 °C, and 900 °C were described in Table 1. The calculated microstrain and dislocation density were listed in Table 2. Interpretations from XRD show that the average crystallite size of 500 °C, 600 °C, 700 °C, 800 °C and 900 °C is 37.65 nm, 37.96 nm, 38.17 nm, 42.41 nm, and 48.23 nm respectively. The crystallite size of the particle improved by increasing the calcined temperature. The crystalline size was determined by the Debye-Scherrer formula,

$$G = \frac{0.899\lambda}{B_{(rad)} \times \cos \theta_B}$$

Where G = Crystallite size (Å)

λ = Wavelength to compute d-spacing ($\lambda = 1.54056 \text{ \AA}$)

B = Full Width at Half Maximum

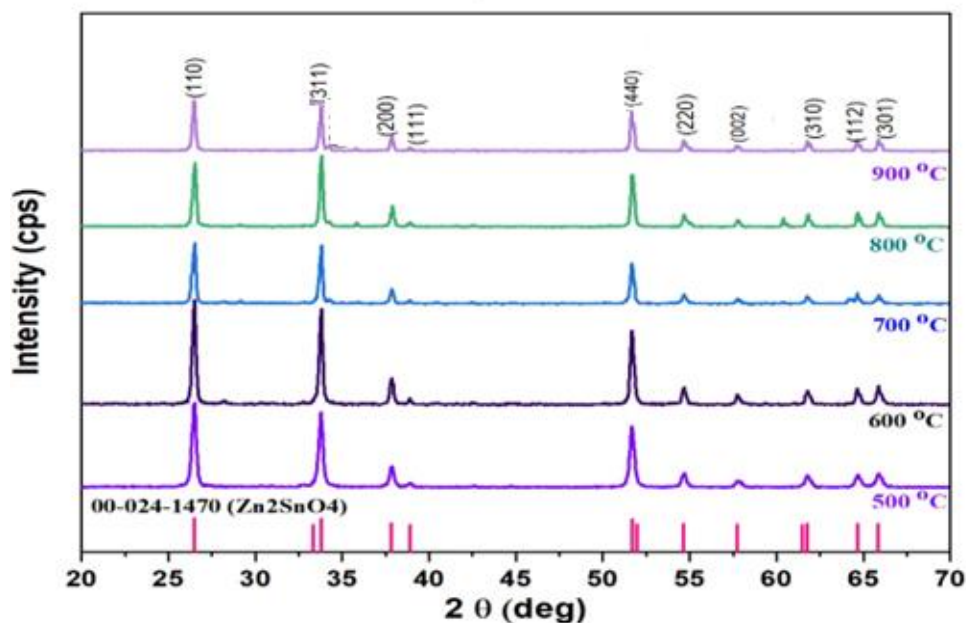
θ_B = Bragg angle (deg)

Table 1 Structural properties of Zinc Stannate Nanoparticles at different temperatures

Temperature	500 °C	600 °C	700 °C	800 °C	900 °C
Average Crystallite size G(nm)	37.65	37.96	38.17	42.41	48.23

Table 2 Dislocation Density and Microstrain of Zinc Stannate Nanoparticles at different temperatures

Temperature	500 °C	600 °C	700 °C	800 °C	900 °C
Average Dislocation Density δ (nm) ⁻²	0.0009	0.0007	0.0007	0.0006	0.0004
Average Microstrain (ϵ)	0.1744	0.1623	0.1647	0.1478	0.1284

**Figure 2** Compare of XRD spectra of Zinc Stannate nanopowder at (500 °C~900 °C)

SEM Analysis of Zinc Stannate Nanofibers

The electrospun PVA/ Zn_2SnO_4 composite fibers on the FTO glass substrate were carried out to examine by SEM images. To study morphology and nanostructural properties of fabricated zinc stannate nanofibers are depicted in Figure 3 (a-e). The as-spun composite nanofibers appeared quite smooth and each nanofiber was quite uniform in cross-section. These nanofibers were found in the formation of aligned and web structures. The diameters of nanofibers were 0.27 μm (~270 nm) for 500 °C, 0.21 μm (~210 nm) for 600 °C, 0.20 μm (~200 nm) for 700 °C, 0.17 μm (~170 nm) for 800 °C and 0.13 μm (~130 nm) for 900 °C respectively. In Figures 3(a) and 3(d), the morphologies of fibers were smooth, uniform, and observed. For the images of figures 3(b), 3(c), and 3(e), the fibers were slightly rough, non-uniform, and found to be web-shaped. According to these results, the electrospun Zn_2SnO_4 nanofibers were successfully deposited on an FTO substrate for nanofiber-based photoanode in DSSC applications.

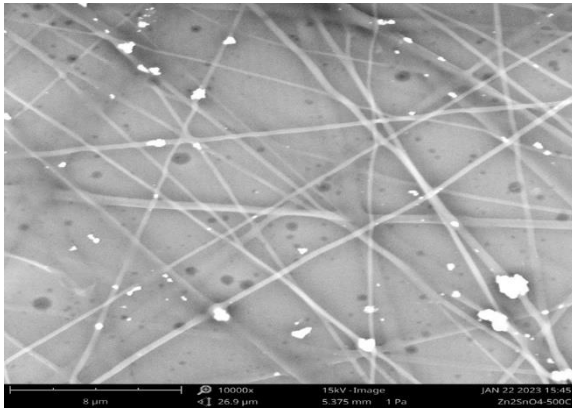


Figure 3(a) Zinc Stannate nanofibers at 500 °C (0.27 μm)

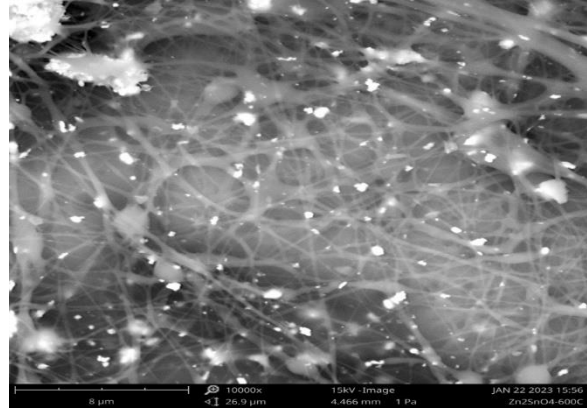


Figure 3(b) Zinc Stannate nanofibers at 600 °C (0.21 μm)

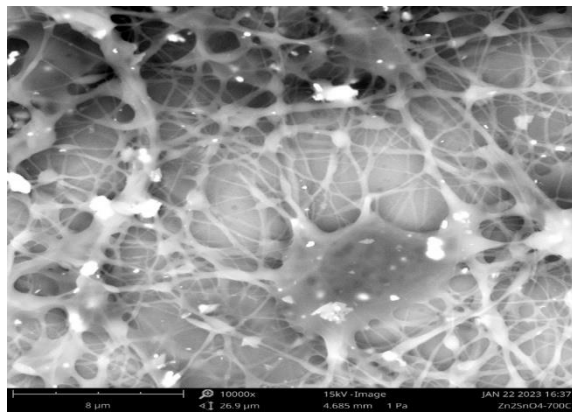


Figure 3(c) Zinc Stannate nanofibers at 700 °C (0.20 μm)

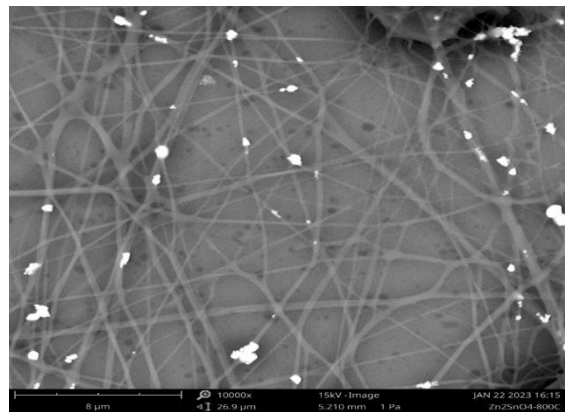


Figure 3(d) Zinc Stannate nanofibers at 800 °C (0.17 μm)

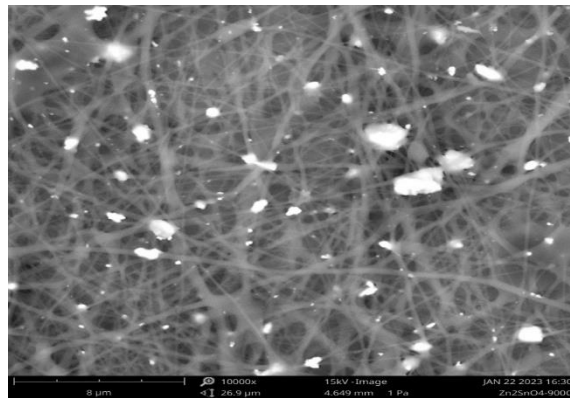


Figure 3(e) Zinc Stannate nanofibers at 900 °C (0.13 μm)

Conclusion

Zinc stannate (Zn_2SnO_4) nanoparticles were firstly prepared by sol-gel technique. Then, the synthesized powders were calcined at five different temperatures. XRD analysis showed that nanopowders in the fabricated zinc stannate at 500 °C, 600 °C, 700 °C, 800 °C, and 900 °C were crystallized in the cubic structure and their average crystallite sizes were observed to be 37.65 nm, 37.96 nm, 38.17 nm, 42.41 nm, and 48.23 nm respectively. From SEM analysis, the surfaces of zinc stannate nanofibers seemed to be more fiber shapes, web nature of fibers, definitely sharp and uniform distribution at 800 °C than other temperatures. As a result, it was concluded that the

average grain size of the zinc stannate powders varied with annealing temperatures. For the images of SEM, the fibers were slightly rough, non-uniform, and found to be web-shaped. The lack of clarity in the image of SEM is due to the need for homogeneity during the experiment, it will be having to do again. These were characterized by XRD and SEM techniques to investigate the structural and surface morphological properties of the samples and also revealed that it was influenced by the temperatures.

Acknowledgments

I would like to express our sincere thanks to Professor Dr. Aye Ngwe, Head of Department of Physics, at Patheingyi University, for his kind encouragement and permission to perform this research work.

I would like to thank Professor Dr. Myint Thu, Professor, Hpa-An University, Dr. Than Than Swe, Professor, Patheingyi University for their kind advice and suggestions for this research.

References

- Baumgarten, P. K, (1971) "Electrostatic spinning of acrylic microfibres, *Journal of Colloid and Interface Science*", 36, 71–9.
- D.H. Reneker, I. Chun, (1996), Nanometer diameter fibers of polymer. Produced by electrospinning, *Nanotechnology*, 7 (3) 216-223.
- F. Huang, Q. Wei, and Y. Cai, (2012) *Surface functionalization of polymer nanofibers*. Woodhead Publishing Limited, doi: 10.1533/9780857095640.1.92.
- Huang, Z. M., Zhang, Y. Z., Kotakic, M., et al, (2003) "A review on polymer nanofibers by electrospinning and their applications in nanocomposites, *Composites Science and Technology*", 63, 2223–53.
- J.H. He, Y. Liu, L.F. Mo, Y.Q. Wan, L. Xu, (2008), *Electrospun Nanofibers and Their Applications*, UK.
- Ondarcuhu, T. and Joachim, C., (1998), Drawing a single nanofiber over hundreds of microns, *Europhysics Letters*, 42(2), 215–20.
- Q. WEI, D. TAO, and Y. XU, China, (2012) "Nanofibers: principles and manufacture", Woodhead Publishing Limited, Jiangnan University
- S. S. Dissanayake, M. A. K. L. Dissanayake, V. A. Seneviratne, G. K. R. Senadeera, and C. A. Thotawattage, (2015) "Performance of Dye-Sensitized Solar Cells Fabricated with Electrospun Polymer Nanofiber Based Electrolyte," *Mater. Today Proc.*, vol. 3, no. Icfmd, pp. S104–S111, 2016, doi: 10.1016/j.matpr.2016.01.014
- W.S. Khan, (2010), *Fabrication and Characterization of Polyvinylpyrrolidone and Polyacrylonitrile Electrospun nanocomposite Fibers*, Ph.D. dissertation, Department of Mechanical Engineering, Wichita State University.
- W.S. Khan, R. Asmatulu, M.M. Elatbey, (2010). Dielectric properties of electrospun PVP and PAN nanocomposite fibers at various temperatures, *J. Nanotechnol. Eng. Med.* 1 041017-1041017-6
- W.S. Khan, R. Asmatulu, Y.H. Lin, Y. Chen, J. Ho, (2012) "Electrospun polyvinylpyrrolidone based nanocomposite fibers containing (Ni_{0.6}Zn_{0.4}) Fe₂O₄, *J. Nanotechnol*", 5 pages. Article ID 138438, doi:10.1155/2012/1384382012.

STRUCTURAL CHARACTERISTICS OF Sodium Calcium Silicate Glass Ceramics

Than Min Khaing¹, Min Maung Maung², Yee Mon Tun³

Abstract

Glass ceramics were prepared by the sol-gel method using sodium metasilicate (Na_2SiO_3) as a silica source. The obtained samples were sintered at three different temperatures (800°C, 900°C, and 1000°C). The presence of sodium calcium silicate was observed by an X-ray diffraction (XRD) pattern. The major phase formation of combeite ($\text{Na}_2\text{Ca}_2\text{Si}_3\text{O}_9$) and the secondary phase formation were also observed. The optical band gap of this sample was investigated with the help of a UV-vis spectrophotometer. The optical band gaps were found to be in the range of 4.7 eV – 4.92 eV. The Fourier Transform Infrared (FTIR) spectroscopy was employed for the characterization of these materials.

Keywords: Glass Ceramics, Sol-Gel, XRD, UV-vis and FTIR

Introduction

The field of biomaterials began to shift emphasis from achieving exclusively a bioinert tissue response to producing bioactive components that could have a controlled action and reaction in the physiological environment. Biomaterials have recently been improved for new medical applications (Abbasi and Hashemi 2014). The original bioactive glass was first discovered in 1970 by Larry L. Hench. Its composition consists of 45 % SiO_2 , 24.5 % CaO , 24.5 % Na_2O , and 6.0 % P_2O_5 (wt. %, noted as 45S5) (Dang et al. 2020). Peitl et al. have developed the first bioactive glass-ceramic in the SiO_2 - CaO - Na_2O - P_2O_5 system with both good mechanical properties and high bioactivity. After that, Ravagnani et al. developed a highly bioactive, fully crystalline glass-ceramic in the SiO_2 - CaO - Na_2O - P_2O_5 system. Almost all the works have shown that $\text{Na}_2\text{Ca}_2\text{Si}_3\text{O}_9$ formation, observed in some glass-ceramics, enhances the mechanical properties of the starting glass and maintains the high bioactivity of particular compositions in the SiO_2 - CaO - Na_2O - P_2O_5 system (Mezahi et al. 2018). Recently, calcium silicate based glass ceramics have been regarded as a potential candidate for bone replacement and regeneration due to their excellent biocompatibility and bioactivity. Controlled surface crystallization of calcium silicate glass ceramics develops such versatile mechanical properties that it can be utilized as a dental implant or as a coating for an implant (Mirza et al. 2017). Bonding between bioactive glass-ceramic and the surrounding tissues takes place through the formation of a hydroxyapatite layer, which is very similar to the mineral phase of bone (Kumar n.d.). One of the more interesting methods to synthesize organic-inorganic hybrid materials at low temperature is the sol-gel technique. Two important reactions are involved; in fact, in this chemical synthesis, the precursor undergoes hydrolysis to form a colloidal suspension (sol), followed by a condensation reaction that allows “sol” evolution into “gel” (Fernandes et al. 2018). Generally, sol-gel-derived glass, with its inherent mesoporosity, provides a larger surface area and consequently a more rapid degradation rate than melt-derived glass of similar composition (Gmeiner et al. 2015). Nevertheless, different results found in the literature show that not just composition but also the preparation method influence on the final structure and the resultant biological properties of the material (Quintero Sierra and Escobar 2019). In this study, glass ceramics powder in a quaternary system was synthesized through the sol-gel route using sodium metasilicate as a cheap silica source. The synthesized glass ceramics were analyzed by X-ray diffraction (XRD). The optical band gap of the glass ceramic powder was characterized by Ultraviolet visible spectrophotometer (UV-vis). The functional groups of the glass ceramics powders were analyzed by Fourier Transfer Infrared (FTIR) spectroscopy.

¹Department of Physics, Patheingyi Education Degree college

²Department of Physics, University of Yangon

³ Department of Physics, Government of Technical Institute (Insein)

Materials and methods

Experimental procedures

Glass ceramics were synthesized through the sol-gel process from sodium metasilicate, Na_2SiO_3 according to the following procedure. The Na_2SiO_3 was stirred in a beaker using a magnetic stirrer in deionised water followed by addition of ethanol to give a clear solution. To the stirred mixture was added 1M HNO_3 drop wise, stirring was continued further for 1 h to allow complete hydrolysis. P_2O_5 and $\text{Ca}(\text{NO}_3)_2 \cdot 4\text{H}_2\text{O}$ were added in sequence under constant stirring. Each reagent was allowed 45 min to react before adding the next reagent, finally the mixture was stirred for 1 h after the last addition. The resulting gel was aged at room temperature for 5 days, dried at 60°C for 72 h. The resulting glass ceramics were sintered at 800°C , 900°C and 1000°C for 2 h. The sintered specimen was analyzed by X-ray diffraction (XRD) using $\text{CuK}\alpha$ radiation source operated at 40 kV and 30 mA. The diffraction patterns were obtained in the 2θ range from 10° - 70° . The obtained glass ceramics were investigated with UV-vis spectroscopy. The functional groups of the materials were studied by FTIR spectroscopy.

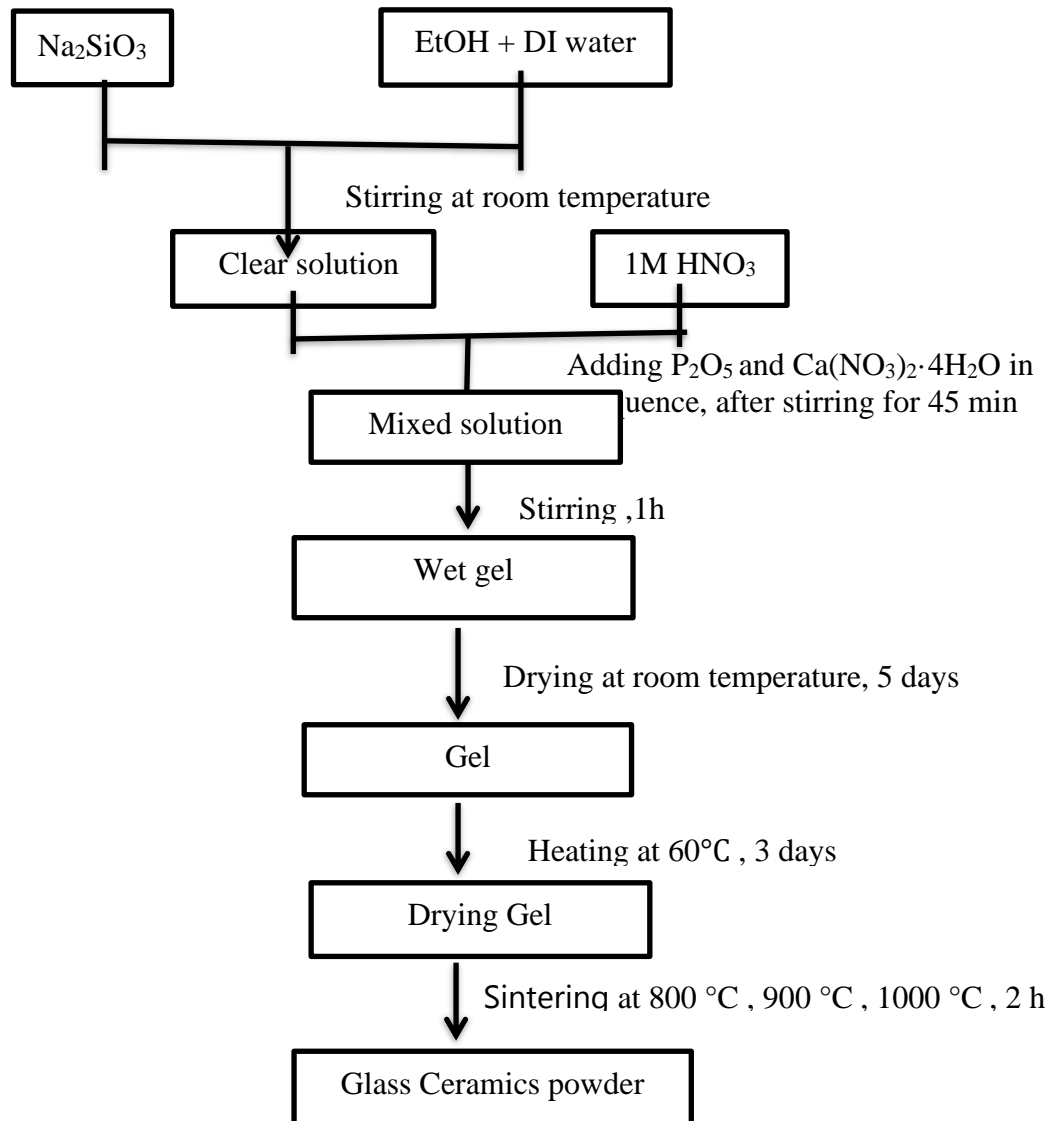


Figure.1 Block diagram of the preparation of glass ceramics

Results and Discussion

X-Ray Diffraction Analysis

The XRD patterns containing crystalline peaks Fig. 2 (d) were used to obtain the crystalline size of combeite at various heat treatment temperatures using the Scherrer equation (Patterson 1939).

$$D = \frac{k\lambda}{\beta \cos\theta} \quad (1)$$

In this formula, $\lambda = 0.154056$ nm presents the wavelength of $\text{CuK}\alpha$, β is for the full width at half maximum (FWHM), k is the Scherrer's constant, which is taken as 0.9 , and θ stands for the diffraction angle. In figure 2(d), the intensity of the peaks was a good match to the standard PDF # 96-900-7712, indicating the formation of the crystalline phase of $\text{Na}_2\text{Ca}_2\text{Si}_3\text{O}_9$. This peak shows agreement with the results from several other researchers (Aswad, Sabree, and H S Abd 2021). Above a sintering temperature of 800 °C, 45S5 starts to crystallize, forming mainly the $\text{Na}_2\text{Ca}_2\text{Si}_3\text{O}_9$ crystalline phase (Kaur et al. 2019). With increasing sintering temperature, the intensity of the peaks increases, and the diffraction peaks become sharper and narrower. This indicates the enhancement of the crystalline nature and an increase in the crystallite size. Peaks in the 2θ range from 33° – 35° , with the corresponding Miller Indices (220), are more intense compared to the remaining peaks across all the samples. This occurs because crystal planes orient along a specific direction over a long-range, leading to a preferred crystallographic orientation. Low-intensity peaks indicate, the random arrangement of the crystals. Thus it could be concluded that the size of the combeite crystals increased up to 33.2 nm by increasing the heat treatment temperature from 800 °C to 1000 °C . The crystallite sizes of combeite calculated using eq. (1) and the XRD patterns of Fig. 2(d) are summarized in table.

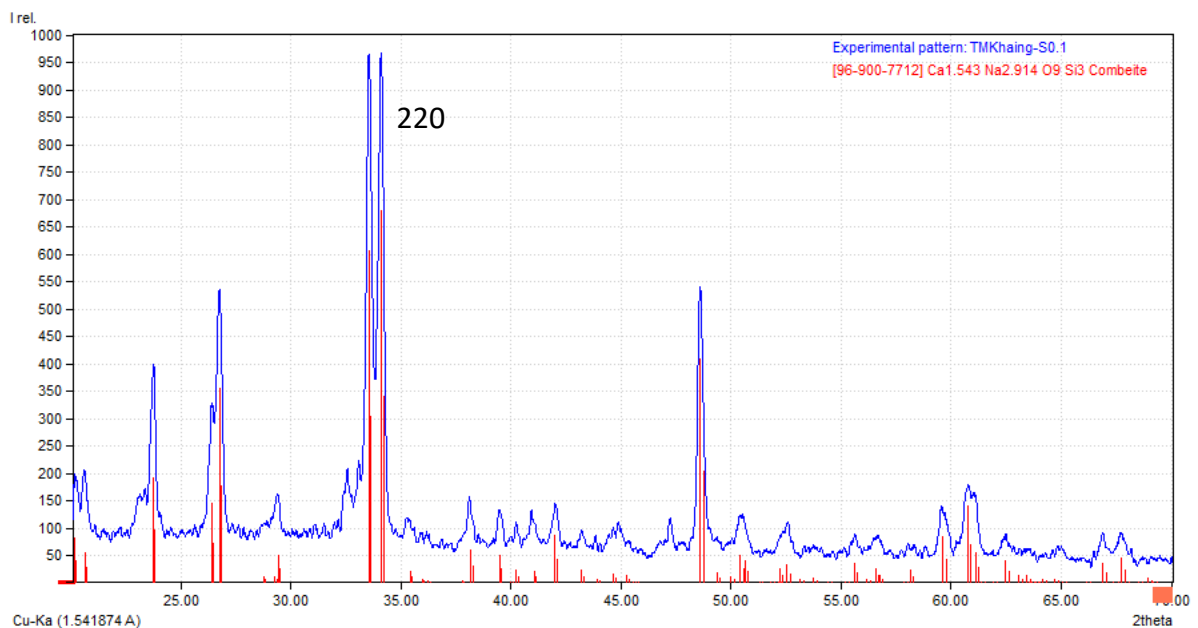


Figure- 2(a) XRD pattern of the glass ceramics sintered at 800 °C for 2 h .

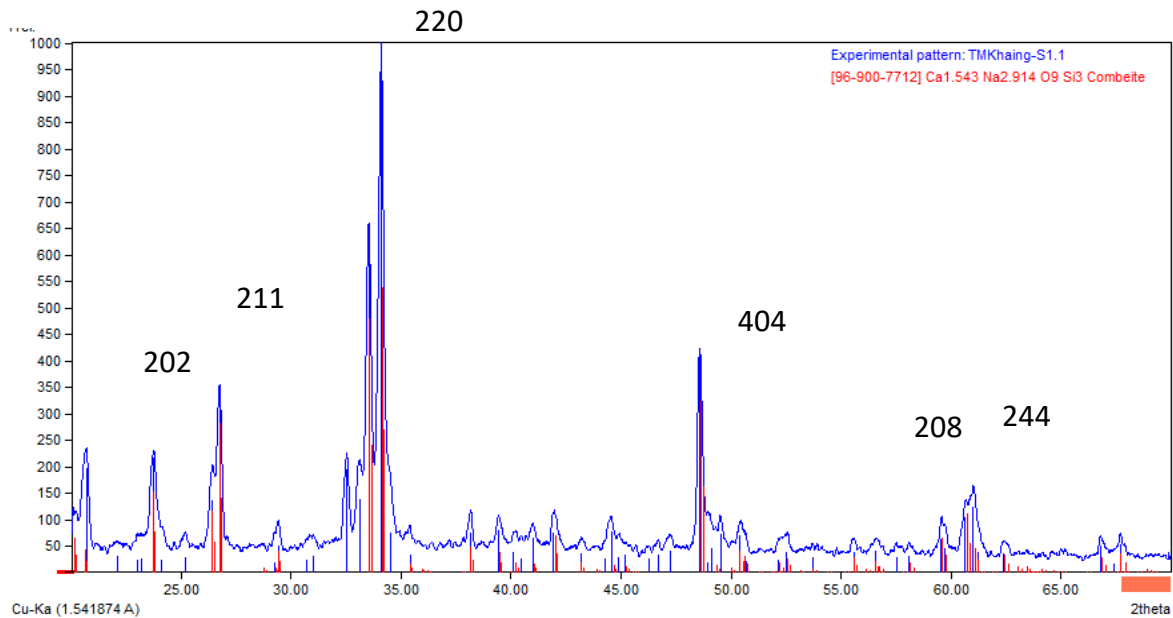


Figure- 2(b) XRD pattern of the glass ceramics sintered at 900 °C for 2 h

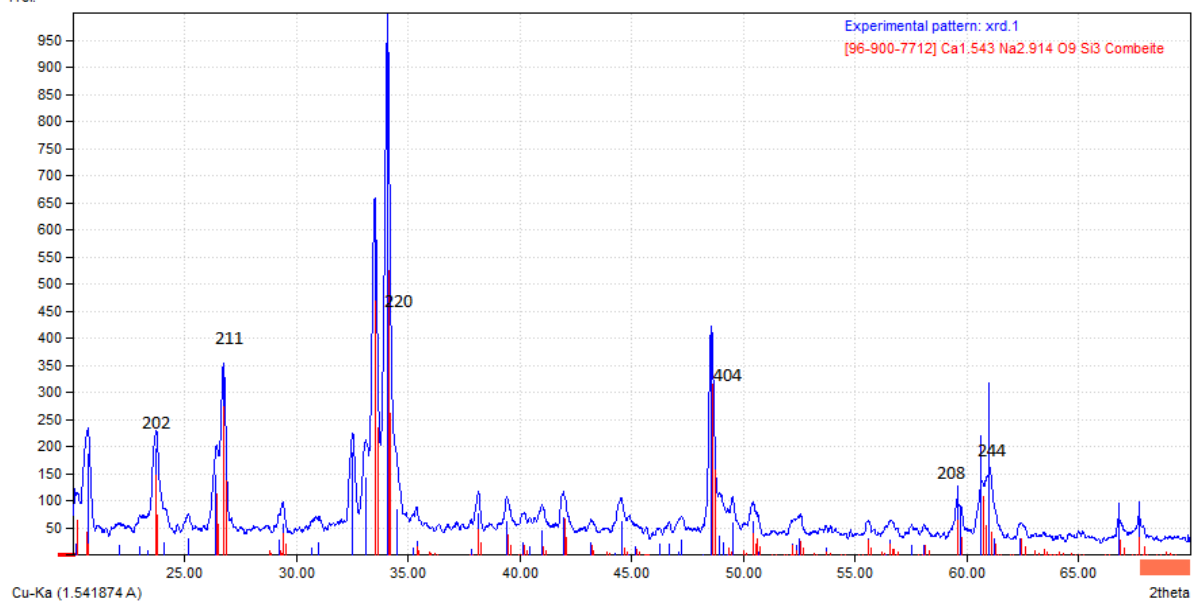


Figure- 2 (c) XRD pattern of the glass ceramics sintered at 1000 °C for 2 h .

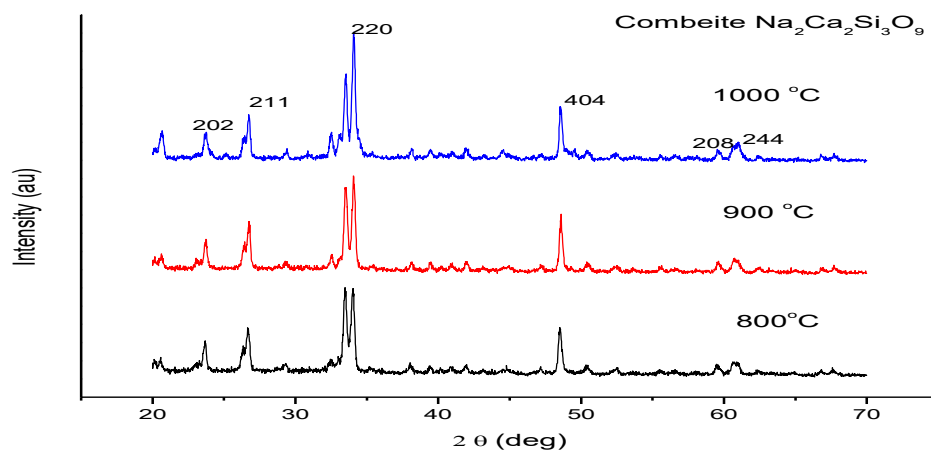


Figure- 2 (d) XRD pattern of the glass ceramics sintered at 1000 °C , 900 °C and 800 °C for 2 h .

Table – The crystallite sizes of the combeite (Na₂Ca₂Si₃O₉) samples at various temperature.

Heat treatment temperature (°C)	800	900	1000
Crystallite sizes (nm)	31.2	31.7	33.2

UV-Vis Analysis

The absorption spectrum and the energy band gap of glass ceramics were measured using a UV-vis spectrometer (PerkinElmer) in the Department of Physics, Yangon University. The energy band gap value E_g could be determined by analyzing the optical data with the optical absorption coefficient α and the photon energy $h\nu$ using Tauc’s relation, $(\alpha h\nu)^2 = A(h\nu - E_g)$. The optical absorption spectra were recorded at room temperature in the range of wavelengths from 202 nm to 1100 nm. The optical band gap was evaluated by plotting $(\alpha h\nu)^2$ vs $h\nu$ as shown in Figure 3(a-c) . Extrapolating the linear portion of the absorption edge $(\alpha h\nu)^2$ the photon energy axis gives the direct energy band gap of the glass ceramics. The band gap energies (eV) for the combeite (Na₂Ca₂Si₃O₉) are 4.7 eV, 4.82 eV, and 4.91 eV, respectively. The values for E_g of the glass–ceramic samples show an increase as the heating temperature increase gradually(Kolli, Kanikaram, et al. 2022). The results of this study indicate that combeite could be employed in optoelectronic devices (Zosiamliana et al. 2022).

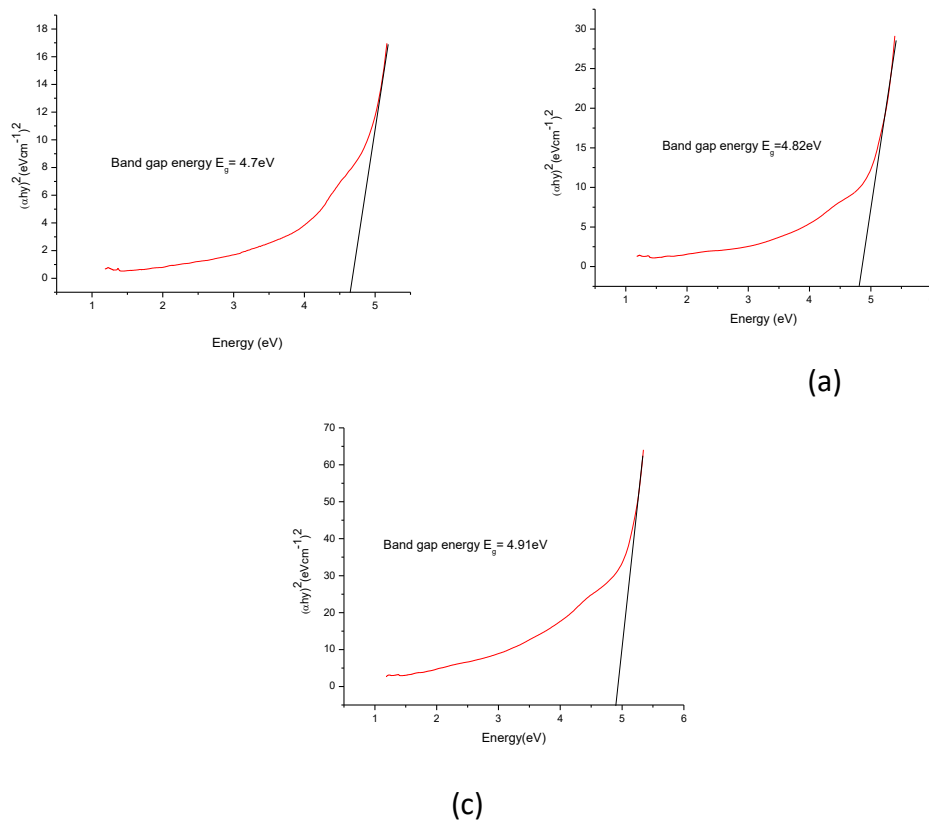


Figure - 3 The energy band gap values of combeite (Na₂Ca₂Si₃O₉) at (a) 800 °C, (b) 900 °C and (c) 1000 °C .

Fourier - transform infrared (FTIR) Analysis

The information from the infrared spectra of the samples can be used to investigate and gain additional information and data regarding the existence of different structural groups in the

materials. Fig. 4(a-c) shows the FTIR spectrum of the glass–ceramics within the range of 400 cm^{-1} and 4000 cm^{-1} sintered at different temperatures. The bands in the low-frequency range around 400 cm^{-1} – 600 cm^{-1} can be attributed to the vibration of Si–O bonding. The mid-frequency band between 600 cm^{-1} to 800 cm^{-1} can be associated with and related to the presence of Si–O and Si–O–Si bond bending symmetric stretching vibrations in the sample. Besides, the higher frequency band within the spectral range 800 cm^{-1} to 1250 cm^{-1} can be related to the Si–O bond inwards the SiO_4 tetrahedron asymmetric stretching modes (Zaid et al. 2020). The 447 cm^{-1} , 449 cm^{-1} and 451 cm^{-1} peaks are assigned to Si-O-Si bending vibration, which is attributed to normal vibration modes of Si-O in the SiO_4 group, indicating the presence of amorphous silicate. The absorption bands at 574 cm^{-1} and 576 cm^{-1} can be assigned to O-P-O bending vibrations of bridging phosphorous, and the one at 518 cm^{-1} to O=P-O vibrations (Gavinho et al. 2021). The band at 621 cm^{-1} and 698 cm^{-1} confirmed that the presence of cristobalite phase in glass ceramics and it was most likely arising from the sodium calcium silicate phase. The broad peaks at 923 cm^{-1} and 931 cm^{-1} indicate the presence of Si-O-Ca vibrations. Similar values were observed for other cyclo-silicates (Kolli, V M, et al. 2022). The spectra at 1031 cm^{-1} , 1033 cm^{-1} and 1039 cm^{-1} showed a strong absorption band of Si-O-Si asymmetric stretching vibration. The peak is located at 1446 cm^{-1} due to the presence of carbonate (CO_3^{2-}). The presence of carbonate bonds is attributed the a carbonation process of the material due to the atmospheric CO_2 as a consequence of the high calcium content in the preparation. The high Ca^{2+} content also causes the formation of a band at 1483 cm^{-1} . The band at 2852 cm^{-1} and 2924 cm^{-1} were assigned the symmetric and asymmetric stretching vibrations of C-H bonding. The broad peak centered at 3400 cm^{-1} , 3442 cm^{-1} and 3452 cm^{-1} and the peak at 1637 cm^{-1} and 1653 cm^{-1} are ascribed to the stretching and bending vibrations of the O-H group in adsorbed water molecules. These bands were present in the sintered samples because the water molecules were unable to escape from the silica matrix.

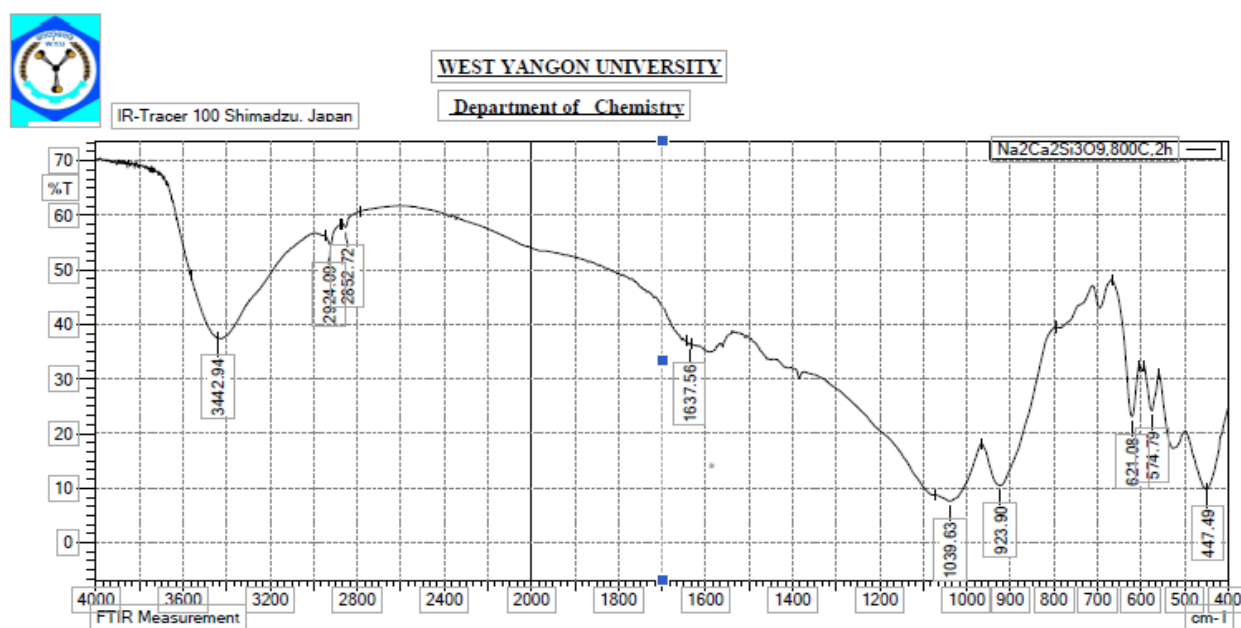


Figure-4 (a) FTIR spectrum the synthesized combeite heat treated at $800\text{ }^{\circ}\text{C}$

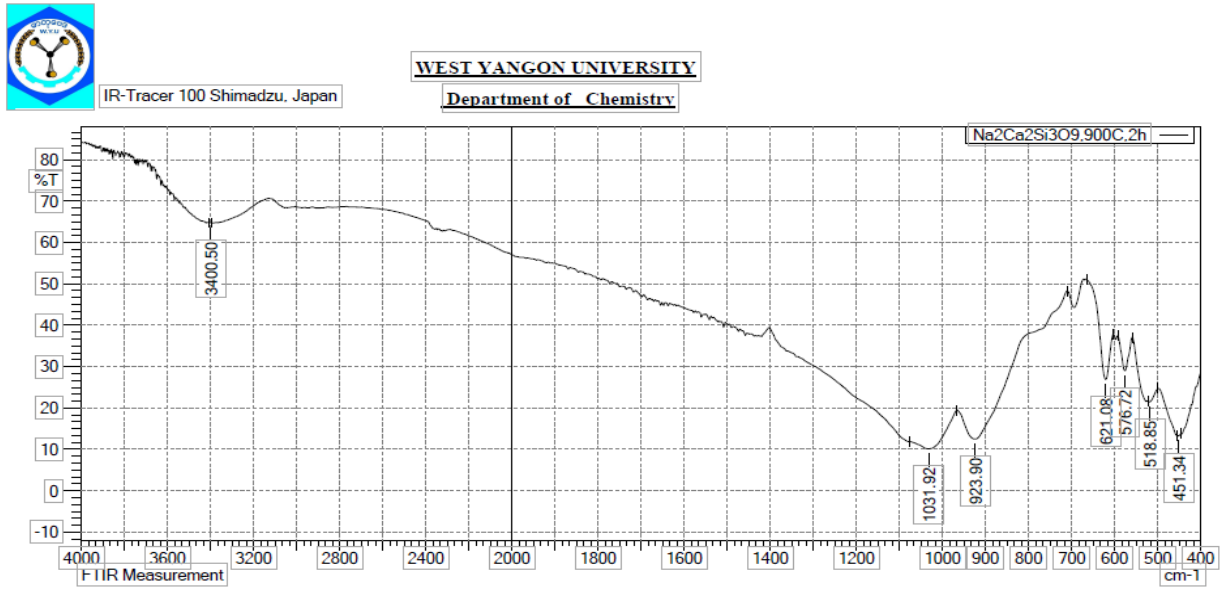


Figure-4 (b) FTIR spectrum the synthesized combeite heat treated at 900 °C

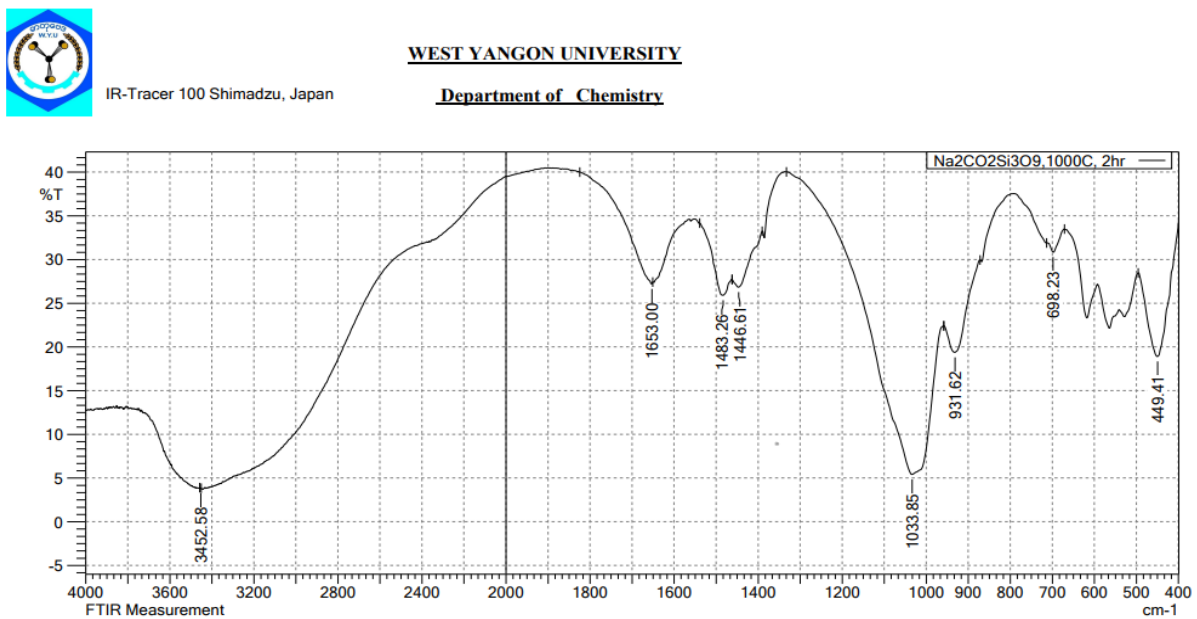


Figure-4 (c) FTIR spectrum the synthesized combeite heat treated at 1000 °C

Conclusion

SiO₂-CaO-Na₂O-P₂O₅-based glass ceramics were synthesized through the sol-gel process using sodium metasilicate as a silica precursor. Extensive thermal treatments and characterizations reveal that the optimized protocol could be employed to produce pure combeite at temperatures between 800 °C – 1000 °C. The X-ray diffraction (XRD) patterns of the glass-ceramics show the presence of crystalline phases of sodium calcium silicate, Na₂Ca₂Si₃O₉. The secondary phase formatting may be P₂O₅ phase. This phase was confirmed by FTIR results. From the optical studies, the optical band gaps were estimated to be in the range of 4.7 eV – 4.91 eV. In the presented spectrum, the absorption bands of silicate groups were clearly evident. This spectrum was indicated high surface area silica structures.

Acknowledgements

The authors would like to express our deepest gratitude to the Department of Physics and Universities' Research Center, University of Yangon, for the supports with research facilities. The author is grateful to Dr Nu Nu Aye, Principle, Pathein Education Degree College, for her kind encouragement and permission. We deeply thank the Myanmar Academy of Arts and Science for submission of research paper.

References

- Abbasi, Mojtaba, and Babak Hashemi. 2014. "Fabrication and Characterization of Bioactive Glass-Ceramic Using Soda-Lime-Silica Waste Glass." *Materials Science and Engineering C* 37(1): 399–404. <http://dx.doi.org/10.1016/j.msec.2014.01.031>.
- Aswad, M A, I K Sabree, and Ali H S Abd. 2021. "An Examination of the Effect of Adding Zirconia to Bioactive Glass-Ceramic Properties." *IOP Conference Series: Materials Science and Engineering* 1067(1): 012121.
- Dang, Tan Hiep et al. 2020. "Characterization of Bioactive Glass Synthesized by Sol-Gel Process in Hot Water." 5: 1–10.
- Fernandes, Hugo R. et al. 2018. "Bioactive Glasses and Glass-Ceramics for Healthcare Applications in Bone Regeneration and Tissue Engineering." *Materials* 11(12): 1–54.
- Gavinho, S. R. et al. 2021. "Structural, Thermal, Morphological and Dielectric Investigations on 45S5 Glass and Glass-Ceramics." *Journal of Non-Crystalline Solids* 562(January): 120780. <https://doi.org/10.1016/j.jnoncrysol.2021.120780>.
- Gmeiner, R. et al. 2015. "Additive Manufacturing of Bioactive Glasses and Silicate Bioceramics." *Journal of Ceramic Science and Technology* 6(2): 75–86.
- Kaur, Gurbinder et al. 2019. "Mechanical Properties of Bioactive Glasses, Ceramics, Glass-Ceramics and Composites: State-of-the-Art Review and Future Challenges." *Materials Science and Engineering C* 104(December 2018): 109895. <https://doi.org/10.1016/j.msec.2019.109895>.
- Kolli, Nishant Kumar, Sai Phalguna Kanikaram, et al. 2022. "Exploring the Potential Structural, Optical, Dielectric Facets and in-Vitro Behavior of Combeite Synthesized by the Sol-Gel Route." *Physica Scripta* 97(7).
- Kolli, Nishant Kumar, Datta Darshan V M, et al. 2022. "Probing into the Potential Features of Sodium Calcium Silicate (Na₂Ca₂Si₃O₉) Synthesized by the Solid-State Route." *Physica Scripta* 97(8).
- Kumar, Sanjeet. "Bioactive Glass Ceramics Using Rice Husk Ash Waste Material by DEPARTMENT OF CERAMIC ENGINEERING."
- Mezahi, Fatima-zohra et al. 2018. "Reactivity Kinetics of Sol-Gel Derived 52S4 Glass versus the Treatment Temperature To Cite This Version : HAL Id : Hal-01915389."
- Mirza, Ambreen et al. 2017. "Effect of Temperature on Mechanical and Bioactive Properties of Glass-Ceramics." *Journal of Alloys and Compounds* 726: 348–51. <http://dx.doi.org/10.1016/j.jallcom.2017.07.285>.
- Patternson, A.L. 1939. "Scherrer Formula.Pdf." *Physical review* 56: 978.
- Quintero Sierra, Lindsey Alejandra, and Diana Marcela Escobar. 2019. "Characterization and Bioactivity Behavior of Sol-Gel Derived Bioactive Vitroceramic from Non-Conventional Precursors." *Boletín de la Sociedad Espanola de Ceramica y Vidrio* 58(2): 85–92.
- Zaid, M. H.M. et al. 2020. "Synthesis and Characterization of Samarium Doped Calcium Soda-Lime-Silicate Glass Derived Wollastonite Glass-Ceramics." *Journal of Materials Research and Technology* 9(6): 13153–60. <https://doi.org/10.1016/j.jmrt.2020.09.058>.
- Zosiamliana, R. et al. 2022. "Electronic, Mechanical, Optical and Piezoelectric Properties of Glass-like Sodium Silicate (Na₂SiO₃) under Compressive Pressure." *RSC Advances* 12(20): 12453–62.

GROWTH AND HIGH TEMPERATURE PHASE CHARACTERISTICS OF PURE AND DOPED (KDP-ADP) CRYSTALS

Ami Soe¹, Khin Htar Swe², Yi Mon Kyaing³, San San Maw⁴, Than Than Swe⁵

Abstract

The pure and doped Potassium Dihydrogen Phosphate (KDP) KH_2PO_4 and Ammonium Dihydrogen Phosphate (ADP) $\text{NH}_4\text{H}_2\text{PO}_4$ have been grown by slow evaporation technique from the supersaturated solution at room temperature. The pure and doped (KDP-ADP) crystals show a phase transition like phenomena named as high temperature phase transition at a characteristic temperature T_p . Upon heating above the T_p , the pure and doped (KDP-ADP) crystals experience a thermal dehydration. In order to investigate the nature of phase transition in MH_2PO_4 -type crystals (M=K or NH_4), temperature-dependent resistivity measurements on mixed KDP-ADP crystals performed. *The activation energies of pure and doped (KDP-ADP) crystals were 0.45eV for KDP, 1.3eV for A-KDP, 1.17eV for K-ADP and 2.87eV for ADP.*

Keywords: high temperature, phase transition, dehydration, resistivity measurements.

Introduction

Crystalline solids play very important role in fabrication of devices for science and Technology (Y.Chaitanya *et al.*,2021). Ammonium dihydrogen phosphate (ADP) and potassium dihydrogen phosphate (KDP) having important applications and harmonic generation was solution grown by slow evaporation technique at room temperature (Kumaraman *et al.*,2008). The enormous advantages in the modern industry during the first few decades succeeded rapidly due to the increasing availability of high-quality single crystals of Semiconductors, Solid State Lasers, Piezo electrics, Ultra-violet and Infra-red sensitive materials crystalline film for microelectronics (Shaikh Kalim *et al.*, 2015).

They are widely used as electro-optic modulator, Q-switch, and high-power laser frequency conversion material due to his magnificent performance as an active element in such devices: piezoelectric, ferroelectric and electro-optics (Shaikh Kalim *et al.*, 2015). Among the applications of high temperature proton conductors are as solid electrolytes for humidity sensors, hydrogen sensors, fuel cells, hydrogen pumps and energy conversion. Ammonium Dihydrogen Phosphate (ADP) $\text{NH}_4\text{H}_2\text{PO}_4$ and Potassium Dihydrogen Phosphate (KDP) KH_2PO_4 belong to MH_2PO_4 type crystals MH_2PO_4 (where M = K, NH_4 , Rb, Cs). Crystal structures of MH_2PO_4 family are isomorphous in room-temperature. In other words, the crystal structure of (KDP-ADP) at room temperature is tetragonal system (Guohui Li *et al.*,2005).

The chemical formula of the salt is pure and doped (KDP-ADP), it is composed of positive potassium ammonium ions (K- NH_4), negative phosphate ions (PO_4), and protons (H_2). Each ammonium ion consists of four hydrogen atoms covalently bonded to a nitrogen atom. Each phosphate ion consists of four oxygen atoms covalently bonded to a phosphorus atom. A phosphate ion carries the extra negative charge of three electrons, one of which it obtains from the ammonium part of the structure and two from the two other hydrogen atoms that furnish in this way two conducting protons (Fabricio Mendes Souza, 2017).

The super protonic conductivity study of the crystal plays important role in the class of solid electrolytes (A.SIERADZKI *et al.*,2011). Many authors have investigated the protonic conductivity or structural phase transition in crystal with short hydrogen bonds MH_2PO_4 family shows a phase transition like phenomena named as high temperature phase transition (HTPT) at a characteristic temperature T_p .

¹ Department of Physics, Patheingyi University.

² Department of Physics, Patheingyi University.

³ Department of Physics, Patheingyi University.

⁴ Department of Physics, Patheingyi University.

⁵ Department of Physics, Patheingyi University.

Materials and Method

Crystal growth, the sample preparation, measurement of conductivity is the essential role in the present experiments work. Some details will be described because they are important in practice.

Crystal Growth and Observation on the Crystal

Most crystals grow from liquid solutions. The liquid is carrier of the atoms or ions necessary for the growth of the crystal, and may be water or a molten substance at room temperature. Chemical substance may dissolve in a particular liquid the solvent. The same solid substance may separate (crystallize) from the solvent when the temperature drops or when the liquid becomes saturated with the dissolve substance. The carrier liquid may be water, a molten salt, a molten metal, a molten rock or an organic solvent. Crystals grow from liquid is response to changes in temperature, pressure, or liquid composition. Many individual crystals may grow simultaneously if the nucleation rate is high. Single crystals of pure and doped (KDP-ADP) were grown by slow evaporation from aqueous solution containing 11.5 g of ADP and 23 ml, 1.5 g of KDP doped 11.5 g of ADP and 28 ml, 1.3 g of ADP doped 13.6 g of KDP and 29.8 ml and 13.6 g of KDP and 27.2 ml of distilled water.

First, the required quantities of KDP and ADP were added to distilled water by stirring. The temperature was slowly increased until all of the salt dissolve for preparing the saturated solution. The solution is heated and a saturated solution of (KDP-ADP) was prepared for 30 minutes at 32 °C. The perfect little seed crystals were hung in a saturated KDP-ADP solution. Beautiful water clear tetragonal crystals of 1-2 cm diameter were obtained within 2 and 3 months, they were dried and placed in a seal bottle. The photographs of pure and doped (KDP-ADP) crystals are shown in Fig. 1, 2, 3 and 4.

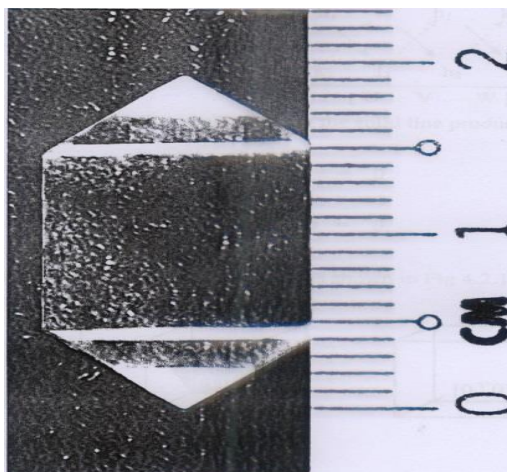


Figure 1 Photograph of KDP grown crystal

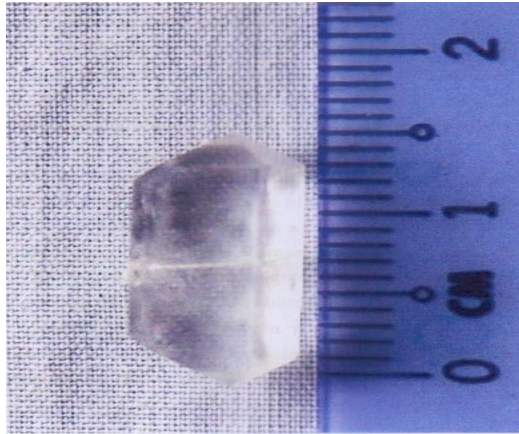


Figure 2 Photograph of A doped KDP grown crystal

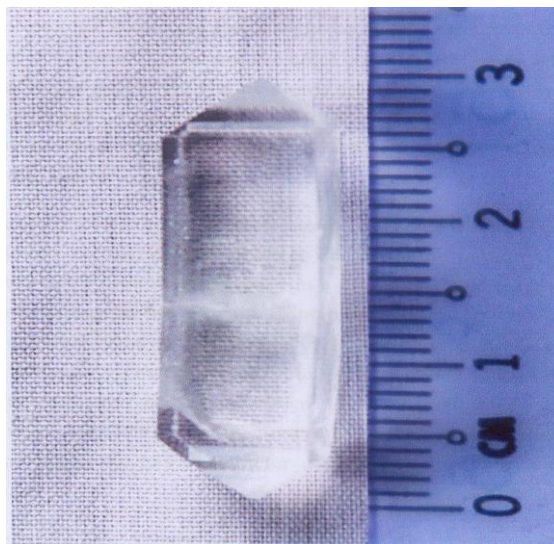


Figure 3 Photograph of K doped ADP grown crystal

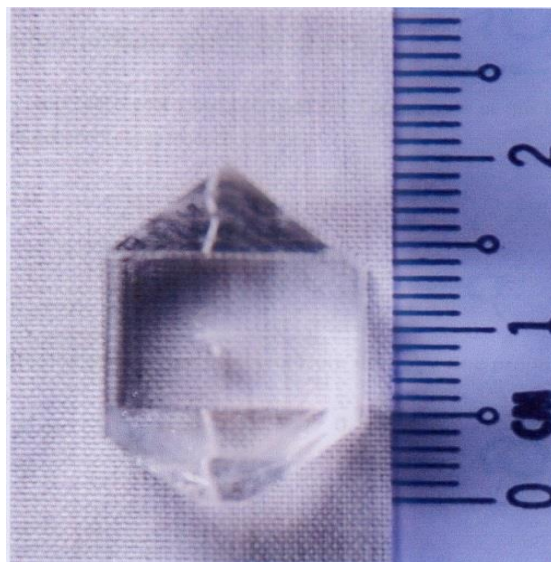


Figure 4 Photograph of ADP grown crystal

Temperature Dependent Conductivity Measurement

The sample was sandwiched between two copper plates that serve as two electrodes. To obtain better electric conduction, silver paste was applied evenly on both surface of the sample. The sample was placed in a sample holder that was immersed in a heating steel cell. Thermal conducting mica shield is used between the sample and the chamber to have a good thermal conductivity and to protect from electrical conduction. Arrangement and experimental set-up for conductivity measurement are shown in Fig. 5 and 6.

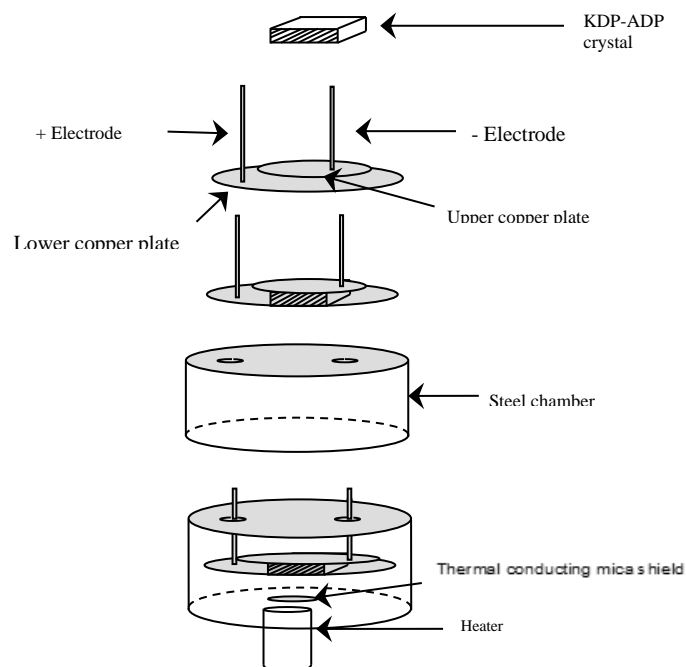


Figure 5 Arrangement for resistivity measurement



Figure 6 Experimental set-up of resistivity measurement

Results and Discussion

High Temperature Phase Transitions of KDP-ADP Crystals

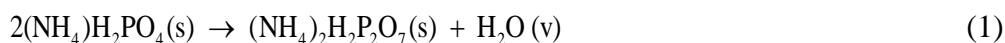
Single crystals of $\text{NH}_4\text{H}_2\text{PO}_4$, $\text{K}_{0.1}(\text{NH}_4)_{0.9}\text{H}_2\text{PO}_4$, $(\text{NH}_4)_{0.1}\text{K}_{0.9}\text{H}_2\text{PO}_4$ and KH_2PO_4 were grown by slow evaporation of aqueous solutions at room temperature. The electrical conductivity measurement was performed in the temperature range between 333 K and 673 K.

Electrical Conductivity Measurement Results

The results of temperature-dependent conductivity measurement on (KDP-ADP) crystals are shown in Fig. 7, 8, 9 and 10.

Two distinct regions are separated by a knee at 365 K for ADP, at 372 K for KDP, at 381 K for A-doped KDP and at 383 K for K-doped ADP. The knees at those temperatures may be attributed to water in the surfaces of the samples at those temperatures.

A sharp change is found in the conductivity at 430 K. Upon heating above the characteristic temperature T_P , the crystal of the KH_2PO_4 type experiences a thermal dehydration taking place on the surface of the sample. The behavior of ADP at 430 K may be interpreted by the chemical reaction



(Where s and v denote solid or vapor state, respectively).

Similarly, for KH_2PO_4 ,



The onset temperatures of the dehydration described by Eq (1) and (2) are about $T_P = 430$ K for ADP and $T_P = 434$ K for KDP and dehydration takes place at reaction sites distributed on the surface of the grains. Above those temperature further decomposition of the samples proceeds also in the bulk.

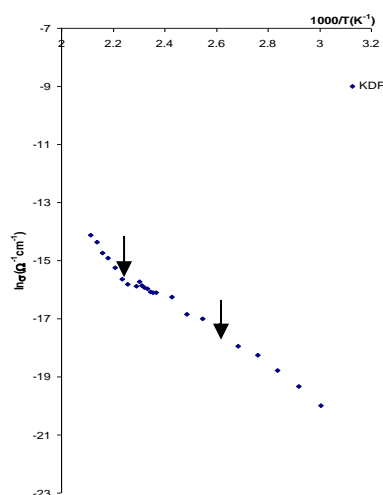


Figure 7 Temperature dependent electrical conductivity of KDP crystal

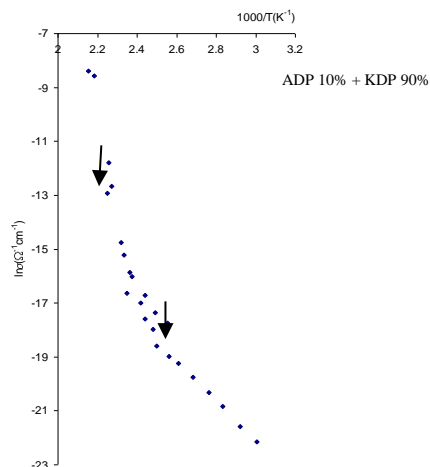


Figure 8 Temperature dependent electrical conductivity of A doped KDP crystal

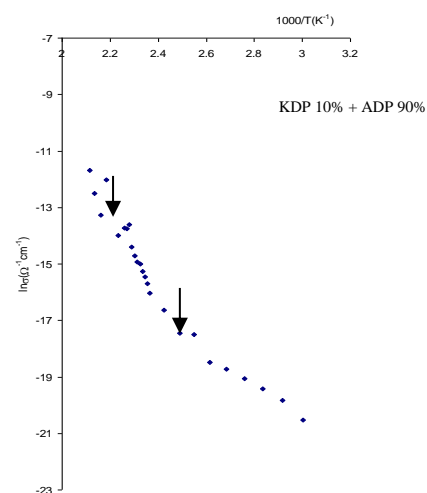


Figure 9 Temperature dependent electrical conductivity of K doped ADP crystal

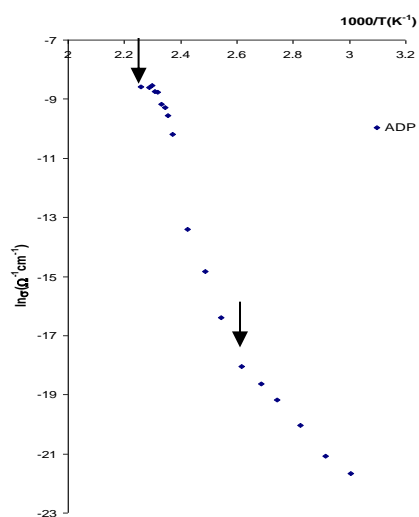


Figure 10 Temperature dependent electrical conductivity of ADP crystal

In the nearly temperature interval ($365 \text{ K} \leq T \leq 439 \text{ K}$), the value of $\ln \sigma$ changes with the temperature $1000/T$ for (KDP-ADP) crystals shown in Fig (11 - 15).

The electrical conductivities of (KDP-ADP) crystals have been investigated and in all the temperature dependence of the conductivity followed Arrhenius relations: $\sigma = \sigma_0 \exp [-E_a/kT]$ where σ is the conductivity, σ_0 is the pre-exponential factor, E_a is the activation energy for conduction, k is the Boltzmann constant and T is the absolute temperature.

$$\ln \sigma = - E_a/kT + \ln \sigma_0$$

$$\ln \sigma = -\left(\frac{E_a}{1000 k} \cdot \frac{1000}{T}\right) + \ln \sigma_0$$

Comparing this equation with the experimental linear equation $y = mx + c$, the value of slope will give the value of $(-E_a/1000 k)$. From Fig 11, the activation energy E_a can be obtained from the least-square method on the slope of $\ln \sigma$ versus $1000/T$.

$$-\left(\frac{E_a}{1000 k}\right) = m$$

$$-\left(\frac{E_a}{1000 k}\right) = - 5.2045$$

$$E_a = 5.2045 \times 1000 \times 1.38 \times 10^{-23} \text{ J}$$

$$= 0.45 \text{ eV}$$

Similarly, from Fig. 12, 13 and 14, the activation energies can be obtained.

The onset temperatures of dehydration and activation energies for (KDP-ADP) crystals are listed in Table 1.

Table 1 Onset temperatures of the dehydration and activation energies for (KDP–ADP) crystals

Sr No.	Crystals	Onset Temperature(K)	Activation Energy (eV)
1	KDP	434	0.45
2	A-KDP	433	1.30
3	K-ADP	439	1.17
4	ADP	430	2.87

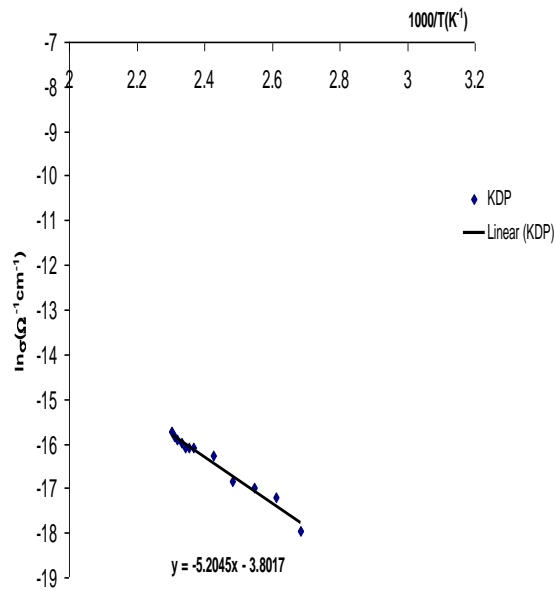


Figure 11 Temperature dependent electrical conductivity of KDP for $(372 \text{ K} \leq T \leq 434 \text{ K})$

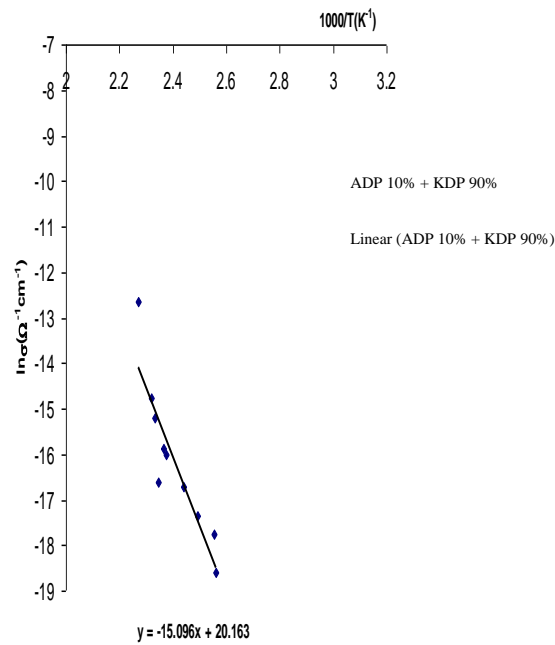


Figure 12 Temperature dependent electrical conductivity of A doped KDP for $(381 \text{ K} \leq T \leq 433 \text{ K})$

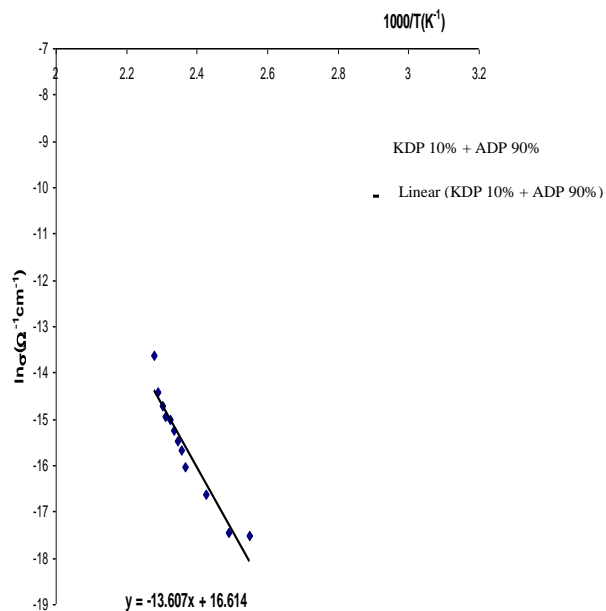


Figure 13 Temperature dependent electrical conductivity of K doped ADP for $(383 \text{ K} \leq T \leq 439 \text{ K})$

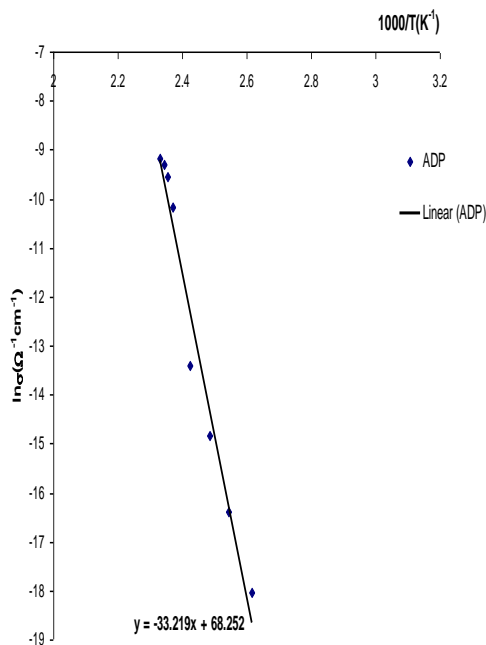


Figure 14 Temperature dependent electrical conductivity of ADP for $(365 \text{ K} \leq T \leq 430 \text{ K})$

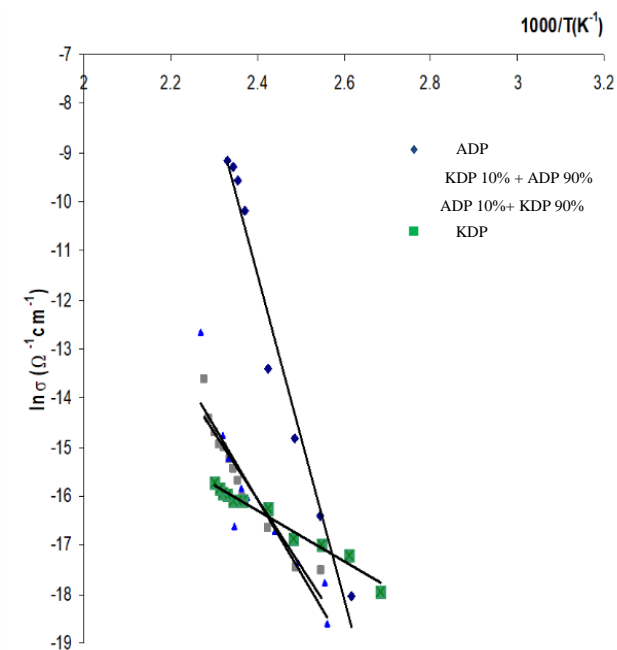


Figure 15 Temperature dependent electrical conductivity of (ADP-KDP) crystals for $(365 \text{ K} \leq T \leq 439 \text{ K})$

Conclusion

Single crystals of (KDP-ADP) were grown by slow evaporation technique. The electrical conductivity measurement results for (KDP-ADP) crystals suggest that $T_P = 430 \text{ K}$ for ADP, 434 K for KDP, 433 K for A doped KDP and 439 K for K doped ADP mark the onset of partial polymerization taking place on the surfaces of the samples, such that the phases above those temperatures are the mixed phases consisting of tetragonal ADP or KDP in the bulk of the samples and ammonium polyphosphate, $(\text{NH}_4)_2\text{H}_2\text{P}_2\text{O}_7$ or potassium polyphosphate, $\text{K}_2\text{H}_2\text{P}_2\text{O}_7$, at the surfaces of the samples. Electrical resistivities of the samples are found to be decrease with increasing temperature. The activation energies of pure and doped (KDP-ADP) crystals were 0.45eV for KDP, 1.3eV for A-KDP, 1.17eV for K-ADP and 2.87eV for ADP.

Acknowledgements

I would like to thank Dr Than Tun, Rector, Patheingyi University, for her kind permission and encouragements to carry out this work.

I would like to thank Dr Aye Ngwe, Professor and Head, Department of Physics, Patheingyi University, for his kind permission and encouragements to carry out this work.

Special thanks are due to Professor Dr Than Than Swe, Department of Physics, Patheingyi University, for his valuable guidance and helpful advice to carry out this work.

I would like to express my gratitude to Professor Dr Khin Myo Ma Ma Saw, Department of Physics, Patheingyi University, for her kind permission and encouragements to carry out this work.

References

- A.SIERADZKI, A.CIZMAN, R.POPRAWSKI, T.MARCINISZYN and E.RYSIAKIEWICZ- PASEK, (2011), "ELECTRICAL CONDUCTIVITY AND PHASE TRANSITIONS IN KDP- AND ADP-POROUS GLASS NANOCOMPOSITES". Journal of Advanced Dielectrics, Vol, No. 3, pp. 337-343
- Fabricio Mendes Souza, (2017) "Electrical Conductivity in the KDP, ADP, and $K_{1-x}(NH_4)_xH_2PO_4$ Crystals". Material Research.
- Guohui Li, Xue Liping, Genbo Su, Xinxin Zhaung, Zhengdong Li and Youping He, (2005), "Study on the growth and characterization of KDP-type crystals". Journal of crystal Growth 274, pp.555-562.
- Kumaraman, S;Prakash, Joseph, (2008) "Crystal Growth and characterization of ADP & KDP". Bulletin of Pure & Applied Sciences – Physics.
- Shaikh Kalim, A. B. Lad and B. H. Pawar (2015), "Growth and properties of ADP single crystal"
- Y.Chaitanya, V.V.Hari Babu, V.Naga Malleswari and W.V.K.Mehar,(2021), " Electrical and Thermo Electrical Properties Of Adp And Kdp Crystals". Turkish Journal of Computer and Mathematics Education, Vol.12 No.7, pp.443-450.

DESALINATION AND WATER QUALITY ASSESSMENT USING SINGLE-SLOPE PASSIVE SOLAR STILL

Myint Kalyar¹, Cho Mar Kyi,² and Nyo Nyo Win³

Abstract

The United Nations' Sustainable Development Goal (SDG-6) emphasizes the need for clean water and sanitation by 2030. This research intended to generate freshwater from seawater by desalination process using conventional single slope passive solar still. This work was carried out from 2023 March 31 to April 10 for 11 days. Freshwater 1061 ml was distilled from 2 L of seawater. Average freshwater productivity was 96.45 ml per day. Water quality assessment was conducted using a Horiba Multiparameter U-54G and Portable Multiparameter DO 110 to measure the physicochemical parameters such as temperature, electrical conductivity (EC), salinity, turbidity, total dissolved solids (TDS), pH, ORP, DO, and O₂. Additionally, heavy metal constituents Cd, Cr, Pb, As, and Cu were analyzed with a Shimadzu (AA- 7000) Atomic Absorption Spectrophotometer. Results were compared with WHO's drinking water quality standards, specifically National Surface Water Quality Standards in Myanmar, (NSWQS) Class II and Class V. The seawater exhibited all its quality parameters within the acceptable range of Class V. For both seawater and freshwater, the concentrations of Cd, Cr, and Cu fall within the WHO drinking water quality norms, but Pb and As slightly exceed permissible limits. The obtained freshwater meets Class II standards with a salinity of 0.02 ppt and a pH value of 7.41. From the point of view of freshwater quality, it is likely attributed to contaminants from solar still construction and the quality of the original seawater. Despite this, the freshwater parameters remain within class II permissible levels. Those findings contribute directly to targets 6.4 and 6.7 within SDG-6, which focus on efforts and initiatives related to water and sanitation. Consequently, this research can provide important access to fresh water for rural communities, while supporting an affordable and simple technology.

Keywords: Desalination, Single-Slope Passive Solar Still, Freshwater, WHO's Water Quality,

Introduction

Access to clean freshwater is vital not only for safeguarding human health but also for mitigating poverty, ensuring food security, fostering peace and human rights, sustaining ecosystems, and supporting education. The World Population in 2023 is about 8.1 Billion (at mid-year) according to the UN. 45% of the world's population live in rural areas. In Myanmar, 70% of the people live in rural areas with 51.48 million of Myanmar's population by UNFPA-Myanmar, 2015. According to the UN World Water Development Report (2023), nearly two-thirds of the global population faces severe water scarcity for at least one month annually. Therefore, desalination is one of the solutions to water scarcity issues and it is also a fact to implement the target 6.7 of SDG 6; "By 2030, expand international cooperation and capacity building support to developing countries in water-related activities and programs including desalination". The main source of water is seawater not only for the people in the coastal area but also for the different types of marine carriers such as scientists and researchers, fishing and shipping, etc. Desalination is indeed a modern innovative technology used to produce freshwater from brackish or saline sources such as seawater [A. Fadi,2018]. This process is particularly valuable in freshwater-scarce resource regions such as coastal, rural, and remote areas. Moreover, the establishment of SDG 6 "Ensure availability and sustainable management of water and sanitation for all" confirms the importance of water and sanitation in the global political agenda. To meet Target 6.4 of SDG 6 is "Increase water use efficiency and ensure freshwater supplies by 2030". Freshwater has an acceptable salinity below 0.5 parts per thousand (ppt) of dissolved salts while seawater has an average salinity of around 35 ppt [M.Saif,2023]. There is a need to develop efficient and sustainable methods for seawater desalination by freshwater scarcity resources. [Dsilva Winfred Rufuss,2016]. Desalination plays a crucial role in providing freshwater for various marine activities and careers in coastal areas [Mulyanef,2018]. Efficient

¹ Department of Physics, Dawei University

² Department of Physics, Dawei University

³ Department of Physics, Mawlamyine University

and cost-effective desalination plants should be built in coastal areas to ensure a regular supply of freshwater [Diabil, H.A.N.,2022].

In this research, the optimal combination of desalination technology and renewable energy was used to generate freshwater from seawater. Using home-crafted single-slope passive solar still across the desalination technology holds particular significance for coastal, rural, and remote areas due to its simplicity, cost-effectiveness, utilization of renewable energy, and simple technology systems.

Materials & Methods

Experimental Set Up: The locally constructed prototype of a single-slope single-basin solar still is designed to harness solar radiation and optimize the evaporation-condensation process. The structure of the still was comprised of 6 mm thick glass panels, and an aluminum liner sealed with silicone rubber to prevent water leakage of the basin. The wooden tray is used as the container of the still. The dimension of the single basin is (60 cm × 35 cm × 17 cm) and the area of the inclined roof is (62 cm × 35 cm) with a 40° inclination angle. To minimize heat loss, the wooden tray container is black-painted and the rice husk serves as an insulator. The condensed water, also known as distilled water, was collected along aluminum grooves situated beneath the roof on all four sides inside the still. The pilot scale of the single-slope single-basin solar still is depicted in Fig.1 (a) & (b) featuring the schematic diagram and a photograph. The luminous intensity of sunlight was measured by HI 97500 Luxmeter and different temperatures were measured by thermometers.

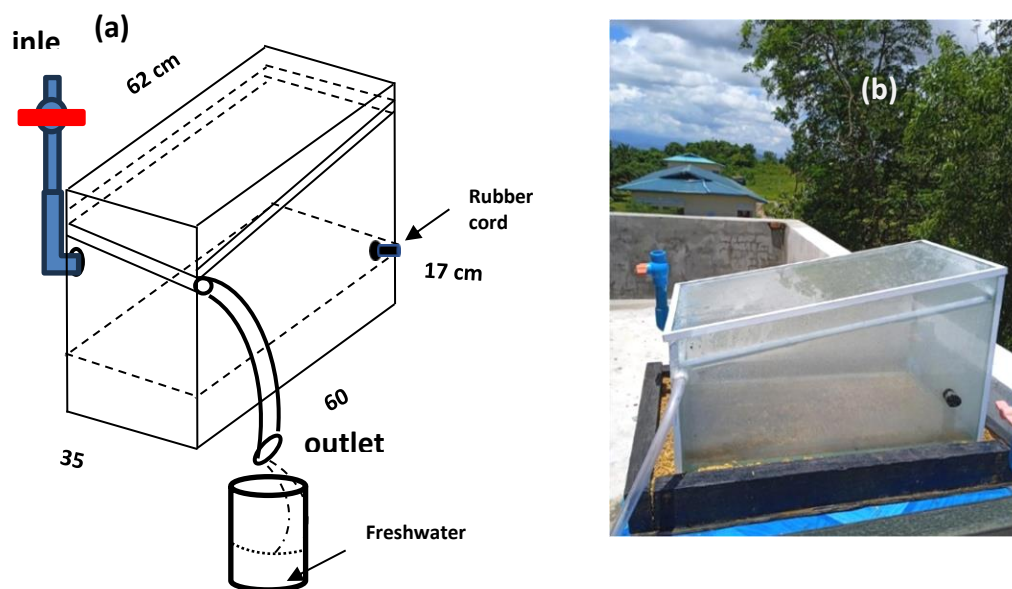


Figure 1(a). Schematic diagram and (b). Photograph of Single Slope Solar Still.

Experimental Procedure

The seawater sample was collected at a depth of 5.5 ft from MaungMaGan Beach in the Tanintharyi Coastal region at Latitude N 14° 8'32'' and Longitude E 98°5'25''. 2 L of seawater was put into the basin and initiated evaporation under a sufficient temperature and leading to condensation due to the temperature difference between the inside and outside of the still cover. Solar radiation intensity and ambient temperature were measured as the climatological factors and glass temperature, seawater temperature, and amount of fresh water were recorded as the solar still's parameters. This work was carried out from 2023 March 31 to April 9 for 11 days. Data collection was made 5 times a day hourly from 10 am to 3 pm.

Equipment for Water Quality Analysis: Physicochemical parameters such as temperature, electrical conductivity (EC), salinity, turbidity, total dissolved solids (TDS), pH, ORP, DO, and O₂ were measured with Horiba Multiparameter U 54 G and Portable Multi-Parameter DO 110. Some of the constituent elements of Cd, Cr, Pb, As, and Cu were measured by Atomic Absorption Spectrophotometer (AA-7000 Shimadzu) as shown in Fig.2.



Figure 2. Atomic Absorption Spectrophotometer (AA-7000 Shimadzu)

Results

Dependence of Freshwater Productivity on Climatic Factors and Solar Still Parameters

Variation of hourly freshwater productivity with climatological factors including solar radiations or luminous flux and ambient temperature (T_a) and different temperatures or still parameters such as the seawater temperature (T_s) or basin water temperature, glass temperature (T_g) (exterior glass surface) were depicted in the following figures (3 -14) for 11 days from 31.3.2023 to 10.4.2023. A comparison of daily freshwater production, overnight freshwater production, and total freshwater production was represented as a histogram in Figure 14. Figure 15 depicts the hourly maximum productivity of freshwater for each day.

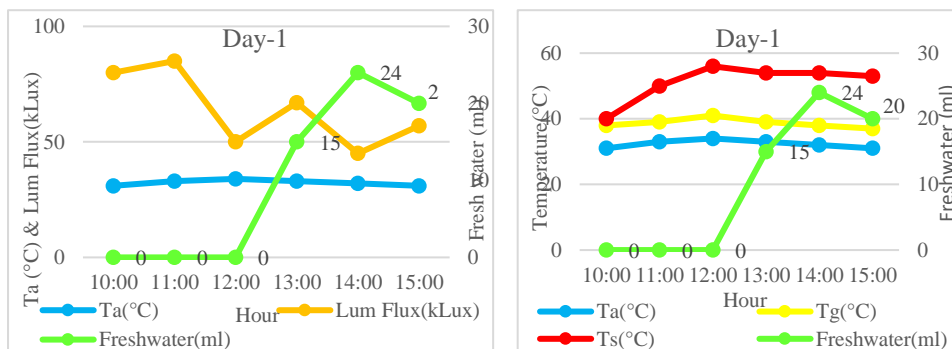


Figure 3(a), (b). Variation of hourly freshwater productivity with climatic factors & different temperatures for 31.3. 2023.

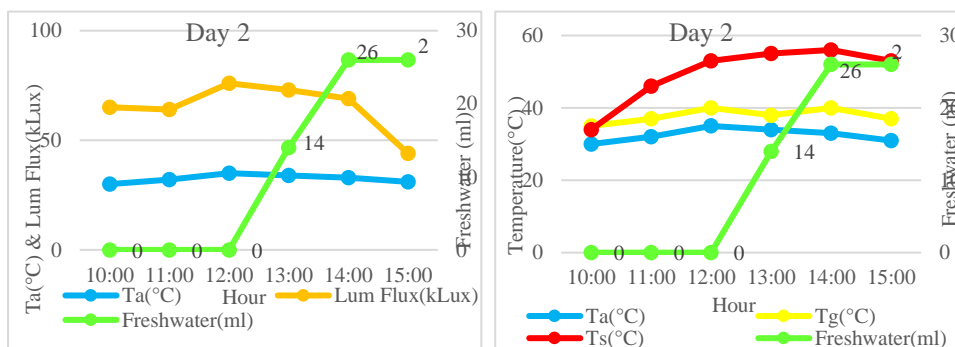


Figure 4(a), (b). Variation of hourly freshwater productivity with climatic factors & different temperatures for 1.4. 2023.

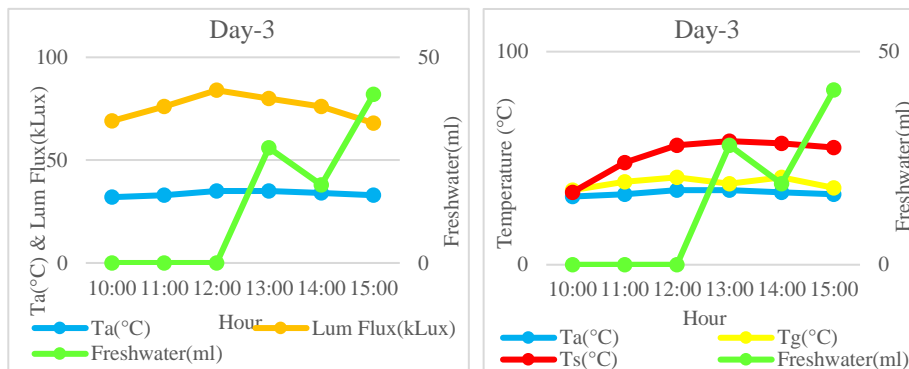


Figure 5(a), (b). Variation of hourly freshwater productivity with climatic factors & different temperatures for 2.4. 2023.

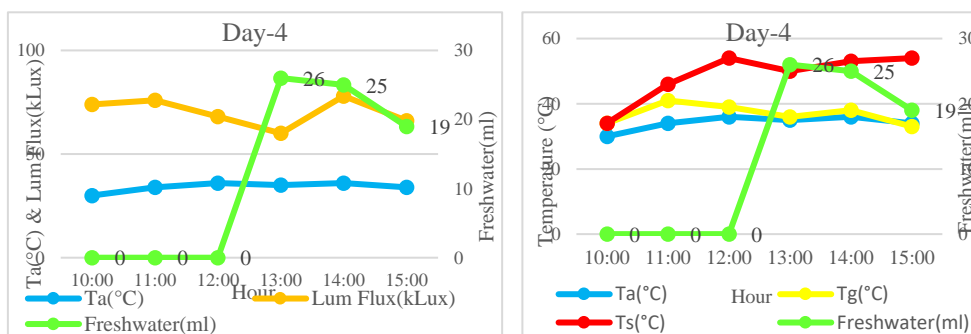


Figure 6(a), (b). Variation of hourly freshwater productivity with climatic factors & different temperatures for 3.4. 2023.

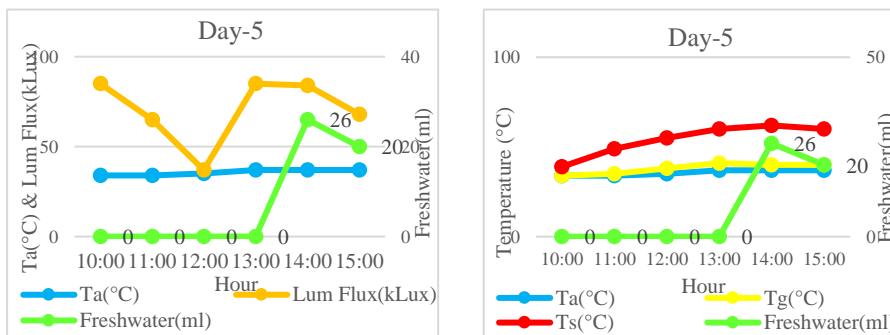


Figure 7(a), (b). Variation of hourly freshwater productivity with climatic factors & different temperatures for 4.4. 2023.

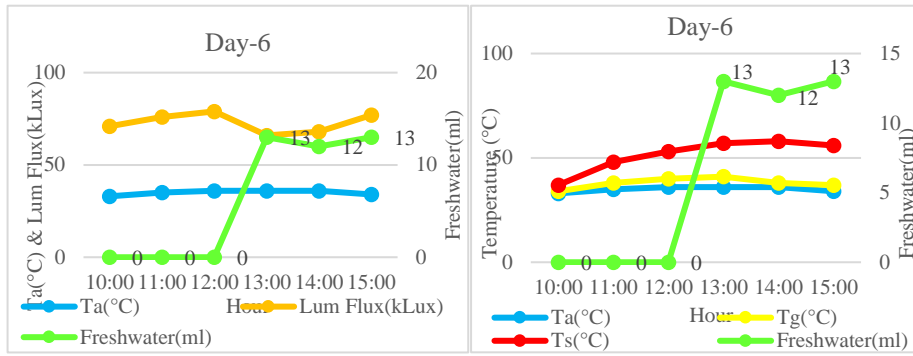


Figure 8(a), (b). Variation of hourly freshwater productivity with climatic factors & different temperatures for 5.4. 2023.

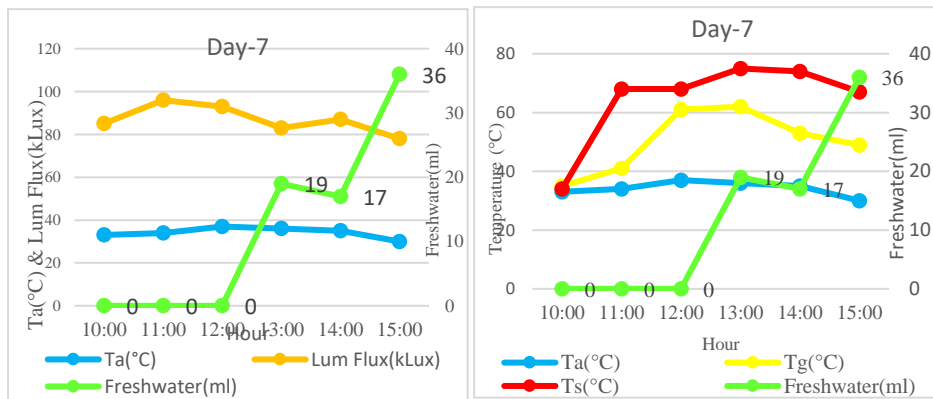


Figure 9(a), (b). Variation of hourly freshwater productivity with climatic factors & different temperatures for 6.4. 2023.

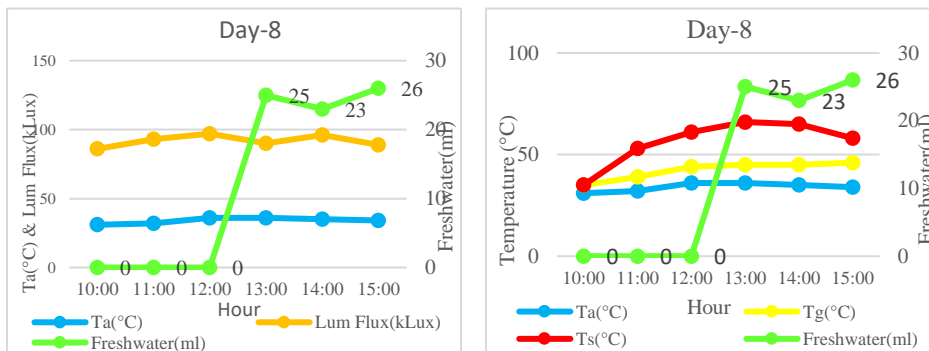


Figure 10(a), (b). Variation of hourly freshwater productivity with climatic factors & different temperatures for 7.4. 2023.

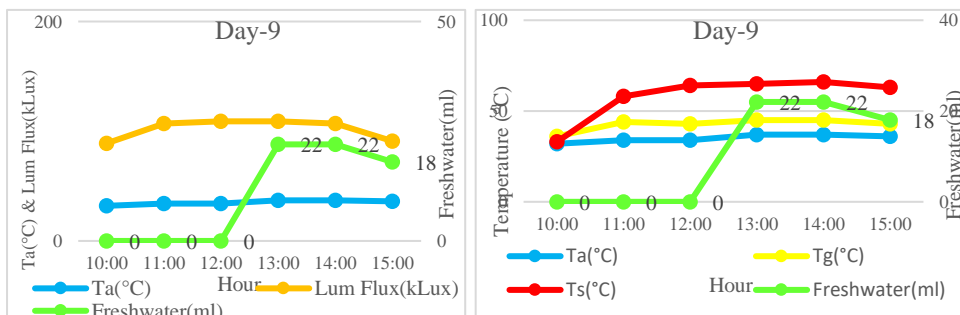


Figure 11(a), (b). Variation of hourly freshwater productivity with climatic factors & different temperatures for 8.4. 2023.

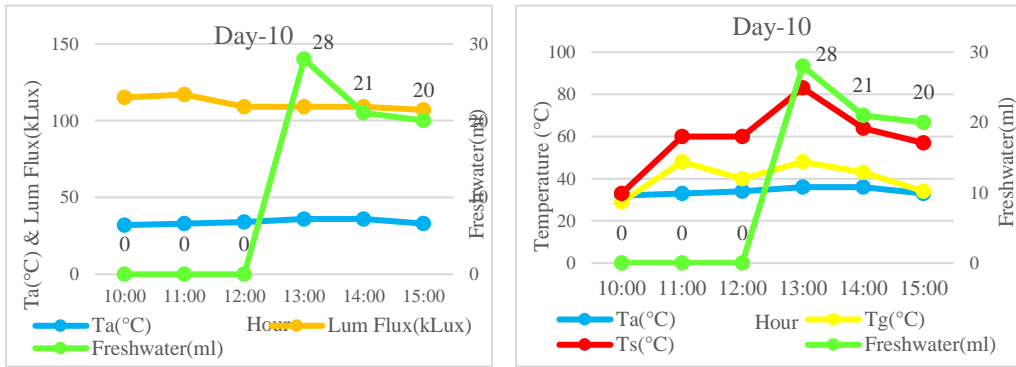


Figure 12(a), (b). Variation of hourly freshwater productivity with climatic factors & different temperatures for 9.4. 2023.

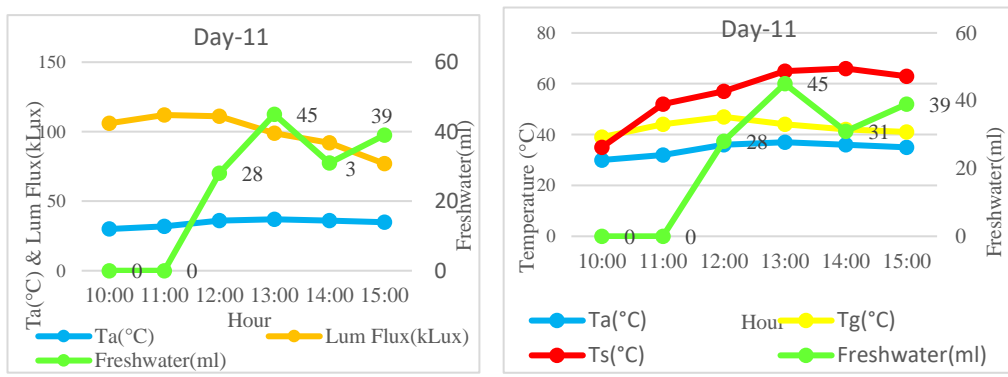


Figure 13(a), (b). Variation of hourly freshwater productivity with climatic factors & different temperatures for 10.4. 2023.

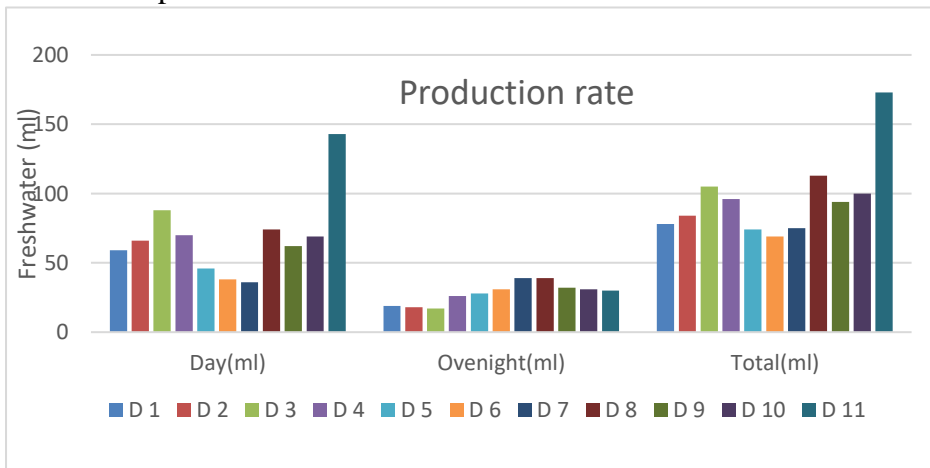


Figure 14. Comparison of daily freshwater production, overnight freshwater production, and total freshwater production

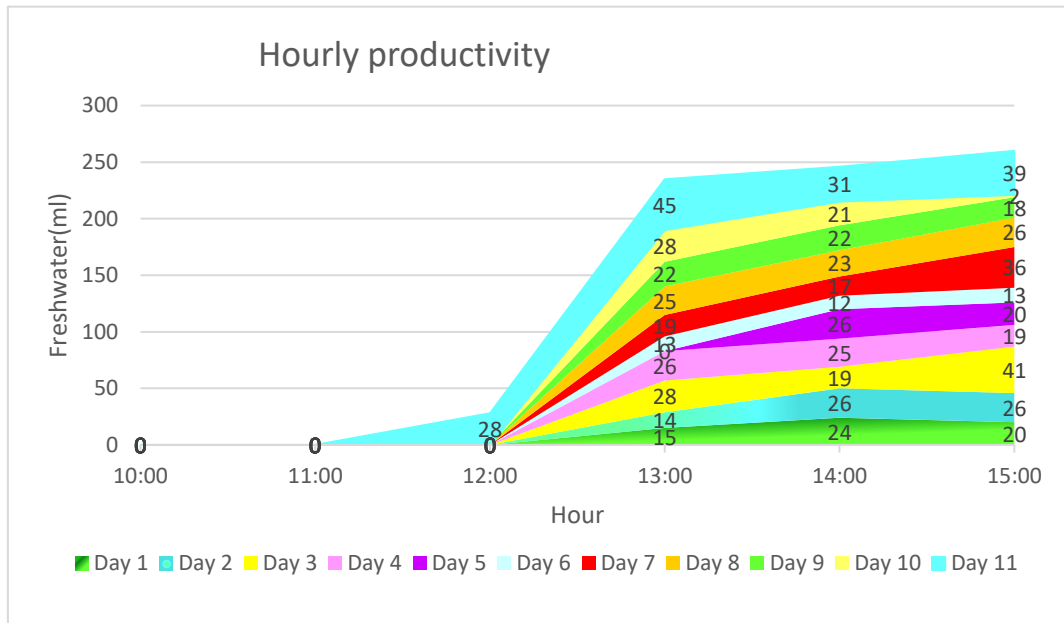


Figure 15. Hourly maximum productivity of freshwater

Water Quality: Physicochemical Parameters

Priority waterbodies shall be classified from Class I to Class V by intended water use. In this study, the obtained data were compared with Class II and Class V of the National Surface Water Quality Standards (NSWQS) adopted from the WHO’s water quality guidelines. The resulting physicochemical parameters of seawater and freshwater are listed in Table 1, Table 2, and Table 3. The resulting physical parameters of both samples, seawater and freshwater are presented in Table 1. The resulting data for seawater was compared with class V standards, while the data for freshwater was compared with class II standards.

Table 1. Comparative Analysis on physical parameters of water samples and standard data (NSWQS)

Quality Parameters	Seawater	Std Class. V (NSWQS)	Freshwater	Std Class. II (NSWQS)
Temperature(°C)	30	-	31	-
EC (mS/cm)	42	6	0.05	1.5
Salinity (ppt)	26.9	35	0.02	0.5
Turbidity (NTU)	51	100	0	25
TDS(NTU)	25.6	2000	0.032	

Table 2. Comparative Analysis on chemical parameters of water samples and standard data (NSWQS)

Quality Parameters	Seawater	Std Class.V(NSWQS)	Freshwater	Std Class.II (NSWQS)
pH	9.5	6-9	7.41	6-9
ORP (mV)	187	-	282	-
DO (mg/L)	5.6	>4	4.32	> 4
O ₂ (%)	8.9	-	6.3	-

Table 3. Comparison of constituent heavy metal concentrations of seawater and freshwater with WHO’s drinking water quality standards

Elements	Seawater	Freshwater	WHO’s Permissible Limits	Unit
Cadmium (Cd)	0.0017	0.0032	0.003	ppm
Chromium (Cr)	0.0097	0.0243	0.05	ppm
Lead (Pb)	0.0186	0.1735	0.01	ppm
Arsenic (As)	0.6989	0.8182	0.05	ppm
Copper (Cu)	0.0076	0.1186	0.3	ppm

Discussion

Freshwater Productivity Analysis:

By observing the graphs of variation of hourly freshwater productivity with climatic factors & different temperatures for 11 days, shown in Figure 3(a),(b). to Figure 13(a),(b)., it was found that condensed freshwater can start after being exposed to sunlight for 3 hours. It was obvious that the rate of freshwater productivity depends on the intensity of solar radiation and ambient temperature because the productivity rate exhibits an increase following periods of elevated luminous flux and higher ambient temperature, particularly around noon and in the afternoon. This phenomenon shows the correlation between climatic factors and productivity rate. Based on the overnight production rate, the maximum milliliters of freshwater were collected on Day 7 and 8. The total amount of collected freshwater was 1061 ml from 2 L of seawater.

Water Quality Assessment:

To examine the quality of seawater and obtained freshwater were analyzed as the physical and chemical parameters. Some physicochemical parameters and constituent elements were investigated as the priority parameters for human health protection and environmental conservation. As shown in Table 2 the resulting physical parameters of both samples, seawater and freshwater were compared with class V and class II respectively.

By observing the histogram of Figure 16., it was found the physical characteristics of seawater and freshwater quality were under the respective permissible levels of the standards NSWQS. In particular, a freshwater’s salinity of 0.02 ppt demonstrates its conformity with accepted standards as freshwater typically maintains a salinity below 0.5 parts per thousand (ppt) in dissolved salts.

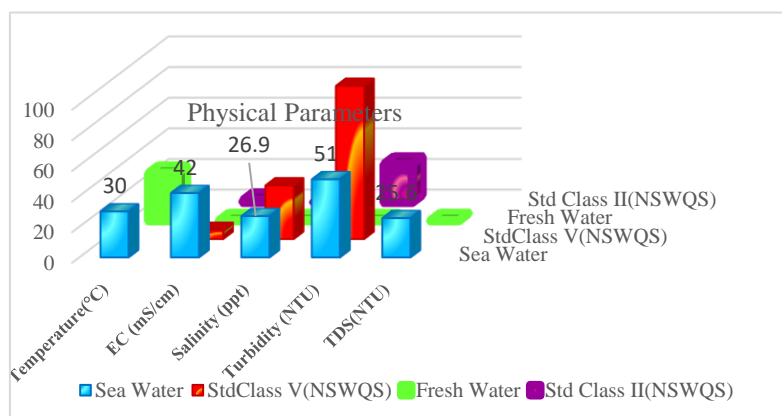


Figure 16. Comparative analysis of physical parameters for seawater and freshwater with corresponding standards.

Chemical parameters

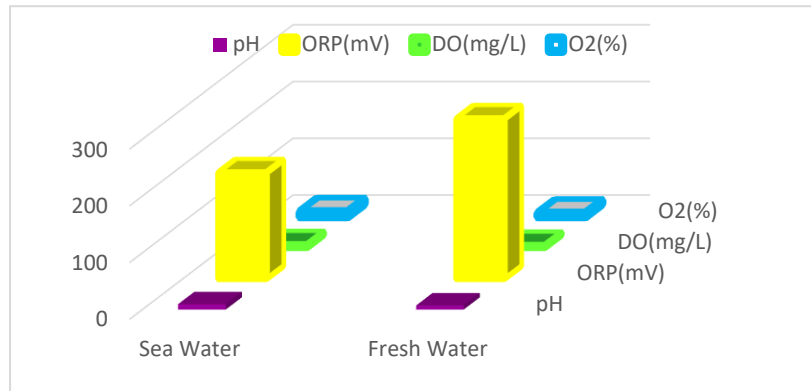


Figure 17. Comparison of chemical parameters for seawater and freshwater

The comparative analysis of chemical parameters of seawater and freshwater such as pH, ORP, DO, and O₂ were shown in the histogram of Figure 17. The key component pH level of freshwater is 7.41 is under the permissible level of class II. Optimal drinking water contains dissolved oxygen (DO) concentrations between 6.5-8 mg/L. In this study, the permissible DO level (>4 mg/L) for both standard Class II and Class V is crucial. The DO content of 5.6 mg/L for seawater and 4.32 mg/L for freshwater falls within the acceptable range, confirming the water’s healthiness. Testing the heavy metal contaminants is essential for assessing water quality for intended use. In this scope, some of the heavy metal content Cd, Cr, Pb, As, and Cu were compared with the WHO’s drinking water quality standards. The concentrations of Cd, Cr, and Cu are within the permissible range except Pb and As.

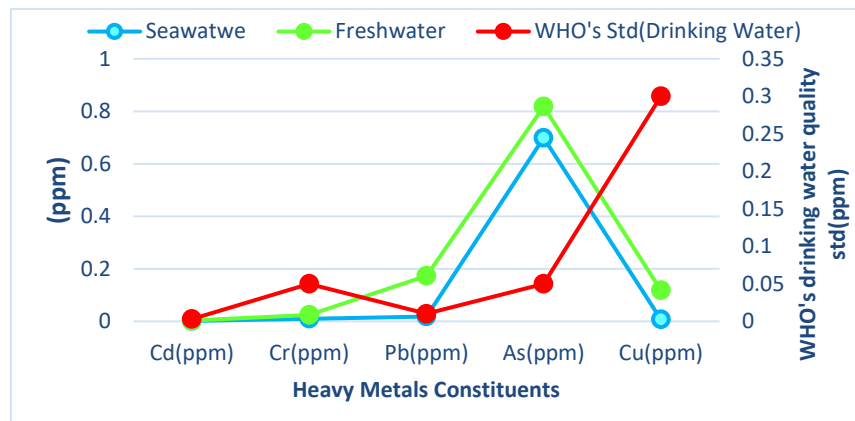


Figure 18. Comparative analysis of heavy metal contents in seawater and freshwater with WHO’s drinking water quality standards.

Conclusion

The noteworthy finding of this research is the successful implementation of home-crafted conventional single-slope passive solar still to generate freshwater from seawater. The research findings of water quality conformed with the WHO’s drinking water quality standards. However, the observed exception of slightly exceeding some of the heavy metal content might be due to the contaminants from the construction of solar still and initial seawater quality. This indicates the need for further research to obtain more reliable water quality data. The optimal combination of cost-effective, eco-friendly solar still and simple technology of desalination contributes directly to the realization of UN’s SDG-6 targets. The integration of desalination and water quality assessment through a single slope passive solar still represents a promising step towards a sustainable water future.

Acknowledgments

I would like to acknowledge Dr Than Than Oo, Rector, and Dr Mi Mi Gyi, Pro-Rector, Dawei University, for their permission and encouragement on this research work. I would like to thank Professor Dr Nyo Nyo, Head of the Department of Physics, for her support and encouragement.

References

- Alnaimat.F., James Klausner, and Bobby Mathew, (2018) Desalination and Water Treatment.
- AI-Mezeini, S.S.S., Mohd Asim Siddiqui, and Mohammad Shariq, (2023) "Design and Experimental Studies on a Single Slope Solar Still for Water Desalination" *Water Journal*, Switzerland, vol.15, pp.704(1-13).
- A. Fadi, K.James and M. Bobby, Desalination and Water Treatment,2018, pp 128-150.Aybar, H.S., (2007) "A Review of Desalination by Solar Still" *Solar Desalination for the 21st Century*, vol.15, pp.207-214.
- Bouzaid.M.,O Ansari, M.Taha-Janan, N.Mouhsin, and Oubrek, (2019) "Numerical Analysis of Thermal Performances for a Novel Cascade Solar Desalination Still Design" *ScienceDirect*, vol.157, pp.1072-1082.
- Diabil, H.A.N., (2022) " Experimental study to enhance the productivity of single-slope single-basin solar still" *Open Engineering*, vol.12, pp. 157-168.
- Dsilva Winfred Rufuss, D. & Iniyani, S. & Suganthi, L. & Davies, P.A., Renewable and Sustainable Energy Reviews, Elsevier, 63(C), 2016, pp. 464-496.
- Diabil, H.A.N., (2022) "Experimental study to enhance the productivity of single-slope single-basin solar still" *Research Article*, *Open Engineering*, vol.12, pp.157-168.
- Dunham, D.C., (1978) *FRESH WATER FROM THE SUN Family-sized Solar Still Technology*. United States Agency for International Development U.S. Department of State Washington.
- Hoque, A., Ashif Hasan Abir, and Kironmay Paul Shourov, (2018) "Solar Still for Saline Water Desalination for Low-income Coastal Areas" *Applied Water Science*, vol.9, pp.104(1-8).
- Khaing,Y.K., Khin Htay Win, and Thidar Khaing, (2019) "Water Quality Assessment and Treatment of Tube Well Water from Selected Areas in Mandalay Region, Myanmar" *International Journal of Scientific and Research Publications*, vol.7, pp.744-749.
- M. Saif, S.Mohnd, Mohammad,A.Talal,A.Inas,A. Abdel-Naser and G. Mohammed, *Desalination. Water* 15,2023, pp. 704
- Magara, Y., (1991) *Classification of water quality standards*. Japan, Hokkaido University, Sapporo Japan.
- Mintz, E.D., F M Reiff, R V Tauxe, (1995) *Safe water treatment and storage in the home*. National Library of Medicine National Center for Biotechnology Information.
- Mulyanef, Duskiardi and Rahmad Hidayat, (2018) "Performance Analysis of Sea Water Solar Still to Produce Fresh Water and Salt Using Flat Plate Collectors" *MATE (Web of Conferences, Indonesia)*, vol.159, pp.02013.
- Nomor, E., Rafiqul Islam, Mohammad A. Alim, and Ataur Rahman, (2021) "Production of Fresh Water by a Solar Still" *Water Journal article*, Switzerland, vol.13, pp.3373(1-16).
- Pesnekar.A.M., Dhiman Chatterjee, and Sadipan Bandyopadhyay, (2018) "Performance evaluation of solar stills" *First International Conference on Mechanical Engineering, Jadavpur University, India*, pp.226(1-4).

ANALYSIS OF THE CONCENTRATION OF Fe IN IRON ORE SAMPLE BY IRRADIATION WITH Am-Be NEUTRON SOURCE

Htoo Nwe Nwe Aung¹, Khin Su Su Han², Kyaw Win³, Myo Zaw Htut⁴, Myo Nyunt⁵

Abstract

The iron concentration in iron ore samples have been observed by means of the instrumental neutron activation analysis technique. In NAA method, the samples were activated by isotope Am-Be (α, n) sealed neutron source. The strength of it is 550 mCi, with an average neutron energy of around 3 MeV, and a half-life of 432 years. After irradiation, the gamma-ray spectra of the samples were collected and analyzed using NaI (Tl) scintillation spectrometer. By NAA method, the iron content of hematite is 65.91%, limonite is 14.24%, and standard iron is 99.12%. NAA method is excellent to detect the mass concentration of iron in the samples. Iron raw materials, especially in small sizes, can be easily detected by NAA to ascertain their authenticity and iron content.

Keywords: Iron (Fe), Gamma radiation, Iron Ore Mine, NaI(Tl) scintillation detector, Activity Concentration, NAA Method.

Introduction

Iron ore was first “discovered” by European settlers when the early land surveyor, Burt, was shown an iron ore by an Indian chieftain near where is now Negaunee, Michigan, in 1844. So far, 22 iron ore occurrences have been observed in Myanmar, excluding numerous other very small occurrences of pyrite. None of these has so far acquired major economic importance. Iron ore consist of 13 limonite-hematite ore occurrences, 3 magnetite ore occurrences, 5 lattice iron ore occurrences, and 1 siderite occurrence. Residual deposits of hematite and limonite in nodules of varying sizes are found in the Southern Shan State and less frequently in the form of lattice iron ores and crusts above basic igneous rocks in the vicinity of basalts in central Myanmar.

Iron, denoted Fe, is unquestionably the world’s cheapest and most useful metal. In its natural state, iron is chemically bonded with oxygen, water, carbon dioxide or sulfur in a variety of minerals. The average iron content of the Earth’s crust is between 5 % and 6%, and the only more abundant and widely distributed elements are silicon, oxygen and aluminum. Iron ore is a commercial term denoting iron-rich minerals with sufficiently high iron content to be commercially available for exploitation. The most important ore-forming minerals are: hematite, Fe₂O₃ (69.94% iron); bloodstone, red iron ore. It occurs in large quantities throughout the world. Goethite, FeO (OH) or FeO (OH)-nH₂O (62.9% iron), limonite, Fe₂O₃.H₂O (at most 62% iron); a collective term for more or less impure goethite and a mixture of hydrated iron oxides, e.g., brown iron ore. Siderite, FeCO₃ (48.2% iron) spatic iron ore, Pyrite, FeS₂ (46.55% iron) the most commonly occurring sulphide mineral in the Earth’s crust. Used in the production of sulfuric acid and gives iron-bearing pyrite residue.¹

Iron ores are rocks and minerals from which metallic iron can be economically extracted. The ores are usually rich in iron oxides and vary in colour from dark grey, bright yellow, deep purple, to rusty red. The iron itself is usually found in the form of magnetite (Fe₃O₄), hematite (Fe₂O₃), goethite, limonite or siderite as shown in Figure (1).

¹ Department of Physics, Defence Services Academy, Pyin Oo Lwin

² Department of Physics, University of Computer Studies, Mandalay

³ Department of Physics, Defence Services Academy, Pyin Oo Lwin

⁴ Department of Nuclear Physics, Defence Services Academy, Pyin Oo Lwin

⁵ Department of Nuclear Physics, Defence Services Academy, Pyin Oo Lwin

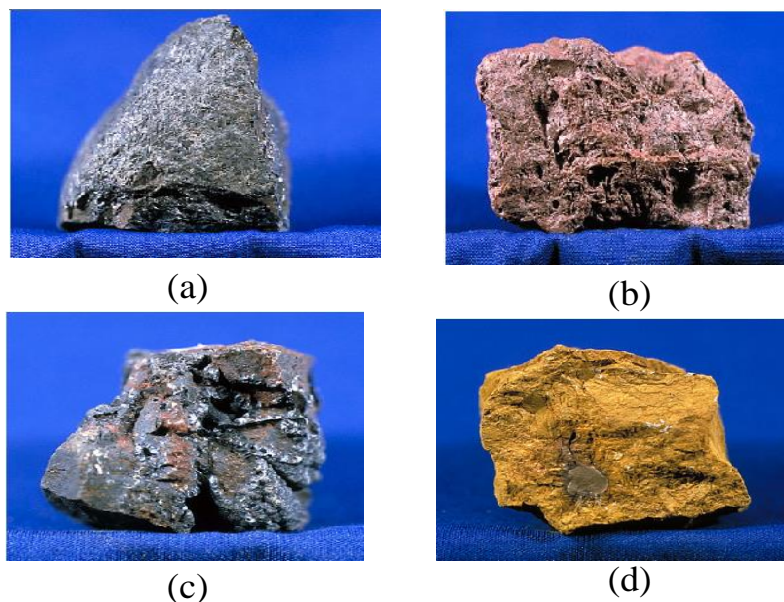


Figure 1. Four Different Types of Iron Ores (a) Magnetite (b) Hematite (c) Goethite (d) Limonite

Experimental Procedure

Sample Collection (Sampling Site) and Preparation

The iron ore mine samples were collected from Pinpet iron ore mine. Pinpet Iron Ore Mine is one of the largest excavated iron ore mines in Myanmar. It is situated in Namsee Village tract, Taunggyi Township in the Southern Shan States. It lies at 97°06'30" longitude and 20°44'30" latitude. It is 4.5 miles from Taunggyi Hopone motor highway and 7.5 miles from Hopone Township.

Each sample was weighed carefully by digital balance. A 55g of iron ore granules from encapsulated in a polyethylene container was used in this work. This container was chosen due to its low background. Then all samples were put in plastic bags very close to the neutron source for one-week irradiation time.

Selection of the best Nuclear Reaction for NAA with Isotopic Am-Be (α, n) Neutron source

Iron exists in nature in the four isotope forms of mass 54, 56, 57 and 58. The most abundant isotope of iron is mass 56, and it is the most useful for the activation analysis with 14 MeV and 3 MeV neutrons. The best nuclear reaction for the identification of the isotope of interest should be chosen. Sometimes there is more than one reaction available for the same isotope. The possible induced nuclear reactions in iron ^{56}Fe together with the reaction characteristics are shown in Table (1).

Table 1. Neutron Activation Reactions with Fe

Reaction	Gamma-Energy (keV)	Half-life (h)	Gamma Emission Probability (%)	Threshold Energy (MeV)	Q-Value (MeV)
$^{54}\text{Fe} (n, 2n) ^{53}\text{Fe}$	377.88	0.142	42	13.878	-13.618
$^{54}\text{Fe} (n, p) ^{54}\text{Mn}$	834.85	7495.2	99.96	-	+0.49
$^{56}\text{Fe} (n, p) ^{56}\text{Mn}$	846.77	2.576	98.9	2.452	-2.408
	2113.12		14.3		
$^{57}\text{Fe} (n, p) ^{57}\text{Mn}$	14.413	0.024	10.56	1.434	-1.409
	122.06		13.9		
$^{58}\text{Fe} (n, \gamma) ^{59}\text{Fe}$	692.03	1068.07	56.5	-	+6.589
	1291.59		43.2		

$^{56}\text{Fe} (n,p) ^{56}\text{Mn}$ is the best reaction because it has suitable energy and half-life. Moreover, the absorption reaction cross-section and target isotope abundance of the $^{56}\text{Fe} (n,p) ^{56}\text{Mn}$ are relatively high Gamma emission probability (98.9%) from first peak energy (846.77keV) of this reaction is very high. It is also the endothermic reaction (Q-Value is negative) and threshold energy is lower than other reactions. Therefore, $^{56}\text{Fe} (n,p) ^{56}\text{Mn}$ reaction is selected from five reactions. The decay scheme is shown in Figure (2). The best choice is this nuclear reaction for iron sample. (^{56}Fe about 98.9%) This reaction is confirmed by calculating the half-life of this reaction.

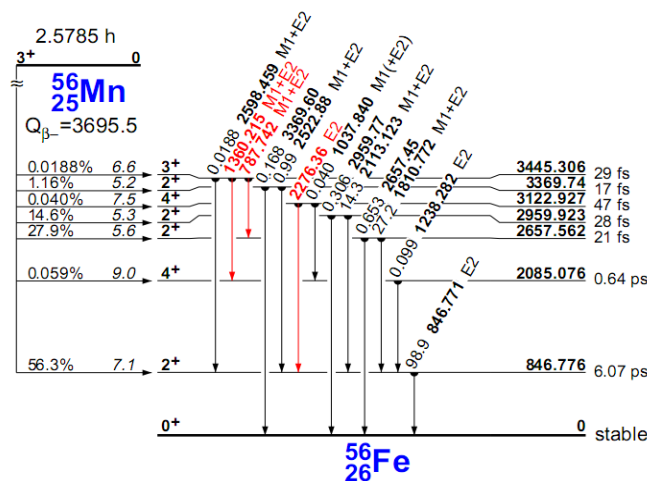


Figure 2. Decay Scheme of ^{56}Mn Radionuclide

Gamma Activity Measurement of Irradiated Samples

Americium also alloys with Beryllium to form Am-Be which produces neutrons via the ${}^9\text{Be} (\alpha, n){}^{12}\text{C}$ reaction was used. ${}^{241}\text{Am}$ has a half-life of about 432 years. Although this isotopic decays by emitting alpha particles of about 5.4 MeV, these particles are following by gamma rays in the 40 to 60 keV region in the majority of the disintegrations. This gamma-ray emission make Americium appear less satisfactory than Plutonium for the preparation of neutron sources. For the Am-Be source in Physics lab, University of Mandalay, total neutron capture from the neutron source $N=1.04\times 10^6$ neutrons/cm²s. Figure (3) shows ${}^{241}\text{Am-Be}$ neutron source for irradiation facility with 550mCi.

The sample material is irradiated by emitted neutrons from a neutron source. In this process, isotopes are converted into radioactive isotopes. These isotopes decay, with half-life varying from seconds to years, which emit γ -radiation of specific energy. This γ -radiation is measured with NaI(Tl) scintillation detector.



Figure 3. Am-Be Neutron Source for Irradiation Facility with 550 mCi

Experimental Set-up for Gamma Emission Measurement

After irradiation, the gamma ray spectra of the radioactive iron ore samples were measured and analyzed by NaI(Tl) scintillation detector and Gamma Vision software. The amplifier gain was adjusted until peaks were obtained at the desired channel numbers. The gamma-ray spectra of four standard sources ${}^{241}\text{Am}$ (60 keV), ${}^{137}\text{Cs}$ (662 keV), ${}^{54}\text{Mn}$ (835 keV) and ${}^{60}\text{Co}$ (1173 keV, 1332 keV) were measured for 600 sec by using NaI(Tl) scintillation detector for the energy calibration. By plotting the counting efficiencies at various energies for source-detector suitable distance, efficiency calibration curve was obtained. The experimental set-up is shown in Figure (4).



Figure 4. Experimental Set-up for Gamma Radiation Measurement

First, the background was measured for about one hour. Then the plastic bag filled with ore samples was put on the NaI(Tl) scintillation detector. The ore samples were measured for about one hour. At the end of the counting period, the spectrum that was recorded may be stored in MCA. The spectra stored in MCA were analyzed by the application of Gamma-Vision 32 software. Using the energy information, an unknown and known radioisotope can be identified radionuclides with activity concentrations and a picture of the spectrum and then determination of the gross area and net area of full energy peak are shown.

The activity (A) of the isotopes also depends on irradiation time. The intensity of the measured gamma line is proportional to the activity.

The equation of the activity after irradiation of the sample is

$$A = \phi \sigma f m \frac{N_A}{M} (1 - e^{-\lambda t_i}) e^{-\lambda t_d} \quad (1)$$

where, A = activity (cps)

ϕ = neutron flux (n/cm²s)

Σ = neutron capture cross section (cm⁻²)

m = the mass of irradiated element (g)

f = isotope abundance (%)

N_A = Avogadro number (6.02 × 10²³ atoms/g.mole)

M = atomic mass of target element

t_i = irradiation time (s)

t_d = decay time (s)

Therefore, the same parameters for the samples are cancelled out each other, the comparative NAA method is obtained as followed;

$$\frac{A_{\text{sam}}}{A_{\text{std}}} = \frac{m_{\text{sam}} (e^{-\lambda t_d})_{\text{sam}}}{m_{\text{std}} (e^{-\lambda t_d})_{\text{std}}} \quad (2)$$

where, A_{sam} = activity of the sample

A_{std} = activity of the standard

m_{sam} = concentration of sample

m_{std} = concentration of standard

t_d = decay time = cooling time + counting time

λ = decay constant = $0.693/T_{1/2}$

Results And Discussion

The experimental work took place at the Nuclear Research Laboratory, Department of Physics, Mandalay University. In the Neutron Activation Analysis (NAA) experiment, one pure iron standard and seven iron samples underwent irradiation using an Am-Be (α, n) isotopic neutron source. Subsequently, the induced gamma rays were detected by a NaI(Tl) (3"x3") scintillation detector and analyzed using MCA, Gamma Vision 32 Software, and Excel Software. The neutron flux from the Am-Be (α, n) isotopic neutron source ($\sim 3\text{MeV}$), calculated using copper foil, was determined to be $1.658 \times 10^6 \text{ n/cm}^2\text{s}$.

Hematite and limonite served as standards in this research, with other samples compared against them. Parameters such as ROI, FWHM, Peak Channel, Gross Area, and Net Area were derived from measured peak data. The iron concentration of the samples was calculated using the relative NAA method. Irradiation time, counting time, and the results are presented in Table (2) and Table (3). Measurement results for all samples through the NAA method are detailed in Table (4). A comparison of iron contents via NAA methods is outlined in Table (4) and Figure (5). Figure (6) displays a comparison with background and an iron standard sample spectrum, while Figure (7) showcases a comparison of gamma spectra with background and hematite in the Pinpet iron ore sample. Finally, Figure (8) illustrates a comparison of gamma spectra with background and limonite in the Pinpet iron ore sample spectrum.

Table 2. Irradiation and Counting Conditions of Research Samples

Sample	Mass (g)	Irradiation Time (h)	Counting Time (s)	Cooling Time (s)	Decay Time (s)
Standard	55	168	3600	60	3660
Hematite	55	168	3600	60	3660
Limonite	55	168	3600	60	3660

Table 3. Peak Data and Counting Results of Research Samples

Sample	ROI	FWHM	Gross Area	Net Area	Error (%)
Standard	770-882	47.57	21738	14179	± 383
	773-885	48.18	22440	14716	± 403
	776-885	47.48	21674	14144	± 381
Hematite	769-873	45.11	16452	9090	± 336
	773-881	45.39	16426	9910	± 347
	776-884	45.30	16408	9622	± 353
Limonite	773-865	23.33	7171	1973	± 276
	778-870	23.40	7201	2202	± 271
	780-872	31.02	7208	2010	± 276

Table 4. The Measurement Results of Fe Concentration in Research Samples by NAA Method

Name of Sample	Mass (g)	NAA Result of Fe concentration (%)
Standard	55	99.12
Hematite	55	65.91
Limonite	55	14.24

Comparison of Iron Concentration in Research Samples

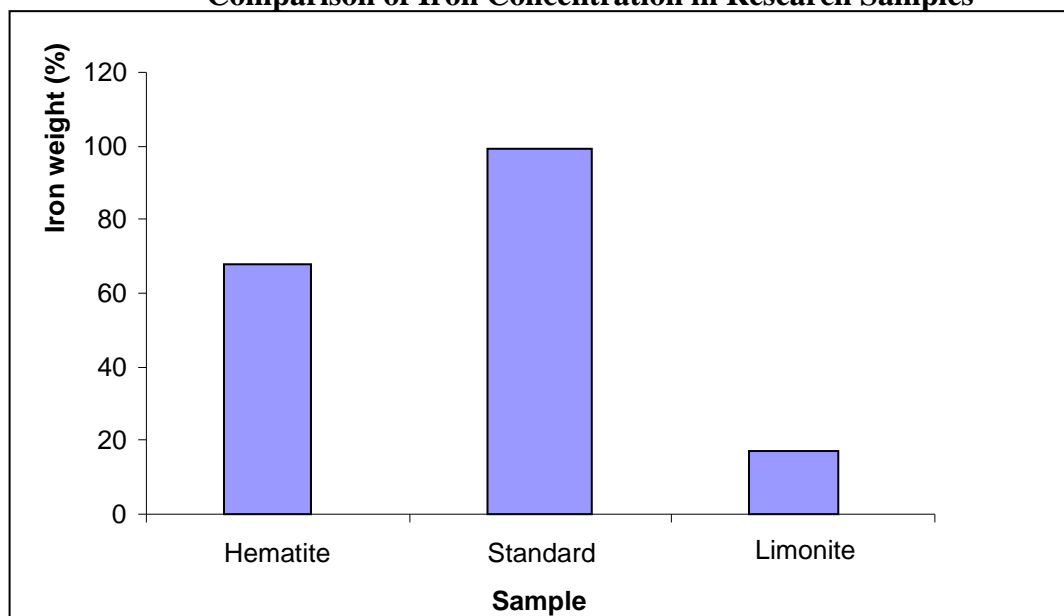


Figure 5. Result of Fe Concentration by NAA Method in Research Samples

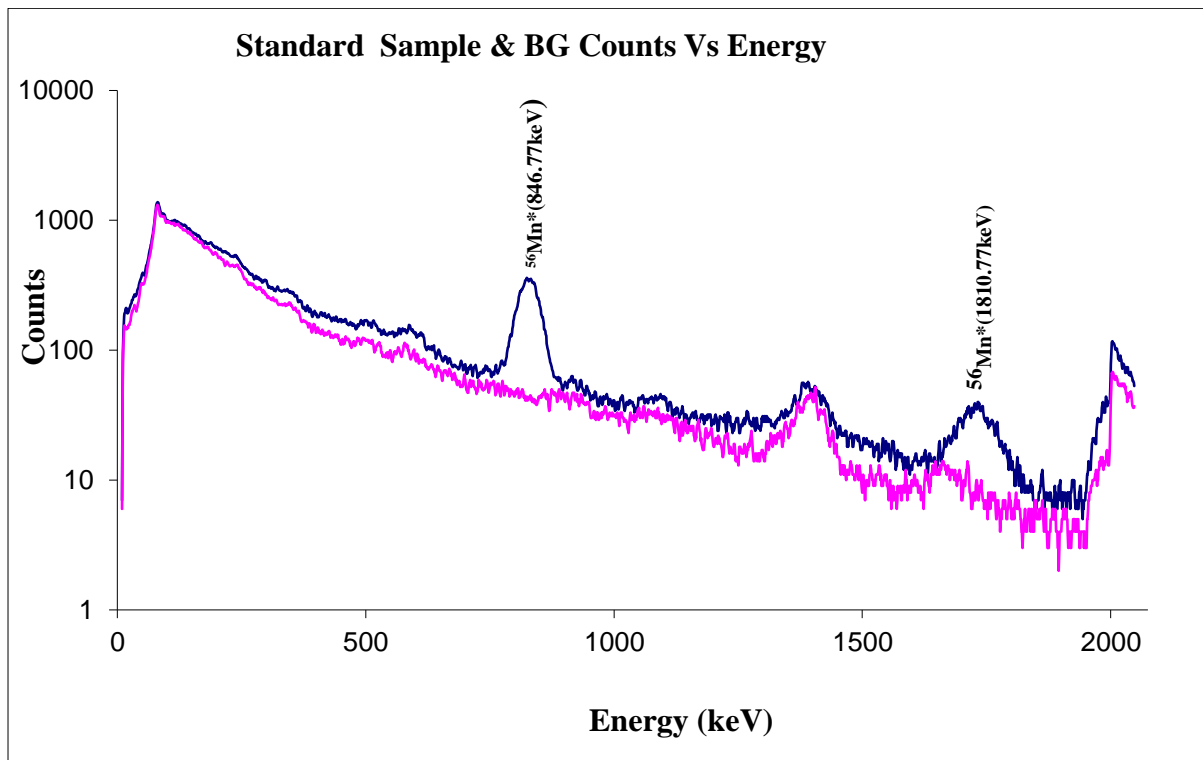


Figure 6. Comparison of Gamma Spectra with Background and Standard Sample Spectrum

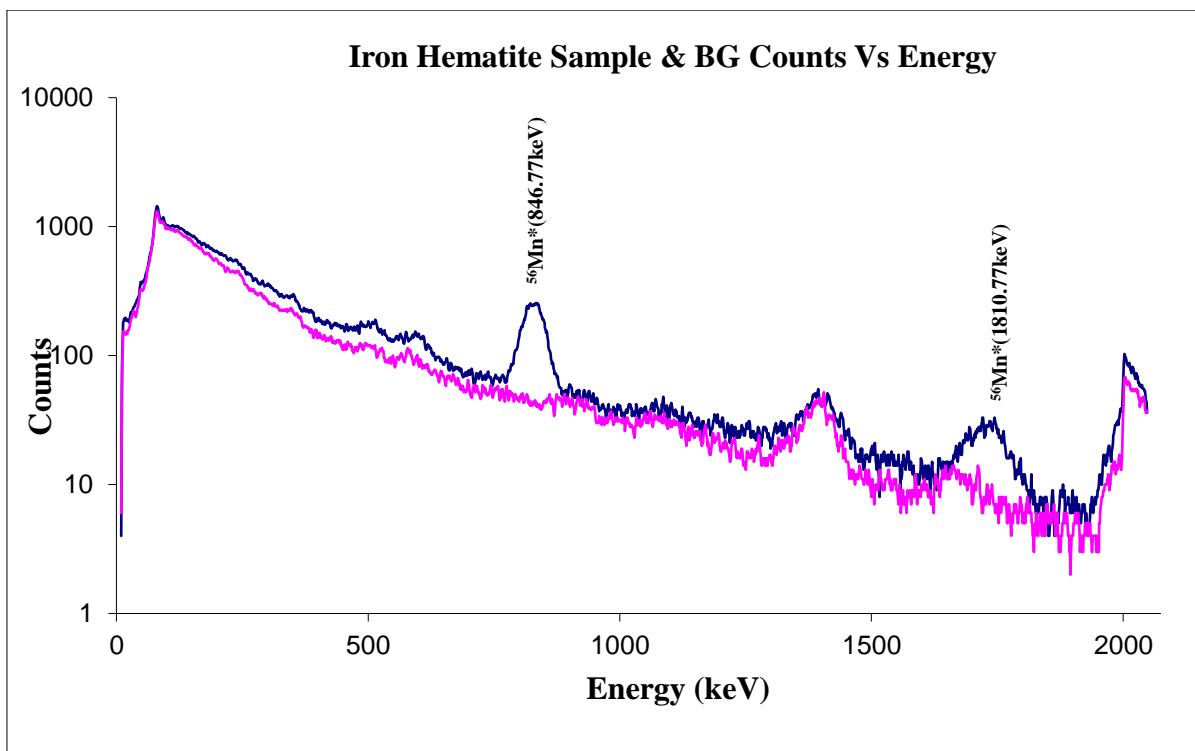


Figure 7. Comparison of Gamma Spectra with Background and Hematite in Pinpet Iron Ore Sample Spectrum

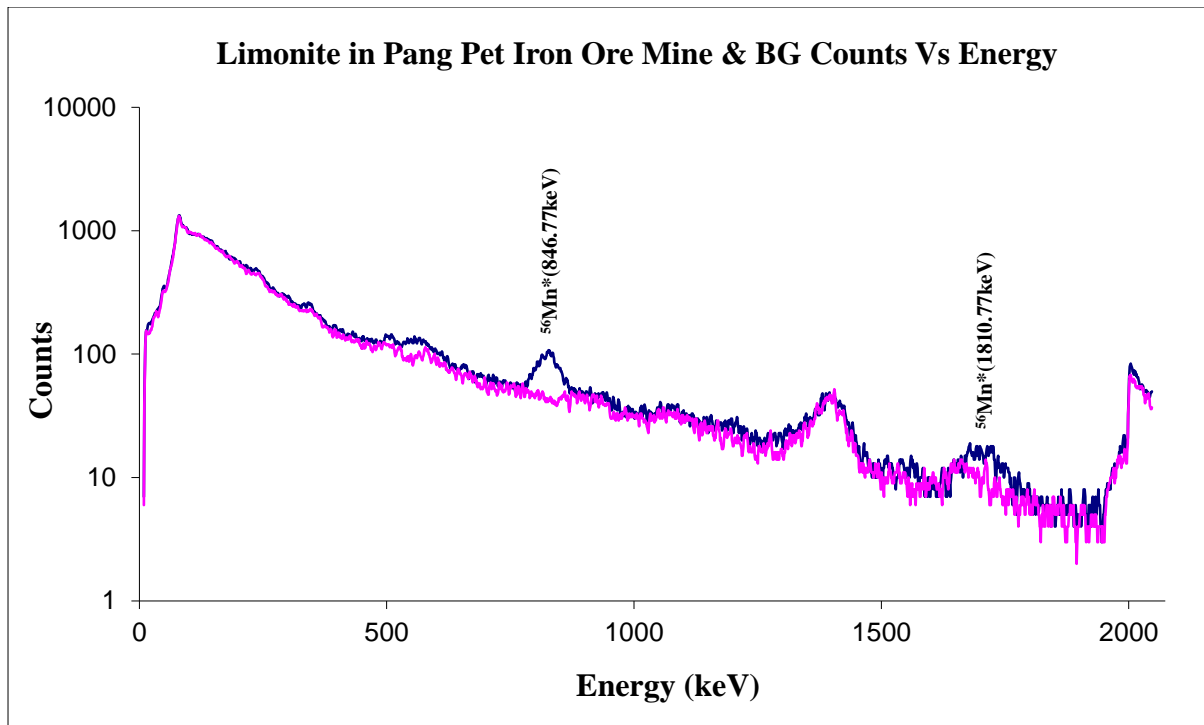


Figure 8. Comparison of Gamma Spectra with Background and Limonite in Pinpet Iron Ore Sample Spectrum

Conclusion

By NAA method, the iron content of hematite is 65.91%, limonite is 14.24%, and standard iron is 99.12%. Thus, the iron weight percent was calculated three times to get a better statistic. By using the analyzed data, the pure iron percent of each sample was evaluated by relative NAA method. NAA method is excellent to detect the mass concentration of iron in the samples. The iron raw materials, especially for small sizes can easily be detected by NAA whether they are real or not and the iron contents. Because of non-destructive testing (NDT) and providing results rapidly, NAA has great advantages over other elemental analysis methods. The study delves into the analysis of iron ore concentration using neutron activation facilitated by an Am-Be neutron source. By leveraging the unique properties of neutron interactions, this method offers a powerful means of quantifying iron content in a non-destructive manner. The results not only aid in understanding the composition of the iron ore sample but also highlight the broader significance of neutron activation analysis in scientific and industrial applications.

Acknowledgements

I would like to extend their appreciation to Dr. Kaythi Tin, Rector of the University of Taunggyi, for granting permission to conduct this research. They also express great gratitude to Lt. Col. Naing Win, Associate Professor in the Department of Physics at the Defence Services Academy in Pyin Oo Lwin, for his invaluable support, insightful guidance, and encouragement throughout the compilation of this paper

References

- A.M. Hassan and J. Madani, "Neutron Activation Analysis of Saudi Hematite and Phosphate Samples Using the ^{241}Am -Be Neutron Irradiation Facility," Al-Azhar University, Egypt (1994).
- "Gamma Spectroscopy," http://en.wikipedia.org/wiki/Gamma_Spectroscopy.html (2007).
- "Mineral Information Institute of Iron Ore," <http://www.mii.org/minerals/photoiron.html>, 4 December (2008)
- Z. Molnar, "Neutron Activation Analysis," <http://www.reak.bme.hu/Education/Wigner-course/Wigner-Manuals/Budapest/NEUTRON-ACTIVATION-ANALYSIS.htm>(2002).

A STUDY ON THE BENEFITS OF LIVING THINGS DUE TO PHYSICAL CHANGE IN MYANMAR TEA LEAVES

Wint Shwe War Hlaing¹

Abstract

In many parts of the world, tea leaves are used for the health of the human and the growth of plants. The purpose of this paper is to study the concentration of elements that will come from the physical change of tea leaves and its effect on living things. In this study, the tea leaf samples were collected from the Shan state. The content concentration value of tea leaves in three stages of physical change is measured by EDXRF spectroscopy. It can be seen that the major nutrients for humans and plants are potassium and calcium. According to the measured values and calculated results, using a 250 ml cup, humans can drink 3-5 cups of green tea or 2-3 cups of black tea. It helps to reduce type II diabetes, cancer, and heart disease, and to improve the immune system. Not that much, the plants will survive in two weeks due to the supply of waste sludge of tea leaves and will grow for four weeks.

Keywords: Green tea leaves, Black tea leaves, Energy-dispersive X-Ray Spectroscopy (EDXRF).

Introduction

Southeast Asia was the first region to cultivate the green tea plant (*Camellia Sinensis*) that it is currently cultivated worldwide. *Camellia Sinensis* is a plant species that is flowering in the area. It is also a species of evergreen shrub [Rolfe J, et al., 2003].

Namh San in northern Shan State, where the Palaung people reside in Myanmar, is the primary tea-producing region. Tea plays an important role as the traditional Myanmar culture of the Myanmar people. The leaves and buds of the tea plant are used to make tea. Tea is the beverage that is most popular in Myanmar and worldwide. It has a pleasant aroma and flavor and has the potential to have a positive effect on mood. Tea is available in white, yellow, green, oolong, dark, and black varieties. Each tea contains aroma, taste, color, and appearance [Karak T, et al., 2010].

Tea has different qualities. Its different qualities distinguish the categories of tea that are the different manners and degrees of oxidation of leaves, stopping the oxidation, forming the tea, and drying time of leaves are involved in producing tea.

The various kinds of tea depend mainly on the age of the leaves at the time of harvest. Also, the quality of the tea varies depending on the element content. Moreover, the elemental composition of the tea also depends on the geographical location and genetic differences, soil composition, the degree of contamination, and climatic conditions [Cambridge M.L., et al., 1900].

The caffeine content in tea has a stimulating effect on humans. Tea is the beverage that is consumed the most globally. In Myanmar, the term for tea is Yay-Nway-Gyan. The main theme of this research is to study the elements contained in the physically changing tea leaves using EDXRF and to know how much tea the human body needs to drink per day. In addition, the effects of waste on plant survival were also studied.

¹ Department of Physics, Yangon University of Education

Experimental Procedure

Sample Preparation

In this research, the physical change of dried tea leaves was studied. Therefore, there are three kinds of samples such as dried tea leaves, tea leaves with boiling water (yay-nway-gyan) and waste sludge of tea leaves. The contained elements of these samples were measured by using EDXRF.



Figure 1 Energy Dispersive X-rays Fluorescence (EDXRF) spectrometer (EDX-7000)

Preparation for stage I (Two Samples I)

To improve the quality of tea, the tea must be picked within 10 a.m. The picked tea buds in a pan were steamed at a temperature (70 degrees Celsius) for about 2-3 minutes. Then, the tea buds were kneaded by hand until they were rolled. After that, the half of the tea buds are dried in the shade for one hour. The tea buds in the shade will become dried green tea leaves. Some residual tea bud leaves spread on the table for a few hours. When the leaves are coppery in color, the leaves are added to a pan and are roasted at temperature (between 80 degrees Celsius and 100 degrees Celsius) for about 2 to 3 minutes. After roasting, it will become black tea leaves. Each sample I was grinded to make the pellet. And then, the contained elements in the two different kinds of samples I were measured by EDXRF spectrometer.

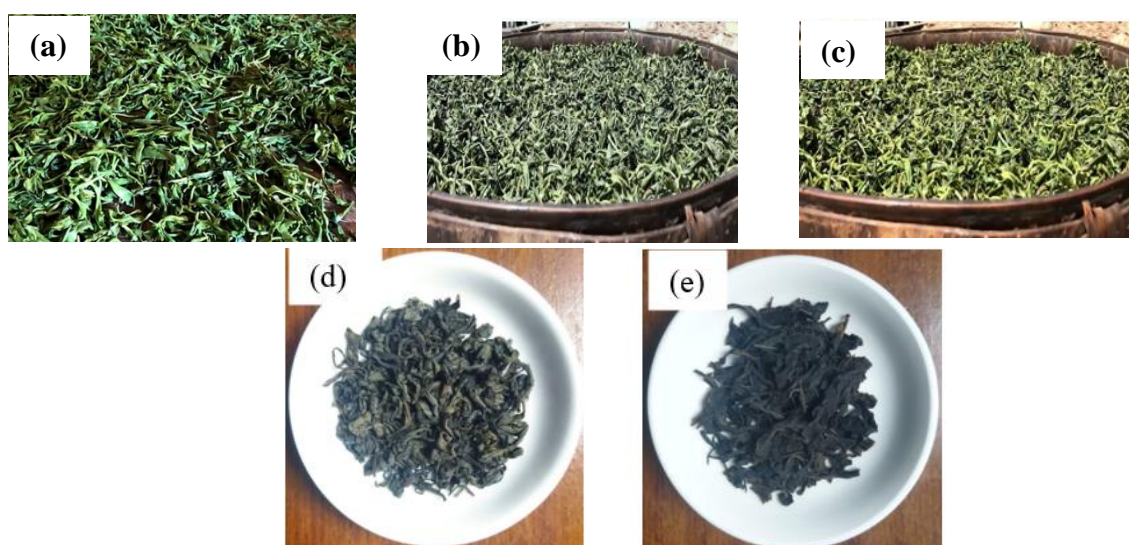


Figure 2 (a) Tea buds and leaves picked from the tea plant (b) Tea buds in the shade (c) After roasting the tea buds at a temperature (between 80°C and 100°C) (d) Green tea leaves (e) Black tea leaves

Preparation for stage II (Two Samples II)

One cup is added to a few teaspoons of dried green tea leaves and another cup is added to a few teaspoons of dried black tea leaves. Subsequently, the two cups were filled with boiling water and covered with a lid for 10 minutes. The resulting raw material is Yay-Nway-Gyan. These samples were poured into two cups of the sample chamber in the EDXRF spectrometer. Then the two cells were shielded with mylar film. After that, the content of elements in the two samples II was measured with the EDXRF spectrometer.

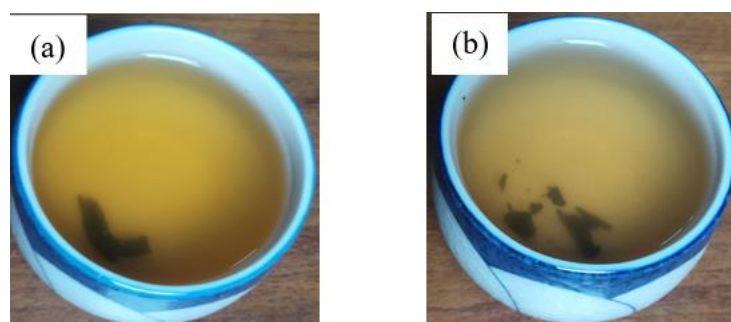


Figure 3 (a) Green tea Yay-Nway-Gyan (b) Black tea Yay-Nway-Gyan

Preparation for stage III (Two Samples III)

The waste sludge of tea leaves (waste of tea leaves) from yay-nway-gyan was collected. It was dried. After that, each sample III was grinded to make the pellet. Then, the content of elements in its tea leaves were measured with the EDXRF spectrometer.

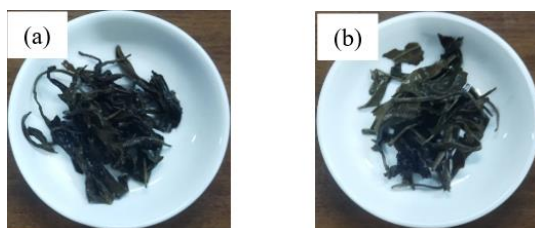


Figure 4 Waste sludge of (a) green tea leaves, and (b) black tea leaves

Results and Discussion

Results

The elemental concentration of the two kinds of tea leaves in physical change is shown in Table 1, and Table 2 shows the calculated values of the elements in a (250 ml) cup of yay-nway-gyan depending on the measured values.

Table 1 Measurement data of the elemental concentration (w%) for the two kinds of tea leaves in the physical change

Samples	Concentration (w%)								
	Potassium (K)	Calcium (Ca)	Phosphorus (P)	Sulfur (S)	Manganese (Mn)	Iron (Fe)	Copper (Cu)	Zinc (Zn)	Silicon (Si)
Sample I (green tea leaves)	0.740	0.131	0.108	0.079	0.018	0.006	0.002	0.001	n.d
Sample I (black tea leaves)	0.289	0.049	0.049	0.043	0.019	0.005	0.002	0.002	0.160
Sample II (green tea)	0.025	0.011	n.d	n.d	0.001	0.002	0.001	n.d	n.d
Sample II (black tea)	0.011	0.006	n.d	0.013	n.d	0.002	0.002	n.d	0.160
Sample III (waste sludge of green tea leaves)	0.020	0.006	n.d	n.d	0.001	0.001	0.002	n.d	n.d
Sample III (waste sludge of black tea leaves)	0.008	0.003	n.d	n.d	0.001	0.001	0.002	n.d	0.160

n.d = not detected

Table 2 The calculated values of the elements included in the tea (yay-nway-gyan)

Elements	Green tea (per cup) (mg)	Black tea (per cup) (mg)	Green tea (2 cups) (mg)	Black tea (2 cups) (mg)	Green tea (3 cups) (mg)	Black tea (3 cups) (mg)	Green tea (4 cups) (mg)	Black tea (4 cups) (mg)	Green tea (5 cups) (mg)	Black tea (5 cups) (mg)
K	0.0100	0.0213	0.0200	0.0426	0.0300	0.0639	0.0400	0.0852	0.0500	0.1065
Ca	0.0044	0.0116	0.0088	0.0232	0.0132	0.0348	0.0176	0.0464	0.022	0.058
S	-	0.0254	-	0.0508	-	0.0762	-	0.1016	-	0.127
Mn	0.0004	-	0.0008	-	0.0012	-	0.0016	-	0.0020	-
Fe	0.0008	0.0039	0.0016	0.0078	0.0024	0.0117	0.0032	0.0156	0.0040	0.0195
Cu	0.0004	0.0039	0.0008	0.0078	0.0012	0.0117	0.0016	0.0156	0.0020	0.0195
Si	-	0.3120	-	0.6240	-	0.9360	-	1.2480	-	1.5600

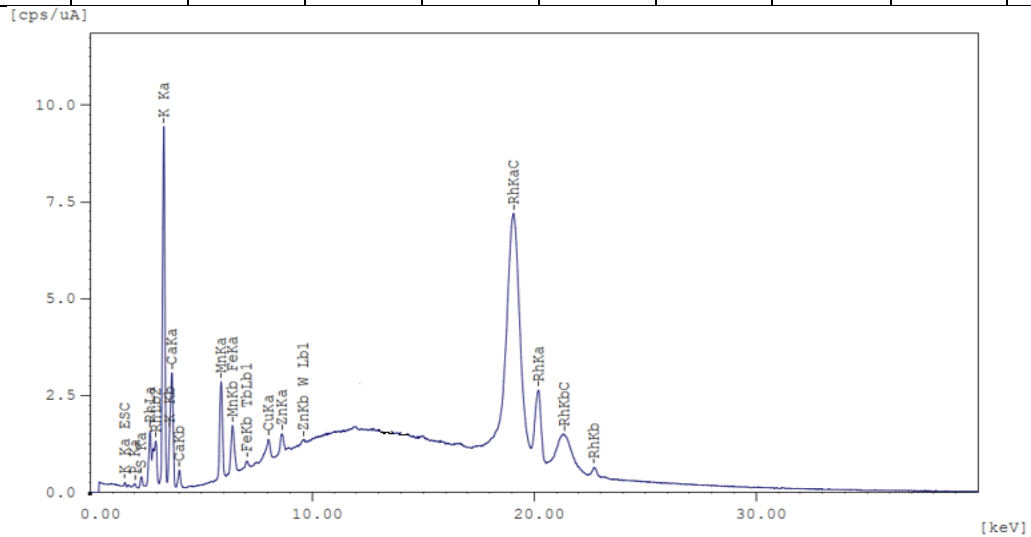


Figure 5 Measurement spectrum for sample I (Green tea leaves)

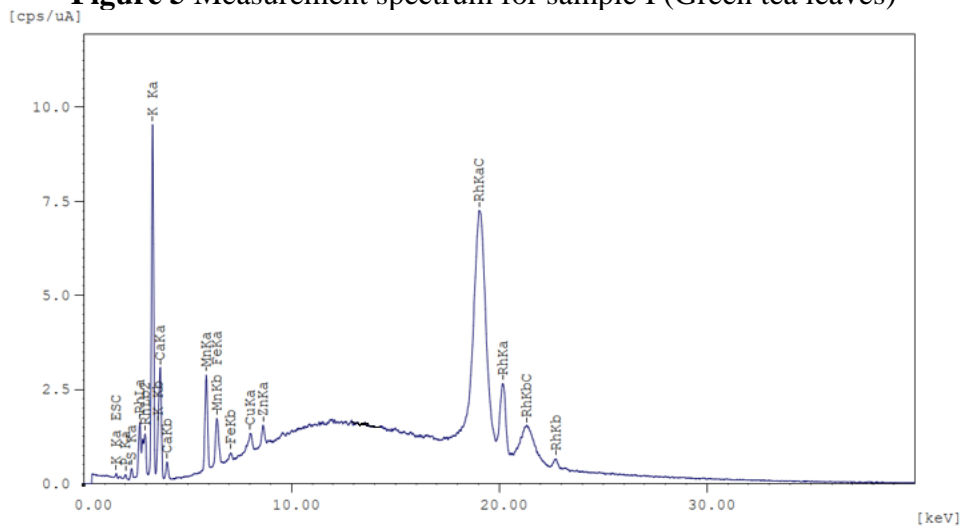


Figure 6 Measurement spectrum for sample I (Black tea leaves)

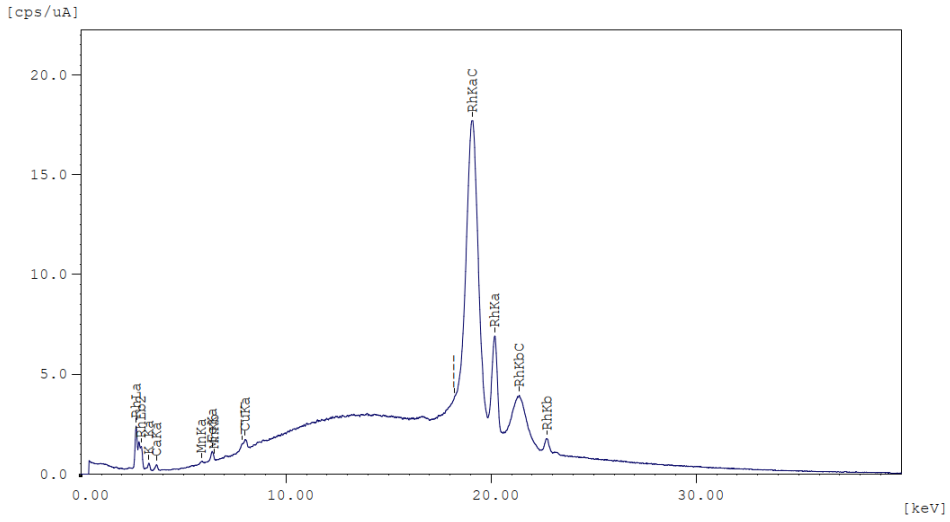


Figure 7 Measurement spectrum for sample II (Green tea yay-nway-gyan)

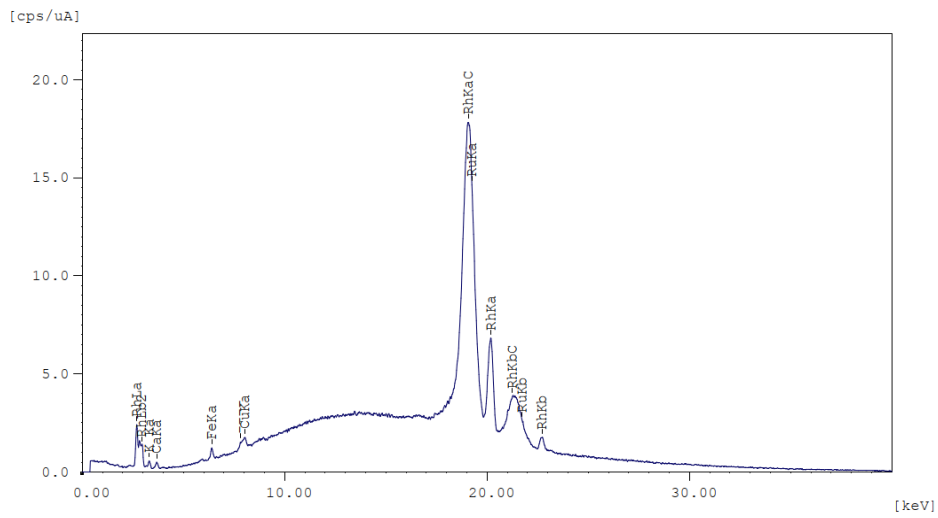


Figure 8 Measurement spectrum for sample II (Black tea yay-nway-gyan)

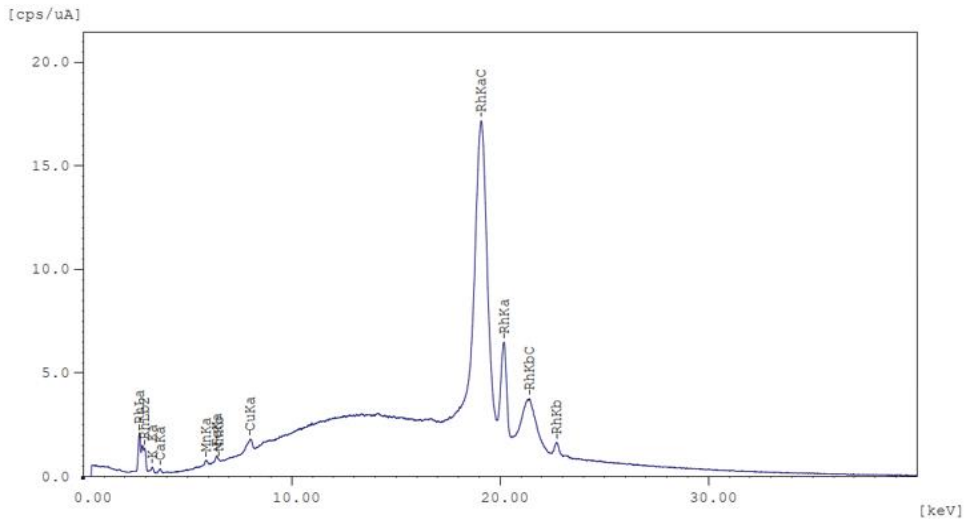


Figure 9 Measurement spectrum for sample III (Waste sludge of green tea leaves)

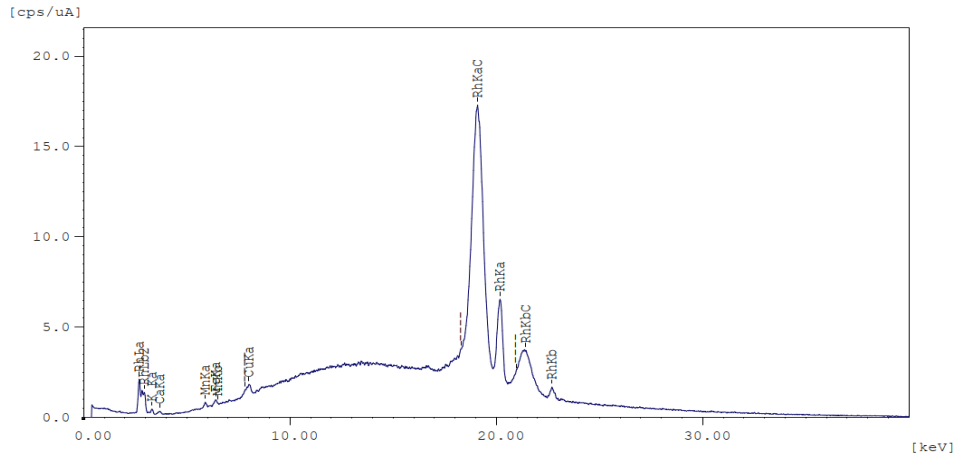


Figure 10 Measurement spectrum for sample III (Waste sludge of black tea leaves)

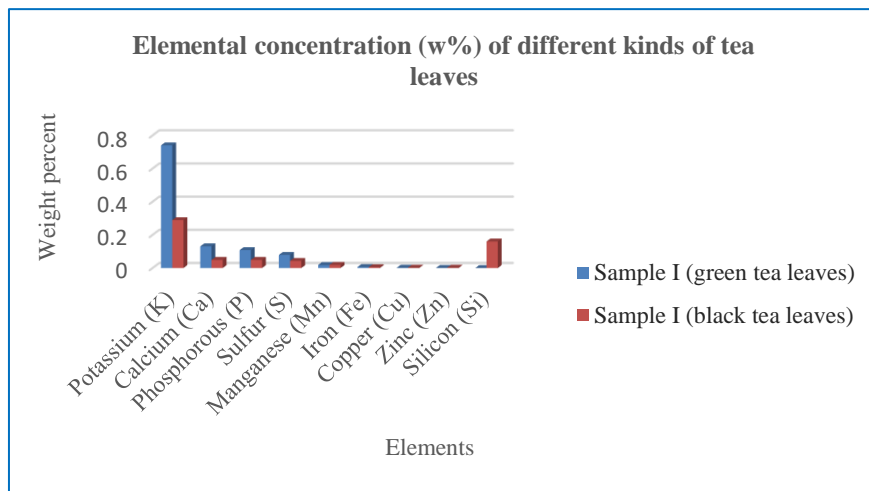


Figure 11 Elemental concentration (w%) of the two kinds of tea leaves

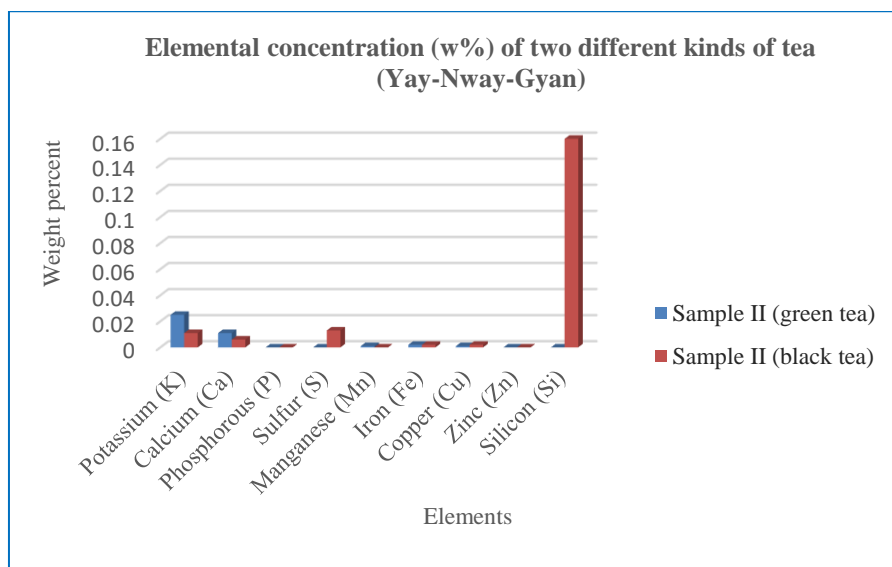


Figure 12 Elemental concentration (w%) of the two kinds of tea (Yay-Nway-Gyan)

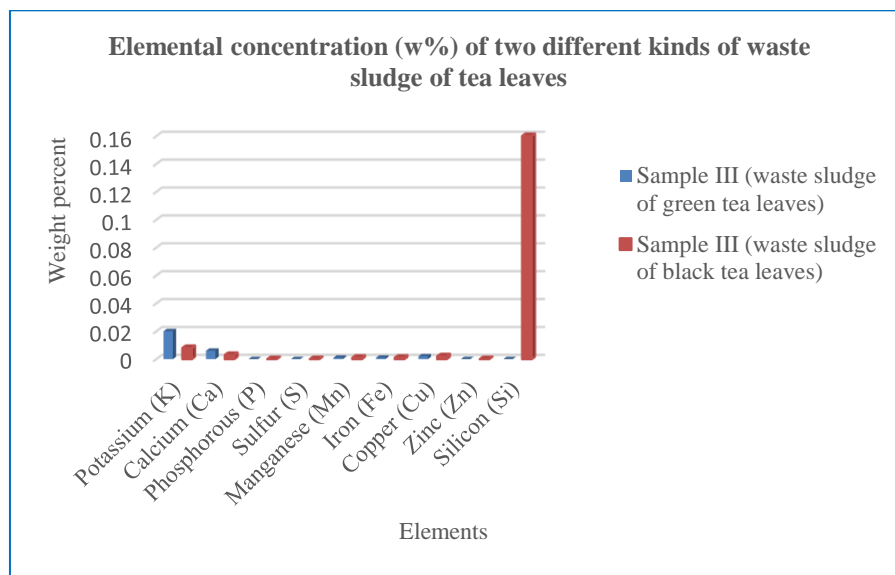


Figure 13 Elemental concentration (w%) of the two kinds of waste sludge of tea leaves

For the EDXRF spectrum of sample I (green tea leaves), the qualitative results that K, Ca, P, S, Mn, Fe, Cu, and Zn were contained as shown in Figure 5. Figure 6 shows that the spectrum of black tea leaves contain K, Ca, P, S, Mn, Fe, Cu, Zn, and Si.

From Figures 7 and 8, it can be seen that green yay-nway-gyan contains K, Ca, Mn, Fe, and Cu, while black yay-nway-gyan contains K, Ca, S, Fe, Cu, and Si.

Figure 9 shows that K, Ca, Mn, Fe, and Cu were observed in the qualitative results provided by the EDXRF spectrum for the waste sludge of green tea leaves. The qualitative results such as K, Ca, Mn, Fe, Cu, and Si can be found in the waste sludge of black tea leaves EDXRF spectrum in Figure 10.

Figure 11 – Figure 13 show the respective graph of the elemental concentration of the two kinds of tea leaves in the physical change.

Discussion

Potassium (K), and calcium (Ca) of the essential macro-minerals elements and phosphorus (P), sulfur (S), manganese (Mn), iron (Fe), copper (Cu), Zinc (Zn), and silicon (Si) of the trace elements were found in these physical changes. Potassium can be seen as the most abundant element in all three stages of physical change, and the second most abundant element is calcium.

About 80 percent of the total potassium in the body was present in muscle cells, and the remaining 20 percent in bone, the liver, and red blood cells was contained. Potassium is easily soluble in water and reacts quickly and then it can help in many metabolic processes and also helps regulate the nervous system and heart rate in humans. In addition, it reduces the occurrence of diseases such as type II diabetes, cancer, and heart disease. The potassium element for the plant is indispensable to plant growth and plays a role in photosynthesis, water regulation,

enzyme activation, and stomata function. Potassium deficiency can stunt plant growth, reduce yield and quality. Calcium element is also stored in bone and capillaries. Calcium can help the communication of nerve systems between cells, and hormone release and can also protect blood clots, and muscle contraction. And also, Calcium is a vital nutrient for plant growth and development that has an impact on cell wall formation, membrane function, enzyme activity, hormone signaling, and the resistance of the disease.

Phosphorus is a crucial element for all living things. The creation of DNA (**deoxyribonucleic acid**), cell membranes, and bone and teeth in humans requires it. Similarly, food production cannot proceed without phosphorus as it is one of the three nutrients (nitrogen, potassium, and phosphorus) used in fertilizer for plants. The average person takes in around 900 mg of sulfur per day is used, that it can get protein. But, if a lot of sulfur is used, it can cause serious vascular damage in the veins of the brain, the heart, and the kidneys, and also can cause fetal damage and congenital effects. Similarly, plants require sulfur as an essential nutrient to form important enzymes and plant proteins. But it is needed in very low amount for the plant.

Manganese also provides the metabolism of cholesterol and carbohydrates for humans. It is also an essential element for the plants. It can used in the Photosynthesis process, enzyme activity, cell division, and elongation. Iron is a vital component of almost all living things, from micro-organisms to humans. All three stages of the samples contain iron. It contributes to the human hemoglobin, which is the red coloring agent of the blood that transports oxygen through the human body. Plants also need iron in small amounts as it is a micronutrient. It is involved in the manufacturing process of chlorophyll and is required for certain enzyme functions.

Copper content supports nutrients for humans and plants. But copper is dangerous if it exceeds the limit value. Zinc helps the human body's immune system. Zinc supports a plant micronutrient. Also, it supports the components of proteins and acts as a functional, structural, or regulatory cofactor of a large number of enzymes. Silicon is found mainly in connective tissues and skin. It is required for bone and connective tissue health for humans. Silicon is essential for plant growth. It supports improving plants' mineral uptake.

In this study, it will be found that the two main mineral elements for humans, such as potassium, and calcium, are needed to protect against disease, and these elements for plants can support plant survival and plant nutrition. And, the trace elements for humans can also support metabolism and for plant growth can also support plant survival and plant nutrition.

According to Table 2, green tea yay-nway-gyan does not contain elements Si and S that are harmful to humans. Mn is contained in this tea, but its content is only the amount needed for metabolism. Black tea contains elements Si and S that are harmful to humans. But, the amount of these two elements was found to be low. However, excessive exposure to certain trace elements can pose a danger to both the human body and the plant.

Conclusion

It concluded that green tea leaves are often considered better for health than black tea leaves. Especially, black tea leaves, if it is aged or stored for a long time, may undergo further

chemical changes that can affect the potassium content. Based on the measurement results of the elements in the yay-nway-gyan, the calculated values are 3-5 cups of green tea per day and 2-3 cups of black tea per day. By taking yay-nway-gyan, it makes cells that do not respond to insulin work properly again and by doing so, the blood sugar level decreases. Not that much, the waste sludge of tea leaves is fed to a testing plant with less nutrients, its plant will become plant survival during two weeks and then it will grow for four weeks.

Acknowledgements

The author deeply grateful to Professor Dr Yin Maung Maung, Head of Department of Physics, University of Yangon, for his kind permission to do. The author sincerely thanks Professor Dr Hla Toe, Head of Department of Physics, Yangon University of Education, for his advice, kind permission, and encouragement through the research period. The author would like to thank Professor Dr Ohnmar Oo, Department of Physics, Yangon University of Education, for her help this paper.

References

- Cambridge M.L, Lambers H., Konings H and Pons T L., (1990) *Causes and Consequences of Variation in Growth Rate and Productivity of Higher Plants*. SPB Academic Publishing by: The Hague. 363 P.
- Göran I Ågren., Torsten Ingestad, (1995) "Plant nutrition and growth: Basic principles" Publishing by: Springer, Netherland, Vol.168/169, pp. 15-20.
- Heiss, Mary Lou., & Heiss, Robert J., (2007) *The Story of Tea: A Cultural History and Drinking Guide*. Berkeley, California: Ten Speed Press; Illustrated edition, Mo3 23-432.
- Karak T., Bhagat R.M., (2010) "Trace Elements in Tea Leaves, made Tea and Tea Infusion" *Food Research International Journal*, Elsevier, 43: pp. 22342252.
- Rolfe J, Yvonne C., (2003) *Camellias: A Practical Gardening Guide*. United States: Timber Press; annotated edition.
- Srividhya B., Subramanian R., Raj V., (2011) "Determination of lead, managanese, copper, zinc, cadmium, nickel and chromium in tea leaves" *Int J Pharm Pharm Sci* 3: pp. 16-173.

STRUCTURAL AND ELECTRICAL PROPERTIES OF LITHIUM DOPED ZINC OXIDE

Khin Htar Swe¹, Phyo Shwe Yi San², Ami Soe³, Su Shine Pwint Thein⁴, Than Than Swe⁵

Abstract

Lithium doped zinc oxide ($Zn_{1-x}Li_xO$) compound is a transparent conducting oxide. According to the stoichiometric compositions, the high purity of zinc oxide and lithium oxide powders were mixed and grinded to obtain the lithium doped zinc oxide compound. This compound was prepared at pre-sintering temperature 800°C for 2 h and final-sintering temperature 900°C for 2 h by solid state method. The crystalline properties of lithium doped zinc oxide compound were investigated by X-ray diffraction (XRD). From XRD results, the crystal structure of this compound can be concluded hexagonal structure. And then the electrical properties of this compound were studied.

Key words: sample preparation, XRD result, resistivity and conductivity measurement

Introduction

A ceramic is a material that is neither metallic nor organic. It may be crystalline, glassy or both crystalline and glassy (Robynl. Johnson). Ceramics are favored for many sensors application because of their wide availability, low cost, and convenient fabrication. Ceramics materials are used in electronics because depending on their composition, they can be semiconducting, superconducting, ferroelectric, or an insulator. They have electrical, optical and magnetic properties of value in the computer and electronic industries (Isabelle Robinson, 2019). At room temperature, zinc oxide has a direct-band-gap 3.3eV. ZnO is a wide band gap oxide semiconductor with hexagonal crystal structure (Schmidt-Mende *et al.*, 2007-05-01). This material seems very promising for low-voltage and short wavelength electro- optical devices such as laser and light emitting diodes; and also, for another application such as ultraviolet absorber films, varistors and gas sensors (Boshra Ghanbari Shohany & Ali Khorsand Zak, 2020). ZnO nanostructures have found uses in environmental, technological and biomedical purposes including ultrafast optical functions, dye-sensitized solar cells, lithium-ion batteries (Zhang Lin Wang 2004). In this work, lithium doped zinc oxide powders have been synthesized by the conventional solid state reaction method. As prepared and heated powders were characterized by X-ray diffraction (XRD) method. The XRD result shows the structure, crystallite size and lattice parameters of this compound. The thermoelectric effects of pellet samples were investigated at various temperature of lithium (0.607g) doped zinc oxide (19.392g) samples had been calculated. And then the electrical properties of this compound were studied by the resistivity and conductivity measurement.

¹ Department of Physics, Patheingyi University.

² Department of Physics, Patheingyi University.

³ Department of Physics, Patheingyi University.

⁴ Department of Physics, Patheingyi University.

⁵ Department of Physics, Patheingyi University.

Materials & Methods

1. Sample Preparation

First of all, 0.1 mole of Li_2O and 0.9 mole of ZnO were used to produce 1 mole of $\text{Zn}_{1-x}\text{Li}_x\text{O}$. $\text{Zn}_{1-x}\text{Li}_x\text{O}$ ceramic compound was prepared by using the lithium oxide and zinc oxide powder. These oxides were mixed according to their mix and weight the required amount of the samples was grind with a few drops of ethanol by using an agate motor for 1 h. And then, the required amount of the samples was grind adding a few drops of ethanol in the beaker. After that, the mixture powder was heated onto the hot plate with 100°C by stirring with a glass rod for 30 minutes and then cooled at the room temperature. To obtain the homogeneous powder, the mixed powder was ground by ball milling machine. The mixture was pre-sintered at 800°C for 2 h in an electrical furnace and then cooled down to room temperature.

2. Pellet Sample Preparation

The mixture powder was ground by an agate motor for 1 h. The powder was pressed into pellet by hydraulic pellet maker at a pressure of ~ 30 tons. The final-sintering was performed at 900°C for 2 h in an electrical furnace. The dimension of sample was 1.53cm in diameter and 0.452cm in thickness. The phase formation and electrical properties of final-sintered pellet sample were investigated by using XRD, electrical resistivity and conductivity measurement. The process of the sample preparation has shown in Figure-1.

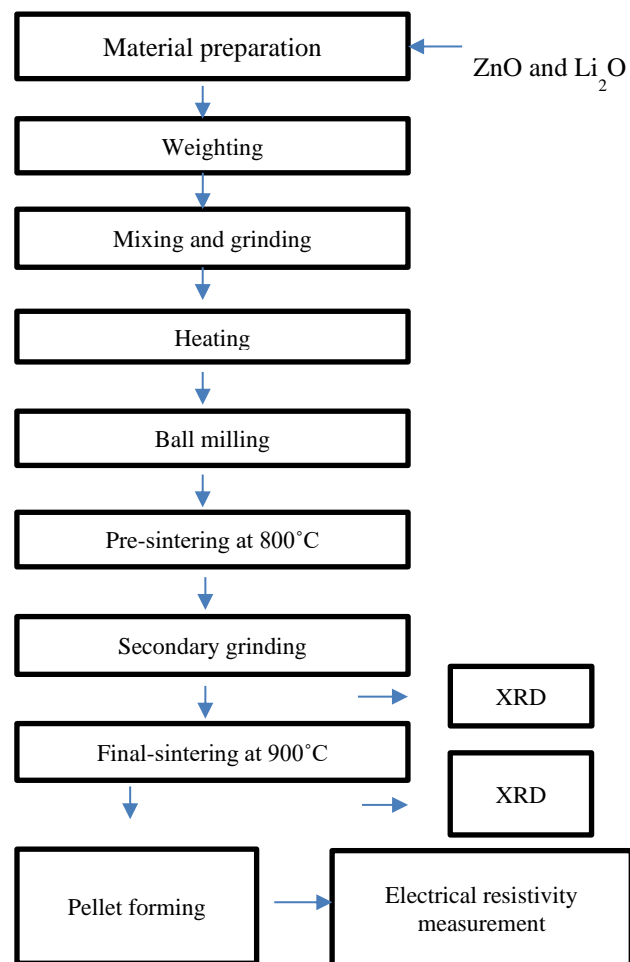


Figure-1 Process of sample preparation

Structural Analysis of XRD

Lithium doped zinc oxide ($Zn_{1-x}Li_xO$) sample has been prepared by solid state method. The phase formation of the pre-sintered sample was checked by using X-ray diffractometer. The XRD spectrum of the pre-sintered sample is shown in Figure-2. According to the XRD characterizations of the pre-sintered sample, it is confirmed that sample has been successfully formed hexagonal structure. The average crystallite size and average lattice parameter in Table-1 and Table-2.

The phase formation of the final-sintered sample has been checked by using X-ray diffractometer. The XRD spectrum of the final-sintered sample is shown in Figure-3. According to the XRD characterizations of the final-sintered sample, it is confirmed that sample has been successfully formed hexagonal structure. The average crystallite size and average lattice parameter in Table-3 and Table-4.

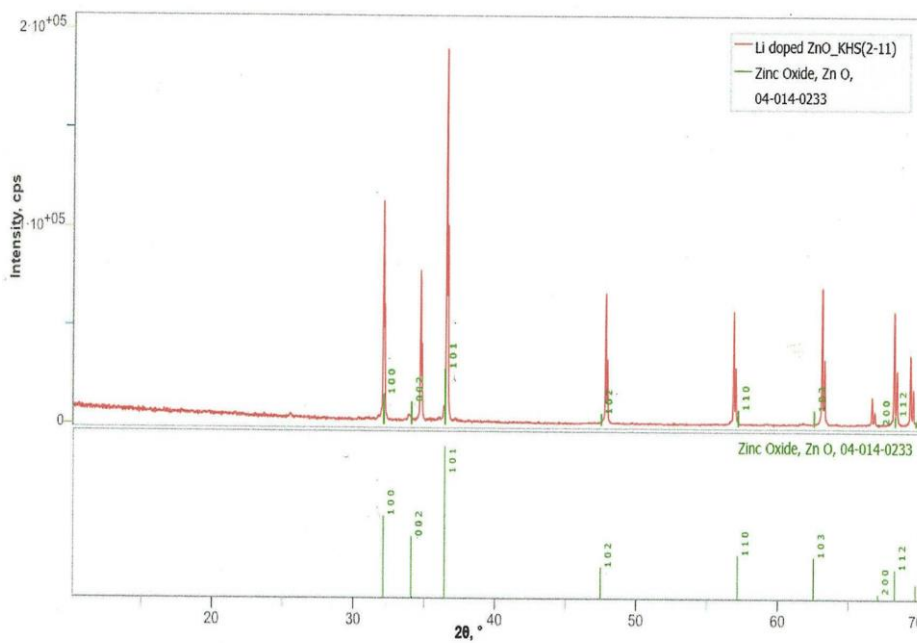


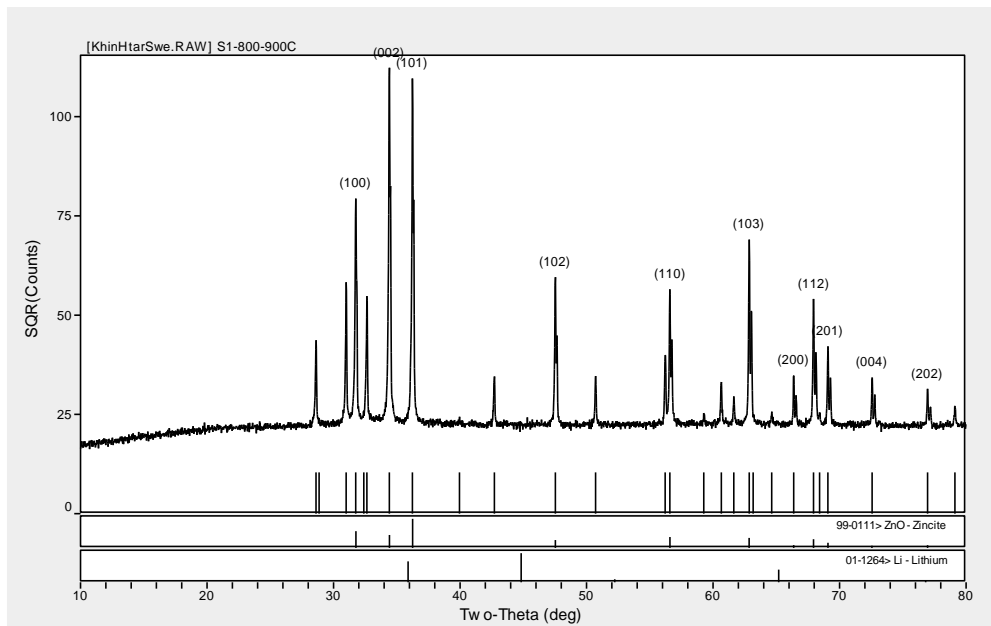
Figure-2 XRD diffractogram for pre-sintered $Zn_{1-x}Li_xO$ powder

Table-1 Crystallite size of planes of $Zn_{1-x}Li_xO$ powder

Plane	FWHM~B (deg)	Peak width B (rad)	2θ (deg)	Cosθ	Size D (nm)
100	0.159	0.0027	32.043	0.961	51.956
002	0.153	0.0026	34.699	0.955	54.377
101	0.160	0.0028	36.527	0.949	52.146
102	0.158	0.0027	47.806	0.914	54.963
110	0.160	0.0027	56.853	0.879	56.538
103	0.159	0.0027	63.106	0.852	58.793
200	0.159	0.0027	66.621	0.835	59.681
112	0.166	0.0028	68.195	0.828	57.943
Average crystallite size					55.799

Table-2 Lattice parameter of each plane of $Zn_{1-x}Li_xO$ powder

Line	Interplanar spacing d (Å)	hkl	a(Å)	c(Å)
1	2.7909	100	3.223	-
2	2.5831	002	-	5.167
3	2.4689	101	3.22	5.2707
4	1.9010	102	3.166	5.198
5	1.6181	110	3.236	-
6	1.4720	103	3.092	5.1987
7	1.4026	200	3.239	-
8	1.3740	112	3.217	5.267
Average lattice parameter			3.1989	5.2203

**Figure-3** XRD diffractogram for final-sintered $Zn_{1-x}Li_xO$ pellet**Table-3 Crystallite size of each plane of $Zn_{1-x}Li_xO$ pellet**

Plane	FWHM~B (deg)	Peak width B (rad)	2θ (deg)	Cosθ	Size D (nm)
100	0.122	0.0021	31.760	0.961	67.71
002	0.126	0.0021	34.417	0.955	66.08
101	0.160	0.0027	36.242	0.951	52.2
102	0.111	0.0019	47.536	0.915	78.49
110	0.114	0.0019	56.583	0.880	79.14
103	0.104	0.0018	62.859	0.853	89.52
200	0.106	0.0018	66.379	0.837	89.58
201	0.105	0.0018	69.082	0.842	91.85
Average crystallite size					76.8211

Table-4 Lattice parameter of each plane of Zn_{1-x} Li_x O pellet

Line	Interplanar spacing d (Å)	hkl	a(Å)	c(Å)
1	2.8151	100	3.2505	-
2	2.6036	002	-	5.207
3	2.4766	101	3.2401	5.1987
4	1.9112	102	3.2504	5.204
5	1.6252	110	3.2503	-
6	1.4772	103	3.2478	5.206
7	1.4071	200	3.249	-
8	1.3585	201	3.249	5.212
Average lattice parameter			3.2481	5.2055

Electrical Resistances Measurement

At first, the dimensions (thickness and diameter) of the sintered pellet sample were measured by Vernier-Caliper. The dimensions of the sample were 1.53cm in diameter and 0.452 cm in thickness.

Temperature dependent electrical resistances of sample were observed in the temperature range of 638K-703K. Photograph showing the experimental set up the temperature dependent electrical resistivity measurement is shown in Figure-4. Temperature dependent resistances of the sample were measured by using Lutron LCR-9073 digital meter. K-type thermocouple was used as the temperature sensor throughout the measurement. The copper block holder was heated by 1000 W heater with 500°C. The electrical conductivity of the sample have been calculated by

$$\text{using formula, } \sigma = \frac{l}{RA} .$$



Figure-4 Temperature dependent electrical resistances measurement

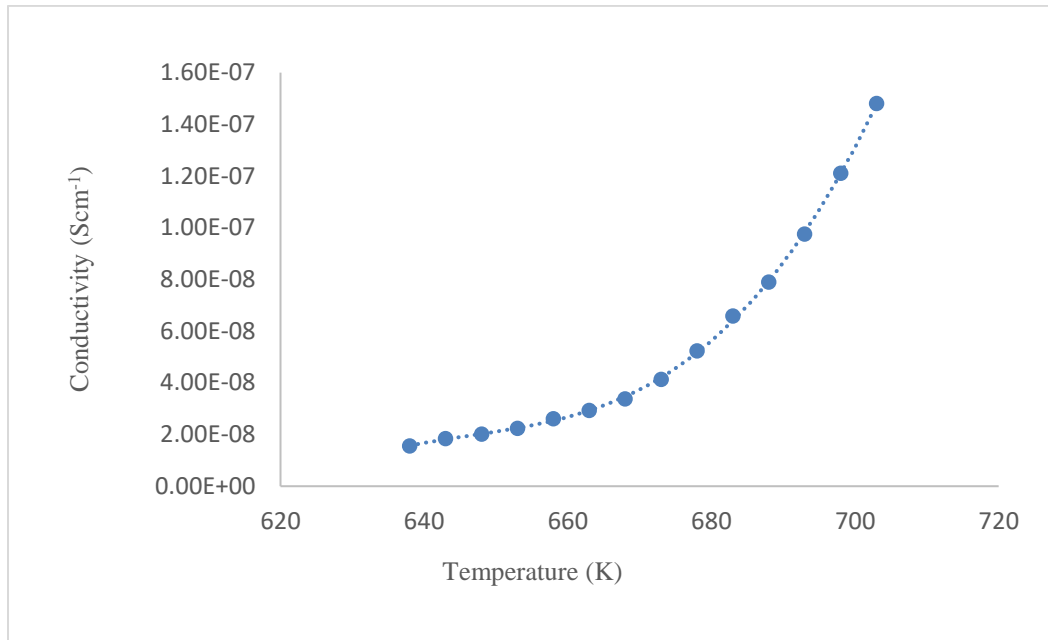


Figure-5 Plot of temperature dependent electrical conductivity curve of $(Zn_{1-x}Li_xO)$ pellet

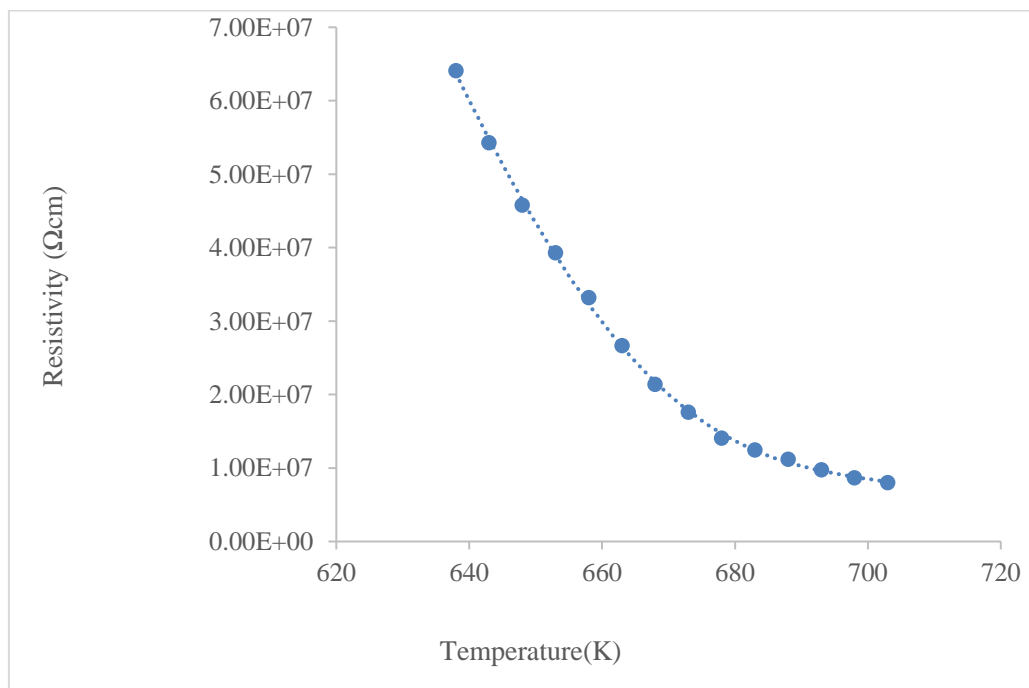


Figure-6 Plot of temperature dependent electrical resistivity curve of $(Zn_{1-x}Li_xO)$ pellet

Discussion

Lithium doped zinc oxide ($Zn_{1-x}Li_xO$) powder has been prepared by solid state method in this result. The XRD investigation, the samples have been successfully formed typical hexagonal structure after the counter diffusion reaction of the metal oxides at pre-sintering temperature of 800°C and final-sintering temperature of 900°C . The average lattice parameter and average crystallite size have been calculated for further characterization.

Lithium doped zinc oxide ($Zn_{1-x}Li_xO$) powder can be presented of average lattice parameters and average crystallite size by $a = 3.1989 \text{ \AA}$, $c = 5.22028 \text{ \AA}$ and $D = 55.799 \text{ nm}$. Lithium zinc oxide ($Zn_{1-x}Li_xO$) pellet can be presented of average lattice parameters and average crystallite size by $a = 3.2481 \text{ \AA}$, $c = 5.2055 \text{ \AA}$ and $D = 76.8211 \text{ nm}$. By using XRD results were obtained hkl (100), (002), (101), (102), (021), (103), (220), (112).

Electrical conductivity of the lithium doped zinc oxide ($Zn_{1-x}Li_xO$) pellet sample has been received from measurement of resistances of the pellet sample. The electrical conductivity of the sample is found to increase with increasing temperature. At 638K (starting temperature), the resistivity of the sample is $64.185 \times 10^6 \Omega\text{cm}$ (conductivity is $0.016 \times 10^{-6} \text{ Scm}^{-1}$) and at 703K (end temperature), the resistivity of the sample is $8.02 \times 10^6 \Omega\text{cm}$ (conductivity is $0.148 \times 10^{-6} \text{ Scm}^{-1}$) respectively.

Conclusion

The main purpose of this result is to prepare and fabricate lithium doped zinc oxide ($Zn_{1-x}Li_xO$) powder and pellet by using solid state method. In theory, for an ideal hexagonal structure, $a = b \neq c$. According to their XRD results and calculations, the crystal structure of lithium doped zinc oxide ($Zn_{1-x}Li_xO$) compound can be concluded hexagonal structure and the ideal c/a ratio is 1.6. And then, the nano-size crystal structure has been investigated. Electrical conductivity of this sample increases as increasing temperature. The purpose of this paper, lithium doped zinc oxide compound can be used lithium-ion battery technology and semiconductor devices. In general, the electrical resistivity of the sample decreases with increasing temperature; it shows that the sample has semiconductor behavior.

Acknowledgements

I would like to thank Professor Dr Than Tun, Rector, Patheingyi University for his valuable suggestions for this research work.

I also greatly indebted to Professor Dr Aye Ngwe, Department of Physics, Patheingyi University for his kind permission to undertake this research.

I also thankful to Professor Dr Than Than Swe, Department of Physics, Patheingyi University for her kind permission to undertake this research.

I would like to express my gratitude to Professor Dr Khin Myo Ma Ma Saw, Department of Physics, Patheingyi University for her kind permission and encouragements to carry out this work.

References

- B.D. Cullity, S.R. Stock, (1995), "Elements of X-ray Diffraction", Third Edition
- Boshra Ghanbari Shohany and Ali Khorsand Zak, (2020), "Doped ZnO nanostructures with selected element-structural, morphology and optical properties:" Ceramic International volume 46, Issue, Page- 5507-5520
- Isabelle Robinson, (2019) "Properties of Nanometallic and Inorganic Ceramics"
- Robynl. Johnson, "Ceramics in the classroom"
- Schmidt-Mende, Lukas; MacManus-Driscoll, Judith L. (2007-05-01) "ZnO- nanostructures, defects, and devices"
- Peter Y. Yu and M. Cardona (2010) "Fundamentals of Semiconductors" Fourth Edition
- Zhang Lin Wang (2004), "Zinc oxide nanostructures: growth, properties and applications" Journal of Physics: Condensed Matter 16

FABRICATION AND CHARACTERIZATION OF $Zn_{1-x}Cu_xO$ CERAMICS COMPOUND

Phyo Shwe Yi San¹, Khin Htar Swe², Ami Soe³, San San Maw⁴, Than Than Swe⁵

Abstract

Copper zinc oxide ($Zn_{1-x}Cu_xO$) ceramic compound is a transparent conducting oxide. Copper zinc ceramic compound was prepared for mixing and grinding by high purity of ZnO (zinc oxide) powder and CuO (copper oxide) powder according to the stoichiometric composition. Copper zinc ceramic oxide ($Zn_{1-x}Cu_xO$) ceramic compound was prepared at various growth temperatures by solid state method. The crystalline properties of copper zinc ceramic compound were investigated by X-ray diffraction (XRD). Copper zinc oxide ceramic compound were also studied by electrical properties.

Keywords- sample preparation, XRD result, conductivity and resistivity measurement

Introduction

Ceramics are classified as inorganic and nonmetallic materials that are essential to our daily lifestyle. Ceramics are favored for many sensors' application because of their wide availability, low cost, and ease fabrication (Yin, Q., Zhu, B., and Zeng, H.2010). The electrical properties of ceramics depend on composition, temperature, atmosphere and microstructure. Nanocrystalline metal oxide has numerous important properties like catalytic, electrical and optical properties. Hence ZnO is one of the metal oxides which attracts due to its band gap energy of 3.37 eV and a larger excitation binding energy of 60 meV at room temperature. ZnO was intensively studied as a material dilute magnetic semiconductor (Kittle C., 1986). When ZnO is doped with the transition metal ions such on Mn, Fe, Cu, Cr and Co, it shows ferromagnetic properties. The optical and electrical properties of ZnO must be tailored effectively to the desirable range by doping with suitable elements (Pillai S.O., 2005).

The Cu doping of ZnO material has been an active research area on the last few years, due to its deep acceptor level, enhanced green luminescence, gas sensitivity etc. The high ionization energy and low formation energy of Cu makes it a fast diffusing impurity into ZnO lattice. Depending upon the oxidation states of Zn, Cu doped ZnO becomes a p type semiconductor (D.B. Buchholz *et al.*, 2005). Ceramic materials are special because of their properties. They typically pass high melting points, low electrical and thermal conductivity values, and high compressive strengths. This paper reports the XRD study and copper zinc oxide ceramic compound were measured by conductivity (Buchanan, R. 1984).

¹ Department of Physics, Patheingyi University.

² Department of Physics, Patheingyi University.

³ Department of Physics, Patheingyi University.

⁴ Department of Physics, Patheingyi University.

⁵ Department of Physics, Patheingyi University.

Material & Methods

Powder Sample Preparation

In the main system, 0.05 mole of CuO and 0.95 mole of ZnO were used to produce 1 mole of $Zn_{1-x}Cu_xO$. Each of the mixture was prepared to produce a 20g batch. $Zn_{1-x}Cu_xO$ ceramic compound was prepared by mixing the copper oxide (CuO) and zinc oxide (ZnO). These oxides were mixed according to their molecular weight and the required amount of the samples was grind with a few drops of ethanol by using an agate motor for 1 h. And then, the required amount of the samples was grind adding a few drops of ethanol in the breaker. After that, the mixture powder was heated onto the hot plate with 100°C by stirring a glass rod for 1 h and then cooled at the room temperature, to obtain the homogeneous powder was used by ball milling machine. The mixture was first-sintered at 500°C for 1 h in an electrical furnace with increasing temperature of 20°C per minute, and then cooled to room temperature with the same rate.

Pellet Sample Preparation

The mixture powder was grinding with an agate motor for 1 h. The powder was pressed into pellet by hydraulic press at a pressure of ~70MPa. The second sintering was performed at 600°C for 1 h with the same heating rate of 20°C per minute. The pellet was polished for further characterizations. The phase formation and electrical property of second-sintered pellet sample were checked by using X-ray diffractometer and electrical resistivity and conductivity measurement. Process of the sample preparation has shown in figure 1.

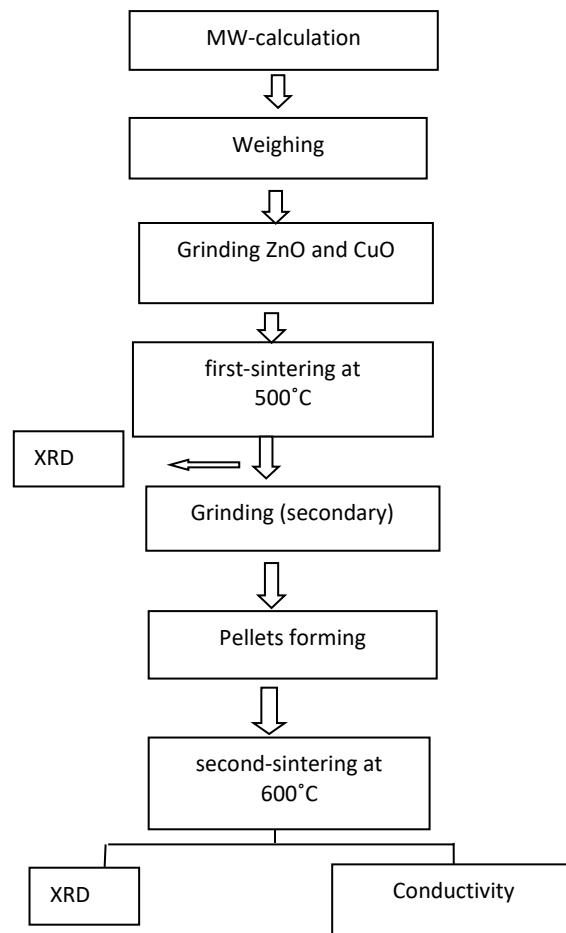


Figure.1. Process of the sample preparation

Experimental Results of XRD

Copper zinc oxide, $Zn_{1-x}Cu_xO$, has been prepared by solid state method. The phase formation of the first-sintered sample was checked by using X-ray diffractometer. The XRD spectrum of the first-sintered sample is shown in figure 2. According to the XRD characterizations of the first-sintered sample, it is confirmed that sample has been successfully formed typical hexagonal sample structure according to (ICDD card 65-3411 and 80-1916). The average crystallite size and average lattice parameter in table 1 and table 2. The average crystallite size is form to be 60.2102 nm and average lattice parameter is $a=3.3534\text{\AA}$ and $c=5.4324\text{\AA}$. The phase formation of the second-sintered sample has been checked by using X-ray diffractometer. The XRD spectrum of the second -sintered sample is shown in figure 3. According to the XRD characterizations of the second -sintered sample, it is confirmed that sample has been successfully formed hexagonal structure according to (ICDD card 89-7102 and 80-1916). The average crystallite size and average lattice parameter in table 3 and table 4. The average crystallite size is form to be 57.5455 nm and average lattice parameter is $a=3.2692\text{\AA}$ and $c=5.1749\text{\AA}$.

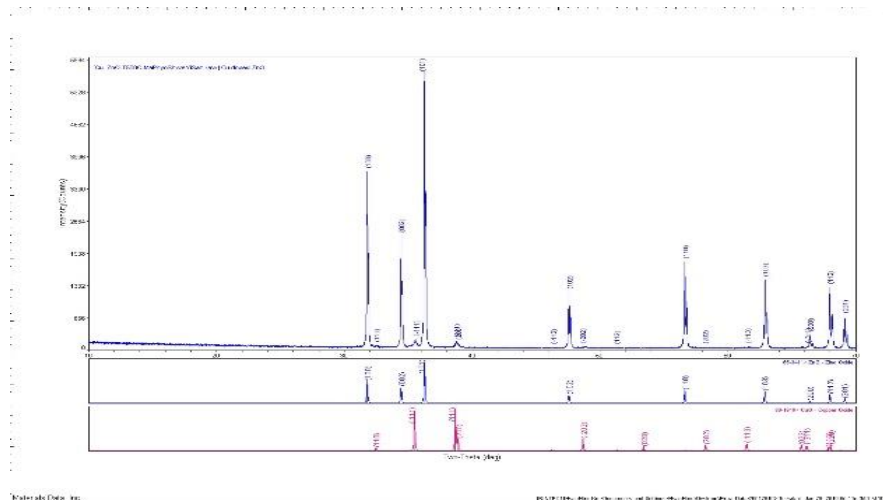


Figure.2. XRD diffractogram for first- sintered $Zn_{1-x}Cu_xO$ powder

Table.1 Crystallite size of each planes of $Zn_{1-x}Cu_xO$ powder

Plane	FWHM ~B (deg)	Peak width B(rad)	2θ(deg)	cos θ	Size D (nm)
100	0.114	0.00198	31.792	0.9618	72.4556
101	0.151	0.00263	36.274	0.9503	55.3604
110	0.233	0.00406	32.471	0.9601	35.5109
002	0.111	0.00193	34.444	0.9552	74.9277
102	0.103	0.00179	47.566	0.9151	84.2845
200	0.525	0.00916	38.853	0.9431	16.0451
112	0.229	0.00399	51.258	0.9016	38.4758
103	0.114	0.00198	62.881	0.8532	81.6765
201	0.116	0.00202	69.108	0.8236	83.1522
Average crystallite size					60.2102

Table.2 Lattice parameter of each planes of $Zn_{1-x}Cu_xO$ powder

Line	Interplanar spacing d(Å)	hkl-fcc	a(Å)	c(Å)
1	2.8123	100	3.2474	-
2	2.4745	101	3.3600	5.7928
3	2.6016	002	-	5.2032
4	1.9101	102	3.3672	5.2235
5	1.4767	103	3.5366	5.3786
6	1.3581	201	3.2559	5.5641
Average Lattice parameter			3.3534	5.4324

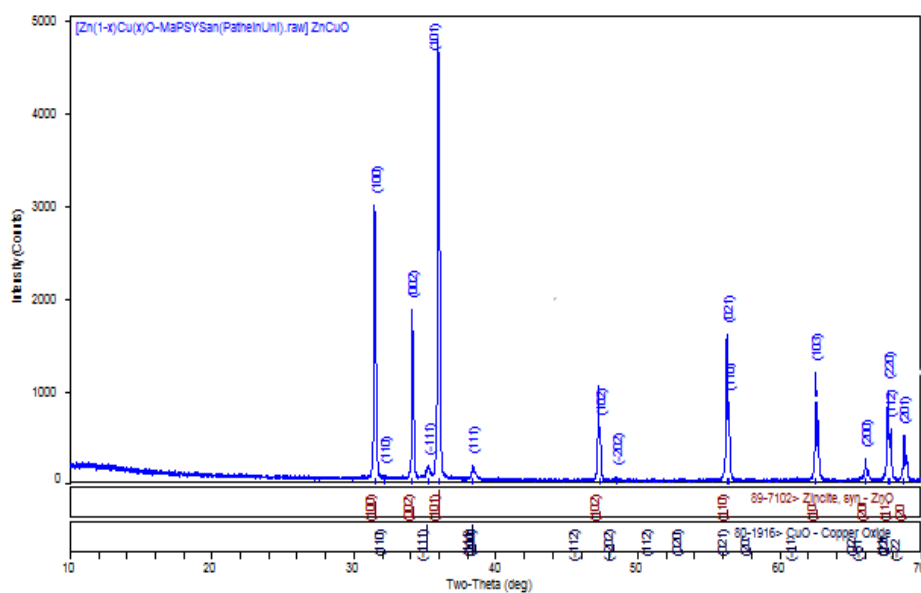
**Figure.3.** XRD diffractogram for second- sintered $Zn_{1-x}Cu_xO$ pellet

Table.3 Crystallite size of each planes of Zn_{1-x}Cu_xO pellet

Plane	FWHM ~ B (deg)	Peak width B(rad)	2θ(deg)	cosθ	Size D (nm)
100	0.155	0.0027053	31.466	0.9625	53.247
101	0.156	0.0027227	35.949	0.9512	53.5358
110	0.093	0.0016232	32.175	0.9608	88.9017
002	0.135	0.0023562	17.0615	0.9559	61.5540
102	0.133	0.0023231	47.311	0.9159	65.2092
200	0.202	0.0035256	66.039	0.8385	46.9026
112	0.311	0.0054279	67.796	0.7783	32.8213
103	0.144	0.0025133	62.535	0.8548	64.5417
201	0.188	0.0032812	68.749	0.8254	51.1965
Average crystallite size					57.5455

Table.4 Lattice parameter of each planes of Zn_{1-x} Cu_xO pellet

Line	Interplanar spacing d(Å)	hkl-fcc	a(Å)	c(Å)
1	2.8407	100	3.2802	-
2	2.4961	101	3.2805	5.2486
3	2.6254	002	-	5.2508
4	1.9198	102	3.2673	5.2146
5	1.3811	112	3.2534	5.1367
6	1.4841	103	3.2699	5.2239
7	1.3643	201	3.2637	4.9752
Average Lattice parameter			3.2692	5.1749

Electrical Conductivity Measurements

At first, the dimensions (thickness and diameter) of the sintered pellet sample were measured by Vernier-Caliper. The dimensions of the sample were 1.55cm in diameter and 0.45cm in thickness. Temperature dependent resistances of sample were observed in the temperature range of 533K-633K. Photograph showing the experimental set up the temperature dependent electrical conductivity measurement is shown in figure 4 clearly shows that temperature dependence of the dc conductivity increases with increasing temperature. Temperature dependent resistances of the sample were measured by using Lutron LCR-9073 digital meter. K-type thermocouple was used as the temperature sensor throughout the measurement. The copper block holder was heated by 1000W heater with 500°C.

The electrical conductivities of the sample have been calculated by using formula $\sigma = \frac{l}{RA}$.



Figure.4. Temperature dependent electrical conductivity measurement

Results of Electrical Conductivity

In the present work the variation of electrical conductivity of the copper zinc oxide, $Zn_{1-x}Cu_xO$ pellet sample in the temperature range 533K-633K is shown in figure.5. In this curve, electrical conductivity of the sample is found to increase with increasing temperature. At 533K (starting temperature), the resistivity of the sample is $82.36 \times 10^6 \Omega\text{cm}$ (conductivity is $0.012 \times 10^{-6} \text{Scm}^{-1}$) and at 633K (end temperature), the resistivity of the sample is $0.5 \times 10^6 \Omega\text{cm}$ (conductivity is $2 \times 10^{-6} \text{Scm}^{-1}$) respectively. Figure.6 shows the temperature dependent electrical resistivity curve of copper zinc oxide ($Zn_{1-x}Cu_xO$) pellet sample. As shown in this curve, electrical resistivity of the sample is found to decrease with increasing temperature. Two points (data) of the sample are presented in figure.6. It indicates the high resistivity of the sample.

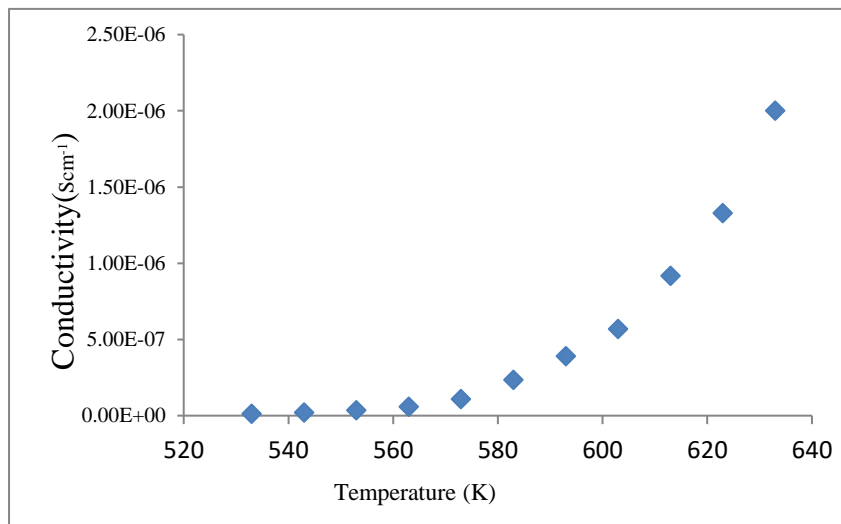


Figure.5. Plot of temperature dependent electrical conductivity versus temperature curve of ($Zn_{1-x}Cu_xO$) pellet

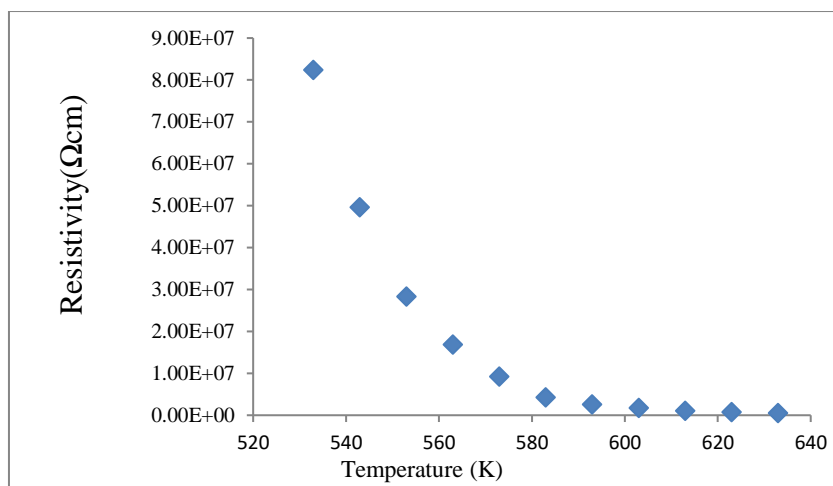


Figure.6. Plot of temperature dependent electrical resistivity versus temperature curve of $(Zn_{1-x}Cu_xO)$ pellet

Discussion

Copper zinc oxide ($Zn_{1-x}Cu_xO$) has been prepared by solid state method in this paper. The XRD characterizations, the samples have been successfully formed typical hexagonal structure after the counter diffusion reaction of the metal oxides at first- sintering temperature of 500°C and second-sintering temperature of 600°C. The average lattice parameter and average crystallite size have been calculated for further characterization.

Copper zinc oxide ($Zn_{1-x}Cu_xO$) powder can be presented of average lattice parameters and average crystallite size by $a = 3.3543\text{Å}$, $c = 5.4324\text{Å}$ and $D=60.2102\text{ nm}$. Copper zinc oxide ($Zn_{1-x}Cu_xO$) pellet can be presented of average lattice parameters and average crystallite size by $a=3.2692\text{Å}$, $c=5.1749\text{Å}$ and $D=57.5455\text{ nm}$. By using XRD results were obtained hkl 100, 002, 101, 102, 021, 110, 103, 220.

Electrical conductivities of the copper zinc oxide ($Zn_{1-x}Cu_xO$) pellet sample have been received from measurement of resistances of the pellet sample. The electrical conductivity of the sample is found to increase with increasing temperature. At 533K (starting temperature), the resistivity of the sample is $82.36 \times 10^6 \Omega\text{cm}$ (conductivity is $0.012 \times 10^{-6} \text{Scm}^{-1}$) and at 633K (end temperature), the resistivity of the sample is $0.5 \times 10^6 \Omega\text{cm}$ (conductivity is $2 \times 10^{-6} \text{Scm}^{-1}$) respectively.

Conclusion

The main objective of this paper is to prepare and fabricate copper zinc oxide ($Zn_{1-x}Cu_xO$) powder and pellet by using solid state method. In theory, for an ideal hexagonal structure, $a = b \neq c$. According to their XRD results and calculations, the crystal structure of copper zinc oxide ($Zn_{1-x}Cu_xO$) compound can be concluded hexagonal structure. And then, the nano-size crystal structure has been investigated. The electrical conductivity of the sample is found to increase with increasing temperature, whereas resistivity decreases. Generally, the electrical resistivity of the sample decreases with the increase of temperature, which shows that sample have semiconductor behavior.

Acknowledgements

I would like to thank Professor Dr Than Tun, Rector, Patheingyi University, for his valuable suggestions for this research work.

I would like to thank Professor Dr Aye Ngwe, Head of Department of Physics, Patheingyi University, for his valuable suggestions for this research work..

I wish to express my thanks to Professor Dr Than Than Swe, Department of Physics, Patheingyi University, for her kind permission to undertake this research.

I am also thankful to professor Dr Khin Myo Ma Ma Saw, Department of Physics, Patheingyi University, for her kind permission to undertake this research.

References

B.D. Cullity, S.R. Stock, 1995, "Elements of X-ray Diffraction", Third Edition.

Boshra Ghanbari Shohany and Ali Khorsand Zak, (2020)," Doped ZnO nanostructures with selected element-structural, morphology and optical properties:" Ceramic International volume 46, Issue, Page-5507-5520

Isabelle-Robinson, (2019) "Properties of Nanometallic and Inorganic Ceramics"

Robynl. Johnson, (2003) " Ceramics in the classroom"

Schmidt-Mende, Lukas; MacManus- Driscoll, Judith L. (2007-05-01) "ZnO- nanostructures defects, and devices"

Peter Y.Yu and M. Cardona (2010) "Fundamentals of Semiconductors" Fourth Edition

Zhang Lin Wang (2004), " Zinc oxide nanostructures: growth, properties and applications" Journal of Physics: Condensed Matter 16

ANALYSIS OF WAVE FUNCTIONS, ENERGY LEVELS AND CROSS-SECTION FOR (π^+ , K^+) REACTIONS USING NUMEROV'S METHOD

Ye Htet Aung¹, Thi Han², Kyaw Kyaw Naing³, Chit Min Thu⁴, Aung Khant Paing⁵

Abstract

In this paper, the wave functions of single lambda particle for Λ -hypernucleus are calculated by using Numerov's method. And then, the single lambda particle energy levels of various Λ -hypernucleus in Woods-Saxon potential have been studied. Moreover, the single Λ -binding energy and differential cross-section for Λ -hyperon production (π^+ , K^+) reactions of $^{10}_{\Lambda}\text{B}$, $^{12}_{\Lambda}\text{C}$, $^{28}_{\Lambda}\text{Si}$ and $^{89}_{\Lambda}\text{Y}$ have been calculated. The calculated theoretical results of single Λ -binding energy and differential cross-section are well in agreement with the experimental results of KEK. All the numerical calculations are conducted with the help of Fortran-2019 Program.

Keywords: Binding Energy, Differential Cross-section, Fortran2019, Numerov's Method, Λ - hypernucleus, Woods-Saxon Potential

Introduction

A nuclear reaction is a process in which the nucleus of an atom is changed by being split apart or joined with the nucleus of another atom. There are many types of nuclear reaction. But, the (π^+ , K^+) reactions are studied. The single lambda binding energy, energy levels and differential cross-section for (π^+ , K^+) reactions are being gone to study by using phenomenological potential.

The ordinary nucleus consists of protons and neutrons which are subatomic particles called by elementary particles. A hypernucleus is similarly a nucleus but consists of the protons and neutrons in addition to at least one hyperon which is a baryon carrying the strangeness quantum number.[11] Baryon is massive composite hadron which is made up of three quarks and is subdivided into two groups: nucleon and hyperon.

Nucleon consists of a proton and neutron. Hyperon, a strange particle, is larger mass than the nucleon and consisting one or more strange quark and is also called the strange particle. Hyperons are produced by the strong force (about 10^{-23} s) and decayed by the weak force (about 10^{-10} s). There are four kinds of hyperons. They are Lambda (Λ), Sigma (Σ), Xi (Ξ) and Omega (Ω). In 1952, Marian Danysz and Jerzy Pniewski discovered the first nucleus.[14] They used the nuclear emulsion technique, based on their energetic but delayed decay.

Nowadays, lambda particle is interested by scientists in the field of nuclear physics. A product of a proton collision with a nucleus was found to live for much longer time than expected: 10^{-10} s instead of the expected 10^{-23} s in 1947 during a study of cosmic ray interactions. This particle name is lambda (Λ) and the property was dubbed "strangeness" and the name stuck to be the name one of the quarks from which the lambda particle is constructed. The composition of Λ^0 is made up of uds which means up, down and strange quark. The mass of Λ^0 is 1115.683 ± 0.006 MeV/c². The spin of Λ^0 particle is 1/2 and isospin is 0.[13] A lambda particle has been produced with (π^+ , K^+), (K^- , π^-) and (π^- , K^+) reactions. Λ -hyperon does not need to obey Pauli's exclusion principle and can penetrate into the nuclear interior and form deeply bound hypernuclear states.

Aim

The research paper aim is to analyze the energy levels, single lambda binding energy and differential cross-section for (π^+ , K^+) reactions using Numerov's method.

¹ Department of Physics, Defence Services Academy, Pyin Oo Lwin

² Department of Physics, Defence Services Academy, Pyin Oo Lwin

³ Department of Nuclear Physics, Defence Services Academy, Pyin Oo Lwin

⁴ Department of Physics, Defence Services Academy, Pyin Oo Lwin

⁵ Department of Physics, Defence Services Academy, Pyin Oo Lwin

Numerov's Method

Numerov's method was developed by Boris Vasil's Numerov who is the Russian astronomer. The Numerov's method, a numerical method, is used to solve the ordinary differential equation of second order in which the first term does not appear.[7]

The Numerov's method can be used to solve differential equation of the form:

$$\frac{d^2y}{dx^2} = -g(x)y(x) + s(x) \quad (1)$$

The three values of y_{n-1} , y_n , y_{n+1} taken at three equidistant points x_{n-1} , x_n , x_{n+1} are related as follows:

$$y_{n+1} \left(1 + \frac{h^2}{12} g_{n+1} \right) = 2y_n \left(1 - \frac{5h^2}{12} g_n \right) + y_{n-1} \left(1 + \frac{h^2}{12} g_{n-1} \right) + \frac{h^2}{12} (s_{n+1} + 10s_n + s_{n-1}) + o(h^6) \quad (2)$$

Woods-Saxon Potential

The Woods-Saxon potential is used in nuclear physics because it is an important part of understanding the interactions between nucleons (protons and neutrons) inside atomic nuclei. By understanding potential, it can pay insight into the behavior of nucleons, which can help better understand the properties of nuclei, such as binding energy and wave functions. Additionally, the potential can be used to calculate the properties of nuclear reactions and scattering particles of the nuclei.

The Woods-Saxon potential, a mean field potential, is a phenomenological potential used to describe the interaction between nucleons (protons and neutrons) inside an atomic nuclei and is used to describe approximately the forces applied on each nucleon, in the nuclear shell model for the structure of the nucleus. This potential is named after Roger D. Woods and David S. Saxon.[12]

The form of the potential, in terms of the distance r from the center of nucleons is:

$$V(r) = - \frac{V_0}{1 + \exp\left(\frac{r-R}{a}\right)} \quad (3)$$

where, V_0 = the potential well depth

a = the length representing the surface thickness of the nucleus

r = the distance from the center of nucleus

R = the nuclear radius

Numerov's Calculation of Binding Energy and Differential Cross-section for Lambda Single Particle

A transition matrix is a matrix that relates the initial and final states of a physical systems undergoing a transition or scattering process. The transition matrix, a square matrix, describes the probabilities of moving from one state to another in a Markov chain.[10] The transition matrix for the (π^+, K^+) reaction provides a quantitative description of the scattering process. The transition probability per unit time for state ψ_i to ψ_f due to the perturbation can be calculated using the time-independent perturbation theory and is given by:

$$W_{fi} = \frac{2\pi}{\hbar} |T_{fi}|^2 \delta(E_i - E_f) \tag{4}$$

where, T_{fi} = the squared matrix element of the perturbation Hamiltonian between the initial and final state

$E_i - E_f$ = the Dirac delta function that enforces energy conservation

In the ${}^A_Z X(\pi^+, K^+) {}^A_Z X$ reaction, the target nucleus ${}^A_Z X$ is consisted of a neutron and a core nucleus. The incident particle π^+ interacts only with the neutron while the core nucleus remains as a spectator. The elementary process is $\pi^+ + n \rightarrow \Lambda + K^+$, and if the emitted Λ sticks to the core nucleus ${}^A_Z X$ hypernucleus is produced. The schematic diagram of reaction process is as follows;

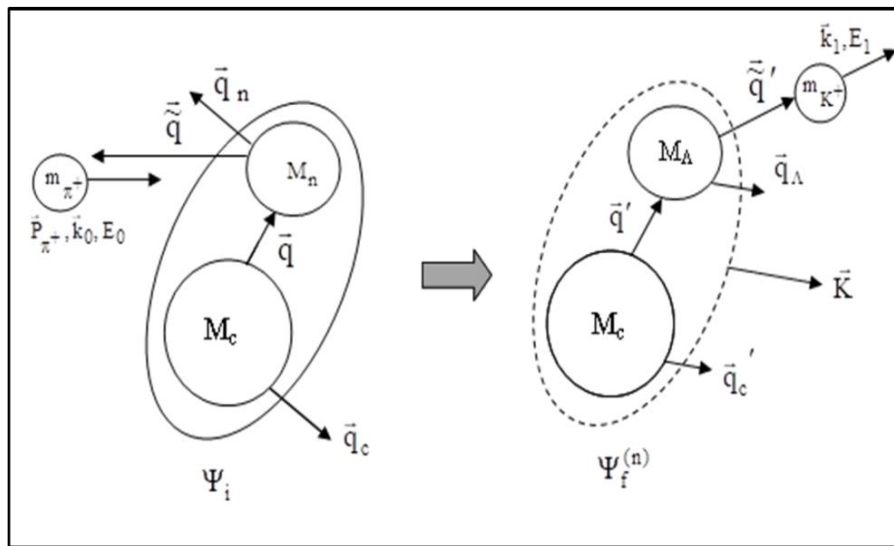


Figure 1. Schematic Diagram of (π^+, K^+) Reaction

The nuclear cross-section in nuclear physics is used to design and optimize nuclear reactor and study the properties of atomic nuclei and develop new nuclear technologies.[9] The differential cross-section is calculated to determine the probability of the various Λ -hyperon production reactions.

$$d^6\sigma = \frac{L^3}{v_0} \frac{2\pi^3}{\hbar} \sum_n \delta(E_i - E_f^{(n)}) \left(\frac{L}{2\pi}\right)^6 d\vec{k}_1 d\vec{k}_2 |T_{fi}^{(n)}|^2 \tag{5}$$

where, $\frac{L^3}{v_0}$ = incident flux

$$v_0 = \frac{\hbar \vec{k}_0 c^2}{E_0} = \text{incident pion velocity}$$

$$\rho(E) = \left(\frac{L}{2\pi}\right)^3 d\vec{k}_1 \left(\frac{L}{2\pi}\right)^3 d\vec{k}_2 = \text{number of allowed final states}$$

$$\delta(E_i - E_f^{(n)}) = \text{energy conservation term}$$

The differential cross-section for (π^+, K^+) reaction becomes

$$\frac{d^3\sigma}{dE_1 d^2\Omega} = \frac{(2\pi)^4}{\hbar^2 k_{0c}^2} \frac{(\hbar c)^2}{4} |\langle t \rangle_{av}|^2 k_1 - \frac{1}{\pi} \text{Im} \left[\int d\vec{r} d\vec{r}' f^*(\vec{r}) \left\langle \vec{r} \left| \frac{1}{E - H_{\Lambda c} + i\epsilon} \right| \vec{r}' \right\rangle f(\vec{r}') \right] \quad (6)$$

Results and Discussions

In this section, the wave functions, energy levels, single Λ binding energy and differential cross-section will be studied.

Wave Functions for $^{10}\text{B}(\pi^+, \text{K}^+)_{\Lambda}^{10}\text{B}$ Reaction

In this $^{10}\text{B}(\pi^+, \text{K}^+)_{\Lambda}^{10}\text{B}$ reaction, it has two states which are $0s_{1/2}$ and $0p_{3/2}$ state. The wave functions have only positive region. The wave functions of $^{10}\text{B}(\pi^+, \text{K}^+)_{\Lambda}^{10}\text{B}$ reaction are shown in figure (2).

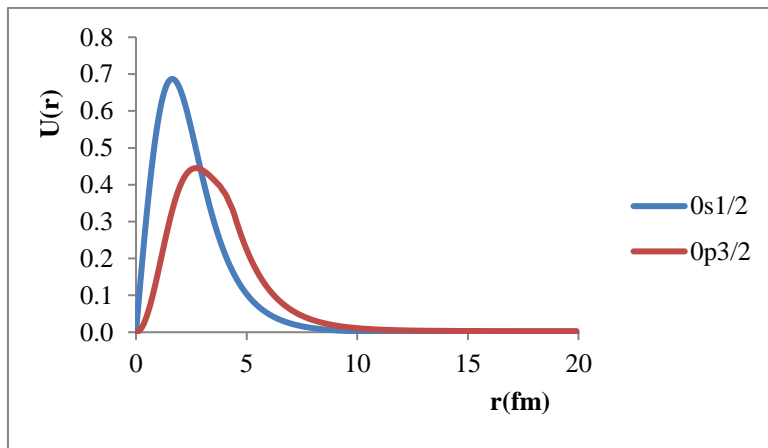


Figure 2. Wave Functions for $^{10}\text{B}(\pi^+, \text{K}^+)_{\Lambda}^{10}\text{B}$ Reaction

Wave Functions for $^{12}\text{C}(\pi^+, \text{K}^+)_{\Lambda}^{12}\text{C}$ Reaction

In this $^{12}\text{C}(\pi^+, \text{K}^+)_{\Lambda}^{12}\text{C}$ reaction, the wave functions have only positive region. The wave functions start increasing from 0 fm. The wave functions for $^{12}\text{C}(\pi^+, \text{K}^+)_{\Lambda}^{12}\text{C}$ reaction are shown in figure 3.

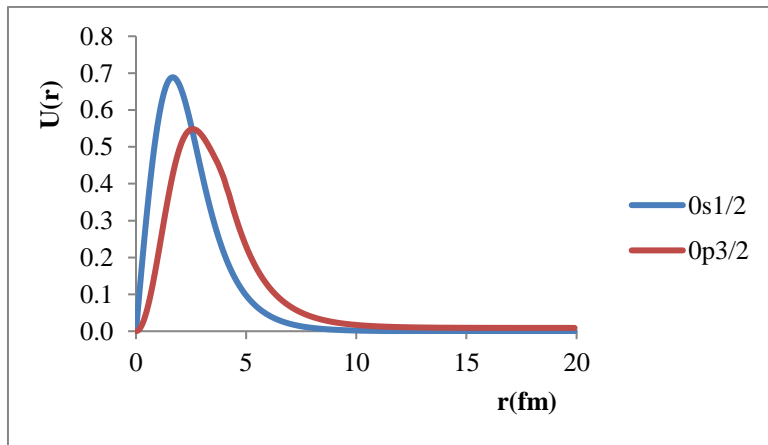


Figure 3. Wave Functions for $^{12}\text{C}(\pi^+, \text{K}^+)_{\Lambda}^{12}\text{C}$ Reaction

Wave Functions for $^{28}\text{Si}(\pi^+, \text{K}^+)_{\Lambda}^{28}\text{Si}$ Reaction

In this $^{28}\text{Si}(\pi^+, \text{K}^+)_{\Lambda}^{28}\text{Si}$ reaction, the four spin states can be found. They are $0s_{1/2}$, $0p_{3/2}$, $0p_{1/2}$ and $0d_{5/2}$ states. The wave functions of $0p_{3/2}$ and $0p_{1/2}$ are nearly identical. The wave functions for $^{28}\text{Si}(\pi^+, \text{K}^+)_{\Lambda}^{28}\text{Si}$ reaction are shown in figure 4.

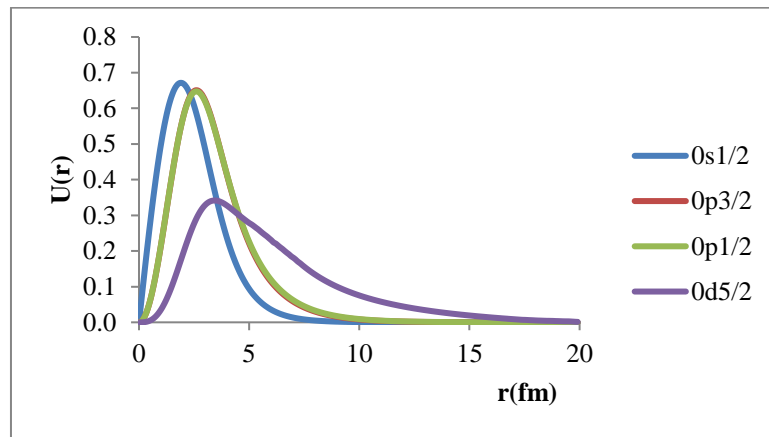


Figure 4. Wave Functions for $^{28}\text{Si}(\pi^+, \text{K}^+)_{\Lambda}^{28}\text{Si}$ Reaction

Wave Functions for $^{89}\text{Y}(\pi^+, \text{K}^+)_{\Lambda}^{89}\text{Y}$ Reaction

The wave functions for $^{89}\text{Y}(\pi^+, \text{K}^+)_{\Lambda}^{89}\text{Y}$ reaction are found positive and negative region which are shown in figure 5. This reaction has $0s_{1/2}$, $0p_{3/2}$, $0p_{1/2}$, $0d_{5/2}$, $1s_{1/2}$, $0d_{3/2}$, $0f_{7/2}$ and $1p_{3/2}$ states. And then, the wave functions of various spin states are found in figure 5.

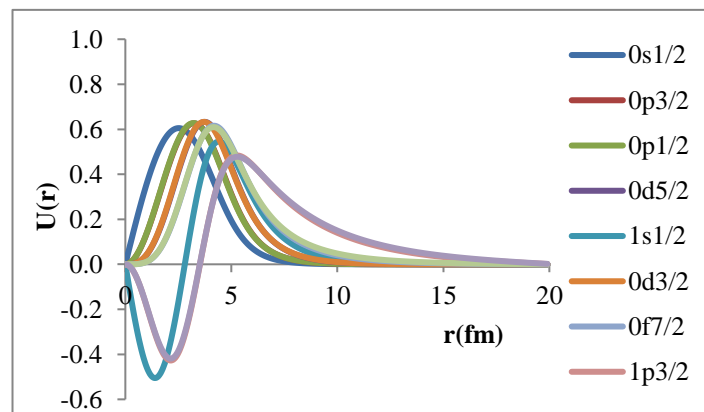


Figure 5. Wave Functions for $^{89}\text{Y}(\pi^+, \text{K}^+)_{\Lambda}^{89}\text{Y}$ Reaction

Lambda Single-particle Energy Levels for Various Hypernuclei

Numerov's method computes for single-particle energy levels of Woods-Saxon Potential which has analytical result. The numerical calculation results replicate the single-particle energy levels using Woods-Saxon potential which justifies the Numerov's method to solve the second order differential equation. The results of calculated energy eigen values for single lambda particle using Woods-Saxon potential are shown in figure 6.

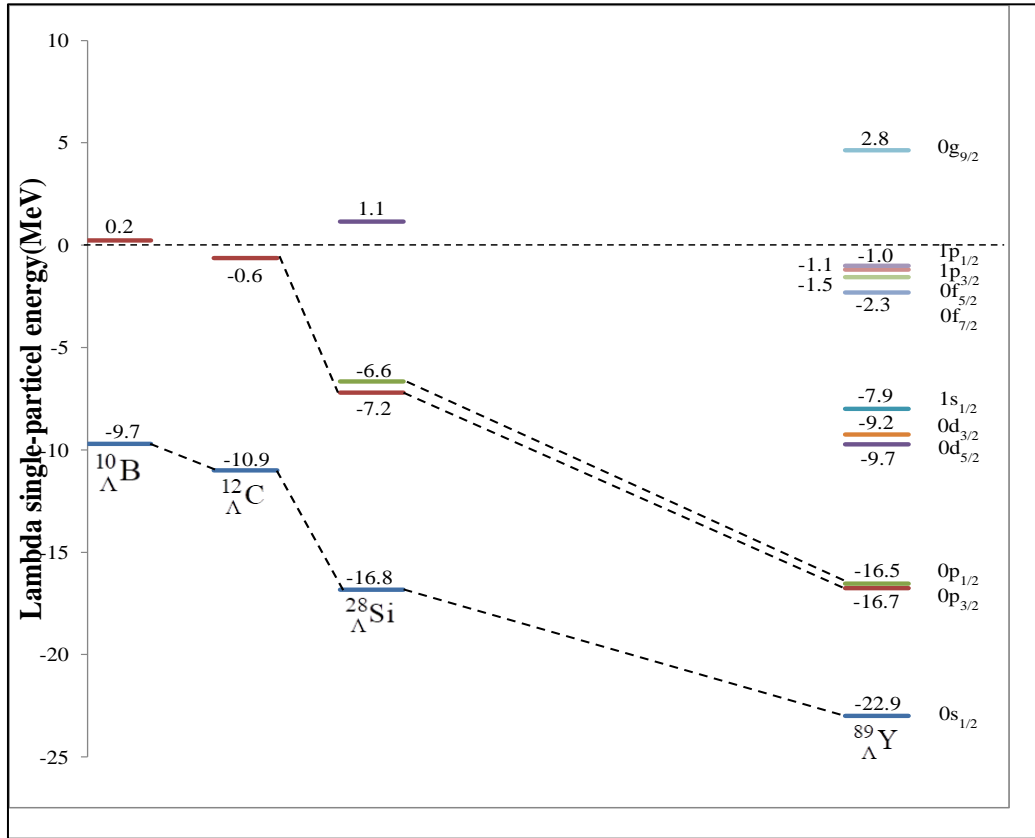


Figure 6. Lambda Single-Particle Energy Levels with Woods-Saxon Potential for Various Hypernuclei

Single Lambda Binding Energy and Differential Cross-section for $^{10}\text{B}(\pi^+, \text{K}^+)_{\Lambda}^{10}\text{B}$ Reaction

In this $^{10}\text{B}(\pi^+, \text{K}^+)_{\Lambda}^{10}\text{B}$ reaction, the two clear peaks of the calculated theoretical spectrum of the Λ -binding energy for $s_{\Lambda}=-9.7$ MeV, $p_{\Lambda}=0.2$ MeV and differential cross-section for $s_{\Lambda}=0.017$ $\mu\text{b}/\text{sr}$, $p_{\Lambda}=0.053$ $\mu\text{b}/\text{sr}$ are shown in figure 7.

The KEK experimental results of the ground state of the single Λ -binding energy at $B_{\Lambda}=-9.1\pm 0.1$ MeV and the excitation state of the single Λ -binding energy at $B_{\Lambda}=0.19\pm 0.2$ MeV and the ground state of the values of differential cross-section at $\sigma=0.017\pm 0.02$ $\mu\text{b}/\text{sr}$ and the excitation state at $\sigma=0.057\pm 0.14$ $\mu\text{b}/\text{sr}$ are shown in figure 8.[6]

The comparison of the theoretical results and the experimental results of KEK for the Λ -binding energy and differential cross-section of $^{10}\text{B}(\pi^+, \text{K}^+)_{\Lambda}^{10}\text{B}$ reaction is shown in table 1. It can be concluded that the theoretical results of Λ -binding energy and differential cross-section are well in agreement with the experimental results of the KEK.

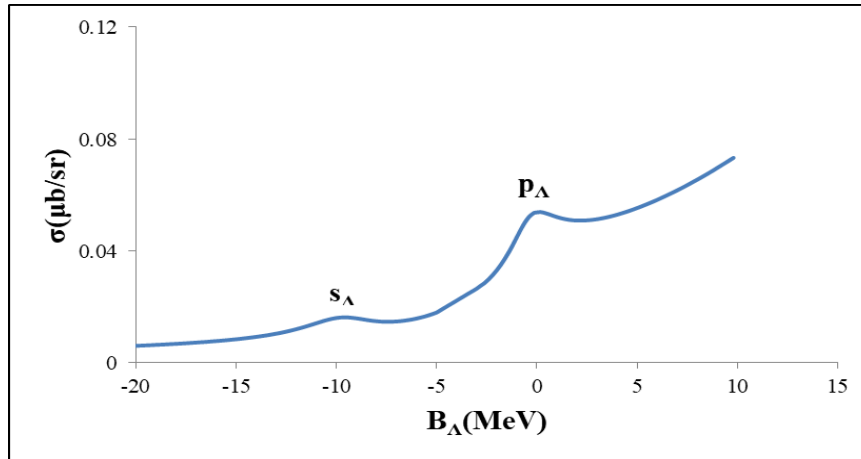


Figure 7. Calculated Results of Single Λ -Binding Energy and Differential Cross-section for $^{10}\text{B}(\pi^+, \text{K}^+)_{\Lambda}^{10}\text{B}$ Reaction

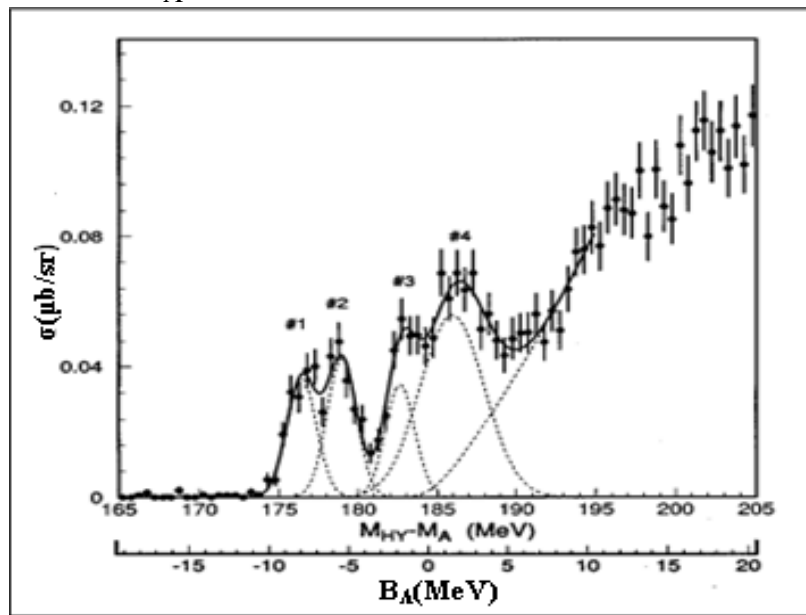


Figure 8. Experimental Results of Single Λ -Binding Energy and Differential Cross-section for $^{10}\text{B}(\pi^+, \text{K}^+)_{\Lambda}^{10}\text{B}$ Reaction.

Table 1. The Comparison with the Calculated Theoretical Results and the Experimental Results of KEK for the Λ -Binding Energy and Differential Cross-section of $^{10}\text{B}(\pi^+, \text{K}^+)_{\Lambda}^{10}\text{B}$ Reaction.

$^{10}\text{B}(\pi^+, \text{K}^+)_{\Lambda}^{10}\text{B}$ Reaction				
	BE(MeV)		Differential Cross-section (σ) ($\mu\text{b}/\text{sr}$)	
Peaks	s_{Λ}	p_{Λ}	s_{Λ}	p_{Λ}
Calculated Results	-9.7	0.2	0.017	0.053
Experimental Results (KEK)[6]	-9.1 ± 0.1	0.19 ± 0.2	0.017 ± 0.2	0.057 ± 0.14

Single Lambda Binding Energy and Differential Cross-section for $^{12}\text{C}(\pi^+, \text{K}^+)_{\Lambda}^{12}\text{C}$ Reaction

In $^{12}\text{C}(\pi^+, \text{K}^+)_{\Lambda}^{12}\text{C}$ reaction, the calculated theoretical spectrum shows the two clear peaks of the Λ -binding energy for $s_{\Lambda} = -10.9$ MeV, $p_{\Lambda} = -0.6$ MeV and differential cross-section for $s_{\Lambda} = 0.166$ $\mu\text{b}/\text{sr}$, $p_{\Lambda} = 0.168$ $\mu\text{b}/\text{sr}$ which are shown in figure 9.

The KEK experimental results of the ground state of the single Λ -binding energy at $B_{\Lambda} = -10.8 \pm 0.1$ MeV and the excitation state of the single Λ -binding energy at $B_{\Lambda} = -0.1 \pm 0.2$ MeV and the ground state of the values of differential cross-section at $\sigma = 0.17 \pm 0.02$ $\mu\text{b}/\text{sr}$ and the excitation state at $\sigma = 0.19 \pm 0.02$ $\mu\text{b}/\text{sr}$ are shown in figure 10.[6]

The comparison with the calculated theoretical results and the experimental results of KEK for the Λ -binding energy and differential cross-section of $^{12}\text{C}(\pi^+, \text{K}^+)_{\Lambda}^{12}\text{C}$ reaction are shown in table 2. The calculated theoretical results of Λ -binding energy and differential cross-section are well in agreement with the experimental results of the KEK.

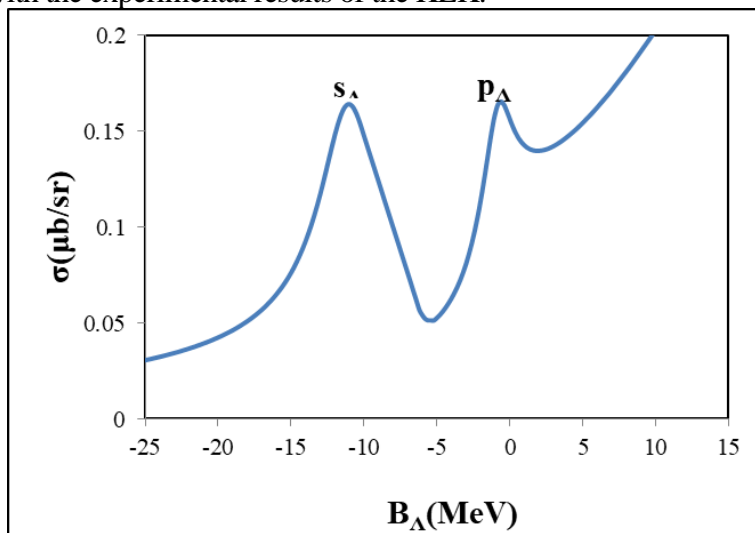


Figure 9. Calculated Results of Single Λ -Binding Energy and Differential Cross-section for $^{12}\text{C}(\pi^+, \text{K}^+)_{\Lambda}^{12}\text{C}$ Reaction

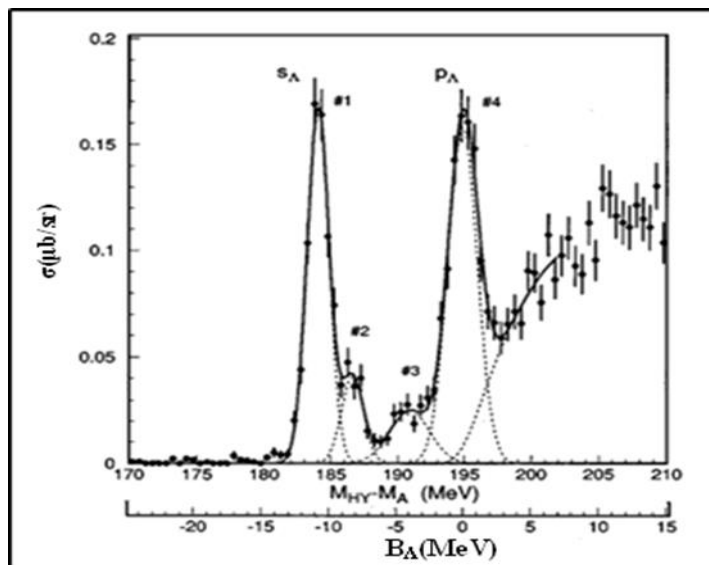


Figure 10. Experimental Results of Single Λ -Binding Energy and Differential Cross-section for $^{12}\text{C}(\pi^+, \text{K}^+)_{\Lambda}^{12}\text{C}$ Reaction

Table 2. The Comparison with the Calculated Theoretical Results and the Experimental Results of KEK for the Λ -Binding Energy and Differential Cross-section of $^{12}\text{C}(\pi^+, \text{K}^+)_{\Lambda}^{12}\text{C}$ Reaction.

$^{12}\text{C}(\pi^+, \text{K}^+)_{\Lambda}^{12}\text{C}$ Reaction				
	BE(MeV)		Differential Cross-section (σ) ($\mu\text{b}/\text{sr}$)	
	s_{Λ}	p_{Λ}	s_{Λ}	p_{Λ}
Peaks	s_{Λ}	p_{Λ}	s_{Λ}	p_{Λ}
Calculated Results	-10.9	-0.6	0.166	0.168
Experimental Results (KEK)[6]	-10.8 ± 0.1	-0.1 ± 0.2	0.17 ± 0.02	0.19 ± 0.02

Single Lambda Binding Energy and Differential Cross-section for $^{28}\text{Si}(\pi^+, \text{K}^+)_{\Lambda}^{28}\text{Si}$ Reaction

In $^{28}\text{Si}(\pi^+, \text{K}^+)_{\Lambda}^{28}\text{Si}$ reaction, the calculated theoretical spectrum shows the two clear peaks of the Λ -binding energy for $s_{\Lambda} = -16.8$ MeV, $p_{\Lambda} = -7.2$ MeV, $d_{\Lambda} = 1.1$ MeV and differential cross-section for $s_{\Lambda} = 0.0138$ $\mu\text{b}/\text{sr}$, $p_{\Lambda} = 0.037$ $\mu\text{b}/\text{sr}$, $d_{\Lambda} = 0.046$ $\mu\text{b}/\text{sr}$ which are shown in figure 11.

The KEK experimental results of the ground state of the single Λ -binding energy at $B_{\Lambda} = -16.6 \pm 0.2$ MeV, -7.0 ± 0.2 MeV and the excitation state of the single Λ -binding energy at $B_{\Lambda} = 1.0 \pm 0.8$ MeV and the ground state of the values of differential cross-section at $\sigma = 0.09 \pm 0.01$ $\mu\text{b}/\text{sr}$, 0.027 ± 0.05 $\mu\text{b}/\text{sr}$ and the excitation state at $\sigma = 0.051 \pm 0.016$ $\mu\text{b}/\text{sr}$ are shown in figure 12.[6]

The comparison with the calculated theoretical results and the experimental results of KEK for the Λ -binding energy and differential cross-section of $^{28}\text{Si}(\pi^+, \text{K}^+)_{\Lambda}^{28}\text{Si}$ reaction are shown in table 3. The calculated theoretical results of Λ -binding energy and differential cross-section are well in agreement with the experimental results of the KEK.

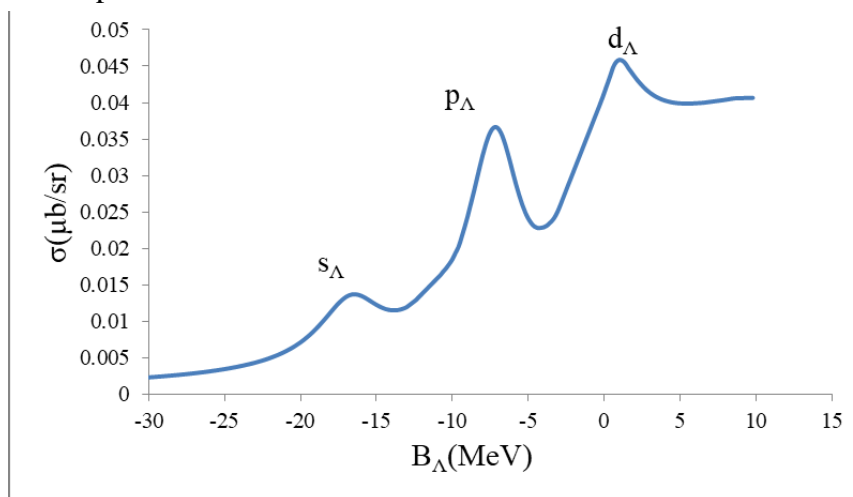


Figure 11. Calculated Results of Single Λ -Binding Energy and Differential Cross-section for $^{28}\text{Si}(\pi^+, \text{K}^+)_{\Lambda}^{28}\text{Si}$ Reaction

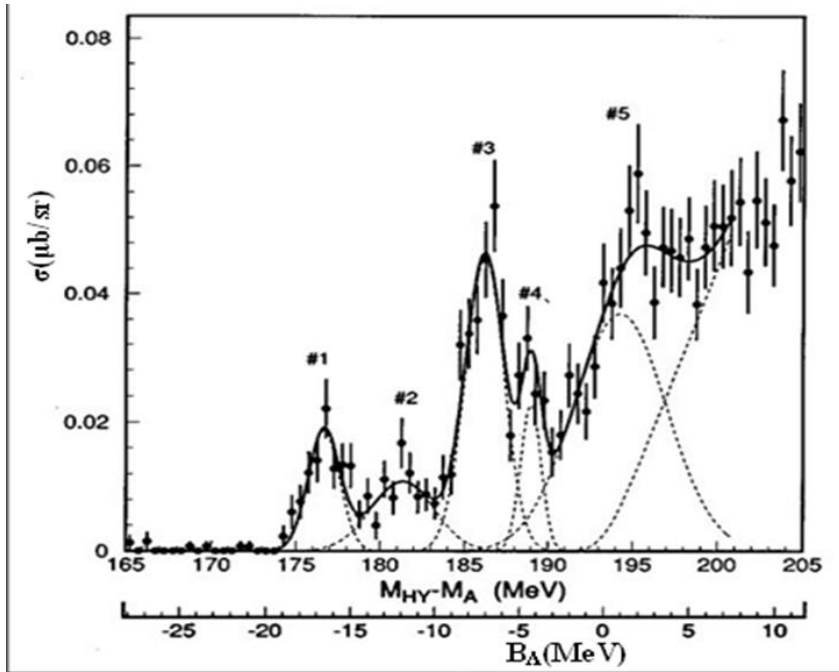


Figure 12. Experimental Results of Single Λ -Binding Energy and Differential Cross-section for $^{28}\text{Si}(\pi^+, \text{K}^+) ^{28}\text{Si}$ Reaction.

Table 3. The Comparison with the Calculated Theoretical Results and the Experimental Results of KEK for the Λ -Binding Energy and Differential Cross-section of $^{28}\text{Si}(\pi^+, \text{K}^+) ^{28}\text{Si}$ Reaction.

$^{28}\text{Si}(\pi^+, \text{K}^+) ^{28}\text{Si}$ Reaction						
Peaks	BE(MeV)			Differential Cross-section (σ) ($\mu\text{b}/\text{sr}$)		
	s_Λ	p_Λ	d_Λ	s_Λ	p_Λ	d_Λ
Calculated Results	-16.8	-7.2	1.1	0.0138	0.037	0.046
Experimental Results (KEK)[6]	-16.6 ± 0.2	-7.0 ± 0.2	1.0 ± 0.2	0.009 ± 0.01	0.027 ± 0.05	0.051 ± 0.016

Single Lambda Binding Energy and Differential Cross-section for $^{89}\text{Y}(\pi^+, \text{K}^+) ^{89}\text{Y}$ Reaction

In $^{89}\text{Y}(\pi^+, \text{K}^+) ^{89}\text{Y}$ reaction, the calculated theoretical spectrum shows the two clear peaks of the Λ -binding energy for $s_\Lambda = -22.99$ MeV, $p_\Lambda = -16.75$ MeV, $d_\Lambda = -9.72$ MeV, $f_\Lambda = -2.31$ MeV and differential cross-section for $s_\Lambda = 0.0078$ $\mu\text{b}/\text{sr}$, $p_\Lambda = 0.0409$ $\mu\text{b}/\text{sr}$, $d_\Lambda = 0.117$ $\mu\text{b}/\text{sr}$, $f_\Lambda = 0.141$ $\mu\text{b}/\text{sr}$ which are shown in figure 13.

The KEK experimental results of the ground state of the single Λ -binding energy at $B_\Lambda = -22.0 \pm 0.5$ MeV, -16.1 ± 0.3 MeV, -9.3 ± 0.4 MeV, -2.3 ± 0.3 MeV and the values of differential cross-section at $\sigma = 0.008 \pm 0.005$ $\mu\text{b}/\text{sr}$, 0.04 ± 0.01 $\mu\text{b}/\text{sr}$, 0.13 ± 0.04 $\mu\text{b}/\text{sr}$, 0.138 ± 0.05 $\mu\text{b}/\text{sr}$ are shown in figure 14.[6]

The comparison with the calculated theoretical results and the experimental results of KEK for the Λ -binding energy and differential cross-section of $^{89}\text{Y}(\pi^+, \text{K}^+)_{\Lambda}^{89}\text{Y}$ reaction are shown in table 4. The calculated theoretical results of Λ -binding energy and differential cross-section are well in agreement with the experimental results of the KEK.

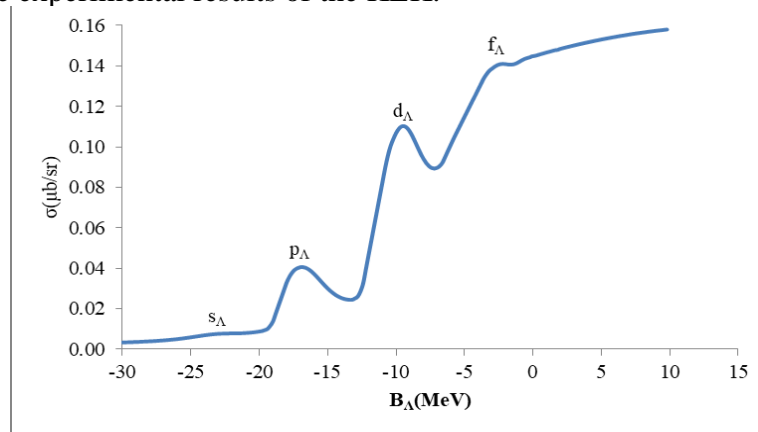


Figure 13. Calculated Results of Single Λ -Binding Energy and Differential Cross-section for $^{89}\text{Y}(\pi^+, \text{K}^+)_{\Lambda}^{89}\text{Y}$ Reaction

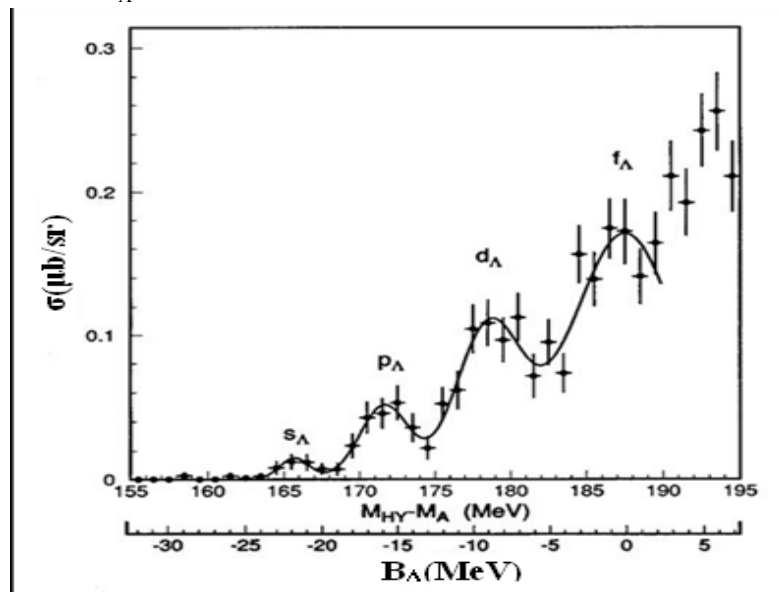


Figure 14. Experimental Results of Single Λ -Binding Energy and Differential Cross-section for $^{89}\text{Y}(\pi^+, \text{K}^+)_{\Lambda}^{89}\text{Y}$ Reaction

Table 4. The Comparison with the Calculated Theoretical Results and the Experimental Results of KEK for the Λ -Binding Energy and Differential Cross-section of $^{89}\text{Y}(\pi^+, \text{K}^+)_{\Lambda}^{89}\text{Y}$ Reaction.

$^{89}\text{Y}(\pi^+, \text{K}^+)_{\Lambda}^{89}\text{Y}$ Reaction				
State	BE(MeV)		Differential Cross-section (σ) ($\mu\text{b}/\text{sr}$)	
	Calculated Results (MeV)	KEK Experimental Results (MeV)[6]	Calculated Results ($\mu\text{b}/\text{sr}$)	KEK Experimental Results ($\mu\text{b}/\text{sr}$) [6]
s_{Λ}	-22.99	-22.0 ± 0.5	0.0078	0.008 ± 0.005
p_{Λ}	-16.75	-16.1 ± 0.3	0.0409	0.04 ± 0.01
d_{Λ}	-9.72	-9.3 ± 0.4	0.117	0.13 ± 0.04
f_{Λ}	-2.31	-2.3 ± 0.3	0.141	0.138 ± 0.05

Conclusion

In this paper, the single lambda energy levels of Λ -hypernuclei have been analyzed. The two-body Schrödinger equation of second order differential form is solved by Numerov's Method and Taylor Series. The energy eigen values for various spin states are carried out by using Fortran-2019 program. Moreover, the energy levels diagrams for ${}^{10}_{\Lambda}\text{B}$, ${}^{12}_{\Lambda}\text{C}$, ${}^{28}_{\Lambda}\text{Si}$ and ${}^{89}_{\Lambda}\text{Y}$ have been computed using Woods-Saxon potential. It is found that the more nuclear mass number, the less lambda single-particle energies in Λ -hypernucleus. Furthermore, it can be concluded that the calculated theoretical results of Λ -binding energy and differential cross-section are well in agreement with the experimental results of KEK.

Acknowledgements

I would like to express my deeply thanks to Dr Kyaw Kyaw Naing, my respectable teacher in DSA, because of helping me throughout this research paper and Dean of Faculty of Physics and Head of Physics Department of Defence Services Academy because of giving opportunity to read this paper in MAAS 2023.

References

- Amaku M., Coutinho F. A. B. and Toyama F. M., "The Normalization of Wavefunctions of the Continuous Spectrum" August 17, 2019.
- Amsler, C; et al., "Review of Particle Physics" 2008.
- Ananthanarayan, B. and Shayan Ghosh , "Pion Interactions and the Standard Model at High Precision" Centre for High Energy Physics, December, 2018.
- Boyer, C. and Merzbach, U., "A History of Mathematics", 1991.
- Daniel Schroeder V., "The Radial Equation", January, 2022.
- Hasegawa, T; et al; "Spectroscopic Study of ${}^{10}_{\Lambda}\text{B}$, ${}^{12}_{\Lambda}\text{C}$, ${}^{28}_{\Lambda}\text{Si}$, ${}^{89}_{\Lambda}\text{Y}$, ${}^{139}_{\Lambda}\text{La}$ and ${}^{208}_{\Lambda}\text{Pb}$ by the (π^+, K^+) Reactions", March, 1996.
- Herbert Goldstein, Charles P. Pille, JR. and John L. Safko, "Classical Mechanics", Third Edition, 2000.
- Hervé Abdi, "The Eigen-Decomposition: Eigenvalues and Eigenvectors", 2007.
- Jackson, C. D., "Classical Electrodynamics", John Wiley and Sons, 1962.
- Povh, B., "Hyperon in Nuclei", May, 1976.
- Schsierz, N., Wiedenhover, I. and Volya, A., "Parameterization of the Woods-Saxon Potential for Shell-Model Calculations", 2007.
- Wasserman Eric, W., "Eigenfunction", 2016.
- Zyla, P.A; et al., "Review of Particle Physics", 2020.

CLOUD BASED REAL-TIME AIR QUALITY AND ENVIRONMENTAL PARAMETERS MONITORING AND LOGGING SYSTEM

Khin Moh Moh Tin¹

Abstract

Cloud based real-time air quality and environmental parameters monitoring and logging system is based on the internet of things (IoT) using the ESP32 board which can process sensor data and upload them to cloud via internet. The system is based on **MQTT protocol** using ESP32, **BME680 integrated environmental sensor**, BH1750 light intensity sensor and UV sensor. The readings from all sensors are processed by the ESP32 board and uploaded to the ThingSpeak cloud. The real-time parameters are also displayed on the TFT LCD as well as serial monitor. The data collected in ThingSpeak cloud can be exported in .csv format. This research highlights the benefits of the advanced cloud-based technology which effectively reduce time and energy waste for human labor.

Keyword: MQTT protocol, ThingSpeak cloud, .csv format

Introduction

In this cloud-based real-time air quality and environmental parameters monitoring and logging system, the air quality and environmental parameters from the surrounding environment or of a particular location is measured with the help of some sensors and then the collected data will be stored on a server after being processed by a microcontroller. The daily activities are inseparable from weather conditions and various environmental factors. The real-time data collected can be used in research and analysis and the results can be helpful in human life and for improving environmental conditions as well.

The application of this environmental parameters monitoring system can also play an important role in the field of agriculture to increase productivity, research application, and reducing manpower. Sometimes in a particular agricultural zone that is hazardous for a human being, it is quite difficult to manually monitor the environment or weather conditions. In such cases, this cloud-based environmental parameter monitoring and logging system can be of great importance. The functional block diagram of the system is shown in Figure 1.

¹ Department of Physics, Taunggyi University

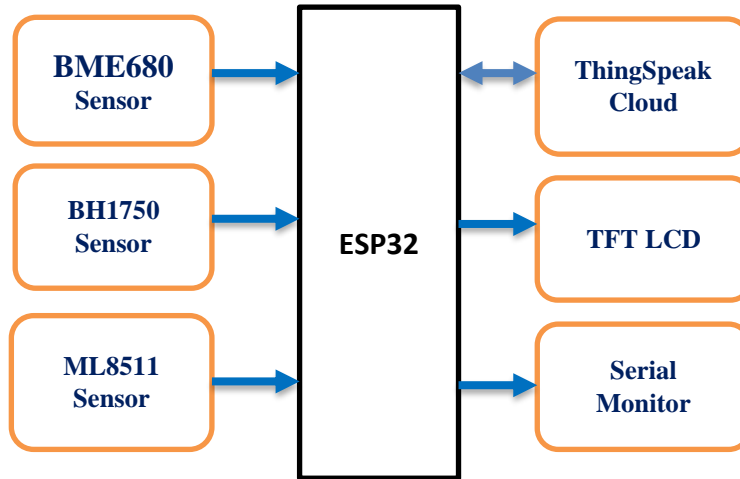


Figure 1. Functional block diagram of the system

Materials and Methods

Constructed system consists of the hardware and software sections. In hardware section, an ESP-WROOM 32 board, BME680 environmental parameter sensor, BH1750 light sensor, LM8511 UV sensor and TFT_LCD (thin-film transistor liquid crystal display) are used. The softwares are the Arduino IDE Software and ThingSpeak cloud.

ESP-WROOM 32

ESP-WROOM 32 microcontroller board composes of the high-speed dual core processor attached with Wi-Fi, Bluetooth classic and Bluetooth low energy (BLE). The cores are protocol CPU (PRO_CPU) and application CPU (APP_CPU). The CPU clock frequency is adjustable from 80 MHz to 240 MHz. The ESP32 also includes a variety of peripherals such as GPIO, I2C, SPI, UART, ADC, CAN, etc which makes it easy to interface with other devices. Photograph of ESP-WROOM 32 microcontroller board is shown in Figure 2.



Figure 2. Photograph of ESP-WROOM 32 microcontroller board

BME680 Environmental Data Sensor

BME680 is the environmental digital sensor which detects gas resistance, temperature, pressure and humidity. The altitude can be approximately determined by knowing atmospheric pressure. Similarly, dew point temperature can be measured using values of temperature and humidity. BME 680 also composes of metal oxide sensor which detects the volatile organic compounds (VOC) such as ethanol, alcohol and carbon monoxide. The resistance of the heated metal oxide sensor is changed due to the amount of VOC in air. Therefore, indoor air quality (IAQ) can be classified according to the quantitative performance of VOC in air. The Figure 3 shows the BME680 sensor module.

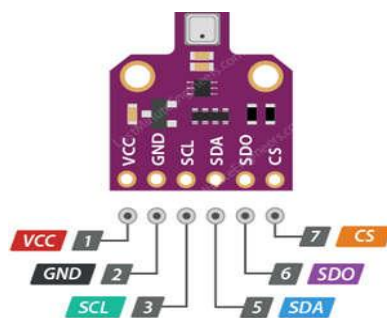


Figure 3. BME680 sensor module

ML8511 UV Sensor

The ML8511 is UV sensor is composed of an internal trans-impedance amplifier that converts photo-current flowing through photo-diode to voltage due to the amount of UV intensity. This unique feature is solution to measure the UV intensity. The relative responsibility of sensor is effective within the wavelength of 280nm and 400nm. The ML8511 UV sensor is shown in Figure 4.

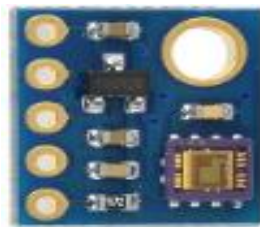


Figure 4. The ML8511 UV sensor

BH1750 Light Sensor

BH1750 is a digital ambient light sensor which can measure light intensity. It consists of photo-diode, amplifier and ADC. The photo-diode is effectively responsive in the visible region. When the ambient light is falling on it, photo-diode produces the current. This photo-current is

converted to analog voltage by using the op-amp amplifier. The analog voltage signal is also converted to 16-bit digital data by means of ADC unit. Figure 5 shows the BH1750 light sensor.

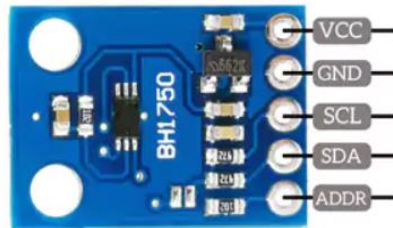


Figure 5. BH1750 Light intensity sensor

2.8" TFT LCD - Thin Film Transistor Liquid Crystal Display

ELT240320ATP is a transmissive type color active matrix liquid crystal display (LCD) which uses amorphous thin film transistor (TFT) as switching devices. This product is composed of a TFT LCD panel, a drive IC, a FPC, and a WLED-backlight unit. The active display area is 2.8 inches diagonally measured and the native resolution is 240*RGB*320. Photograph of TFT LCD is shown in Figure 6.

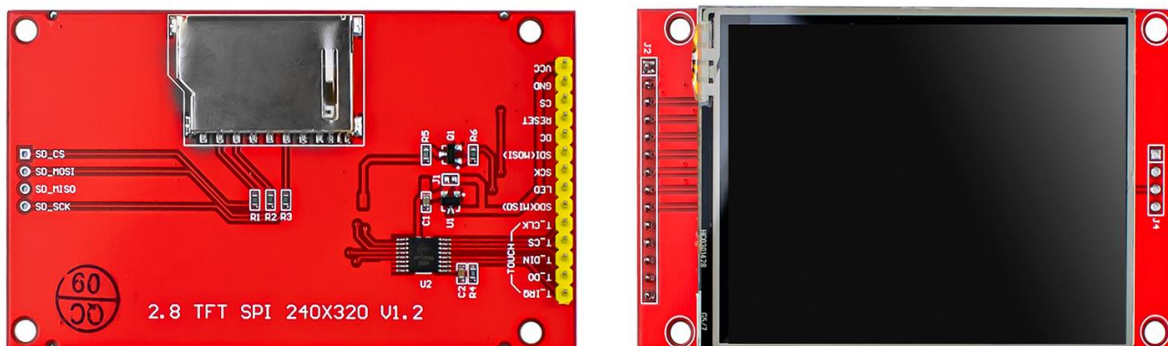


Figure 6. Photograph of TFT LCD

Arduino Integrated Development Environment (Arduino Software IDE)

The Arduino Integrated Development Environment or Arduino Software (IDE) contains a text editor for writing code, a message area, a text console, a toolbar with buttons for common functions and a series of menus. It connects to the Arduino hardware to upload programs and communicate with them.

ThingSpeak Cloud

ThingSpeak cloud server is a place where one can store data online and can access that data at any time and from anywhere in the world. A real-time data is created with the help of a web-server. ThingSpeak web service provided by MathWorks which allows us to send sensor readings to the cloud. The ThingSpeak is an open-source data platform for the Internet of Things

(IoT) applications. We can also visualize and act on or access the data (calculate the data) sent to the ThingSpeak server from ESP32. ThingSpeak is frequently used for IoT prototyping and proof-of-concept systems that require analytics.

Hardware Preparation

This research is based on the environmental data acquisition system using internet of thing (IoT) technology. BH1750sensor, BME680 sensor and ML 8511 sensor are used in this research. ESP32 implements two functions; one is data detection and logging like a microcontroller and another is data uploaded to cloud via internet. The schematic circuit diagram is drawn by easyEDA software as shown in Figure 7.

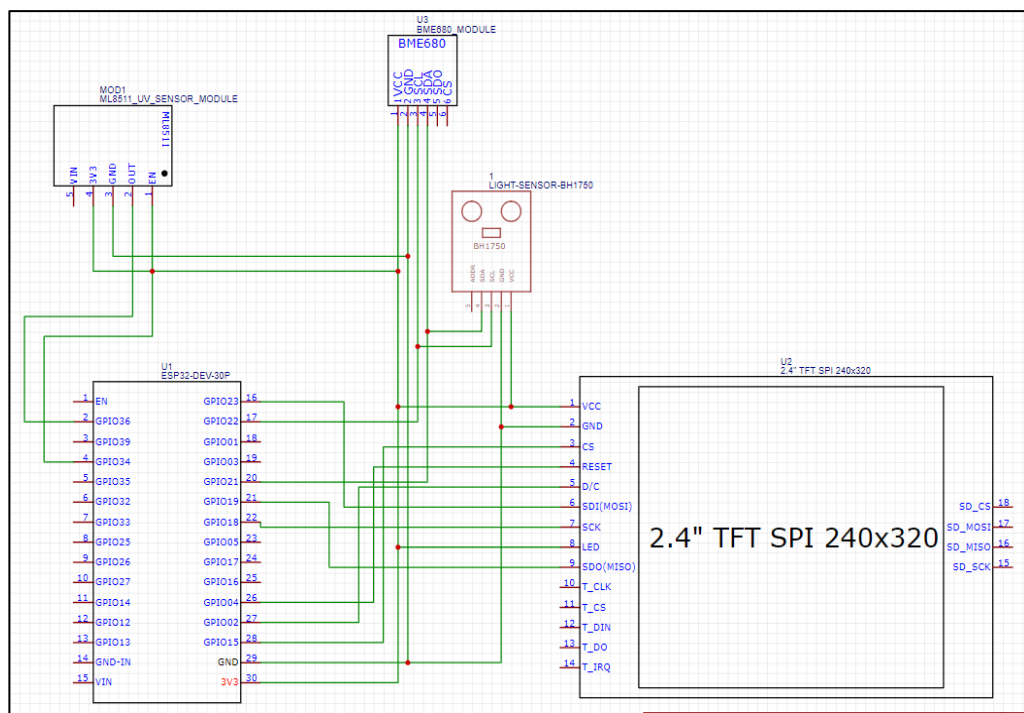


Figure 7. Circuit diagram of constructed system

Software Preparation

ESP32 is used because it composes of the microcontroller which is integrated with Wi-Fi module to communicate the cloud via internet. Although the Arduino IDE software is compatible for ESP32. The libraries of ThingSpeak, ESP32, BME680, BH1750 and TFT_LCD are included in Arduino IDE. The whole system of flow chart is illustrated in Figure 8.

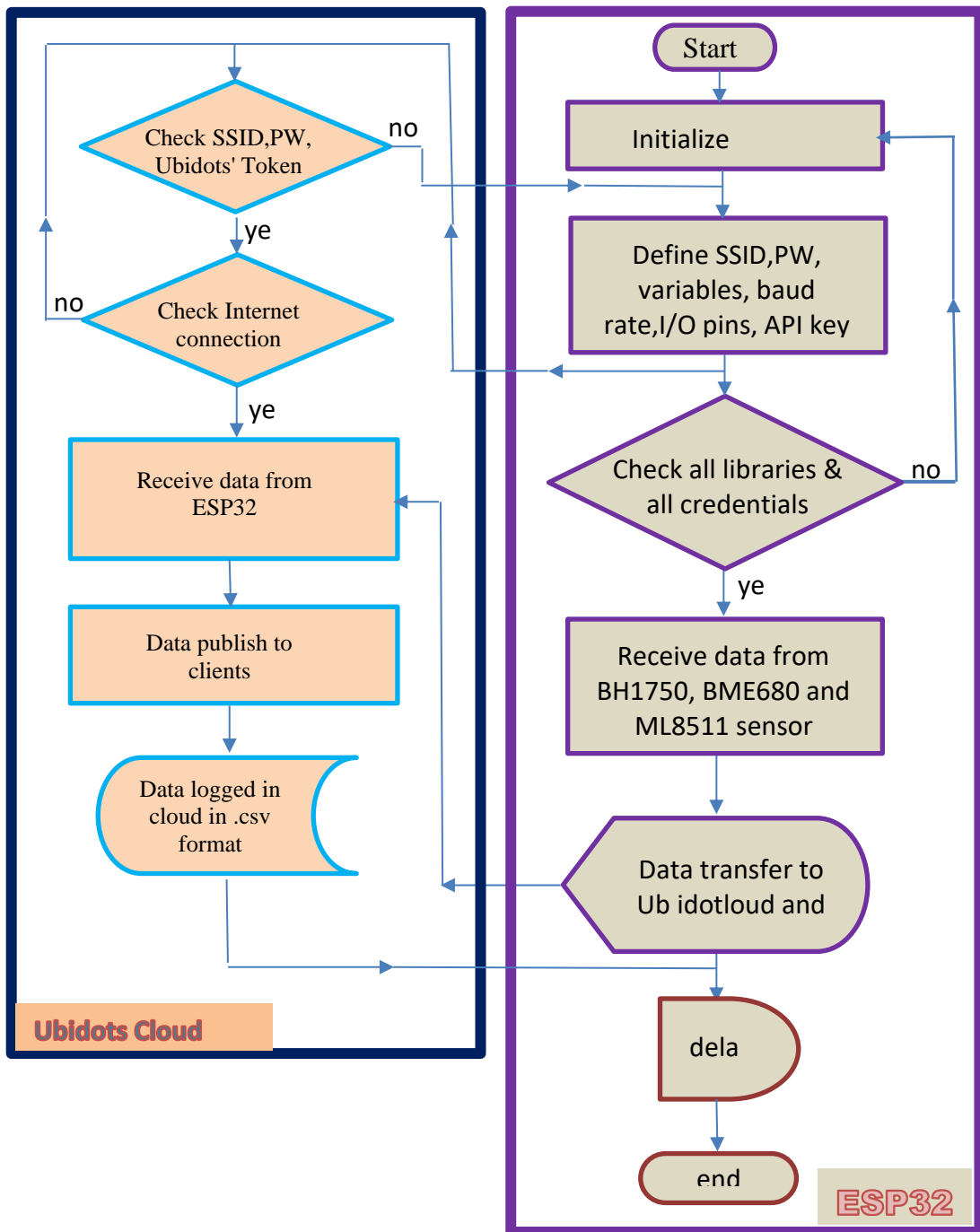


Figure 8. Software flow chart

Results

The eight different environmental conditions which include temperature, humidity, pressure, altitude, light intensity, UV index, gas resistance and IAQ (indoor air quality) were observed. The sensor data collected by ESP32 from BME680, BH1750 and LM8511 sensors is published to the ThingSpeak web server. A channel was created on ThingSpeak that contains eight fields to store eight different environmental parameters. Figure 9 shows the system location. The ‘Field 1’ which was containing the temperature readings published or communicated from the ESP32 module and saved on the ThingSpeak server as in Figure 10.

Similarly, fields 2, 3, 4,5,6,7 and 8 are displaying the humidity, pressure, altitude, light intensity, UV index, gas resistance and IAQ respectively were shown in Figure 11 to 17.

The serial monitor displayed the **temperature** in degree Celcius, **humidity** in percentage, atmospheric **pressure** in hPa, **altitude** in meters, **dew Point** in degree Celcius and **gas** as a **resistance value**. The sensor is used to obtain the so-called gas resistance and then calculate an **Index of Air Quality (IAQ)** from a combination of humidity and the gas content readings of the air. UV intensity and Light intensity were also displayed in $mWcm^{-2}$ and lux respectively as in Figure 18. Complete circuit diagram with real-time results were displayed on TFT_LCD as in Figure 19. Live data from ThingSpeak cloud is shown in Table 1.

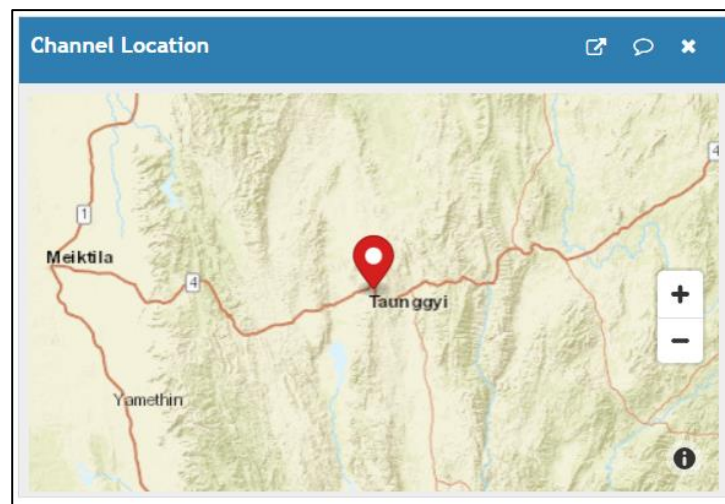


Figure 9. Sensor location

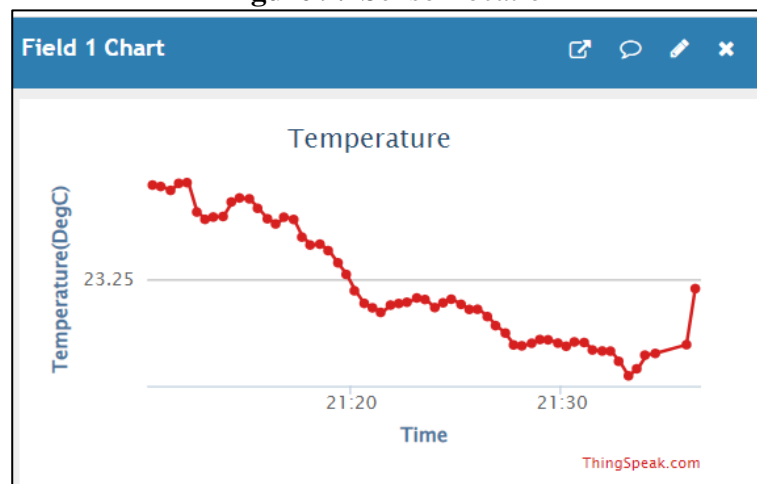


Figure 10. Live data of temperature (deg C)

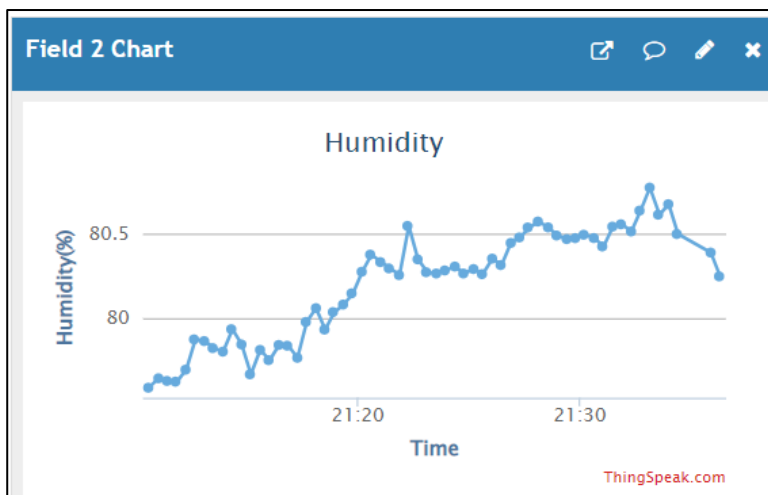


Figure 11. Live data of humidity (%)



Figure 12. Live data of pressure (hPa)

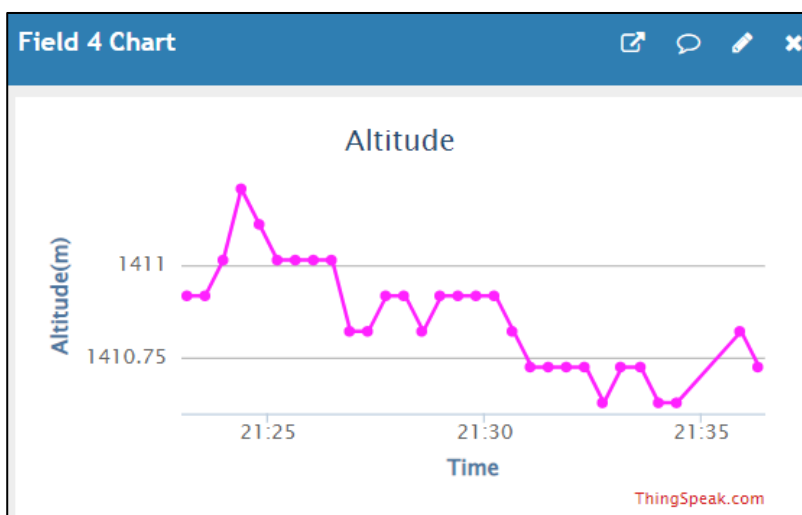


Figure 13. Live data of altitude (m)

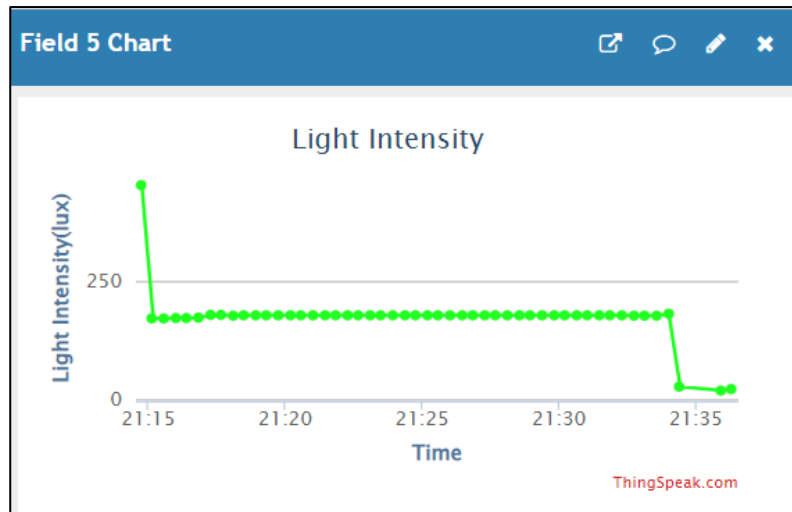


Figure 14. Live data of light intensity (lux)

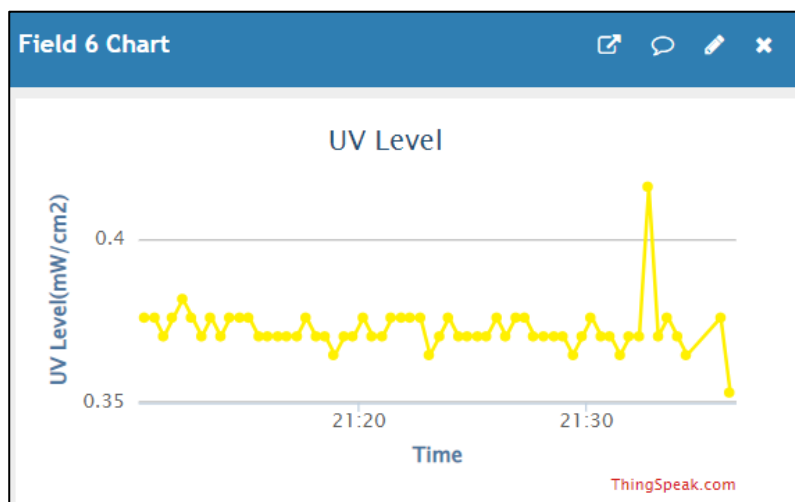


Figure 15. Live data of UV level ($\text{mW}\cdot\text{cm}^{-2}$)

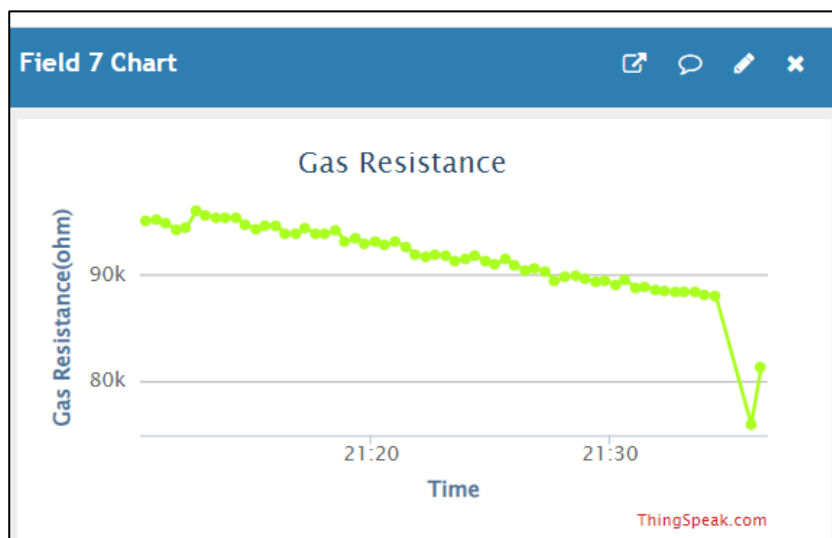


Figure 16. Live data of gas resistance (ohm)

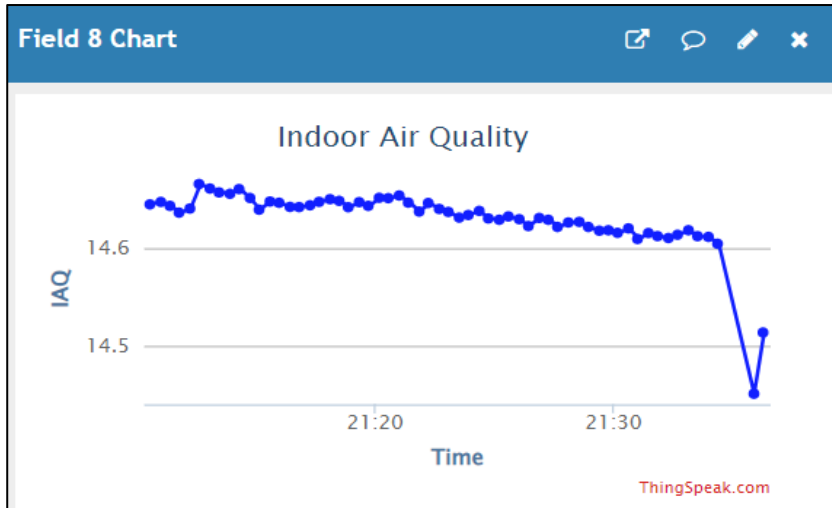


Figure 17. Live data of indoor air quality

```
COM7
21:40:40.321 -> IAQ = 14.62   IAQ: Good
21:40:40.321 ->
21:40:41.721 -> Channel updated successfully!
21:40:42.809 -> Temperature = 23.08 °C
21:40:42.809 -> Humidity = 80.08 %
21:40:42.809 -> Dew Point = 19.10 °C
21:40:42.809 -> Pressure = 854.89 hPa
21:40:42.809 -> Gas = 106.36 KOhms
21:40:42.809 -> Approx. Altitude = 1410.63 m
21:40:42.809 -> Light intensity =175.83lx
21:40:42.809 -> UV intensity =0.37 mW/cm^2
21:40:42.809 -> Gas Resistance =106.36 kOhms
21:40:42.854 -> IAQ = 14.78   IAQ: Good
```

Figure 18. Serial monitor display

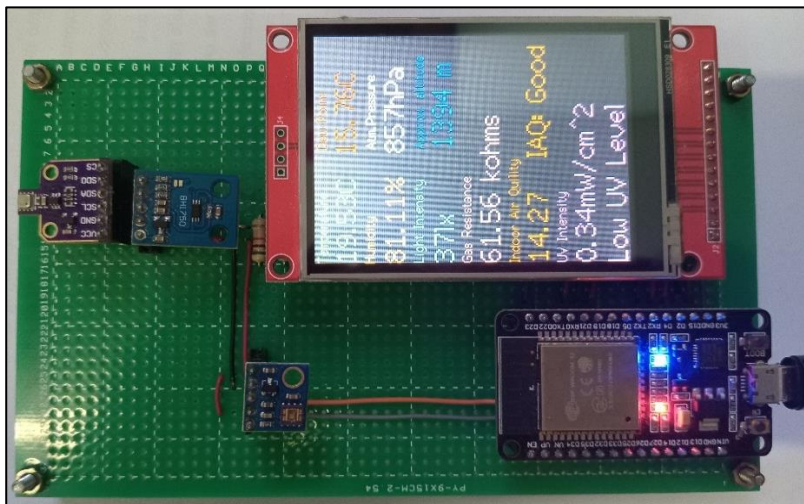


Figure 19. Complete circuit diagram with real-time data display on TFT_LCD.

Table 1. Live data (sample) from ThingSpeak cloud

created_at	entry id	Temp (degC)	Humidity (%)	Pressure (hPa)	Altitude (m)	Light Int(lux)	UV (mWcm ⁻²)	Gas res(Ω)	IAQ
2023-08-18 T15:58:04+06:30	1	26.36	73.79	84786	1478.02	153.33	0.46	22417	12.96
2023-08-18 T15:58:34+06:30	2	26.17	74.31	84790	1477.73	155.83	0.45	34298	13.41
2023-08-18 T15:58:59+06:30	3	26.09	74.37	84792	1477.54	126.67	0.45	46693	13.72
2023-08-18 T15:59:24+06:30	4	26.16	75.22	84790	1477.73	144.17	0.45	56456	13.95
2023-08-18 T15:59:50+06:30	5	26.20	74.14	84791	1477.73	140.83	0.45	65075	14.05
2023-12-12 T21:26:54+06:30	186	23.15	80.45	85486	1410.82	176.67	0.38	90613	14.63
2023-12-12 T21:27:19+06:30	187	23.13	80.48	85487	1410.82	176.67	0.38	90317	14.63
2023-12-12 T21:27:44+06:30	188	23.11	80.54	85487	1410.92	176.67	0.37	89443	14.62
2023-12-12 T21:28:10+06:30	189	23.10	80.58	85486	1410.92	176.67	0.37	89829	14.63
2023-12-12 T21:28:35+06:30	190	23.11	80.54	85488	1410.82	176.67	0.37	89927	14.63

Discussion

The benefits of using BME680, BH1750 and ML8511 sensor are as follows: (i) Air quality monitoring, (ii) Warning system for high temperature and low-humidity condition, (iii) Altitude tracking and calories expenditure for sports activities, (iv) Solar radiation monitoring, (v) UV index monitoring and (vi) Advanced-protecting the impact of UV radiation. BME680 sensor can sense the quantity of VOC gas but cannot distinguish what kind of gases contained.

ThingSpeak is a versatile platform that simplifies the process of collecting, storing, analyzing, and visualizing IoT data, making it a valuable tool for IoT developers and businesses. Its ease of use, customization options, and integration capabilities contribute to its popularity in the IoT community.

Conclusion

The adoption of cloud-based real-time air quality and environmental parameters monitoring and logging systems has brought about significant advancements in the field of environmental data collection and analysis. These systems have demonstrated their ability to efficiently gather real-time data from diverse sources, offering unprecedented insights into our surroundings. By leveraging cloud technology, these solutions have overcome traditional limitations, enabling seamless data storage, analysis, and remote access. As technology continues to evolve, this system can anticipate further enhancements in these systems, leading to even more accurate, accessible, and actionable environmental data.

Acknowledgements

I would like to thank Rector Dr Kaythi Thin, Pro-rectors Dr Ko Ko Naing and Dr Aung Nay Myo, Taunggyi University, for their kind permission for this research work.

I would like to thank Professor Dr Khin Khin San, Head of Department of Physics, Professors Dr Aye Aye Mar and Dr Nwe Ni Aung, Taunggyi University, for their kind permission to carry out this work.

References

Babalola T.E, A. D. Babalola and M. S. Olokun, 2022, Development of an ESP-32 Microcontroller Based Weather Reporting Device , 22(11): 27-38; Article no.JERR.88570 ISSN: 2582-292

Gahiwad P, Pallewar M.G, (2023) Development of IOT Based Weather Monitoring & Reporting System, Volume 10, Issue 5 www.jetir.org (ISSN-2349-5162)

Megantoro P, Aldhama S.A, (2021), IoT-based weather station with air quality measurement using ESP32 for environmental aerial condition study, Vol. 19, No. 4, pp. 1316~1325

https://www.espressif.com/sites/default/files/documentation/esp32-wroom_32_datasheet_en.pdf

<https://www.etechnophiles.com/esp32-dev-board-pinout-specifications-datasheet-and-schematic/>

<https://how2electronics.com/uv-index-meter-esp32-uv-sensor-ml8511/>

<https://www.circuitschools.com/uv-index-meter-interfacing-arduino-or-esp32-with-ml8511/>

<https://www.elprocus.com/bh1750-specifications-and-applications/>

<https://wolles-elektronikkiste.de/en/bh1750fvi-gy-30-302-ambient-light-sensor/>

<https://components101.com/displays/2-4-tft-lcd-display>

<https://microcontrollerslab.com/2-4-tft-lcd-touch-screen-module/>

<https://how2electronics.com/weather-monitoring-on-esp32-with-tft-touch-display/>

<https://www.circuitschools.com/interfacing-bme680-with-arduino-also-measure-indoor-air-quality-index/>

<https://how2electronics.com/interfacing-arduino-bme680-integrated-environmental-sensor/>

https://www.espressif.com/sites/default/files/documentation/esp32_datasheet_en.pdf

<https://www.sparkfun.com/datasheets/LCD/ELT240320ATP.pdf>

<https://docs.arduino.cc/software/ide-v1/tutorials/arduino-ide-v1-basics>

DETERMINATION OF REFLECTION COEFFICIENTS OF THE PARALLEL-POLARIZED AND PERPENDICULARLY POLARIZED WAVES INCIDENT ON THE DIELECTRIC MATERIALS

Sa Nanda Aung¹, Ei Ei Phy², Yadanar Htwe³ and Myat Shwe Wah⁴

Abstract

Parallel-polarized and perpendicularly polarized waves are considered to be incident on the dielectric material. Reflection coefficients for these waves incident on some media (cotton, cotton seed oil, quartz, castor oil, wood (dry), wax, slate, ruby, silicon and salt) are studied by using Maxwell's equations. The variation of reflection coefficients with respect to the angles of incidence is also studied by using MATLAB computation software.

Keywords: Dielectric Materials, Reflection coefficients, Maxwell's equations, MATLAB computational software

Introduction

Maxwell's equations describe electromagnetic radiation as a transverse wave of oscillating electric and magnetic fields. The direction of the electric vibration is called the direction of polarization of the linearly polarized wave. An incident electromagnetic wave that approaches a plane interface between two different media generally will result in a transmitted wave in the second medium and a reflected wave in the first [3].

The fact that electromagnetic waves can be polarized is conclusive evidence that they are transverse waves. Interference and diffraction give evidence of their wave nature, but these effects do not differentiate between longitudinal and transverse waves. Sound waves, for example, are longitudinal and do show interference, but they cannot be polarized, only transverse waves can be polarized [1].

In this work, the variation of the reflection coefficient is studied for the perpendicularly polarized and parallel-polarized waves incident on the media of cotton, cotton seed oil, quartz, castor oil, wood(dry), wax, slate, ruby, silicon and salt [5].

Background Theory

Perpendicularly Polarized Wave Incident on Dielectric Material

A linearly polarized plane wave is obliquely incident on a boundary between two media. The electric field is perpendicular to the plane of incidence (the xy-plane) [4]. Perpendicularly polarized wave incident on a boundary between two media. The relation of reflection coefficient is obtained by using Boundary conditions.

$$\rho_{\perp} = \frac{\cos\theta_i - \sqrt{\left(\frac{\epsilon_2}{\epsilon_1}\right) - \sin^2\theta_i}}{\cos\theta_i + \sqrt{\left(\frac{\epsilon_2}{\epsilon_1}\right) - \sin^2\theta_i}} \quad (1)$$

where ϵ_1 = permittivity of the medium 1, ϵ_2 = permittivity of the medium 2,
 θ_i = angle of incidence,

¹ Department of Physics, West Yangon University, Yangon, Myanmar

² Department of Physics, West Yangon University, Yangon, Myanmar

³ Department of Physics, West Yangon University, Yangon, Myanmar

⁴ Department of Physics, West Yangon University, Yangon, Myanmar

Parallel-Polarized Wave Incident on Dielectric Media

Parallel-polarized wave is incident on the boundary between two media. Incident electric field E_i , reflected electric field E_r , and transmitted electric field E_t vectors are parallel to the plane of incidence (xy-plane)[2].

For lossless nonmagnetic dielectrics equation (2) becomes by using Boundary conditions.

$$\rho_{//} = \frac{-(\epsilon_2/\epsilon_1) \cos\theta_i + \sqrt{(\epsilon_2/\epsilon_1) - \sin^2\theta_i}}{(\epsilon_2/\epsilon_1) \cos\theta_i + \sqrt{(\epsilon_2/\epsilon_1) - \sin^2\theta_i}} \tag{2}$$

where ϵ_1 = permittivity of the medium 1, ϵ_2 = permittivity of the medium 2,

θ_i = angle of incidence

Computation of Variation of Reflection Coefficient for the Wave Incident on the Dielectric Materials

Reflection Coefficient for Perpendicularly Polarized Wave

By using equation (1), reflection coefficients (ρ_{\perp}) are calculated for various angles of incidence. Reflection coefficient (ρ_{\perp}) for cotton, cotton seed oil, quartz, castor oil, wood(dry), wax, slate, ruby, silicon and salt are shown in Table 1. Since medium 1 is air ($\epsilon_{r1} = 1$) and medium 2 is dielectric material, where $\frac{\epsilon_2}{\epsilon_1} = \frac{\epsilon_0 \epsilon_{r2}}{\epsilon_0 \epsilon_{r1}} = \epsilon_{r2}$ (ϵ_{r2} = relative permittivity of medium 2).

Table 1 Reflection coefficients for perpendicularly polarized waves

Angle of incidence	Cotton	Cotton seed oil	Quartz	Castor oil	Wood (dry)	Wax	Slate	Ruby	Silicon	Salt
θ_i	ϵ_{r2}									
	1.4	3.1	4.2	4.7	6	6.5	7.5	11.3	12	15
0	0.08	0.27	0.34	0.36	0.42	0.43	0.46	0.54	0.55	0.58
10	0.09	0.28	0.35	0.37	0.43	0.44	0.47	0.55	0.56	0.59
20	0.09	0.29	0.36	0.38	0.44	0.45	0.48	0.56	0.57	0.61
30	0.11	0.32	0.39	0.41	0.46	0.48	0.51	0.58	0.59	0.63
40	0.12	0.36	0.43	0.45	0.51	0.52	0.55	0.62	0.63	0.66
50	0.16	0.42	0.49	0.51	0.56	0.58	0.60	0.67	0.68	0.71
60	0.23	0.51	0.57	0.59	0.64	0.65	0.67	0.73	0.74	0.76
70	0.35	0.62	0.68	0.70	0.73	0.74	0.76	0.81	0.81	0.83
80	0.70	0.78	0.82	0.83	0.85	0.86	0.87	0.84	0.90	0.91
90	1.00	1.00	1.00	1.00	1.00	1.00	1.00	1.00	1.00	1.00

Reflection Coefficient for Parallel- Polarized Wave

By using equation (2), reflection coefficients ($\rho_{//}$) are calculated for various angles of incidence. Reflection coefficient ($\rho_{//}$) for cotton, cotton seed oil, quartz, castor oil, wood(dry), wax, slate, ruby, silicon and salt are shown in Table 2.

Table 2 Reflection coefficient for parallel-polarized waves

Angle of incidence	Cotton	Cotton seed oil	Quartz	Castor oil	Wood (dry)	Wax	Slate	Ruby	Silicon	Salt
θ_i	ϵ_{r2} 1.4	ϵ_{r2} 3.1	ϵ_{r2} 4.2	ϵ_{r2} 4.7	ϵ_{r2} 6	ϵ_{r2} 6.5	ϵ_{r2} 7.5	ϵ_{r2} 11.3	ϵ_{r2} 12	ϵ_{r2} 15
0	0.08	0.28	0.34	0.37	0.42	0.43	0.46	0.54	0.55	0.59
10	0.08	0.27	0.33	0.36	0.41	0.43	0.45	0.53	0.54	0.58
20	0.07	0.25	0.32	0.34	0.39	0.41	0.44	0.52	0.53	0.57
30	0.06	0.22	0.29	0.31	0.36	0.38	0.41	0.49	0.50	0.54
40	0.03	0.18	0.26	0.26	0.32	0.33	0.36	0.45	0.45	0.50
50	0.00	0.11	0.19	0.19	0.24	0.26	0.29	0.38	0.39	0.43
60	0.07	0.00	0.08	0.08	0.13	0.15	0.18	0.27	0.28	0.33
70	0.20	0.16	0.09	0.09	0.04	0.03	0.00	0.09	0.10	0.15
80	0.45	0.46	0.42	0.40	0.36	0.35	0.32	0.24	0.22	0.18
90	1.00	1.00	1.00	1.00	1.00	1.00	1.00	1.00	1.00	1.00

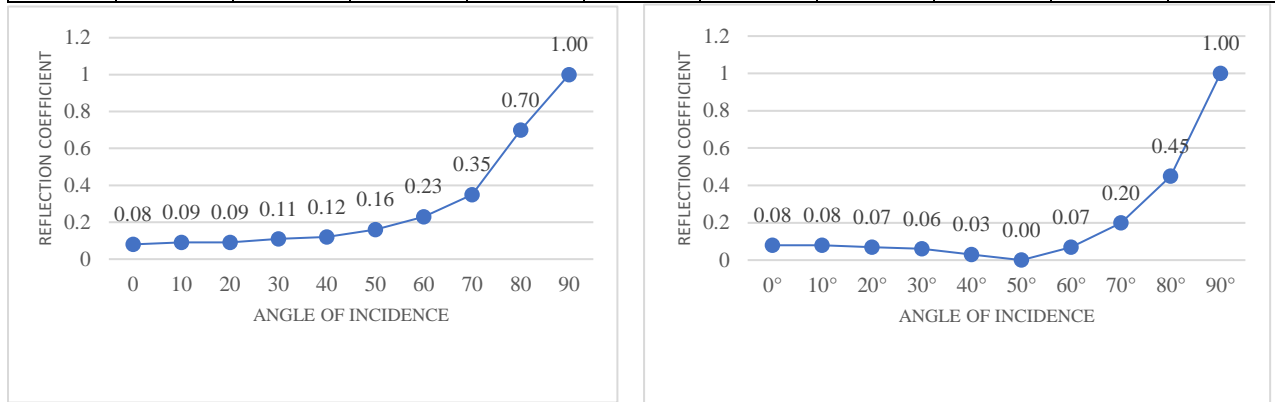


Figure 1 Variation of reflection coefficient with angles of incidence for cotton (Perpendicularly polarized wave and Parallel- polarized wave)

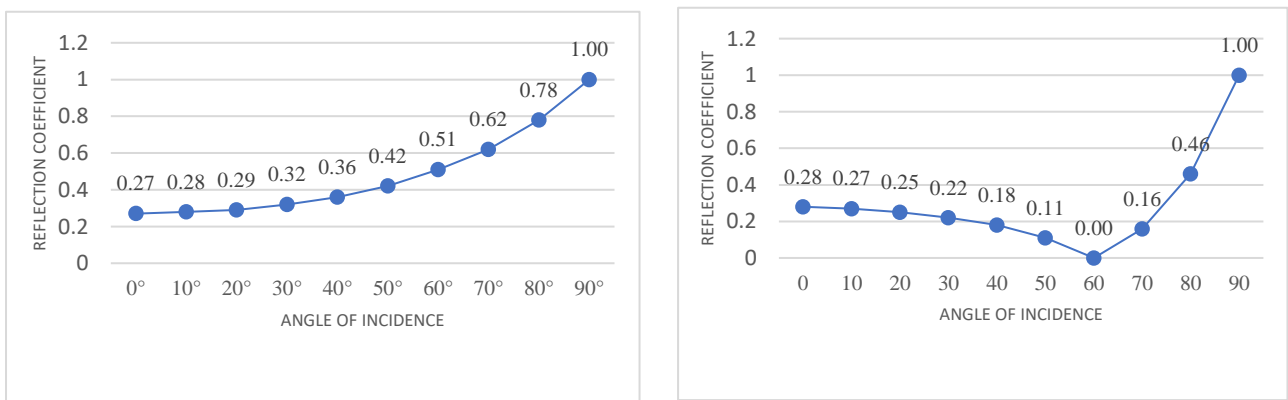


Figure 2 Variation of reflection coefficient with angles of incidence for cotton seed oil (Perpendicularly polarized wave and Parallel- polarized wave)

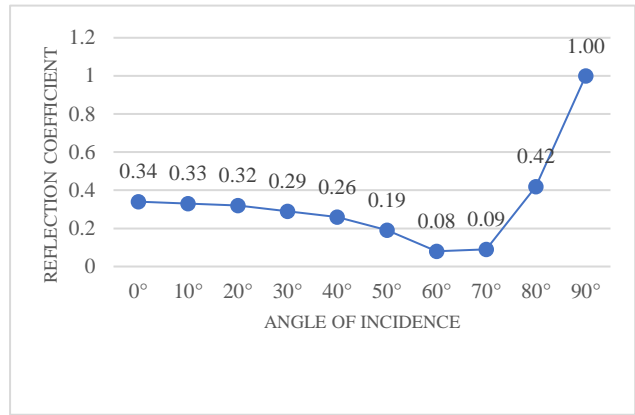
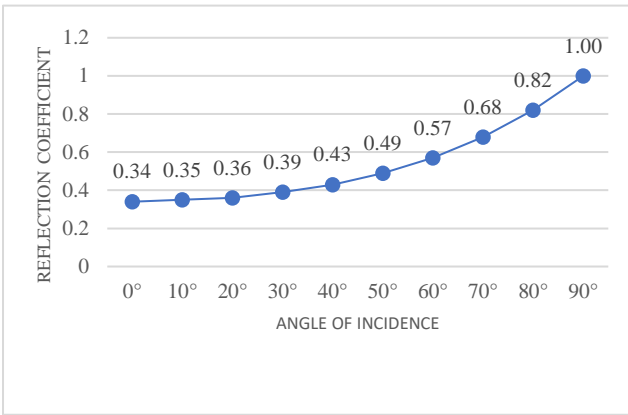


Figure 3 Variation of reflection coefficient with angles of incidence for quartz (Perpendicularly polarized wave and Parallel- polarized wave)

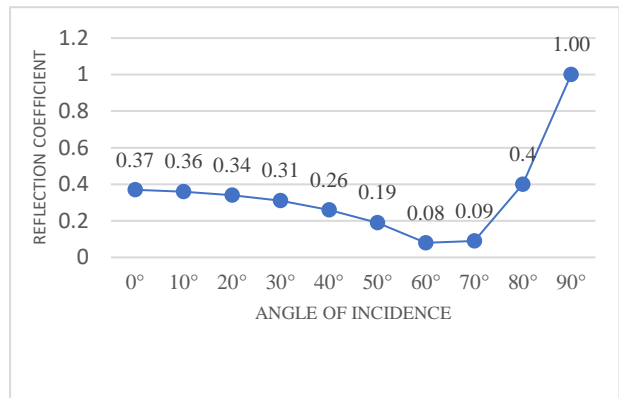
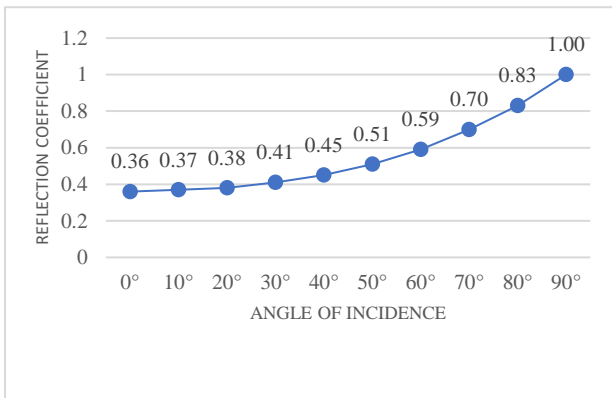


Figure 4 Variation of reflection coefficient with angles of incidence for castor oil (Perpendicularly polarized wave and Parallel- polarized wave)

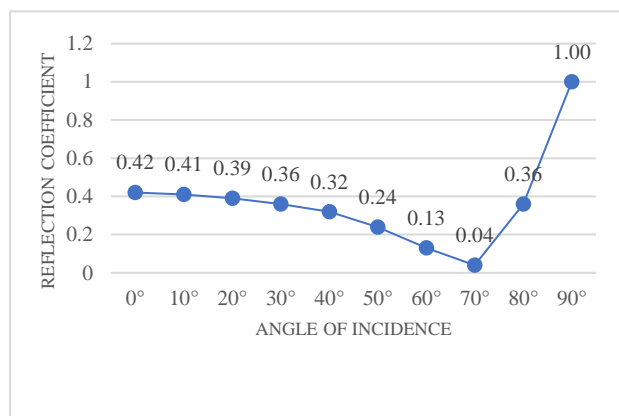
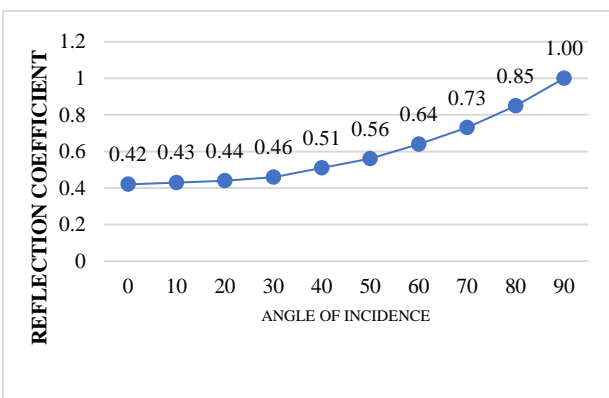


Figure 5 Variation of reflection coefficient with angles of incidence for wood (dry) (Perpendicularly polarized wave and Parallel- polarized wave)

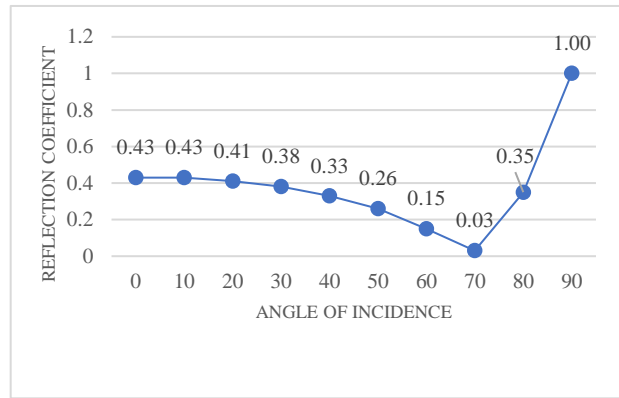
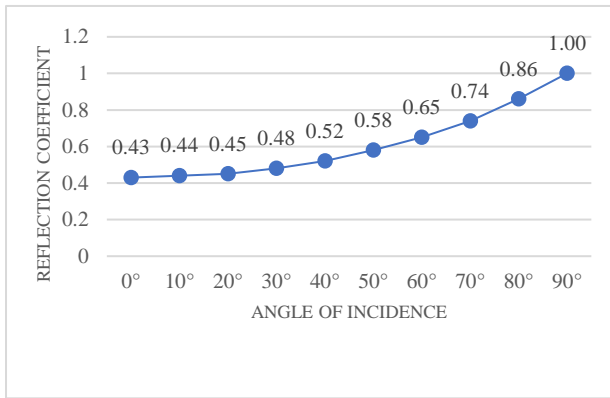


Figure 6 Variation of reflection coefficient with angles of incidence for wax (Perpendicularly polarized wave and Parallel- polarized wave)

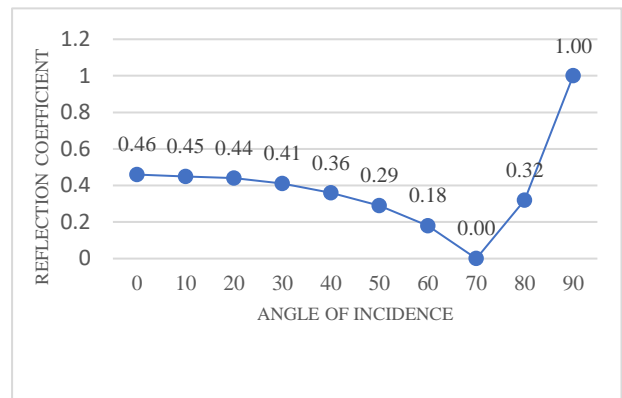
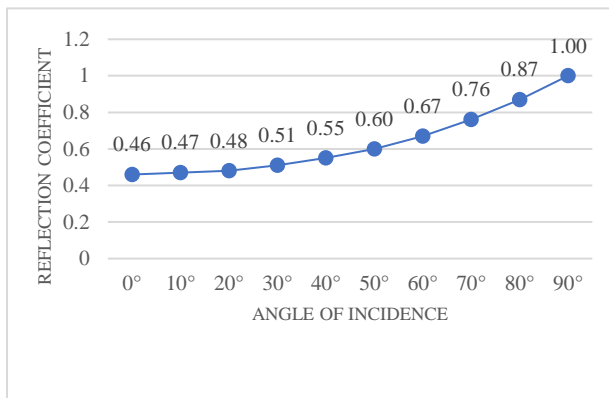


Figure 7 Variation of reflection coefficient with angles of incidence for slate (Perpendicularly polarized wave and Parallel- polarized wave)

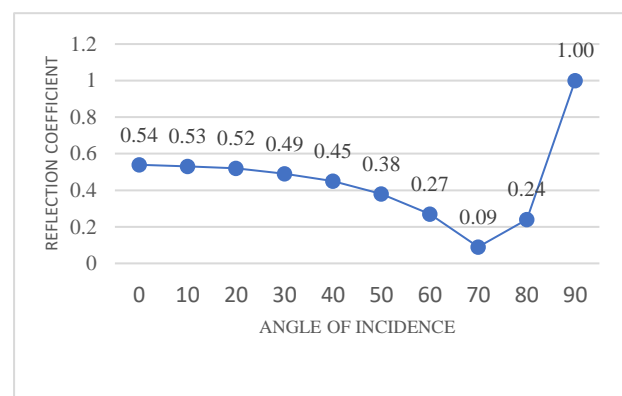
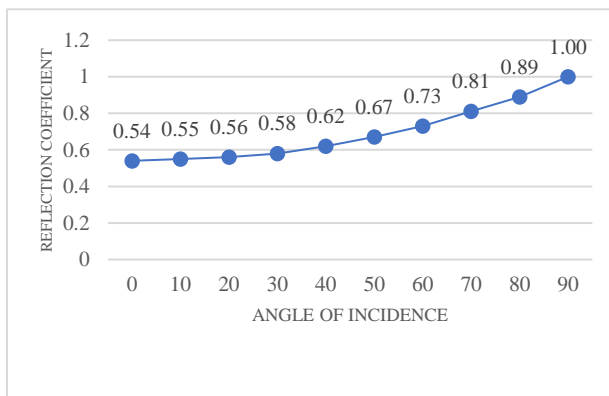


Figure 8 Variation of reflection coefficient with angles of incidence for ruby (Perpendicularly polarized wave and Parallel- polarized wave)

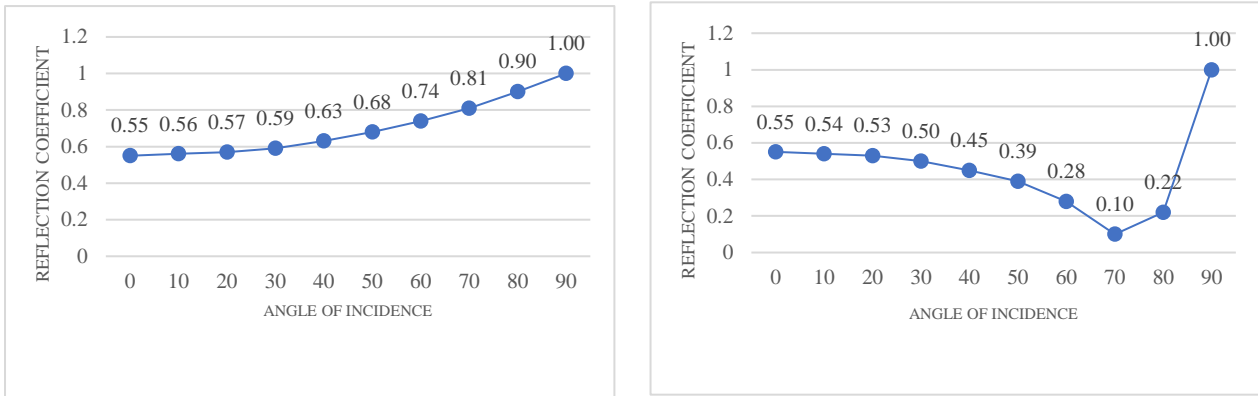


Figure 9 Variation of reflection coefficient with angles of incidence for silicon (Perpendicularly polarized wave and Parallel- polarized wave)

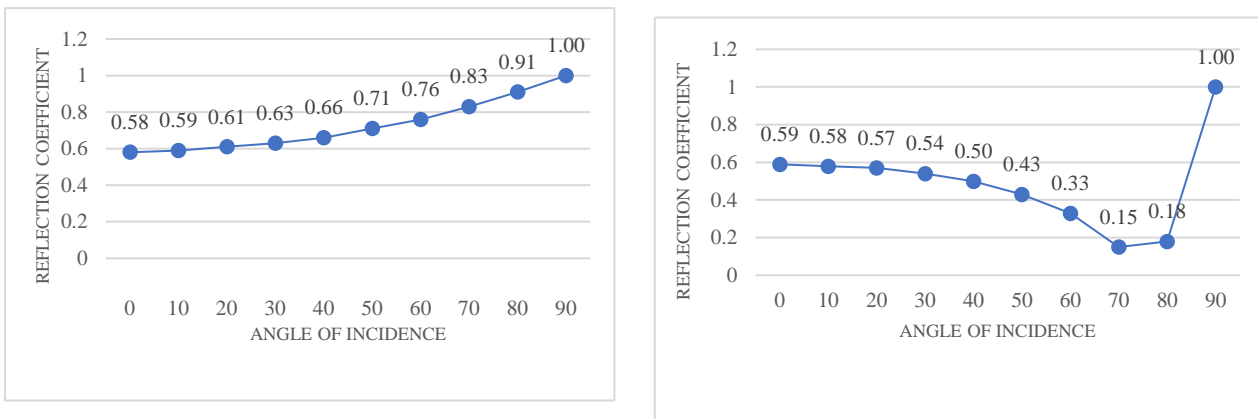


Figure 10 Variation of reflection coefficient with angles of incidence for salt (Perpendicularly polarized wave and Parallel- polarized wave)

The variation of reflection coefficient with angles of incidence for cotton, cotton seed oil, quartz, castor oil, wood (dry), wax, slate, ruby, silicon and salt for perpendicularly polarized wave and parallel- polarized wave were shown in Figure 1, 2,3,4,5,6,7,8,9 and 10.

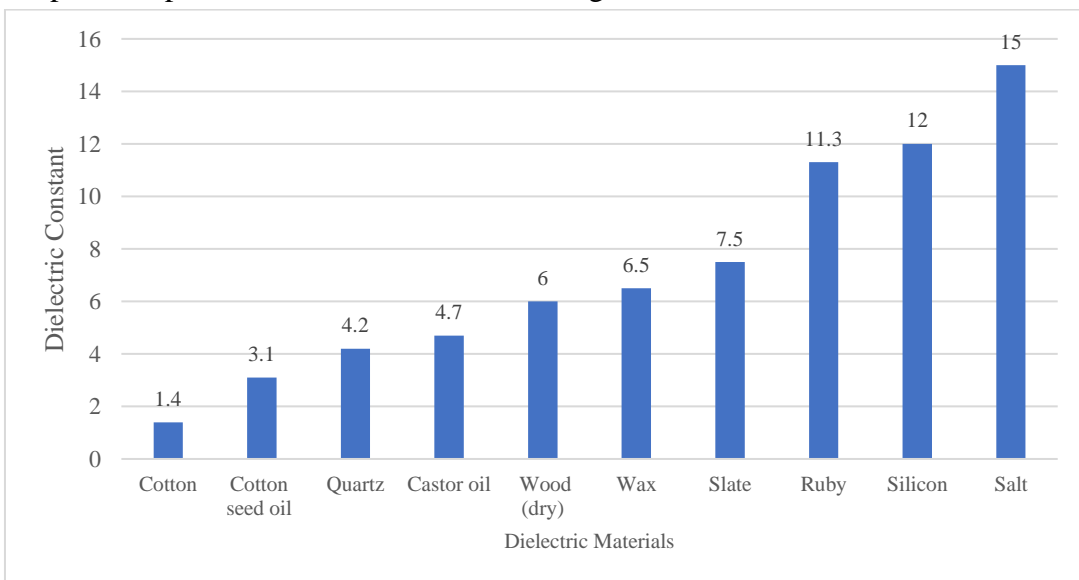


Figure 11 Variation of dielectric Constant vs dielectric Materials

MATLAB Program for the Computation of Reflection Coefficient

For Cotton,

```
% Program for the calculation of reflection coefficient
% for the perpendicularly polarized wave.
thitai=[0:10:90];
% angle of incidence from 0 to 90.
epsir2=1.4;
% relative permittivity of medium 2.
a=cosd(thitai)-sqrt(epsir2-sind(thitai).^2);
b=cosd(thitai)+sqrt(epsir2-sind(thitai).^2);
rho=a./b;
d=abs(rho);
% absolute value of reflection coefficient.
plot(thitai,d, 'k', 'linewidth', 2.2)
xlabel('Angle of incidence(degree)')
ylabel('Reflection coefficient") reflection coefficient
%Program for the calculation of % for the parallel-polarized wave.
thitai [0:10:90];
% angle of incidence from 0 to 90.
epsir2=1.4;
% relative permittivity of medium 2.
a=(-epsir2)*cosd(thitai)+sqrt(epsir2-sind(thitai).^2);
b=epsir2*cosd(thitai)+sqrt(epsir2-sind(thitai).^2);
rho=a./b; d=abs(rho);
% absolute value of reflection coefficient.
plot(thitai,d, 'k', 'linewidth',2.2)
xlabel('Angle of incidence (degree)')
ylabel("Reflection coefficient")
```

Discussion and Conclusion

In this work, the variation of reflection coefficient with respect to the angle of incidence has been studied for perpendicularly polarized wave and parallel-polarized wave. The direction of propagation of the wave is only from air to those media (cotton, cotton seed oil, quartz, castor oil, wood (dry), wax, slate, ruby, silicon and salt).

In the case of perpendicularly polarized wave, as the relative permittivity becomes higher, the graphs (reflection coefficient versus angles of incidence) shift move towards higher reflection coefficient. Reflection coefficient is between 0.0839 and 1 for the medium of cotton and 0.5896 and 1 for the medium of salt. No angle of incidence, at which reflection coefficient is zero, was found. Reflection coefficient is 1 at the angle of incidence of 90° for all media.

In the case of parallel- polarized wave, as the relative permittivity becomes higher, reflection coefficient becomes greater for the same angle of incidence. Reflection coefficient is between 0.0839 and 1 for the medium of cotton and 0.5896 and 1 for the medium of salt. Reflection coefficient is 1 at the angle of incidence of 90° for all media.

Acknowledgements

I would like to thank Dr Myat Shwe Wah, Professor and Head of Department of Physics, Dr ZayaAung, Professor of Department of Physics and Dr Khin Thitsar Shin , Professor of Department of Physics, West Yangon University, for their kind permission to carry out this paper.

References

- Joseph A. Edminister, 1993 "*Theory and problems of Electromagnetics*"
- Kraus and Carver, 1973 "*Electromagnetics*"
- Paul Lorrain and Dale Carson, 1970 "*Electromagnetic fields and waves*"
- Robert Plonsey, 1976 "*Principles and applications of electromagnetic fields*"
- Yamamoto Electric Industrial, 2007 "*All Right Reserved*"

Fabrication and Characterization of Natural Dyes based ZnONPs Photoelectrode for Dye Sensitized Solar Cells (DSSCs)

Bhone Pyae Linn¹, San San Thwin², Lwin Lwin Than³

Abstract

This research focuses on the green synthesis of ZnONPs using Banana Peel Extract (BPE) from *Musa Balbisiana* Banana. ZnONPs powders were synthesized with three different ratios of Banana Peel:distilled water (2:10, 4:10, 6:10) and $Zn(NO_3)_2 \cdot 6H_2O$. The structural and morphological properties of the synthesized ZnONPs powders were characterized by XRD and SEM. The crystal structure of ZnONPs (2:10, 4:10, 6:10) were found to be hexagonal wurtzite structure and their crystallite sizes were 43.06 nm, 29.40 nm and 22.23 nm respectively which form irregular grains having sizes of 2.77 μm , 2.39 μm , and 2.22 μm . ZnONPs (6:10) was deposited onto the fluorine doped tin oxide (FTO) substrates by using spin coating technique. Chlorophyll and Anthocyanin dyes solutions were extracted from Spinach Leaves and Grape Peel to use as sensitizer. ZnONPs substrates were dipped into two different natural dyes solutions, and natural dyes based ZnONPs photoelectrodes were prepared. The ZnONPs substrate, the natural dyes solutions and natural dyes based ZnONPs photoelectrodes were characterized by UV-Vis spectrophotometer. The energy band gap of ZnONPs substrate was found to be 2.48 eV. The optical band gap values were obtained 2.76 eV and 2.77 eV for Chlorophyll and Anthocyanin dyes solutions. Moreover, the optical band gap values of Chlorophyll and Anthocyanin based ZnONPs photoelectrodes were observed 2.63 eV and 2.49 eV respectively. According to obtained results, it can be reported that the two different natural dyes based ZnONPs photoelectrodes were suitable to use in DSSCs.

Keywords: Nanomaterials, ZnONPs, Photoelectrode, Natural Dyes, DSSCs

Introduction

Over the last years, various types of solar cells have been developed to convert sunlight to electricity. Crystalline, polycrystalline, and amorphous silicon solar cells have been widely used for different domestic and industrial application. Multi-junction semiconductor solar cells have shown the world record efficiency of 46%. However, their applications are mostly limited to space industry. There are other types of less efficient and low-cost cells, such as dyesensitized solar cells (DSSCs) and organic solar cells. DSSC was firstly reported by O'Regan and Gratzel in 1991. One of the main challenges of DSSCs is the long-term stability, electrolyte leakage, dyes desorption, and degradation of the dye itself are considered the most important parameters affecting the cell stability. Nanoparticles have packed interests in many researches in these recent years due to their advantageous application in various industries such as medicine, manufacturing electronics device, etc. A great example of nanoparticles with a wide array of uses is zinc oxide nanoparticles (ZnONPs). ZnONPs are used in a variety of applications including antibacterial agents, solar cell manufacturing materials, cosmetic ingredients, and so on.

One of environmental-friendly method for synthesis of ZnONPs nanoparticles is green method (Green synthesis of metal oxide nanoparticles is a fascinating issue of the nanoscience and nanobiotechnology fields). The nanoparticles prepared with plant extract are relatively cheap, efficient and ecological catalysts that help pollution. Green synthesis of ZnONPs has been carried out by many researchers including various kinds of fruits, leaves, petal of flowers, and so on. Bananas are used for various purpose in Myanmar and this subsequently lead to large amount

¹ Department of Physics, Yenanchaung University

² Department of Physics, Yenanchaung University

³ Department of Physics, Yenanchaung University

of wastes in the form of banana peels which are often discarded without further thought to its potential. This research work, Banana Peel Extract used as a capping agents in ZnONPs synthesis. The use of Banana Peel Extract as a capping agent is possible because the banana peel extract contains secondary metabolite compounds such as flavonoids, polyphenols, alkaloids and saponins with various amounts.

In a solar application, improved photon absorption and load carriers' production are the essential requirements in the form of DSSCs. Therefore, because of their fundamental properties that can improve solar cells' converting power, nanomaterials are used in photovoltaic (PV) technology. They can found promising for visible spectral area light harvesting because of the improved electron mobility resulting from the generation of fast charging carrier. Due to their unique physical and chemical properties, ZnONPs nanoparticles have been used in solar cell applications.

In this research work, ZnONPs were synthesized from Banana Peel and distilled water with three different ratios of (2:10), (4:10), and (6:10) by a green synthesis method. Among the three different ratios, one of the ratios that have the smallest crystallite size using as an electron conducting medium (semiconducting materials) to fabricate the natural dyes based ZnONPs photo electrode. The natural dyes were extracted from Grape Peel and Spinach Leave used as sensitizer for photoelectrode.

Experimental Procedure

Materials: Banana Peel (*Musa Balbisiana*), Red-Brown Grape Peel (*Vitis Vinifera L.*) and Spinach Leaves (*Alternanthera Blitum L.*) used in this study were collected from Yenanchaung's Myoma Market, Yenanchaung Township, Magway. Zinc nitrate hexahydrate ($Zn(NO_3)_2 \cdot 6H_2O$), Distilled water, Ethanol, citric acid, filter paper, and Fluorine doped Tin Oxide (FTO) glass substrates were purchased from Academy Chemical Shop, Yangon, Myanmar.

Synthesis of Zinc Oxide Nanoparticles

In this research work, the synthesis of ZnONPs has two major steps. The first step is the preparation of Banana Peel Extract (BPE) solution and the second one is the preparation of Zinc oxide nanoparticles with BPE solution. Firstly, Banana Peel Extract (BPE) solutions were prepared by using Banana Peel and Distilled water with three different ratios (2:10), (4:10) and (6:10). The Banana Peels were cleaned by not only tap water but also distilled water, and allowed to dry at room temperature overnight to remove excess moisture. Next, the peels were cut into small pieces and (20g, 40g, and 60 g) of the peels were dispersed to the 100 ml of the distilled water in 500 ml beaker for three different ratios. After that, each ratios of the solution were heated at 100°C for 90 minutes and stirred using a magnetic stirrer. The mixing solutions were filtered through the filter paper to remove the Banana Peels. Then, the three different ratios of Banana Peel Extract (BPE) solutions [(2:10), (4:10) and (6:10)] had been prepared and these solutions were stored in the dark for the further use.

The second step is the preparation of ZnONPs. In this part, Zinc nitrate hexahydrate [$Zn(NO_3)_2 \cdot 6H_2O$] precursor solution was prepared first. 0.5 M of $Zn(NO_3)_2 \cdot 6H_2O$ and 0.2 M of citric acid were added to 50 ml of distilled water. The solution was stirred for 30 minutes to get homogeneous solution. Then, zinc nitrate precursor solution was obtained. After that, the zinc nitrate precursor solution was mixed into 40 ml of Banana Peel Extract (BPE) solutions with

three different ratios of (2:10), (4:10) and (6:10). The mixed solutions (three different ratios) were heated at constant temperature and stirred on the hot plate (magnetic stirrer). Then, the mixed solutions were change into “gel” about 2 hours. These gel was continuously heated with constant temperature. After a few minutes, these gel changed into dust gray slices. These slices were calcined at 500°C for 4 hours in the furnace. Moreover, the calcined slices were ground for 2 hours to get fine powder. After that, a dust gray powder of zinc oxide nanoparticles with three different ratios was obtained as shown in the following Figure 1.

Extraction of the Natural Dyes

Red-Brown Grape Peel and Spinach Leaves were used as the starting materials to extract the natural dyes in this work. Distilled water used as the extraction solvent for Red-Brown Grape Peel and Spinach Leaves. 10 g of Grape Peel (fresh) and 10g of Spinach leaves (fresh) were dispersed into 100 ml of distilled water. The dispersions were heated up at 90°C for one and half hours on the hotplate. The dispersions were filtered through filter paper to extract the natural dyes for the use as sensitizers, after cooling down to room temperature. The Grape Peel extract solution was used as an Anthocyanin dye and the Spinach Leaves extract solution was used as Chlorophyll dye respectively. The flow-chart for the extraction of natural dyes are shown in Figure 2.

Fabrication of Natural Dyes based ZnONPs Photoelectrodes

At first, FTO conductive glass substrates (1" × 1" × 1.1 mm) were firstly cleaned tap water with soap for 15 minutes. Secondly, these FTO conductive glass substrates were washed with ethanol for 1 hour and distilled water for 30 minutes in an ultrasonic cleaner for impurity clearance and dry at room temperature. After that, a colloidal solution of ZnONPs (6:10) was prepared by mixing 50 mg of the zinc oxide nanopowders with 20 ml of ethanol. The mixed solution was stirred for 4 hours to get homogeneous solution. Then, the ZnONPs solutions were deposited onto the FTO glass substrates with the use of spin-coater (1000 rpm for 10s followed by 3000rpm for 60s) for three times and ZnONPs glass substrates were obtained. Those ZnONPs glass substrates were heated at 60°C for 30 minutes. Then, the heated glass substrates were cooled down to room temperature for 30 minutes. After that, the ZnONPs glass substrates were dipped into natural dyes (Anthocyanin and Chlorophyll) solutions for 24 hours. The dipped ZnONPs glass substrates were dried at room temperature about 2 hours after taking the glass substrates from the natural dyes. Finally, natural dyes (Anthocyanin and Chlorophyll) based ZnONPs photoelectrodes were obtained as shown in Figure 3.

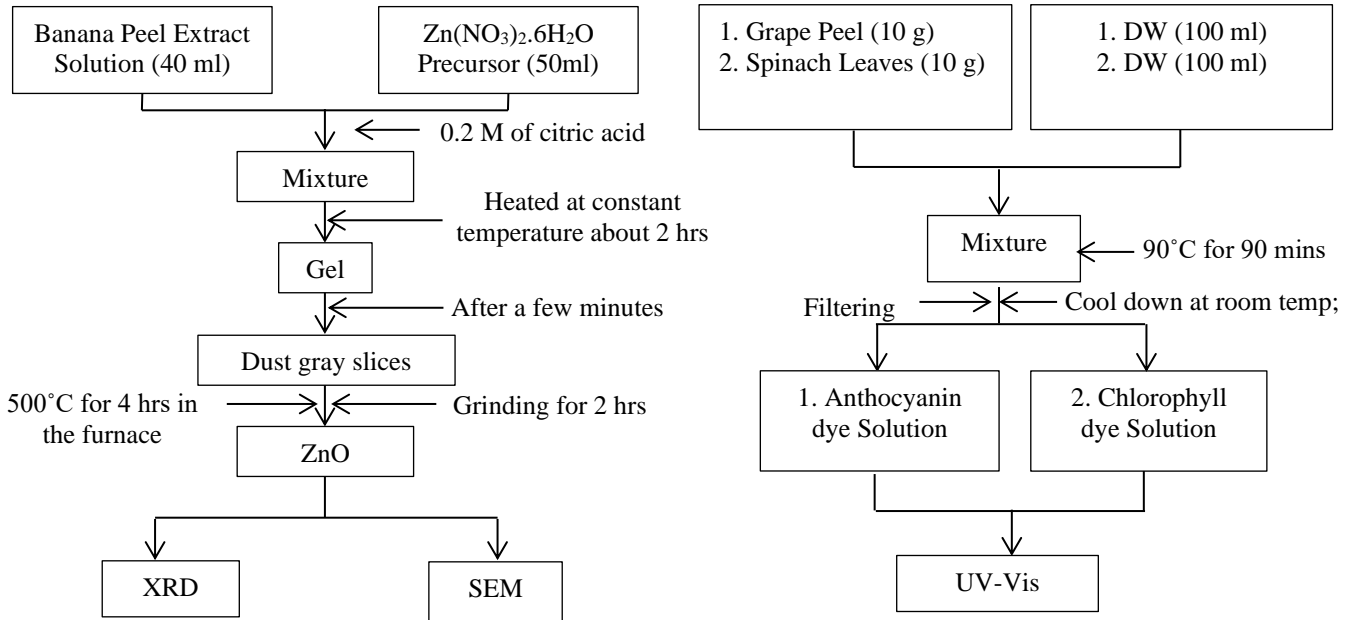


Figure 1 Flow-chart for green synthesis of Oxide Nanoparticles **Figure 2** Flow-chart for the extraction of natural dyes

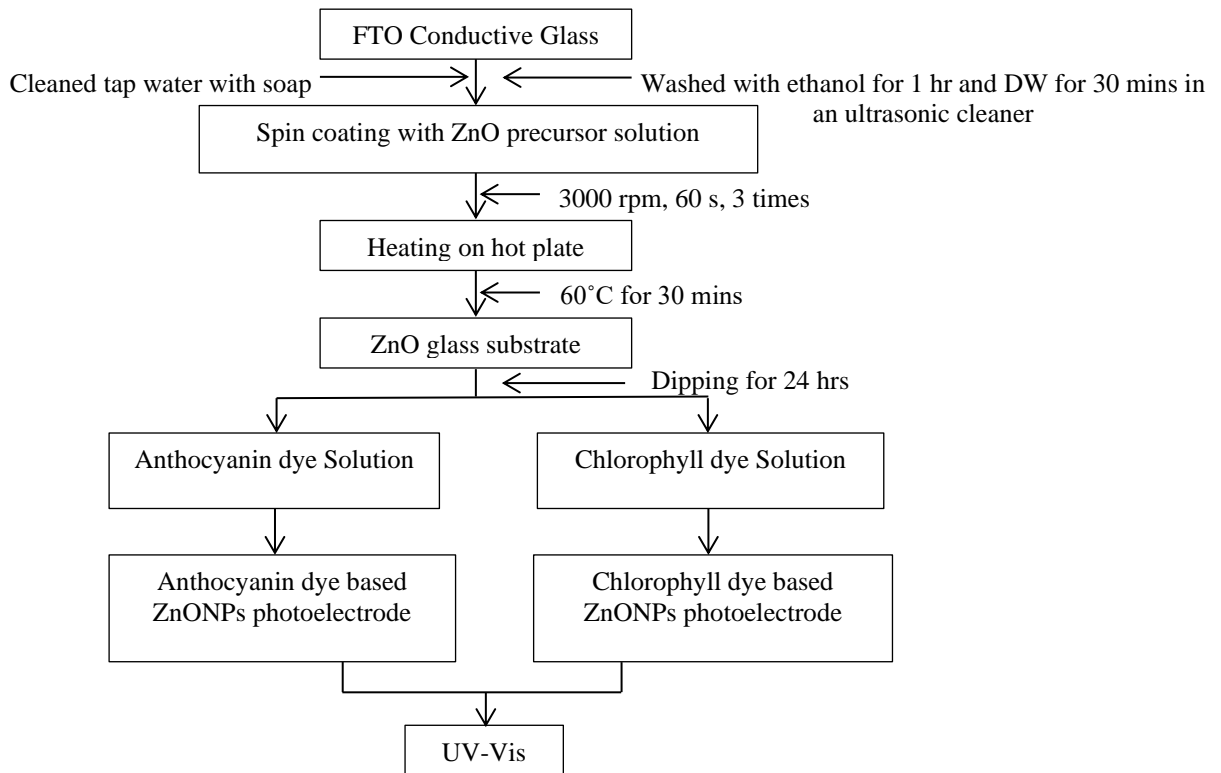


Figure 3 Flow-chart for the fabrication of natural dyes based ZnONPs photoelectrodes

Characterization

The structural properties of ZnONPs powders were examined by using X-ray diffractometer (Lab XRD-6100, University Research Centre, Magway) which operates at 30 mA and 40 kV to generate radiation at a wavelength of 1.54050Å. The morphological properties of the ZnONPs powders were characterized by using Scanning Electron Microscopy (SEM Coxem – 610, University Research Centre, Patheingyi). The UV-Vis spectrophotometer (Shimadzu UV-Vis 2600, University Research Centre, Magway) was used to analyse the optical performance of ZnONPs glass substrates, natural dyes (Anthocyanin and Chlorophyll) solutions, and natural dyes (Anthocyanin and Chlorophyll) based ZnONPs photoelectrodes.

Results and Discussions

XRD Analysis

X-ray diffraction with $\text{CuK}\alpha$ ($\lambda = 1.54060 \text{ \AA}$) was used to analyze the crystal structure and crystallite size of prepared ZnONPs powders. The XRD patterns of ZnONPs with three different ratios of (2:10), (4:10), and (6:10) were shown in Figure 4. By referring to these figures, the Bragg's reflection peaks are (100), (002), (101), (102), (110), (103), (200), (112), and (201) respectively. Among these peaks, (100), (002), and (101) are the strongest reflection peaks. The lattice parameters of ZnONPs with three different ratios of (2:10), (4:10) and (6:10) are $a = b = 3.24962 \text{ \AA}$ and $c = 5.20313 \text{ \AA}$, $a = b = 3.24910 \text{ \AA}$ and $c = 5.20242 \text{ \AA}$, and $a = b = 3.24955 \text{ \AA}$ and $c = 5.20401 \text{ \AA}$. The $\frac{c}{a}$ ratio of three different ZnONPs powders was 1.6 as tabulated in Table 4. Therefore, this reveals that the resultant ZnONPs powders belong to a hexagonal wurtzite structure.

The diameter of the crystallite size of the ZnONPs powders were determined from the most prominent reflection peaks of (100), (002), and (101) by using Debye Scherrers' equation $D = \frac{k\lambda}{B\cos\theta}$. The crystallite sizes of ZnONPs powders with three different ratios were tabulated in Table 1, 2, and 3. The obtained mean crystallite sizes of three different samples were also tabulated in Table 4.

According to XRD result, when the peaks intensity of ZnONPs are decreased, increasing the peaks broadening from (2:10) to (6:10). Generally, the peaks in the XRD will broaden as crystallite size decrease. Therefore, the crystallite sizes are decreased from 40.06 nm (2:10) to 22.23 nm (6:10). Therefore, the smallest crystallite size of ZnONPs (6:10) was chosen to use as a semiconducting material.

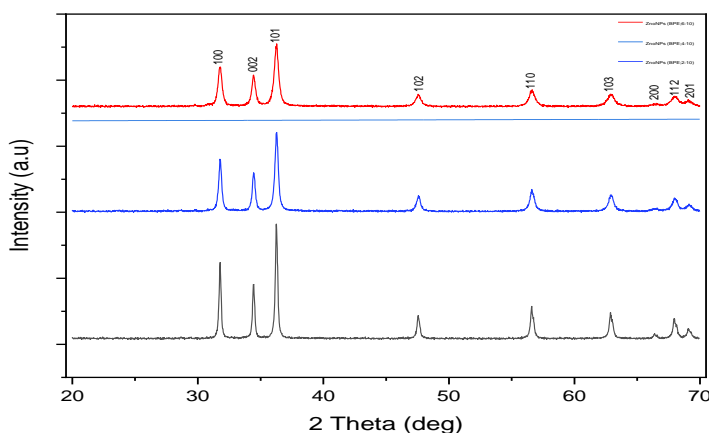


Figure 4 XRD patterns of ZnONPs (2:10, 4:10, 6:10)

Table (1) XRD parameters and crystallite sizes of Zinc Oxide Nanoparticles (2:10)

Types of sample	(hkl)	2 θ (deg)	FWHM (deg)	Crystallite Sizes (nm)
ZnONPs	100	31.7918	0.19560	42.23
	002	34.4564	0.18800	44.25
	101	36.2761	0.19570	42.72
Average Crystallite Size				43.06

Table (2) XRD parameters and crystallite sizes of Zinc Oxide Nanoparticles (4:10)

Types of sample	(hkl)	2 θ (deg)	FWHM (deg)	Crystallite Sizes (nm)
ZnONPs	100	31.7973	0.27990	29.51
	002	34.4656	0.26810	31.03
	101	36.2812	0.30210	27.67
Average Crystallite Size				29.40

Table (3) XRD parameters and crystallite sizes of Zinc Oxide Nanoparticles (6:10)

Types of sample	(hkl)	2 θ (deg)	FWHM (deg)	Crystallite Sizes (nm)
ZnONPs	100	31.7344	0.37630	21.95
	002	34.4581	0.34810	23.89
	101	36.2669	0.40110	20.84
Average Crystallite Size				22.23

Table (4) Lattice parameters, lattice distortion and mean crystallite sizes for zinc oxide nanoparticles

Types of Sample	a (Å)	c (Å)	$\frac{c}{a}$	Mean Crystallite Sizes (nm)
ZnONPs (2:10)	3.24962	5.20313	1.60	43.06
ZnONPs (4:10)	3.24910	5.20242	1.60	29.4
ZnONPs (6:10)	3.24955	5.20401	1.60	22.23

SEM Analysis

The surface morphological features of synthesized ZnO nanoparticles with three different ratios were examined by Scanning Electron Microscope (SEM) as shown in Figure 5. These micrographs indicate that a good microstructure with no discontinuities in terms of microcracks, some pores are found among the grains, and a few number of large grain size are also found. Grain sizes are little difference and they were measured by using well known bar code system with Image J software. The grain sizes were estimated to be 2.77 μm, 2.39 μm, and 2.22 μm for three different ratios (2:10, 4:10, and 6:10) respectively. From the result, it is found that the grain size is smallest for the ratio (6:10) among the three ratios.

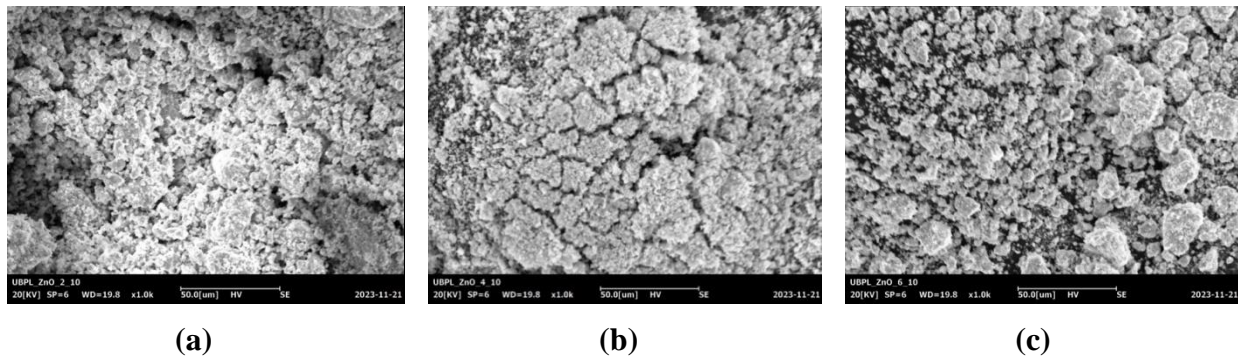


Figure 5 SEM photographs of ZnONPs (a) (2:10), (b) (4:10), and (c) (6:10)

UV-Vis measurement for ZnONPs films

The absorption spectrum of zinc oxide nanopowder films (colloidal nanoparticles) is shown in Figure 6. This figure shows that the UV absorption of the ZnONPs film is in the visible region with maximum wavelength at 542 nm (absorption intensity is 0.0025) indicating that band to band excitation of ZnONPs, which is used for calculation of optical band gap of nanoparticle by using equation, $\lambda (nm) = \frac{1240}{E_g (eV)}$

The optical absorption provides the dependence of the absorption coefficient (α) on the photon energy ($h\nu$) for direct allowed.

$(\alpha h\nu)^2 = K(h\nu - E_g)$, Tauc Plot equation was applied to find the optical band gap by plotting $(\alpha h\nu)^2$ vs photon energy ($h\nu$) using the data obtained from the optical absorption spectrum of ZnONPs film. The optical band gap of ZnONPs film determined from this curve (absorption spectrum) is 2.48 eV as shown in Figure 7.

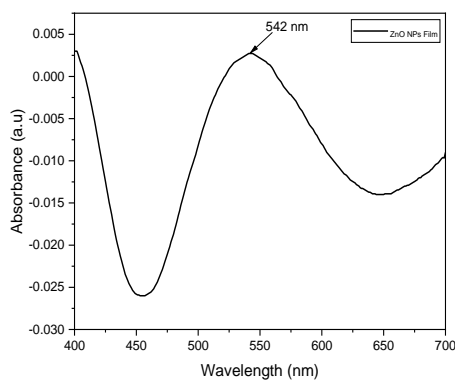


Figure 6 Absorption spectrum of ZnONPs film

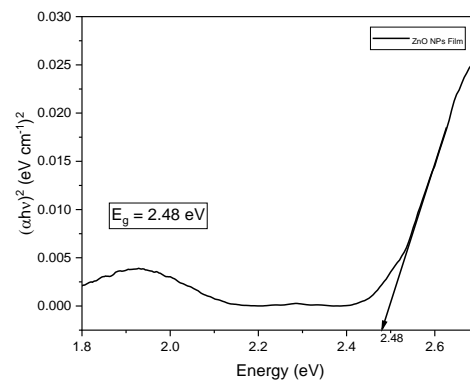


Figure 7 Energy band gap of ZnONPs film

UV-Visible Spectroscopy for the Natural Dyes

The absorption spectra of Chlorophyll and Anthocyanin dyes solutions were shown in Figure 8 and 9. Figure 8 showed that the presence of distinct absorption peak in the visible region at about 665 nm and the absorption intensity is 0.24 for the extract solution from the Spinach Leaves (Chlorophyll dyes). Figure 9 showed that the presence of absorption peak at about 512 nm and the absorption intensity is 1.07 for the Anthocyanin pigment dye solution (extracted from Grape Peel). The optical band gap value of Anthocyanin dye solution and Chlorophyll dye solution are 2.77 eV and 2.76 eV respectively as shown in Figure 10 and 11. From the result, the optical band gap values of two different dyes solutions were nearly equal while the absorption intensity of Anthocyanin dye solution is higher than that of Chlorophyll dye solution. It can be seen that the absorption peaks of two different dyes are in the visible region (approximately 500 – 670 nm). Therefore, these two natural dyes (Anthocyanin & Chlorophyll) were possibility used as sensitizers in DSSCs.

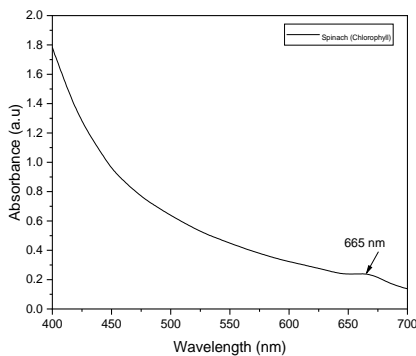


Figure 8 Absorption Spectrum of Chlorophyll dye solution

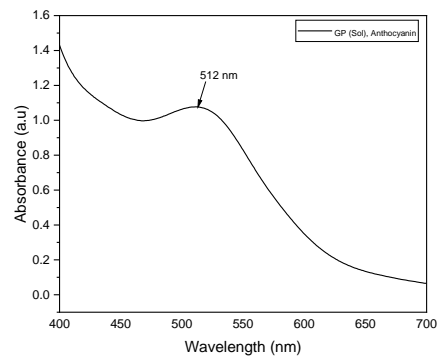


Figure 9 Absorption Spectrum of Anthocyanin dye solution

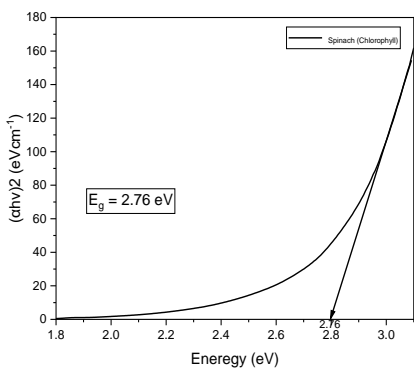


Figure 10 Energy band gap of Chlorophyll dye solution

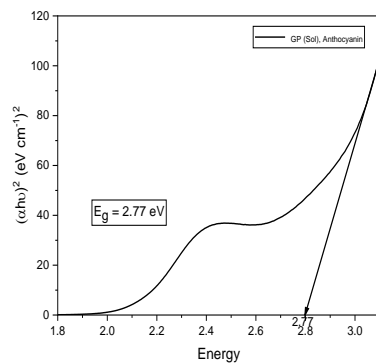


Figure 11 Energy band gap of Anthocyanin dye solution

Optical Energy Gap (E_g) of Natural Dyes based ZnONPs Photoelectrodes

The two different natural dyes (Chlorophyll & Anthocyanin) solutions, ZnONPs glass substrates and natural dyes (Chlorophyll & Anthocyanin) based ZnONPs Photoelectrodes had been prepared. In this section, the optical performance of prepared natural dyes based ZnONPs photoelectrodes were characterized by UV-Vis spectrophotometer. The absorption spectrum of Chlorophyll dyes based ZnONPs photoelectrode and Anthocyanin dyes based ZnONPs photoelectrode are shown in Figure 12 and 13. The absorption intensity of Chlorophyll dyes based ZnONPs photoelectrode are 0.147 and 0.0840 at 400 nm and 541 nm. The absorption peaks of Anthocyanin dyes based ZnONPs photoelectrode are presented at 420 nm and 578 nm with absorption intensity of 0.069 and 0.059. The absorption peaks of both photoelectrodes were in visible region and the optical band gap values of both photoelectrodes were 2.63 eV and 2.49 eV as shown in Figure 14 and 15. From the above result, the optical band gap value of two different natural dyes based ZnONPs photoelectrodes are lower than the suitable value used in DSSCs. Because of the optical band gap value of the ZnONPs glass substrate was low. The reason why the optical band gap of ZnONPs glass substrates is low due to the temperature of these substrates was low. It is mentioned in the paper “Amal Bouich, Muhammad Aamir Shafi, et.al, Effect of deposition cycles on the properties of ZnO thin films deposited by spin coating method for CZT based solar cells, Vol-258, May 22”, there is a relationship between the E_g of the film and the temperature. However, the optical band gap values of the two different natural dyes based ZnONPs photoelectrodes are above 2 eV. Therefore, they were suitable for use as a photoelectrode in DSSCs.

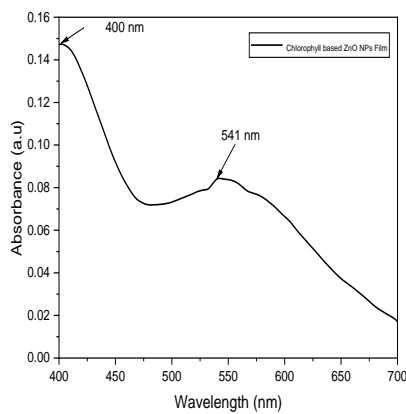


Figure 12 Absorption spectrum of Chlorophyll dye based ZnONPs Photoelectrode

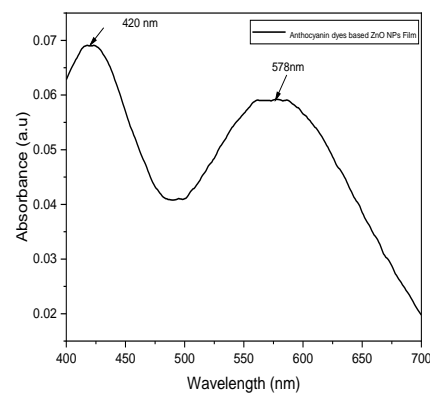


Figure 13 Absorption spectrum of Anthocyanin dye based ZnONPs

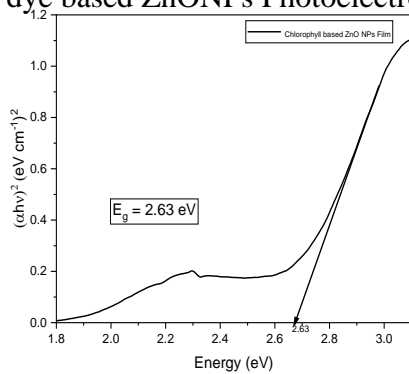


Figure 14 Energy band gap of Chlorophyll dye based ZnONPs Photoelectrode

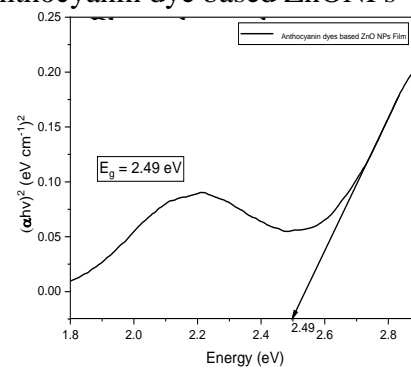


Figure 15 Energy band gap of Anthocyanin dye based ZnONPs Photoelectrode

Conclusion

In this research work, Chlorophyll and Anthocyanin dyes based zinc oxide nanoparticles (ZnONPs) photoelectrodes were fabricated for DSSCs. The crystal structure of ZnONPs (2:10, 4:10, 6:10) were found to be hexagonal wurtzite structure and their crystallite sizes were 43.06 nm, 29.40 nm and 22.23 nm respectively. The micrographs of three different ZnONPs have no cracking and some pores were formed among the grains and also found irregular particles structure. The grain sizes of ZnONPs with three different ratios (2:10, 4:10, 6:10) were 2.77 μm , 2.39 μm , and 2.22 μm respectively. Among them, ZnONPs of (6:10) will be chosen to construct natural dye based ZnONPs photoelectrodes because it has smallest crystallite size of 22.23 nm and smallest grain size of 2.22 μm . Then, ZnONPs (6:10) was deposited onto FTO substrates and the band gap value of this substrates was found to be 2.48 eV. The optical band gap values of Chlorophyll and Anthocyanin dyes were found to be 2.76 eV and 2.77 eV respectively. Natural dyes based ZnONPs photoelectrodes were successfully fabricated by using ZnONPs coated glass substrates and Chlorophyll and Anthocyanin natural dyes. The band gap values of Chlorophyll and Anthocyanin dyes based ZnONPs photoelectrodes were obtained 2.63 eV and 2.49 eV and they were slightly increased compare to the band gap value of ZnONPs coated glass substrate. The band gap value has changed slightly because of the dye molecules which attached to ZnONPs weakly. According to the above results, the optical band gap values of the two different natural dyes based ZnONPs photoelectrodes are lower than suitable values of the optical energy gap (3-3.2eV) in DSSCs. As the optical band gap values of the two different natural dyes based ZnONPs photoelectrodes are above 2 eV (wide band gap semiconductor materials have band gaps in the range above 2eV), they were suitable photoelectrode to be used in DSSCs.

Acknowledgements

I am very grateful to Department of Physics, Yenanchaung University and University Research Centre, Magway.

References

- Andualem, A., Demiss, S. (2018) "Review on Dye-Sensitized Solar Cells (DSSCs)". *Edelweiss Appli Sci Tech* 2:145–150.
- O'Regan, B. and Grätzel, M., (1991) "A low-cost, high-efficiency solar cell based on dye-sensitized colloidal TiO_2 films," *Nature*, vol. 353, no. 6346, pp. 737–740.
- Schindler, F., Fell, A., Müller, R., et al., (2018) "Towards the efficiency limits of multicrystalline silicon solar cells," *Solar Energy Materials and Solar Cells*, vol. 185, pp. 198–204.
- Wong, H.L. (2016). Green Synthesis, "Characterization of Zinc Oxide Nanoparticles and Their Photocatalytic Activity", Department of Chemical Science, Faculty of Science, Universiti Tunku Abdul Rahman, pp.1-108.

DETERMINATION OF ENERGY LOSS CHARACTERISTIC IN DIFFERENT DENSITY MATERIALS BY ALPHA SPECTROSCOPIC SYSTEM

Myo Nyunt¹, Ye Win Nyunt², Myo Zaw Htut³, Htin Lin⁴, Tay Zar Htein Win⁵,
Htoo Nwe Nwe Aung⁶

Abstract

Nowadays, alpha Spectroscopy system is very popular and widely used radionuclide assay method in human resources and various research topics. The alpha particles are emitted from the well of the nucleus. Alpha spectroscopy is important role in the identification of radioisotope, radiation protection and radiation therapy in which alpha particle have the ability to deliver their energies to the target. In this research work, characteristics of α -radiation in different density materials were investigated by using silicon semiconductor detector and α -radiation sources: ²⁴¹Am and ²²⁶Ra. In the present study, the measurement of alpha spectroscopy was performed for the determination of α -radiation characteristic such as energy loss, range, stopping power and effective path length not only in air medium but also in aluminum (Al) and gold (Au) foils samples of 8 μ m and 2 μ m respectively. Radionuclide Identification (RID) program is created in this research work. The measured spectra were analyzed by using this program based on the CASSY Lab and MATLAB software packages. Moreover, the experimental results data were compared with the theoretical calculated values by using Geiger Law, Bragg's Law and Bethe-Bloch formula. The results data from the measurement were found in good agreement with the theoretical values less than 10%.

Keywords- α -spectroscopy, Bethe-Bloch, Bragg Curve, CASSY Lab, Energy loss, Geiger Law, MATLAB, Range, Silicon Semiconductor, Stopping Power.

Introduction

Alpha particles were first described in the investigations of radioactivity by Ernest Rutherford in 1899, and by 1907 the identified as He²⁺ ions. By 1928, George Gamow had solved the theory of alpha decay via tunneling. The alpha particles trapped in a potential well by the nucleus. In the classical sense, escaping is not allowed. However, based on the recently uncovered principles of quantum mechanics, there exists a minuscule chance of "tunneling" through the barrier and emerging on the opposite side to exit the nucleus.[6]

Gamow tackled a theoretical potential model for nucleus. He deduced a connection between the half-life and the emission of energy from fundamental principles. This relation was observed empirically before and was called the Geiger-Nuttall Law. Americium -241, an alpha-emitting substance finds use in smoke detectors. These alpha particles cause air to become ionized within an open chamber, leading to a slight flow of current through the ionized air. Alpha decay offers a secure energy supply for radioscope thermoelectric generators applied in space missions and was also utilized in artificial heart pacemakers. Alpha decay is more effectively blocked compared to other types of radioactive decay. In the case of static eliminators, they commonly employ polonium-210, an alpha emitting material, to ionize the air [4].

AIM

The aim of this research work is to investigate energies loss of alpha particles in gold and aluminum foils by using alpha spectroscopic method.

¹ Department of Nuclear Physics, Defence Services Academy, Pyin Oo Lwin

² Department of Nuclear Physics, Defence Services Academy, Pyin Oo Lwin

³ Department of Nuclear Physics, Defence Services Academy, Pyin Oo Lwin

⁴ Department of Nuclear Physics, Defence Services Academy, Pyin Oo Lwin

⁵ Department of Physics, Defence Services Academy, Pyin Oo Lwin

⁶ Department of Physics, Defence Services Academy, Pyin Oo Lwin

Background Theory

Heavy charged particles, such as alpha particle, interact with matter primarily through coulomb forces between their positive charges of the orbital electrons within the absorber atoms. Although interactions of particle with nuclei (Rutherford scattering or alpha particle-induced reactions) are also possible, such encounters occur only rarely and they are not normally significant in the response of radiation detectors. Instead, charged particle detectors must rely on the results of interactions with electrons for their response.

The linear stopping power S for charged particles in a given absorber is simply defined as the differential energy loss for that particle within the material divided by the corresponding differential path length:

$$S = - \frac{dE}{dx} \quad (1)$$

The value of $-dE/dx$ along a particle track is also called its *specific energy loss* or, more casually, its "rate" of energy loss. Particles with a given charge state energy loss increases as the particle velocity is decreased. The classical expression that describes the specific energy loss is known as the Bethe formula and is written

$$- \frac{dE}{dx} = \frac{4\pi e^4 z^2}{m_0 v^2} NB \quad (2)$$

where, $B = z \left[\ln \frac{2m_0 v^2}{I} - \ln \left(1 - \frac{v^2}{c^2} \right) - \frac{v^2}{c^2} \right]$

$$\frac{dE}{dx} = 4\pi r_0^2 z^2 \frac{mc^2}{\beta^2} NZ \left[\ln \left(\frac{2mc^2}{I} \beta^2 \gamma^2 \right) - \beta^2 \right] \quad (3)$$

In these expressions, v and ze are the velocity and charge of the primary particle, N and Z are the number density and atomic number of the absorber atoms, m_0 is the electron rest mass, and e is the electronic charge. The parameter I represents the average excitation and ionization potential of the absorber and is normally treated as an experimentally determined parameter for each element.[8].

Energy Loss in Thin Absorbers

For thin absorbers (or detectors) that are penetrated by a given charged particle, the energy deposited within the absorber can be calculated from

$$\Delta E = - \left(\frac{dE}{dx} \right)_{avg} t \quad (4)$$

where, t is the absorber thickness and $(-dE/dx)$, ΔE is the linear stopping power averaged over the particle-energy while in the absorber. The energy of α - particle is consumed after it has passed the path length:

$$R = \int_{E_0}^0 \frac{dx}{dE} \cdot dE \quad (5)$$

This range is a measure for the initial energy E_0 of α - particle. Empirically, the relation between E_0 and R is given by the *Geiger law*:

$$R \propto E_0^{\frac{3}{2}} \quad (6)$$

For air,

$$R_{air}[cm] = 0.46E_0^{\frac{3}{2}} (MeV) \tag{7}$$

Material And Method

The experimental research was under alpha spectroscopy system, which installed at Nuclear Physics laboratory of the Department of Nuclear Physics in Défense Services Academy. In this alpha particle spectroscopy system, absorbers (gold and aluminium) and standard radioactive sources (²⁴¹Am and ²²⁶Ra) were used. In this present research work, the alpha radiation sources of ²⁴¹Am and ²²⁶Ra were used at Nuclear Physics Laboratory. The isotope Am-241 decays into Np-237 by emitting α-particle.

Table 1. Technical Data of Sources use in Experiment

Radioisotope	Decay mode	Decay energy [MeV]	Half-life [Years]
Americium-241	Alpha	5.468	432.2
	Gamma	0.059	
Radium-226	Alpha	4.871	1600
	Gamma	0.186	



(a) (b)

Figure.1 Standard Radioisotopes (a) ²⁴¹Am and (b) ²²⁶Ra Source Preparation



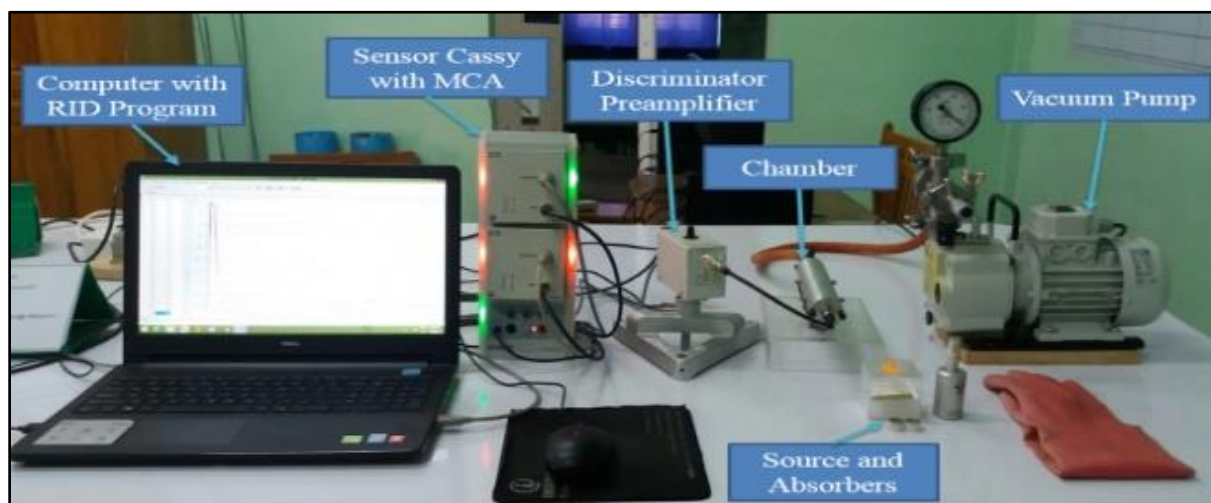
(a) (b)

Figure2. Thin Absorbers (a) Gold Foil and (b) Aluminium Foil

Table 2. Technical Data of Aluminium and Gold Foils Used in Experiment

Properties	Absorber Element Properties	
Element	Al	Au
Atomic Number (Z)	13	79
Mass Number (A)	26	197
Density	2.7 g/cm ³	19.32 g/cm ³
Mean Ionization Potentials(I)	160 eV	771 eV
Thickness	8 μm	2 μm

For analysis of energy loss in different density materials by alpha spectroscopic method, the energy loss of the α radiation from the ^{241}Am and ^{226}Ra source are measured in the spectroscopy chamber in dependence on the air. Alpha spectrometer system also consists of vacuum chamber, vacuum pump, silicon-semiconductor detector, discriminator preamplifier, sensor CASSY with multichannel analyzer (MCA) and computer installed CASSY Lab spectrum analysis software or implemented RID program. Schematic diagram of alpha spectrometer shown in figure3.

**Figure3.** Experimental Setup of Alpha Spectroscopic Measurement

Applied Programs of Radionuclide Identification (RID) for Analysis of Energy Loss of Alpha Particles

Experimental design of radionuclide identification system is constructed in Nuclear Physics Laboratory, Department of Nuclear Physics at Defence Services Academy. This system is the identification and concentration analysis system, which is based on the gamma and alpha spectroscopy measurement systems. In this present research work, the measurement and analysis programs were created for alpha spectroscopic measurements of standard sample, mineral ore sample and other research samples by using with the MATLAB software and CASSY modules.

- (a) Measurement program for gamma radiation measurement based on NaI detector and detection assembly.

- (b) Measurement program for alpha radiation measurement based on silicon semiconductor detector and detection assembly.

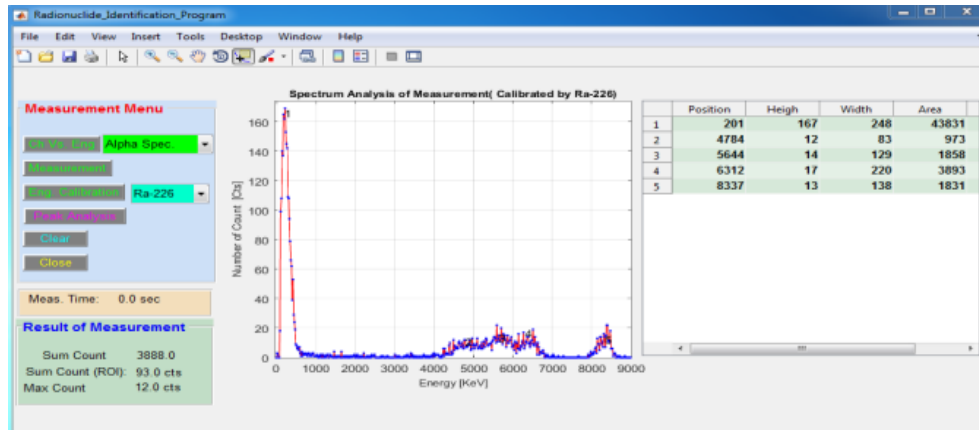


Figure 4. The Result Interface of in Peak Analysis Radionuclide Identification Program

Results And Discussion

In this experimental result of energy loss characteristics of Au and Al different densities materials by using with alpha spectroscopic system and created program based on CASSY Lab and MATLAB software packages are represented.

Energy loss of alpha particles for americium-241 source in air medium, in gold foil with mass thickness of 2 μm and 8 μm are determined in different air pressures. The gold foil and aluminum foil are suitable absorbers for determination of energy loss per unit distance, dE/dx measurements. The resolution of alpha particles energy in gold foil become poor and spectra are broadened than in the air medium due to the density and thickness of absorbing medium. The loss energy of alpha particle in gold foil for the entire energy range are measured and calculated.

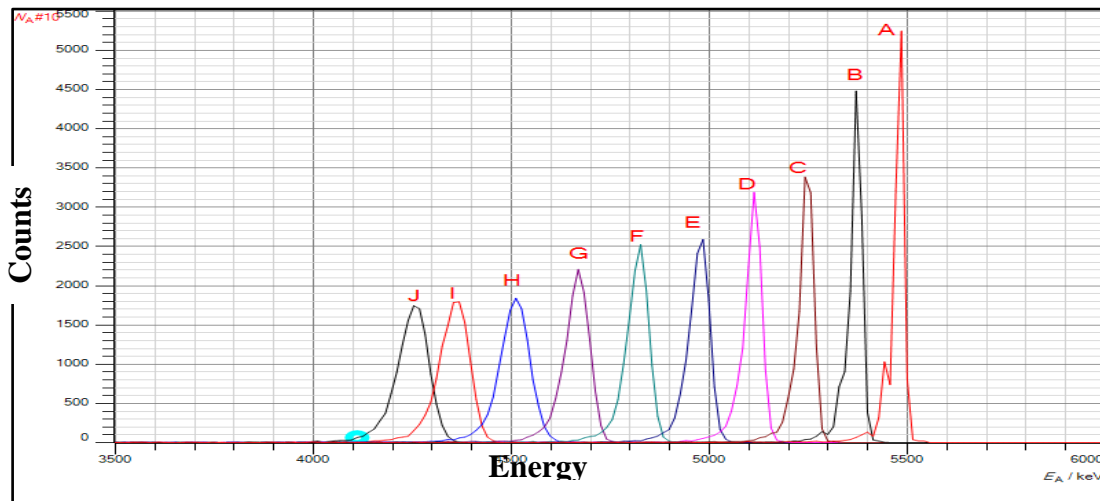


Figure 5. Measured Loss Energy of Alpha Particles in Air Medium (Without Absorber) Using Am-241 Source

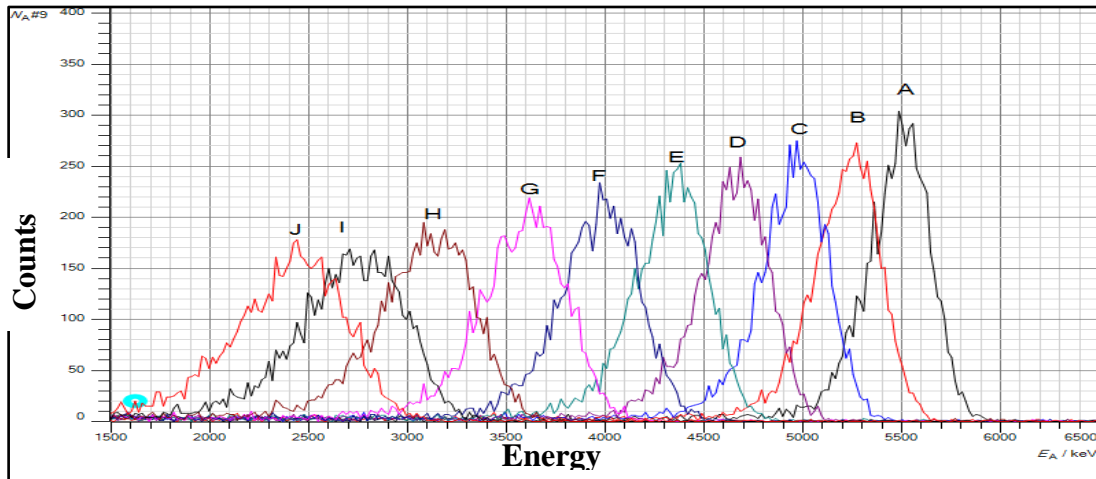


Figure 6. Measured Loss Energy of Alpha Particles in Gold Absorber Using Am-241 Source

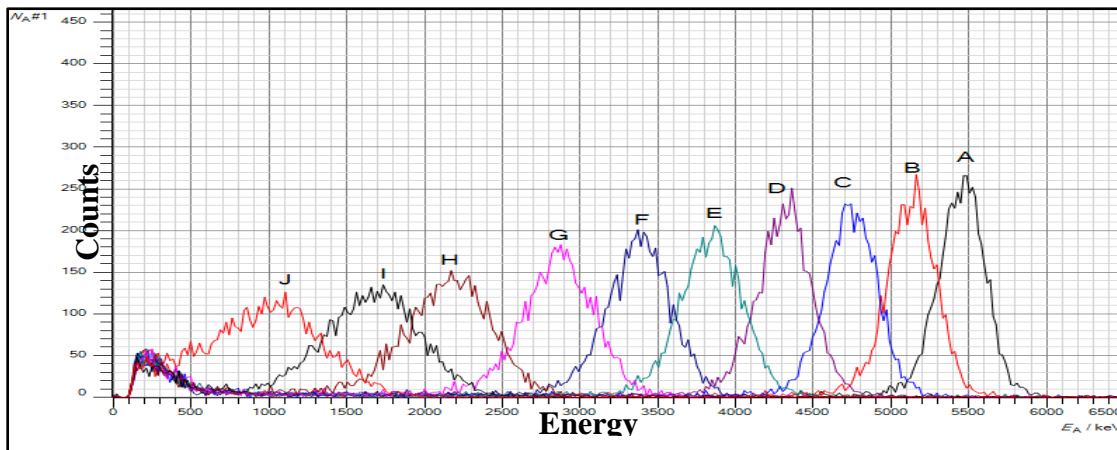


Figure 7. Measured Energy Loss of Alpha Particles in Aluminium Absorber Using Am-241 Source

Table 3. Results Data of Range and Energy Relation of Alpha Particle in Gold Foil using Am-241 Source

Pressure [mbar]	Energy [MeV]	Stopping Power [MeV/mg/cm ²]	Range [mg/cm ²]
100	5.4729	0.228	18.9
200	5.219	0.231	17.5
300	4.946	0.234	16.1
400	4.653	0.236	14.6
500	4.332	0.239	13
600	3.995	0.240	11.7
700	3.597	0.241	10
800	3.121	0.244	8
900	2.738	0.245	6.7
1000	2.428	0.255	5.7

Table 4. The Result Data of Range and Energy Relation of Alpha Particle in Aluminum Foil Using Am-241 Source

Pressure [mbar]	Energy [MeV]	Stopping Power [MeV/mg/cm ²]	Range [mg/cm ²]
100	5.4702	0.615	7
200	5.109	0.640	6.3
300	4.763	0.673	5.6
400	4.613	0.715	4.8
500	3.863	0.769	4.1
600	3.396	0.831	3.4
700	2.886	0.912	2.7
800	2.172	1.061	1.9
900	1.682	1.200	1.4
1000	1.074	1.398	0.9

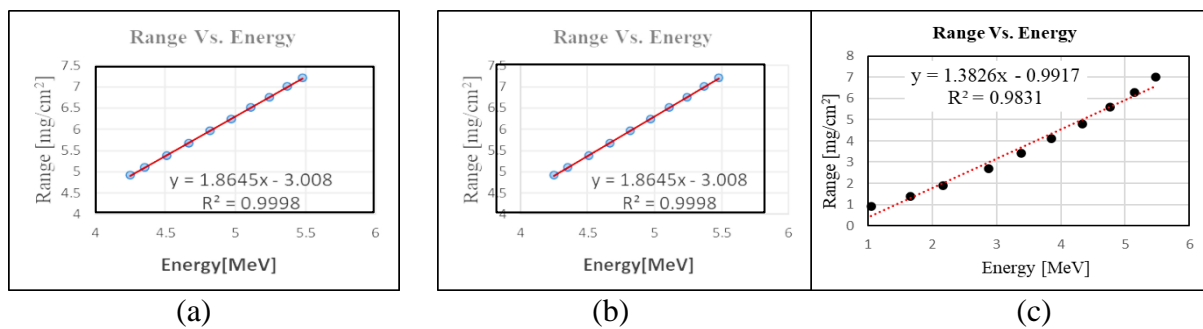


Figure 8. Range and Energy Relation of Alpha Particle (a) in Air Medium (b) in Gold and (c) in Aluminium using Am-241 Source

Table 5. The results data of theoretical and experimental energy loss of alpha particle in gold and aluminium foils using Am-241 source

Curves	Pressure [mbar]	Foil Thickness of Al [mg/cm ²]	Foil Thickness of Au [mg/cm ²]	ΔE[MeV] in Al			ΔE[MeV] in Au		
				Meas. Energy Loss	Theory Energy Loss	Error %	Meas. Energy Loss	Theory Energy Loss	Error %
A	100	2.16	3.86	0.0058	0.006	3	0.0031	0.003	3
B	200	2.16	3.86	0.216	0.232	6	0.151	0.153	1
C	300	2.16	3.86	0.478	0.454	5	0.295	0.303	2
D	400	2.16	3.86	0.499	0.545	8	0.459	0.454	1

Curves	Pressure [mbar]	Foil Thickness of Al [mg/cm ²]	Foil Thickness of Au [mg/cm ²]	ΔE[MeV] in Al			ΔE[MeV] in Au		
				Meas. Energy Loss	Theory Energy Loss	Error %	Meas. Energy Loss	Theory Energy Loss	Error %
E	500	2.16	3.86	1.120	1.161	3	0.651	0.663	1
F	600	2.16	3.86	1.430	1.794	2	0.841	0.868	3
G	700	2.16	3.86	1.782	1.970	9	1.071	1.027	4
H	800	2.16	3.86	2.339	2.293	2	1.390	1.405	1.0
I	900	2.16	3.86	2.686	2.592	3	1.630	1.661	1.8
J	1000	2.16	3.86	3.193	3.019	5	1.839	1.793	2.5

Range of alpha particles for Ra-226 source in air medium, gold foil with mass thickness of 2μm and aluminum foil with thickness of 8μm are determined in different air pressures. The gold foil is suitable absorbers for determination of range R measurements. The resolution of alpha particles energy in gold foil become lower. The range of alpha particles in without absorbers in air pressures and the range of alpha particle in gold foil for the entire energy range are measured and calculated.

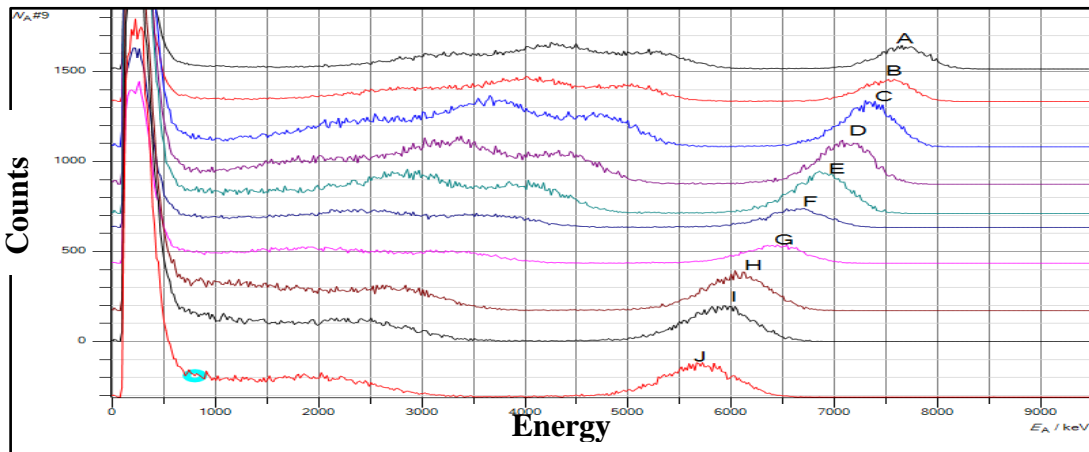


Figure 9. Energy loss of Alpha Particles in Gold Absorber Using Ra-226 Source

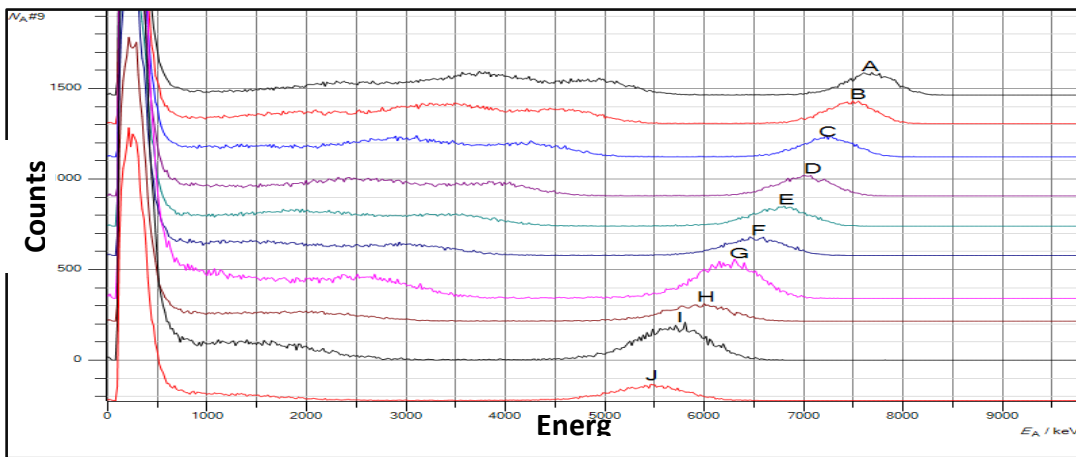


Figure 10. Energy loss of Alpha Particles in Aluminium Absorber Using Ra-226 Source

Table 6. Range and Energy Relation of Alpha Particles in Gold Foil at Different Pressure Using Ra-226 Source

Pressure [mbar]	Energy [MeV]	Range [mg/cm²]
100	7.7601	32.4
200	7.381	31.3
300	7.262	30
400	7.074	28.6
500	6.861	27
600	6.646	25.4
700	6.480	24.3
800	6.149	22.2
900	5.975	21.1
1000	5.655	19.8

Table 7. Range and Energy Relation Graph of Alpha Particles in Aluminium Foil at Different Pressures Using Ra-226 Source

Pressure [mbar]	Energy [MeV]	Range [mg/cm²]
100	7.7562	12
200	7.344	11.5
300	7.224	10.9
400	7.027	10.4
500	6.831	9.8
600	6.628	9.3
700	6.464	8.7
800	6.123	8
900	5.937	7.5
1000	5.615	7

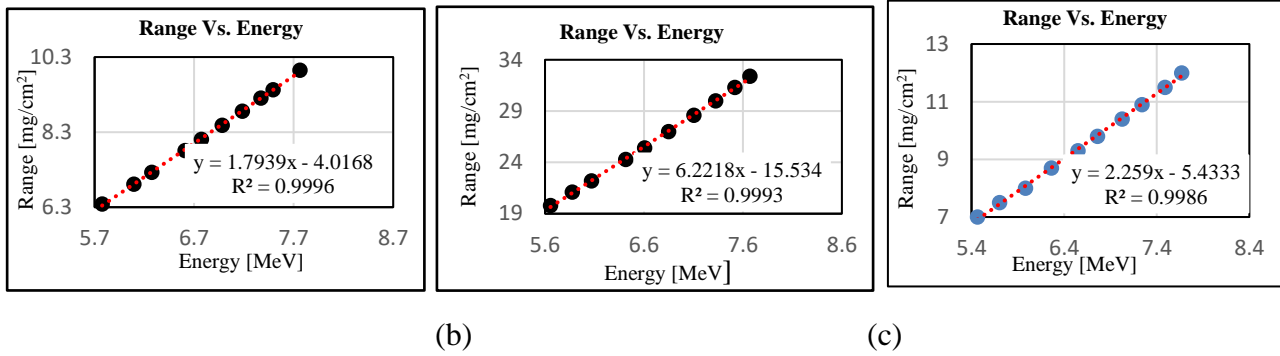


Figure 11. Range and Energy Relation of Alpha Particle (a) in Air Medium (b) in Gold and (c) in Aluminium using Ra-226 Source

Table 8. The Results Data of Theoretical and Experimental Energy Loss of Alpha Particle in Au and Al Foils using Ra-226 Source

Curves	Pressure [mbar]	Foil Thickness of Al [mg/cm ²]	Foil Thickness of Au [mg/cm ²]	ΔE[MeV] in Al			ΔE[MeV] in Au		
				Meas. Energy Loss	Theory Energy Loss	Error %	Meas. Energy Loss	Theory Energy Loss	Error %
A	100	2.16	3.86	0.0078	0.008	2.5	0.0039	0.004	2.5
B	200	2.16	3.86	0.148	0.150	1.3	0.111	0.115	3.4
C	300	2.16	3.86	0.148	0.154	3.8	0.110	0.116	5.1
D	400	2.16	3.86	0.159	0.157	1.2	0.112	0.117	4.2
E	500	2.16	3.86	0.151	0.161	6.2	0.121	0.119	1.6
F	600	2.16	3.86	0.145	0.165	12	0.127	0.121	4.9
G	700	2.16	3.86	0.144	0.170	15	0.128	0.122	4.9
H	800	2.16	3.86	0.152	0.175	13	0.126	0.124	1.6
I	900	2.16	3.86	0.157	0.181	13	0.119	0.125	4.8
J	1000	2.16	3.86	0.160	0.186	13.9	0.120	0.127	5.5

Comparison Results of Energy Loss of Alpha Particle in Gold and Aluminium Foils for Americium and Radium Sources at 100mbar

Energy loss of alpha particles in different absorbing media of gold and aluminium are compared for americium source. Measured energy loss spectra for the americium and radium sources in aluminium and gold are shown in Figures 12 (a) and (b). According to the results alpha particle energy loss is greater in aluminium foil than in gold foil due to greater absorber thickness. The calculated results for energy loss in gold and aluminium foils are shown in table 9. The relation between initial and final energy of alpha particles in gold and aluminium measured at 100mbar is shown in Figure 13. Stopping power of alpha particles in gold and aluminium is shown in Table 9. According to the results stopping power of alpha particles in gold is greater

than in aluminium due to high atomic number of golds have greater chance to Coulomb interaction between the atoms.

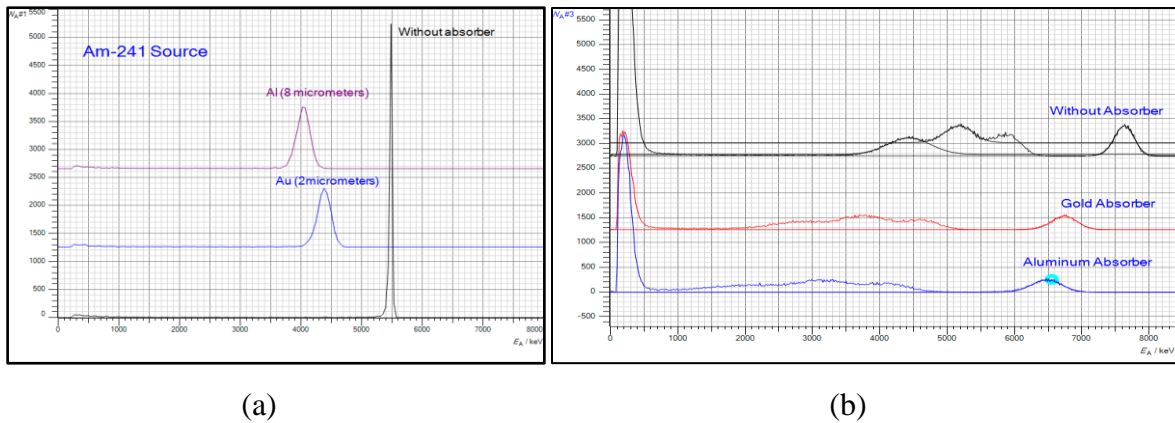


Figure 12. Energy Loss Spectra of Alpha Particles at 100 mbar using (a) Am-241 and (b) Ra-226 Source

Table 9. Initial and Final Energy Relation of Alpha Particles and Energy Loss

Elements	Without Absorber Energy [MeV]	After Passing Au Foil Energy [MeV]	After Passing Al Foil Energy [MeV]	Energy Loss in Au [MeV]	Energy Loss in Al [MeV]
Ra-226	4.777	3.154	2.450	1.623	2.327
Rn-222	5.249	4.288	3.380	0.961	1.869
Am-241	5.476	5.473	5.470	0.003	0.014
Po-218	5.980	5.327	4.992	0.653	0.988
Po-214	7.684	7.671	7.670	0.013	0.013

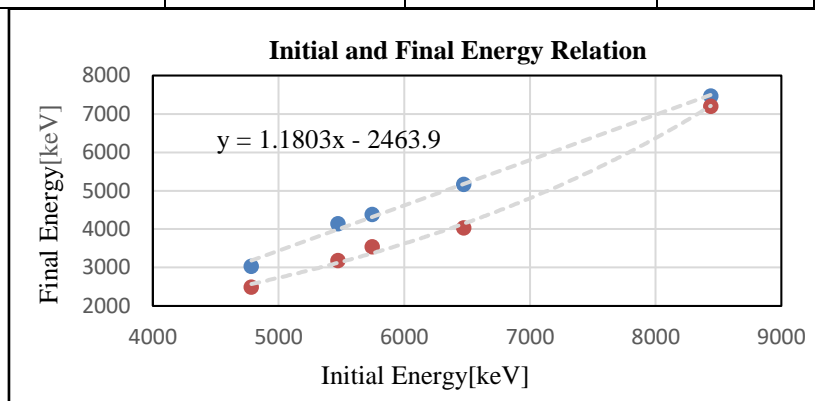


Figure 13. Initial and Final Energy Relationship of Alpha Particles at 100 mbar using Two Sources

Conclusion

In this research work, the alpha spectroscopic method was studied and determined the characteristics of alpha particles in the air and different absorbing medium of gold and aluminium foils using both two sources. Measurements were carried out using silicon semiconductor detector and the measured spectra are also analysed by RID program. In the present research work, the quantitative analysis of characteristics of alpha particles energy loss, range, stopping power and effective path length in air and in different density materials of Al and Au. The measured energy loss of alpha particles increases with an increase in the pressure inside the vacuum chamber. It was due to the reduction of air molecules in the vacuum chamber or in traversing path of the ions in the medium at higher pressures. This was resulted in a higher energy loss at high pressures or standard temperature and pressure. Further, the transmitted energy of alpha particles decreases exponentially as pressure decreases and that was resulted in the lower projected range of alpha particles. Measured energy loss and calculated energy loss, range and stopping power are also studied. In the case of transmitted energy of alpha particles increases the stopping power decreases exponentially. The measured energy loss characteristics are consistent with theoretical values. Experimental data of current experimental setup using with applied program are good in agreement with theoretical data. The current experimental research work could be used in determination of alpha energy and characteristics of energy loss in materials and also applied to radiation monitoring, safety, protection health physics and many other cases.

Finally, we conclude that the current experimental research work could be used in determination of alpha energy and characteristics of energy loss in materials and also applied to radiation safety and protection health physics.

Acknowledgements

The authors would like to thank Lt. Col. Kyaw Htay Naing, the head of our department, Lt. Col. Zaw Tun Oo, the head of Nuclear Physics Department, honorable supervisors, our colleagues and all persons who directly and indirectly contributed towards the success of this work.

References

- Andrius Poskus., “*Study of the alpha energies of Radium226*”, Experiment No.11. Vilnius University, 2015.
- Andrius Poskus., “*Absorption of alpha particles and electrons*”, Experiment No.9. Vilnius University, 2015
- Dulov E.N., Voronina E.V., Tagirov L.R., Bikchantaev M.M., “*Alpha Spectroscopy passing of alpha radiation through matter*”, Kazan Federal University publishing house, 2013.
- Evan RD., “*The Atomic Nucleus*”, Tata McGraw-Hill Publishing Company Ltd., 1955.
- Etim I.P., William E.S., Ekwe S.O., “*Alpha-Particle Spectroscopy and Ranges in Air.*”, International Journal of Scientific and Engineering Research, January 2014.
- Gamow, “*Gamow theory of alpha decay*”, ASP Conference Series, Vol.129, November 1996.
- H. H Anderson & J. F. Ziegler, “*Heavy Ions Stopping Power and Ranges*”, Cyclotron Institute, Texas A&M University, Vol.5, 1995.
- Knoll, G.F., “*Radiation Detection and Measurements, 3rd ED*”, John Wiley and Sons, Inc., 2000.

MECHANICAL TENSILE STRENGTH ANALYSIS OF POLY VINYL ALCOHOL(PVA) POLYMER REINFORCED WITH WASTE SCRAPED TIRE RUBBER FIBERS

Khin Sandar Lin¹, Chan Nyein Aung², Lwin Maung³

Abstract

The waste tire fibers were sourced and processed to reinforce Poly Vinyl Alcohol (PVA) polymer. The blended composite materials were prepared and tested for mechanical tensile strength analysis using a universal testing machine, EEU/20kN. The mechanical properties such as tensile strength, elongation at break, tensile modulus, yield strength and ultimate strength were determined by the Stress-Strain Analysis. Five PVA tested samples for each mix ratio are experimentally tested until the failure occurs by the Universal Material Testing Unit, EEU/20kN. The pure PVA has tensile strength is 48.71 MPa and the highest Scraped Tire Reinforced mixed with PVA by the 20 w/v% ratio has highest tensile strength is 52.218 MPa. The value of Elongation break (%), Tensile modulus (MPa), Yield strength (MPa) and Ultimate strength (MPa) are decreased as the filler percent increased. The waste tire fibers can be effectively utilized as a reinforcing agent in PVA composites, leading to improved mechanical properties. The significant implications for the development of sustainable composite materials and could contribute to reducing the environmental impact of waste tire disposal.

Keywords: Scraped Tire Rubber fibers, PVA, composites

Introduction

Nowadays PVA based polymers are being widely used in additive manufacturing. Poly (vinyl alcohol) PVA is a water-soluble synthetic polymer. It has the idealized formula $[\text{CH}_2\text{CH}(\text{OH})]_n$. Polyvinyl alcohol has a melting point of 180 to 190°C. Poly vinyl alcohol is a hydrophilic semi-crystalline polymer produced by polymerization of vinyl acetate to poly vinyl acetate (PVAc), and subsequent hydrolysis of PVAc to PVA. Commercial PVA is available in highly hydrolyzed grades (degree of hydrolysis above 98.5%) and partially hydrolyzed ones (degree of hydrolysis from 80.0 to 98.5%). The content of hydrolysis or the content of acetate groups in PVA affects its chemical properties, solubility and crystal growth ability [Wang T, M. T, S. G, et al., 2004].

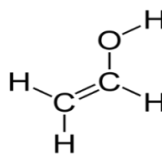


Figure-1 Molecular Structure of Poly vinyl alcohol (PVA)

¹ Department of Physics, Yangon University

² Department of Physics, Yangon University

³ Department of Physics, Mandala University

Polymeric scraped tire rubber fiber (STRF) is one of the byproducts derived from the processing of used vehicle tires. Presently, significant quantities of STRF are generated annually in most developed countries of the world. However, and unfortunately, STRF been an amalgam of crumb rubber, steel and other particles, its reusability has been limited. Hence, STRF is mainly used as a fuel source in kilns or landfilled. Sulfur vulcanization of rubber is the most commonly used chemical process, by which cross-links are formed between rubber polymer chains by heating, thereby enhancing the physical properties of vulcanizes. Thus, as a consequence of vulcanization, a typical tire rubber contains about 1.52–1.64% sulfur and other chemical constituents such as 81.2–85.2% carbon, 7.22–7.42% hydrogen, 1.72–2.07% oxygen and 0.31–0.47% nitrogen [Chen J, K, L, et al., 2001], nitrogen oxides (NO_x), Sulfur dioxide (SO₂), carbon monoxide (CO) and polycyclic aromatic hydrocarbon (PAH) are emitted during scrap tire combustion [Levendis Y, A, J, Y, P, et al., 1996]. The sulfur gases are also produced during scrap tire pyrolysis [Murena F, 2000]. Toxic hydrogen sulfide gas was also observed as a major byproduct of scrap tire pyrolysis [Tang L, H, et al., 2004]. Therefore, to avoid the inherent environmental pollution associated with the combustion of waste car tire rubber, it is imperative that alternative benign and value-added applications for STRF be developed.

The waste tire fibers were sourced and processed to reinforce Poly Vinyl Alcohol (PVA) polymer. The blended composite materials were prepared and tested for mechanical tensile strength analysis using a universal testing machine, EEU/20kN. The mechanical properties such as tensile strength, elongation at break, tensile modulus, yield strength and ultimate strength were determined by the Stress-Strain Analysis. Five PVA tested samples with the five weights per volume mix ratios of the waste scraped Tire fibers are experimentally tested until the failure occurs by using the Universal Material Testing Unit, EEU/20kN.

Materials and Experimental Methods

2.1. Materials

Poly Vinyl Alcohol (PVA, molecular weight of 186,000 g/mol, Sigma Aldrich, Germany) was purchased and used without further purification. The waste car tire was collected from the car workshop and cleaned to scrap the rubber filament from the waste vulcanized rubber car tire. Deionized water was used in the preparation of the blending PVA.

2.2 Preparation and Characterization of Waste Scraped tire rubber fiber

The waste car tire was collected and washed in water by using iron brush. The scrap tire rubber fibers were scraped from the washed pieces of the waste car tire by the iron brush rotor machine and put the scraped tire rubber fibers into the pure water to separate the rubbers and the iron dust, metal pieces of the tire by the floating method. The floating scraped tire rubber fibers were filtered and dried in the oven at 150°C for 2 hr. Finally, the remaining iron dust in the scraped tire rubber fibers were eliminated by the magnet.

The 2 g of PVA were dispersed in 10ml of deionized water and was stirred for 20 min at 80 °C with 500 rpm to get the transparent and homogeneous 20 w/v% PVA solution. The 20 w/v% PVA solution was poured into the ceramic mold to cast the pure PVA by solution-casting method and the resultant PVA was dried at 60 °C in the desiccator to synthesize pure PVA. The 0.5 g of the scraped tire rubber fiber (STRF) were slightly added into the homogenous 20 w/v% PVA solution and was stirred for 20 min at 80 °C with 500 rpm. The resultant rubber fiber mixed PVA solution was casted into ceramic mold by the solution casting method to get the 5 w/v%, STRF reinforced PVA. The 10 w/v%, 15 w/v% and 20 w/v% STRF reinforced PVA were also prepared by the use of 1 g, 1.5 g and 2g of the scraped tire rubber fiber (STRF) as the above solution-casting method. The resultant STRF blended PVAs were dried and kept at 60 °C in the desiccator. The sample preparation procedures of the pure PVA and scraped tire rubber fiber (STRF) blended PVA were exhibited as in the Figure-2. Five PVA- tested samples with the five weights per volume mix ratios of the waste scraped Tire fibers are experimentally tested until the failure occurs by the Universal Material Testing Unit, EEU/20kN, as in the Figure-3.

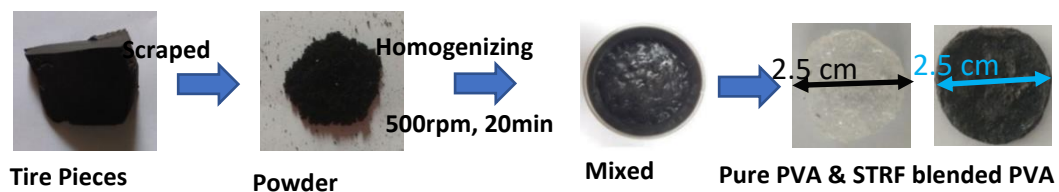


Figure-2 Preparation of the Waste Scraped Tire Rubber Fibers (STRF) Blended Polyvinyl Alcohol (PVA).



Figure-3 EEU 20KN/Universal Testing Machine Unit.

Results and Discussions

The pure PVA has tensile strength is 48.71 MPa and the highest mixed ratio of the Scraped Tire Reinforced mixed with PVA by the 20 w/v% has maximum tensile strength, 52.218 MPa. The value of Elongation break (%), Tensile modulus (MPa), Yield strength (MPa) and Ultimate strength (MPa) are decreased as the filler percent increased. Mechanical Properties of PVA Reinforced with Waste Scraped Tire Rubber Fibers were shown in the Table-1. The Stress-strain analysis curves of PVA and PVA reinforced with STRF were depicted as in the Figure- 4 to 8. The effect of Scraped tire rubber fibers (STRF) fillers on the stress-strain mechanical properties were depicted as in the Figure 9 to 13. The optimum w/v% ratio of the STRF filler is the 20 w/v% to achieve the maximum tensile strength, 52.218 MPa. The mechanical stress -strain analysis value of the pure PVA is well agreed with the literature, Research work of the Naman Jain, G.B Pant University of Technology, India [Jain, Naman et al., 2017].

Table-1 Mechanical Properties of PVA Reinforced with Waste Scraped Tire Rubber Fibers.

Properties	Result				
	Pure PVA	(5w/v%)	(10w/v%)	(15w/v%)	(20w/v%)
Tensile strength (MPa)	48.71	38.62	28.089	28.93	52.218
Elongation break (%)	223.5	3.625	4.094	5.07	3.93
Tensile modulus (MPa)	705.07	144.31	36.217	7.62	91.6
Yield strength (MPa)	47.056	3.63	26.71	24.21	40.27
Ultimate strength (MPa)	68.459	38.623	28.089	28.93	52.218

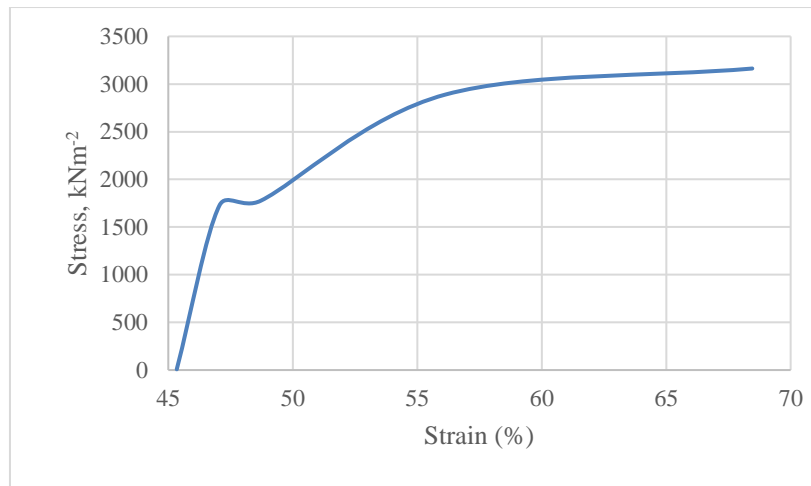


Figure 4- Stress-strain analysis curve of pure PVA

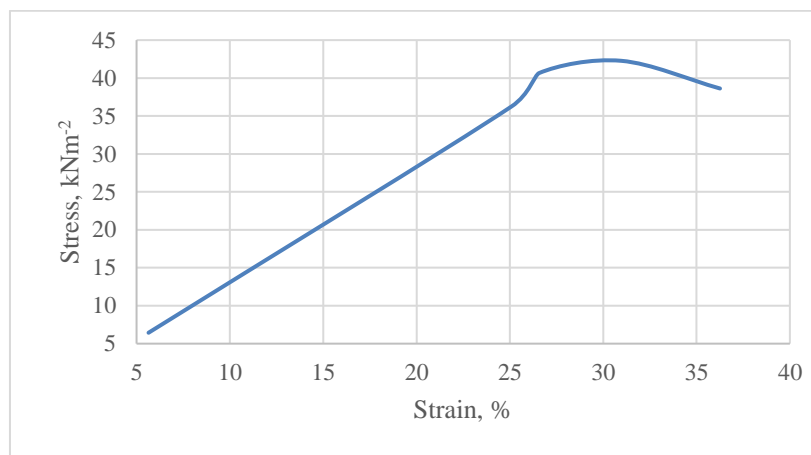


Figure 5- Stress-strain analysis curve of (5w/v%) pure PVA reinforced STRF

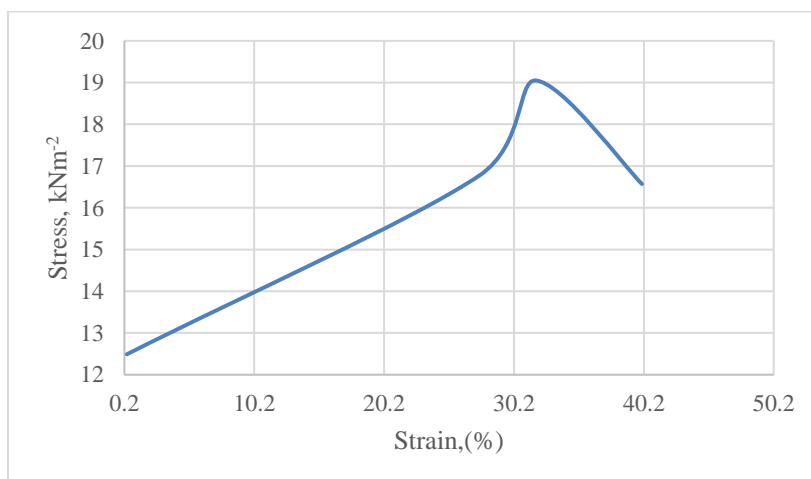


Figure 6- Stress-strain analysis curve of (10 w/v%) pure PVA reinforced STRF

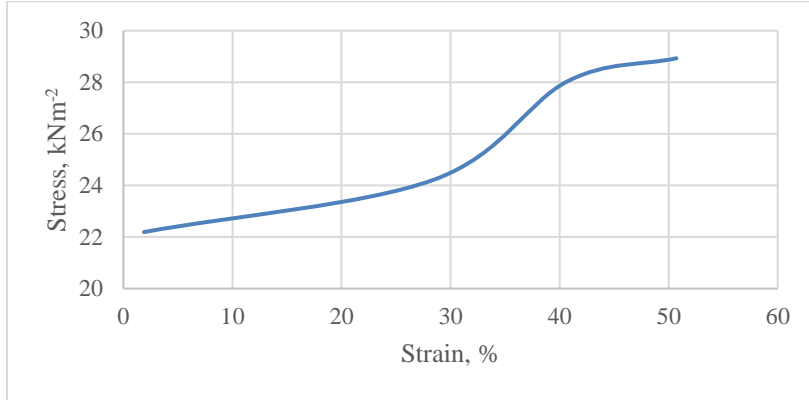


Figure 7- Stress-strain analysis curve of (15w/v%) pure PVA reinforced STRF

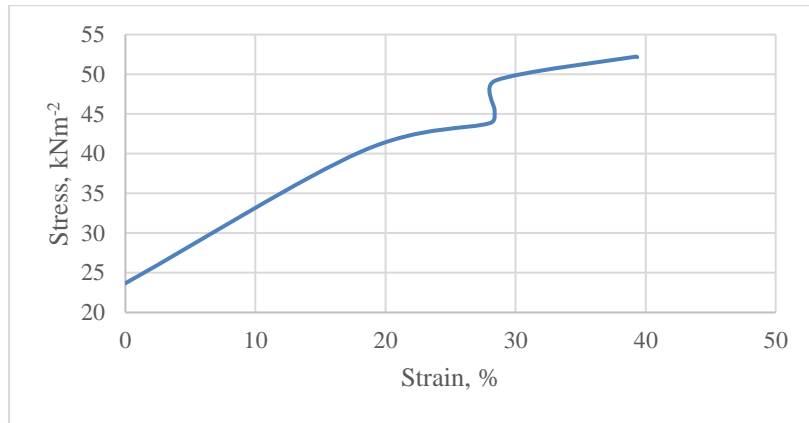


Figure 8- Stress-strain analysis curve of (20w/v%) pure PVA reinforced STRF

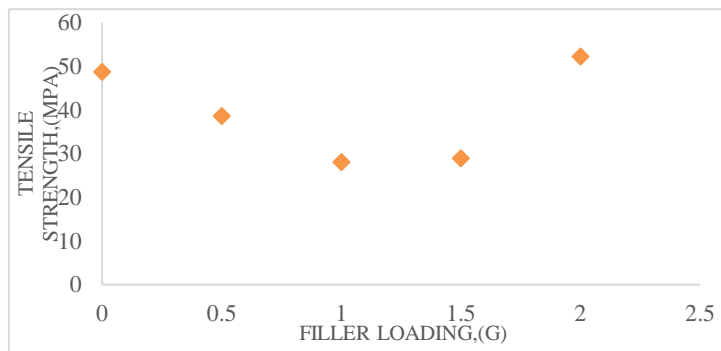


Figure 9 - Effect of filler loading on tensile strength of Pure PVA and PVA reinforced STRF

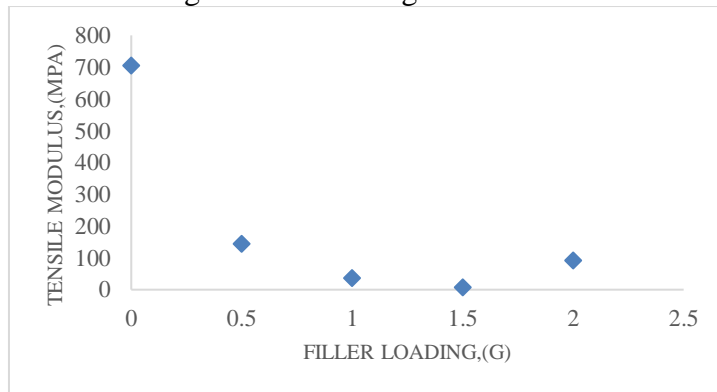


Figure 10- Effect of filler loading on tensile modulus of Pure PVA and PVA reinforced STRF

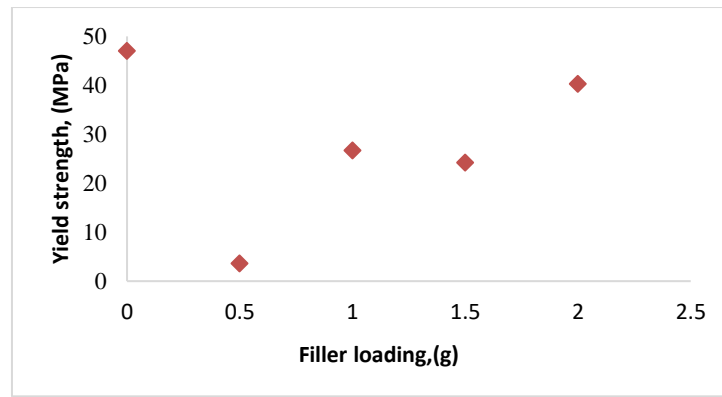


Figure 11- Effect of filler loading on yield strength of Pure PVA and PVA reinforced STRF

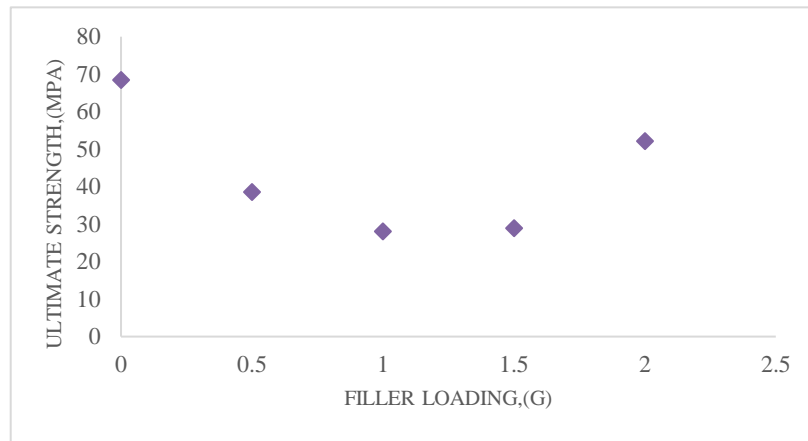


Figure 12- Effect of filler loading on ultimate strength of Pure PVA and PVA reinforced STRF

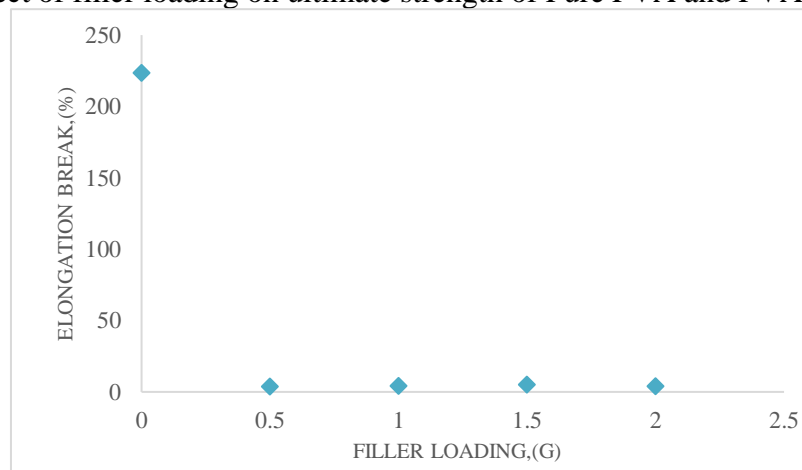


Figure 13- Effect of filler loading on Elongate break of Pure PVA and PVA reinforced STRF

Conclusion

Although the values of the mechanical stress-strain were decreased as weight per volume ratio of the STRF increased, the maximum value of the Tensile Strength, 52.218 MPa was achieved at the 20 w/v% ratio of the STRF filler. The waste tire fibers can be effectively utilized as a reinforcing agent in PVA composites, leading to improved mechanical properties. The significant implications for the development of sustainable composite materials and could contribute to reducing the environmental impact of waste tire disposal.

Acknowledgements

I wish to thank Professor Dr Yin Maung Maung, Head of Department of Physics, University of Yangon, for his permission and suggestion in this research. I would also like to thank my Supervisor, Associate Professor, Dr Chan Nyein Aung, Department of Physics, University of Yangon, for his helpful advice to do this research. I would like to thank Professor Dr Aye Ngwe, Department of Physics, Patheingyi University for his kind advice, encouragements and suggestions for this research.

References

- Chen JH, Chen KS, Tong LY (2001) On the pyrolysis kinetics of scrap automotive tires. *J Hazard Mater* B84:43–550.
- Jain, Naman (2017) A review on mechanical and water absorption properties of polymer vinyl alcohol based composite film. *J Mechanical Behavior of Materials* 26: 213-222
- Levendis YA, Atal A, Carlson J, Dunayevskiy Y, Vouros P(1996) Comparative study on the combustion and emissions of waste tire crumb and pulverized coal. *Environ Sci Technol* 30:2742–2754.
- Murena F (2000) Kinetics of sulphur compounds in waste tyres pyrolysis. *J Anal Appl Pyrol* 56:195–205.
- T. Wang, M. Turhan, S. Gunasekaran, *Polymer International* 53 (2004)911.
- Tang L, Huang H (2004) An investigation of sulfur distribution during thermal plasma pyrolysis of used tires. *J Anal Appl Pyrol* 72:35–40.

Study on Physical and Chemical Properties of Soil at Kalay University Campus

Kyaw Swar Min¹, Kay Khing Oo², Moe Sandar Win³, Hnin Nu Nu Aung⁴ Sitar Kyaw⁵

Abstract

Five soil samples were taken from Kalay University campus. Next, five soil samples were grounded with mortar for 1hr and then sieved by a 0.01cm sieve. Then, each sample was weighed 600 grams. To obtain more samples, 100 grams of each from five samples were re-weighed, mixed, and grounded by agate mortar. Finally, a total of six fine soil samples were obtained. Potential Hydrogen (pH) of all soil samples was measured to consider soil acidity or alkalinity. Electrical conductivities of soil samples were tested to investigate the amounts of salts in the soil. Measurements of soil content of Nitrogen(N), Phosphorus(P), and Potassium(K) of two fine samples were analyzed. Energy Dispersive of X-ray Fluorescence (EDXRF) measurements of two fine samples were carried out to determine the elemental contents of soils.

Keywords: re-weighed, Potential Hydrogen, NPK, EDXRF.

Introduction

Soil

Soil supports the richest biodiversity on earth and functions as a filter for, and a buffer of inorganic and organic contaminants as well as pathogenic microorganisms and viruses. Soil is very important and useful for growing crops. It can be categorized into sand, clay, silt, peat, chalk and loam types of soil based on the dominating size of the particles within a soil.

Heavy Metals

Heavy metals occur naturally in soils and in source materials. Metal pollutants in soil may be absorbed by the plants through their roots and vascular systems. Heavy metals are important environmental pollutants that cause toxic effects on plants, thus lessening productivity and posing dangerous threats to the agro-ecosystems. There are numerous essential heavy metals like Copper, Iron, Magnesium, Cobalt, Zinc, and Nickel required by plants as they form cofactors that are structurally and functionally vital for enzymes and other proteins. Nevertheless, when they exceed their threshold concentrations, their actions are considered toxic to plant development.

Sample Preparation and Experimental Technics

Descript of the Study Area

This study was carried out in Kalay University Campus, Kalay Township, Sagaing Region at 23°12'23" North and 93°58'9" East, in December, 2022.

Sample Collection and Preparation

Soil sampling was used by a zone-based method. Each of the five soil samples was taken from Kalay University campus. Each soil sample was dug to a depth of 6 inches and was measured 20 feet between each other. Each soil sample was grounded with mortar for 1hr and

¹ Department of Physics, Kalay University

² Department of Physics, Kalay University

³ Department of Physics, Kalay University

⁴ Department of Physics, Kalay University

⁵ Department of Physics, Kalay University

sieved by using a 0.01cm sieve. Then, each sample was weighed at 600 grams. To obtain a fine sample, 100 grams of each five samples with 600 grams were re-weighed, mixed and grounded by agate mortar. And then, 500 grams of fine sample was obtained as sample 6. All soil samples were dried at room temperature 25°C.



Figure 1 Photographs of soil samples with the depth of 6 inches



Figure 2 Photographs of grinding by mortar and sieving by 0.01cm sieve

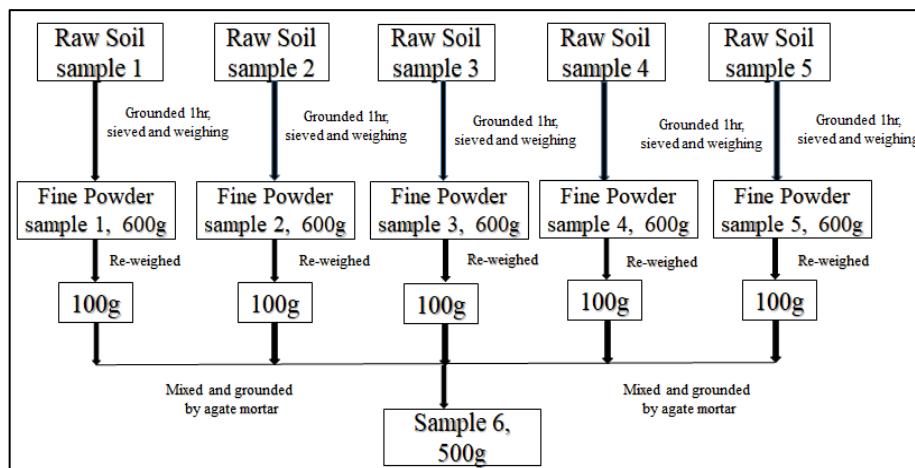


Figure 3 Flow chart of sample preparation for Kalay University campus



Figure 4 Photograph of weighing soil samples with 100grams and the collection and preparation of fine soil samples.

Calibration Procedure of pH Meter

To measure the pH level and the amount of water in the soil, the Kelway Soil Acidity and Moisture Tester was used.

1. The top dial on the tester must be look and make sure that the top of the needle points to the number 7. If not, it must calibrate the device.
2. The top of the tester was rotated two to three times to clean the tip.
3. The white bottom on the side of the tester was pressed to measure the soil moisture.
4. The bottom of the needle stabilizes and is continuously held for two to three minutes.
5. It is necessary to see the top dial where the top of the needle is pointing to determine the pH level of the soil.

The pH of soil samples was measured three times at room temperature, one week apart.



Figure 5 Photographs of Kelway Soil Acidity and Moisture Tester



Figure 6 Photographs of measured the pH (potential hydrogen) of soil sample.

Calibration Procedure of HI 8633 Conductivity Meter

HI 8633 Conductivity Meter was used to measure the amount of salts in soil samples. Conductivity is measured by taking a soil sample, making a saturated paste of soil and deionized water, extracting the water, and then measuring the electrical conductivity of the extracted solution.

1. The conductivity probe to the meter was switched on and then, immersed in the calibration solution and the temperature was checked.
2. The temperature of the buffer solution was recorded at 25° C and the 19.99mS/cm range was selected by pressing the appropriate key.
3. While measuring, the probe was shaken into the soil sample solution, and then, in the electrical conductivity meter, the result was kept stable and monitored.



Figure 7 Photograph of HI 8633 Conductivity Meter



Figure 8 Photographs measuring the conductivity of Kalay University's soil sample

NPK (Nitrogen, Phosphorus, and Potassium)

The letters NPK stand for the three major nutrients that plants need to live and grow- nitrogen, phosphorus, and potassium.

Test Procedure of Soil Nitrogen

1. Deionized water was filled to the 50ml mark in the sample container.
2. One level scoop of Extract N was added to the deionized water.
3. One 2ml scoop of soil was added to the deionized water / Extract N solution, replaced the lid, and shaken for one minute.
4. One level spoonful of *Nitratest*TM powder was added to the soil using the scoop contained within *Nitratest*TM.
5. A filter paper was folded into quarters and inserted into the filter funnel and then Extract N solution was poured into the filter paper and allowed the extraction filtrate to collect in the second container.
6. Once 10ml of the filtrate was available to the 10ml mark and blanked the soil-test 10 photometer.
7. The soil Nitrogen result was displayed by photometer as mg/l N.



Figure 9 Photographs of Soiltest 10 photometer and Chemical box



Figure 10 Procedure of N (Nitrogen Test)

Test Procedure of Soil Phosphorus

1. The sample container was filled to the 50ml mark with deionized water.
2. Five Extract P tablets was added to the deionized water, replaced the lid and shaken gently to dissolve.
3. One 2ml scoop of soil was added to the deionized water/ Extract P solution, replaced the lid and shaken for one minute.
4. A filter paper was folded into quarters and inserted into the filter funnel.
5. One acidifying S tablet was added, crushed and mixed gently to dissolve fully.
6. The soil test 10 photometer was blanked and then one phosphate P tablet was added, crushed and mixed to dissolve fully.
7. The sample solution was inserted into the soil test 10 photometer for ten minutes. Finally, the soil phosphorus result was displayed by soil test 10 photometer as mg/ l P.



Figure 11 Procedure of P (Phosphorus Test)

Test Procedure of Soil Potassium

1. The sample container was filled to the 50ml mark with deionized water.
2. One level scoop of Extract K was added to the deionized water and shaken.
3. Further, 2 ml of soil was added to the solution and shaken for one minute.
4. A filter paper was folded into quarters and inserted into the filter funnel.
5. 10 ml of filtered sample was placed into the tube and then blanked.
6. After blanking, one potassium K tablet was added to the filtered sample and the soil sample solution was inserted into soil test 10 photometer for ten minutes.
7. The soil potassium result was displayed by a photometer as mg/l K.



Figure 12 Procedure of K (Potassium Test)

X-Ray Fluorescence Spectrometry

X-ray fluorescence spectrometry (XRF) is a non-destructive analytical method, it is fast and can simultaneously measure many elements, both solid and liquid samples. XRF is used in controlling the quality of many products, such as Fe determination in milk powder or determination of vitamins and essential minerals, as new examples of XRF applications in human health.



Figure 13 Measurement condition of Energy Dispersive X-Ray Fluorescence (EDXRF) Spectrometer (EDX 7000 Shimadzu)

Results and Discussion

Potential Hydrogen (pH) Analysis

The pH of six soil samples was measured three times at room temperature, one week apart. Therefore, the result data of pH values of all soil samples were different. So, the pH (potential hydrogen) values depend on the moisture of soils. Generally, 6.6 or lower indicates acidic soil, 6.7 to 7.3 means neutral soil, and soils are generally alkaline from high pH 8.0 to 8.5.

Table 1 Result data of pH (potential hydrogen) measurements of samples

No	Sample Name	Measurements of potential hydrogen(pH) soil level			Average values of pH
		1 st Week	2 nd Week	3 rd Week	
1	Sample 1	6.7	6.7	6.7	6.7
2	Sample 2	6.7	6.7	6.4	6.6
3	Sample 3	6.6	6.7	6.5	6.6
4	Sample 4	6.3	6.4	6.2	6.3
5	Sample 5	6	6.2	6	6.1
6	Sample 6(mixed)	6.6	6.5	6.5	6.5

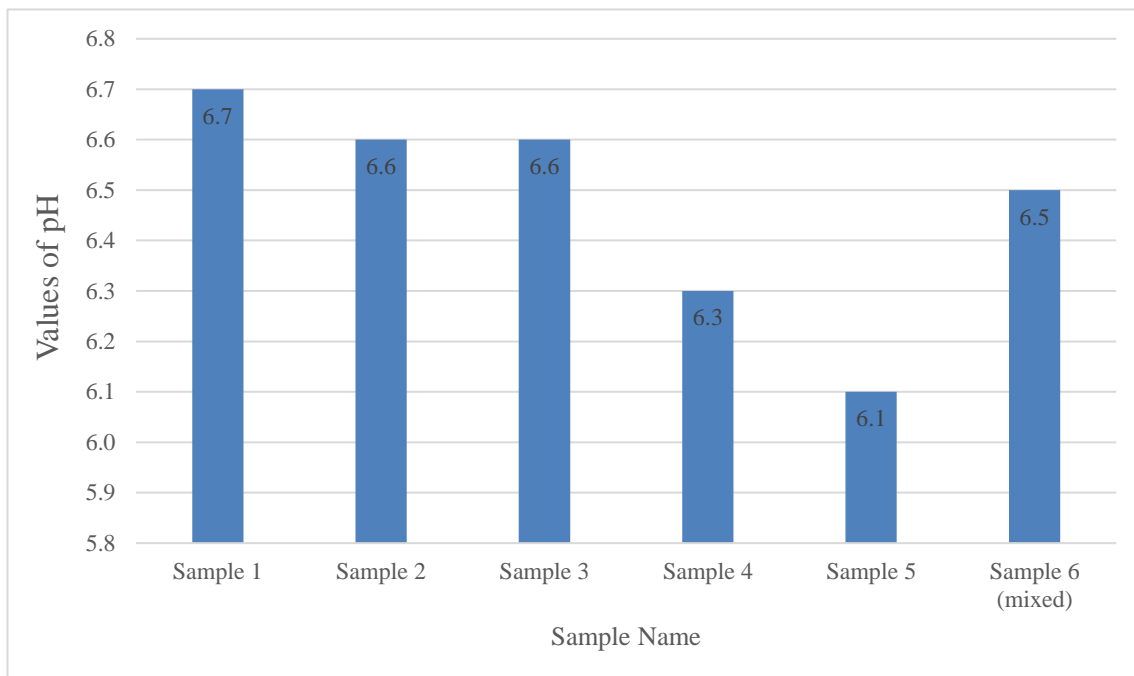


Figure 14 The comparison of average values of pH in six samples

At 1st week, the samples 1 and 2 were neutral soils and samples 3, 4, 5 and 6 were acidic soils. After one week apart, 2nd week, the values of pH of samples were changed due to moisture of soils at room temperature. The result data of samples 1, 2 and 3 were neutral soil and samples 4, 5 and 6 were acidic soils. Next, 3rd week, the sample 1 was neutral soil and samples 2, 3, 4, 5 and 6 were acidic soils.

Electrical Conductivity Analysis

Table 2 Test results of electrical conductivity of six samples

No	Sample Name	Room temperature	Measurements of Electrical Conductivity(mS/cm)
1	Sample 1	25°C	25.4 mS/cm
2	Sample 2	25°C	23.3 mS/cm
3	Sample 3	25°C	24.5 mS/cm
4	Sample 4	25°C	26.1 mS/cm
5	Sample 5	25°C	24.1 mS/cm
6	Sample 6(mixed)	25°C	23.8 mS/cm

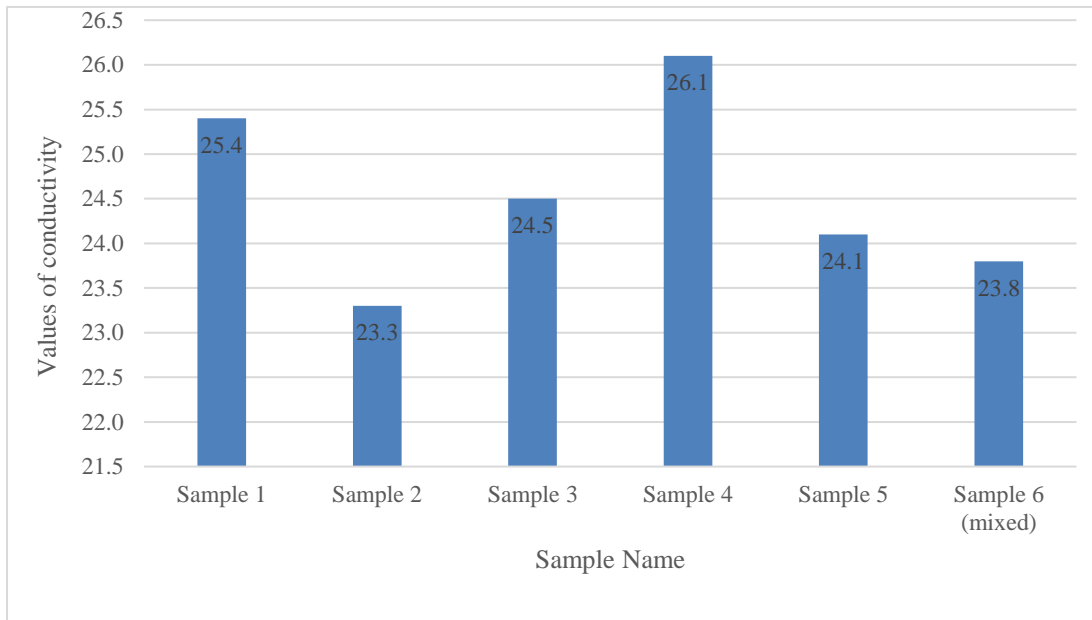


Figure 15 The comparison of values of electrical conductivity in six samples

The Multi-Range of HI 8633 Conductivity Meter is from 0.0 $\mu\text{S}/\text{cm}$ to 199.9 mS/cm . Sands have a low conductivity, silts have a medium conductivity, and clays have a high conductivity. Thus, all the soil samples collected from Kalay University campus were sandy soils, the amounts of salts in soil samples were low and enough nutrients were not given due to low conductivities.

NPK (Nitrogen, Phosphorus and Potassium) Analysis

Nitrogen is responsible for leaf and stem growth and applying it will give big green leaves. Phosphorus is responsible for energy transfer and utilization in plants. Applying it will help plant grow and mature, and help its root systems develop better. Soil potassium is responsible for sugars and water movement around plant cells and applying it will help fruit and flower quality. Healthy levels of nitrogen in soil range 40 ppm or 0 to 25 mg/l N. Healthy levels of phosphorus in soil range from 25 to 50 ppm (or) 0 to 150 mg/l P. Healthy levels of potassium in soil range from 40 to 80 ppm (or) 0 to 450 mg/l K.

Table 4 Test result of soil NPK

No	Sample name	Measurements of soil NPK result (mg/l)					
		Soil Nitrogen		Soil Potassium		Soil Phosphorus	
		1 st	2 nd	1 st	2 nd	1 st	2 nd
1	Sample 6 (mixed)	3.0 $\text{mg}/\text{l}_\text{N}$	0.0 $\text{mg}/\text{l}_\text{N}$	85 $\text{mg}/\text{l}_\text{K}$	50 $\text{mg}/\text{l}_\text{K}$	$\ll\text{mg}/\text{l}_\text{P}$	$\ll\text{mg}/\text{l}_\text{P}$

Source: Laboratory Test result from Department of Geography

The result data of soil sample were found that not only nitrogen but also potassium was present but phosphorus was absent in soil. Due to presence of nitrogen and potassium, the

samples were suitable for planting fruits and flowers and then leaf and stem growth but root system need to be taken care of due to phosphorus deficiency.

Energy Dispersive of X-Ray Fluorescence Analysis

Table 5 The quantitative result of EDXRF of sample 6

Analyte	Result (%)	Standard Deviation	Calculated Procedure	Line	Intensity
Si	57.053	[1.256]	Quan-FP	SiK α	7.6966
Al	19.727	[5.464]	Quan-FP	AlK α	0.5019
Fe	12.745	[0.033]	Quan-FP	FeK α	619.8347
K	7.237	[0.091]	Quan-FP	K K α	25.5751
Ti	1.616	[0.021]	Quan-FP	TiK α	23.3316
Ca	0.882	[0.018]	Quan-FP	CaK α	5.2584
Mn	0.344	[0.005]	Quan-FP	MnK α	12.5076
Zr	0.134	[0.003]	Quan-FP	ZrK α	26.4726
V	0.051	[0.011]	Quan-FP	VK α	1.0686
Zn	0.049	[0.004]	Quan-FP	ZnK α	3.7620
Sr	0.045	[0.003]	Quan-FP	SrK α	8.2695
Cu	0.043	[0.005]	Quan-FP	CuK α	2.8035
Cr	0.026	[0.007]	Quan-FP	CrK α	0.7733
Y	0.020	[0.003]	Quan-FP	Y K α	3.7107
Rb	0.016	[0.003]	Quan-FP	RbK α	2.7514
Ni	0.013	[0.005]	Quan-FP	NiK α	0.6795

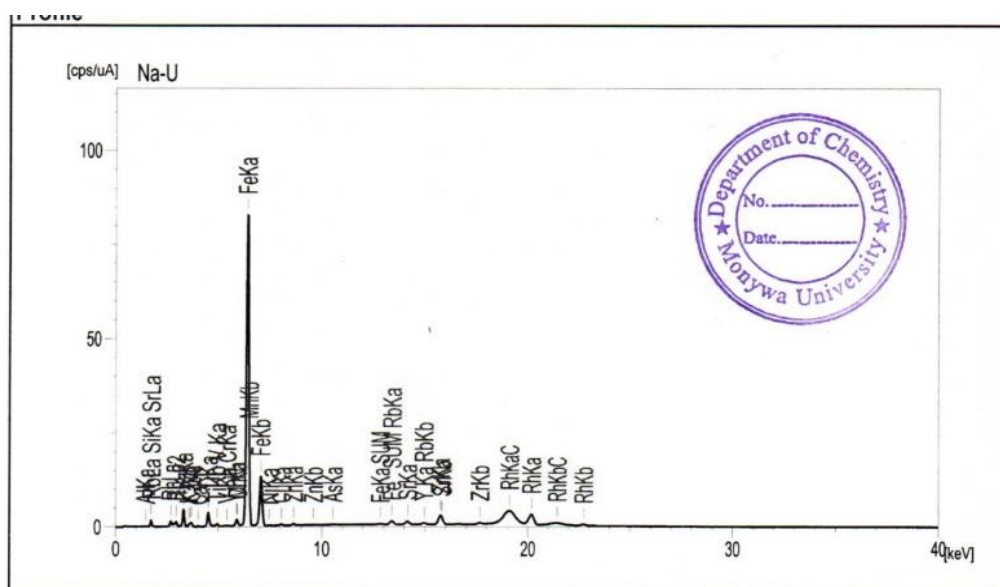


Figure 16 The comparison of intensity of metals in soil

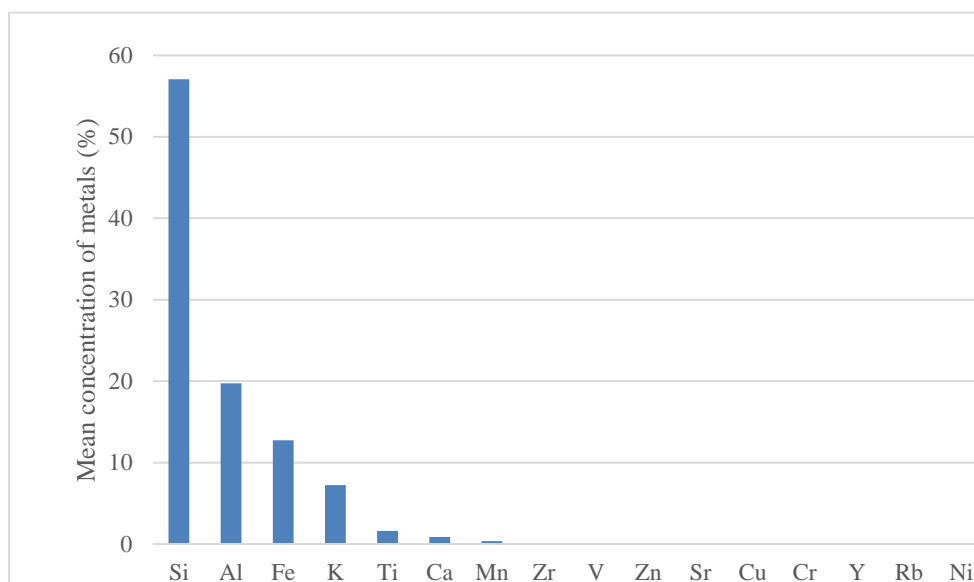


Figure 17 The comparison of mean concentration of metals in soil

It was found that the decreasing order of heavy metal concentration was Si > Al > Fe > K > Ti > Ca > Mn > Zr > V > Zn > Sr > Cu > Cr > Y > Rb > Ni. The mean value of concentration of Silicon (Si) was the highest and that of Nickel (Ni) was the lowest value. Elements like Silicon, Aluminum, Iron, Potassium and Titanium can be clearly identified; traces of Calcium, Manganese, Zirconium, Vanadium, Zinc, Strontium, Copper, Chromium, Yttrium, Rubidium and Nickel in lower concentration can be also observed. The peak FeK α was highest and then peak AlK α was lowest.

Conclusion

As the values of pH (pH<7) in all soil samples were low, it was found that Kalay University's soil samples were acidic soils. It was suitable for growing only acid-loving plants.

All of six soil samples were sandy soils, amount of salts in soil samples were low and enough nutrients due to low conductivities.

Then, the content of nitrogen and potassium of the sample 6 was suitable for planting fruits and flowers and then leaf and stem growth but root system need to be taken care of due to phosphorus deficiency.

The sixteen metals were found in soil samples 6. The mean concentration of Silicon (Si) was extremely higher than the other metals. The concentrations of micronutrients of Copper, Zinc, Iron, Manganese, Zirconium, Strontium, Chromium, Rubidium, Vanadium, Nickel and Yttrium become toxic only when a concentration limit is exceeded.

Acknowledgements

We wish to express our gratitude to Dr Yaw Han Htun, Rector of Kalay University, for his kind permission to carry out this research.

References

- Barrea, R.A., Mainardi, R.T, (1998) X-Ray Spectrometry.
- B. Beckhoff B. Kanngeier, N. Langhoff, (2006) "Handbook of Practical X-ray Fluorescence Analysis,"
- F. Visconti and J.M.de Paz, (2016) "Electrical Conductivity Measurements in Agriculture: The Assessment of Soil salinity," in New Trends and Developments in Metrology, In Tech,.
- Janssens. K. (2003), 'X-ray Fluorescence Analysis.'
- Smith, J.L., and J.W. Doran. (1996). Measurement and use of pH and electrical conductivity for soil quality analysis.

APPLYING ONE-DIMENSIONAL DIFFERENTIAL TRANSFORM METHOD TO PARTIAL DIFFERENTIAL EQUATIONS

Hnin Ei Phyu¹

Abstract

In this paper, definitions of one-dimensional differential transform (reduced differential transform) and inverse differential transform are described. And then, properties of one-dimensional differential transform are expressed. After that, one-dimensional differential transform is utilized to solve the initial value problems for linear one-dimensional partial differential equations with constant coefficients and variable coefficients. Finally, one-dimensional differential transform is applied to solve the initial value problems for two-dimensional second-order partial differential equations.

Keywords: partial differential equations, one-dimensional differential transform, applications

Introduction

This paper is a continuation of our previous work [Hnin and Khin, 2023]. In [Hnin and Khin, 2023], the one-dimensional differential transform method was used for solving initial value problems for ordinary differential equations with constant coefficients and variable coefficients. Differential transform method can be used for solving initial value problems for differential equations and integral equations. In this paper, we are interested in solving one-dimensional and two-dimensional second-order partial differential equations by using a one-dimensional differential transform method.

The rest of this paper is organized as follows: In Section 2, basic concepts of one-dimensional differential transforms are recalled. The main results are demonstrated in Section 3 and Section 4 respectively by solving the initial value problems for one-dimensional partial differential equations and two-dimensional partial differential equations using one-dimensional differential transform method.

Preliminaries

In this section, the definitions of one-dimensional differential transform and its properties are described.

Definition 1[Raslan, Biswas and Abu Sheer, 2012]

If $u(x, t)$ is analytic and differentiable continuously in the domain of interest, then let

$$U_k(x) = \frac{1}{k!} \left[\frac{\partial^k}{\partial t^k} u(x, t) \right]_{t=t_0}, \quad (1)$$

where the spectrum $U_k(x)$ is the **transformed function**, which is called **T-function**.

Definition 2 [Raslan, Biswas and Abu Sheer, 2012]

Differential inverse transform of $U_k(x)$ is defined as follows:

$$u(x, t) = \sum_{k=0}^{\infty} U_k(x) (t - t_0)^k. \quad (2)$$

Substitution (1) into (2), we obtain

* Special Award(2023)

¹Department of Mathematics, University of Mandalay

$$u(x, t) = \sum_{k=0}^{\infty} \frac{1}{k!} \left[\frac{\partial^k u(x, t)}{\partial t^k} \right]_{t=t_0} (t - t_0)^k. \quad (3)$$

When (t_0) are taken as $(t_0 = 0)$, then (3) is expressed as

$$u(x, t) = \sum_{k=0}^{\infty} \frac{1}{k!} \left[\frac{\partial^k u(x, t)}{\partial t^k} \right]_{t=t_0} t^k,$$

and (1) is shown as

$$u(x, t) = \sum_{k=0}^{\infty} U_k(x) t^k. \quad (4)$$

In real application, the function $u(x, t)$ by a finite series of (4) can be written as

$$u(x, t) = \sum_{k=0}^n U_k(x) t^k, \quad (5)$$

usually, the value of n is decided by convergence of the series coefficients.

Some Properties of One-Dimensional Differential Transform

Theorem 1 [Khatib, (2016)]

If $z(x, t) = \alpha u(x, t) + \beta v(x, t)$, the differential transform of $z(x, t)$ be $Z_k(x)$, then $Z_k(x) = \alpha U_k(x) + \beta V_k(x)$, where α and β are constants.

Proof: Let $z(x, t) = \alpha u(x, t) + \beta v(x, t)$. Then,

$$\begin{aligned} Z_k(x) &= \frac{1}{k!} \left[\frac{\partial^k}{\partial t^k} z(x, t) \right]_{t=0} \\ &= \frac{1}{k!} \left[\frac{\partial^k}{\partial t^k} (\alpha u(x, t) + \beta v(x, t)) \right]_{t=0} \\ &= \frac{1}{k!} \left[\frac{\partial^k}{\partial t^k} (\alpha u(x, t)) + \frac{\partial^k}{\partial t^k} (\beta v(x, t)) \right]_{t=0} \\ &= \frac{\alpha}{k!} \left[\frac{\partial^k}{\partial t^k} u(x, t) \right]_{t=0} + \frac{\beta}{k!} \left[\frac{\partial^k}{\partial t^k} v(x, t) \right]_{t=0} \\ &= \alpha U_k(x) + \beta V_k(x). \end{aligned}$$

Therefore, $Z_k(x) = \alpha U_k(x) + \beta V_k(x)$. □

Theorem 2 [Khatib, (2016)]

If $z(x, t) = \frac{\partial}{\partial x} u(x, t)$, and the differential transform of $z(x, t)$ be $Z_k(x)$, then

$$Z_k(x) = \frac{\partial}{\partial x} U_k(x).$$

Proof: Let $z(x, t) = \frac{\partial}{\partial x} u(x, t)$. Then, we have

$$\begin{aligned} Z_k(x) &= \frac{1}{k!} \left[\frac{\partial^k}{\partial t^k} z(x, t) \right]_{t=0} \\ &= \frac{1}{k!} \left[\frac{\partial^k}{\partial t^k} \left(\frac{\partial}{\partial x} u(x, t) \right) \right]_{t=0} \\ &= \frac{\partial}{\partial x} \left[\frac{1}{k!} \left(\frac{\partial^k}{\partial t^k} u(x, t) \right) \right]_{t=0} \\ &= \frac{\partial}{\partial x} U_k(x). \end{aligned}$$

Therefore, $Z_k(x) = \frac{\partial}{\partial x} U_k(x)$. □

Theorem 3 [Khatib, (2016)]

If $z(x, t) = \frac{\partial^2}{\partial x^2} u(x, t)$, and the differential transform of $z(x, t)$ be $Z_k(x)$, then

$$Z_k(x) = \frac{\partial^2}{\partial x^2} U_k(x).$$

Proof: Let $z(x, t) = \frac{\partial^2}{\partial x^2} u(x, t)$. Then, we have

$$\begin{aligned} Z_k(x) &= \frac{1}{k!} \left[\frac{\partial^k}{\partial t^k} z(x, t) \right]_{t=0} \\ &= \frac{1}{k!} \left[\frac{\partial^k}{\partial t^k} \left(\frac{\partial^2}{\partial x^2} u(x, t) \right) \right]_{t=0} \\ &= \frac{\partial^2}{\partial x^2} \left[\frac{1}{k!} \left(\frac{\partial^k}{\partial t^k} u(x, t) \right) \right]_{t=0} \\ &= \frac{\partial^2}{\partial x^2} U_k(x). \end{aligned}$$

Therefore, $Z_k(x) = \frac{\partial^2}{\partial x^2} U_k(x)$. □

Theorem 4 [Khatib, (2016)]

If $z(x, t) = \frac{\partial^m}{\partial t^m} u(x, t)$, and the differential transform of $z(x, t)$ be $Z_k(x)$, then

$$Z_k(x) = \frac{(k+m)!}{k!} U_{k+m}(x).$$

Proof: Let $z(x, t) = \frac{\partial^m}{\partial t^m} u(x, t)$. Then, we have

$$\begin{aligned}
Z_k(x) &= \frac{1}{k!} \left[\frac{\partial^k}{\partial t^k} z(x, t) \right]_{t=0} \\
&= \frac{1}{k!} \left[\frac{\partial^k}{\partial t^k} \left(\frac{\partial^m}{\partial t^m} u(x, t) \right) \right]_{t=0} \\
&= \frac{(k+m)!}{k!(k+m)!} \left[\frac{\partial^{k+m}}{\partial t^{k+m}} u(x, t) \right]_{t=0} \\
&= \frac{(k+m)!}{k!} U_{k+m}(x).
\end{aligned}$$

Therefore, $Z_k(x) = \frac{(k+m)!}{k!} U_{k+m}(x)$. □

Theorem 5 (Leibniz's theorem)

If $y = uv$, where u and v are any functions of x , then

$y_n = u_n v + {}^n C_1 u_{n-1} v_1 + {}^n C_2 u_{n-2} v_2 + \dots + {}^n C_r u_{n-r} v_r + \dots + uv_n$, where, suffixes of u and v denote the number of times they are differentiated.

Proof: [See, Kishan, 2007]. □

Theorem 6 [Khatib, (2016)]

If $z(x, t) = u(x, t)v(x, t)$, and the differential transform of $z(x, t)$ be $Z_k(x)$, then

$$Z_k(x) = \sum_{r=0}^k U_r(x) V_{k-r}(x).$$

Proof: Let $z(x, t) = u(x, t)v(x, t)$. Then,

$$\begin{aligned}
Z_k(x) &= \frac{1}{k!} \left[\frac{\partial^k}{\partial t^k} z(x, t) \right]_{t=0} \\
&= \frac{1}{k!} \left[\frac{\partial^k}{\partial t^k} (u(x, t)v(x, t)) \right]_{t=0}.
\end{aligned}$$

Now, Leibnitz's theorem for partial derivatives of function of several variables

$$\frac{\partial^k}{\partial t^k} (u(x, t)v(x, t)) = \sum_{r=0}^k \binom{k}{r} \frac{\partial^r}{\partial t^r} u(x, t) \frac{\partial^{k-r}}{\partial t^{k-r}} v(x, t).$$

Then, we get

$$\begin{aligned}
Z_k(x) &= \frac{1}{k!} \left[\sum_{r=0}^k \binom{k}{r} \frac{\partial^r}{\partial t^r} u(x, t) \Big|_{t=0} \frac{\partial^{k-r}}{\partial t^{k-r}} v(x, t) \Big|_{t=0} \right] \\
&= \frac{1}{r!(k-r)!} \left[\sum_{r=0}^k \frac{\partial^r}{\partial t^r} u(x, t) \Big|_{t=0} \frac{\partial^{k-r}}{\partial t^{k-r}} v(x, t) \Big|_{t=0} \right] \\
&= \sum_{r=0}^k U_r(x) V_{k-r}(x).
\end{aligned}$$

Therefore, $Z_k(x) = \sum_{r=0}^k U_r(x)V_{k-r}(x)$. □

Now we can extend definitions and theorems of differential transform and inverse differential transform for solving two-dimensional heat and wave equations.

Definition 3

If $u(x, y, t)$ is analytic and differentiable continuously in the domain of interest, then let

$$U_k(x, y) = \frac{1}{k!} \left[\frac{\partial^k}{\partial t^k} u(x, y, t) \right]_{t=t_0}, \tag{6}$$

where the spectrum $U_k(x, y)$ is the **transformed function**, which is called **T-function**.

Definition 4

Differential inverse transform of $U_k(x, y)$ is defined as follows:

$$u(x, y, t) = \sum_{k=0}^{\infty} U_k(x, y)(t - t_0)^k. \tag{7}$$

Substitution (6) into (7), we obtain

$$u(x, y, t) = \sum_{k=0}^{\infty} \frac{1}{k!} \left[\frac{\partial^k u(x, y, t)}{\partial t^k} \right]_{t=t_0} (t - t_0)^k. \tag{8}$$

When (t_0) are taken as $(t_0 = 0)$, then (8) is expressed as

$$u(x, y, t) = \sum_{k=0}^{\infty} \frac{1}{k!} \left[\frac{\partial^k u(x, y, t)}{\partial t^k} \right]_{t=t_0} t^k,$$

and (6) is shown as

$$u(x, y, t) = \sum_{k=0}^{\infty} U_k(x, y)t^k. \tag{9}$$

In real application, the function $u(x, y, t)$ by a finite series of (9) can be written as

$$u(x, y, t) = \sum_{k=0}^n U_k(x, y)t^k, \tag{10}$$

usually, the value of n is decided by convergence of the series coefficients.

Theorem 7

If $z(x, y, t) = \alpha u(x, y, t) + \beta v(x, y, t)$, then $Z_k(x, y) = \alpha U_k(x, y) + \beta V_k(x, y)$, where α and β are constants.

Proof: Let $z(x, y, t) = \alpha u(x, y, t) + \beta v(x, y, t)$ and the differential transform of $z(x, y, t)$ be $Z_k(x, y)$. Then,

$$\begin{aligned}
Z_k(x, y) &= \frac{1}{k!} \left[\frac{\partial^k}{\partial t^k} z(x, y, t) \right]_{t=0} \\
&= \frac{1}{k!} \left[\frac{\partial^k}{\partial t^k} (\alpha u(x, y, t) + \beta v(x, y, t)) \right]_{t=0} \\
&= \frac{1}{k!} \left[\frac{\partial^k}{\partial t^k} (\alpha u(x, y, t)) + \frac{\partial^k}{\partial t^k} (\beta v(x, y, t)) \right]_{t=0} \\
&= \frac{\alpha}{k!} \left[\frac{\partial^k}{\partial t^k} u(x, y, t) \right]_{t=0} + \frac{\beta}{k!} \left[\frac{\partial^k}{\partial t^k} v(x, y, t) \right]_{t=0} \\
&= \alpha U_k(x, y) + \beta V_k(x, y).
\end{aligned}$$

Therefore, $Z_k(x, y) = \alpha U_k(x, y) + \beta V_k(x, y)$.

Theorem 8

If $z(x, y, t) = \frac{\partial}{\partial x} u(x, y, t)$, then $Z_k(x, y) = \frac{\partial}{\partial x} U_k(x, y)$.

Proof: Let $z(x, y, t) = \frac{\partial}{\partial x} u(x, y, t)$, and the differential transform of $z(x, y, t)$ be $Z_k(x, y)$. Then,

$$\begin{aligned}
Z_k(x, y) &= \frac{1}{k!} \left[\frac{\partial^k}{\partial t^k} z(x, y, t) \right]_{t=0} \\
&= \frac{1}{k!} \left[\frac{\partial^k}{\partial t^k} \left(\frac{\partial}{\partial x} u(x, y, t) \right) \right]_{t=0} \\
&= \frac{\partial}{\partial x} \left[\frac{1}{k!} \left(\frac{\partial^k}{\partial t^k} u(x, y, t) \right) \right]_{t=0} = \frac{\partial}{\partial x} U_k(x, y).
\end{aligned}$$

Therefore, $Z_k(x, y) = \frac{\partial}{\partial x} U_k(x, y)$.

Theorem 9

If $z(x, y, t) = \frac{\partial}{\partial y} u(x, y, t)$, then $Z_k(x, y) = \frac{\partial}{\partial y} U_k(x, y)$.

Proof: Let $z(x, y, t) = \frac{\partial}{\partial y} u(x, y, t)$, and the differential transform of $z(x, y, t)$ be $Z_k(x, y)$. Then,

$$\begin{aligned}
Z_k(x, y) &= \frac{1}{k!} \left[\frac{\partial^k}{\partial t^k} z(x, y, t) \right]_{t=0} \\
&= \frac{1}{k!} \left[\frac{\partial^k}{\partial t^k} \left(\frac{\partial}{\partial y} u(x, y, t) \right) \right]_{t=0} \\
&= \frac{\partial}{\partial y} \left[\frac{1}{k!} \left(\frac{\partial^k}{\partial t^k} u(x, y, t) \right) \right]_{t=0} \\
&= \frac{\partial}{\partial y} U_k(x, y).
\end{aligned}$$

Therefore, $Z_k(x, y) = \frac{\partial}{\partial y} U_k(x, y)$.

Theorem 10

If $z(x, y, t) = \frac{\partial^2}{\partial x^2} u(x, y, t)$, then $Z_k(x, y) = \frac{\partial^2}{\partial x^2} U_k(x, y)$.

Proof: Let $z(x, y, t) = \frac{\partial^2}{\partial x^2} u(x, y, t)$, and the differential transform of $z(x, y, t)$ be $Z_k(x, y)$.

Then,

$$\begin{aligned} Z_k(x, y) &= \frac{1}{k!} \left[\frac{\partial^k}{\partial t^k} z(x, y, t) \right]_{t=0} \\ &= \frac{1}{k!} \left[\frac{\partial^k}{\partial t^k} \left(\frac{\partial^2}{\partial x^2} u(x, y, t) \right) \right]_{t=0} \\ &= \frac{\partial^2}{\partial x^2} \left[\frac{1}{k!} \left(\frac{\partial^k}{\partial t^k} u(x, y, t) \right) \right]_{t=0} \\ &= \frac{\partial^2}{\partial x^2} U_k(x, y). \end{aligned}$$

Therefore, $Z_k(x, y) = \frac{\partial^2}{\partial x^2} U_k(x, y)$.

Theorem 11

If $z(x, y, t) = \frac{\partial^2}{\partial y^2} u(x, y, t)$, then $Z_k(x, y) = \frac{\partial^2}{\partial y^2} U_k(x, y)$.

Proof: Let $z(x, y, t) = \frac{\partial^2}{\partial y^2} u(x, y, t)$, and the differential transform of $z(x, y, t)$ be $Z_k(x, y)$.

Then,

$$\begin{aligned} Z_k(x, y) &= \frac{1}{k!} \left[\frac{\partial^k}{\partial t^k} z(x, y, t) \right]_{t=0} \\ &= \frac{1}{k!} \left[\frac{\partial^k}{\partial t^k} \left(\frac{\partial^2}{\partial y^2} u(x, y, t) \right) \right]_{t=0} \\ &= \frac{\partial^2}{\partial y^2} \left[\frac{1}{k!} \left(\frac{\partial^k}{\partial t^k} u(x, y, t) \right) \right]_{t=0} \\ &= \frac{\partial^2}{\partial y^2} U_k(x, y). \end{aligned}$$

Therefore, $Z_k(x, y) = \frac{\partial^2}{\partial y^2} U_k(x, y)$.

Theorem 12

If $z(x, y, t) = \frac{\partial^m}{\partial t^m} u(x, y, t)$, then $Z_k(x, y) = \frac{(k+m)!}{k!} U_{k+m}(x, y)$.

Proof: Let $z(x, y, t) = \frac{\partial^m}{\partial t^m} u(x, y, t)$ and the differential transform of $z(x, y, t)$ be $Z_k(x, y)$.

Then,

$$\begin{aligned} Z_k(x, y) &= \frac{1}{k!} \left[\frac{\partial^k}{\partial t^k} z(x, y, t) \right]_{t=0} \\ &= \frac{1}{k!} \left[\frac{\partial^k}{\partial t^k} \left(\frac{\partial^m}{\partial t^m} u(x, y, t) \right) \right]_{t=0} \\ &= \frac{(k+m)!}{k!(k+m)!} \left[\frac{\partial^{k+m}}{\partial t^{k+m}} u(x, y, t) \right]_{t=0} \\ &= \frac{(k+m)!}{k!} U_{k+m}(x, y). \end{aligned}$$

Therefore, $Z_k(x, y) = \frac{(k+m)!}{k!} U_{k+m}(x, y)$.

Theorem 13

If $z(x, y, t) = u(x, y, t)v(x, y, t)$, then $Z_k(x, y) = \sum_{r=0}^k U_r(x, y)V_{k-r}(x, y)$.

Proof: Let $z(x, y, t) = u(x, y, t)v(x, y, t)$ and the differential transform of $z(x, y, t)$ be $Z_k(x, y)$.

Then, we have

$$\begin{aligned} Z_k(x, y) &= \frac{1}{k!} \left[\frac{\partial^k}{\partial t^k} z(x, y, t) \right]_{t=0} \\ &= \frac{1}{k!} \left[\frac{\partial^k}{\partial t^k} (u(x, y, t)v(x, y, t)) \right]_{t=0}. \end{aligned}$$

Now, Leibnitz's theorem for partial derivatives of function of several variables

$$\frac{\partial^k}{\partial t^k} (u(x, y, t)v(x, y, t)) = \sum_{r=0}^k \binom{k}{r} \frac{\partial^r}{\partial t^r} u(x, y, t) \frac{\partial^{k-r}}{\partial t^{k-r}} v(x, y, t).$$

Then, we get

$$\begin{aligned} Z_k(x, y) &= \frac{1}{k!} \left[\sum_{r=0}^k \binom{k}{r} \frac{\partial^r}{\partial t^r} u(x, y, t) \Big|_{t=0} \frac{\partial^{k-r}}{\partial t^{k-r}} v(x, y, t) \Big|_{t=0} \right] \\ &= \frac{1}{r!(k-r)!} \left[\sum_{r=0}^k \frac{\partial^r}{\partial t^r} u(x, y, t) \Big|_{t=0} \frac{\partial^{k-r}}{\partial t^{k-r}} v(x, y, t) \Big|_{t=0} \right] \\ &= \sum_{r=0}^k U_r(x, y)V_{k-r}(x, y). \end{aligned}$$

Therefore, $Z_k(x, y) = \sum_{r=0}^k U_r(x, y)V_{k-r}(x, y)$. □

Solving Initial Value Problems for One-Dimensional Partial Differential Equations

In this section, initial value problems for one-dimensional heat equations and wave equations are solved by using one-dimensional differential transform method.

Example 1

We consider the one-dimensional heat equation with variable coefficients as

$$u_t(x, t) + \frac{x^2}{2} u_{xx}(x, t) = 0, \tag{11}$$

and the initial condition

$$u(x, 0) = x^2, \tag{12}$$

where $u = u(x, t)$ is a function of the variables x and t .

Taking differential transform of (11),

$$(k+1) U_{k+1}(x) = -\frac{x^2}{2} \frac{\partial^2}{\partial x^2} U_k(x), \tag{13}$$

using the initial condition (12),

$$U_0(x) = x^2. \tag{14}$$

Substitution (14) into (13) and using the recurrence relation,

$$U_1(x) = -x^2, \quad U_2(x) = \frac{x^2}{2}, \quad U_3(x) = -\frac{x^2}{6}, \quad U_4(x) = \frac{x^2}{24}, \quad U_5(x) = -\frac{x^2}{120},$$

$$U_6(x) = \frac{x^2}{720}, \dots, \quad U_k(x) = \begin{cases} \frac{x^2}{k!}, & k \text{ is even,} \\ -\frac{x^2}{k!}, & k \text{ is odd.} \end{cases}$$

Finally, the differential inverse transform of $U_k(x)$ gives: $u(x, t) = \sum_{k=0}^{\infty} U_k(x) t^k$.

Then, the exact solution is

$$u(x, t) = x^2 e^{-t}.$$

Example 2

We consider the one-dimensional heat equation with variable coefficients as

$$u_t(x, t) - \frac{x^2}{2} u_{xx}(x, t) - 2u_x(x, t) = 0, \tag{15}$$

and the initial condition

$$u(x, 0) = x^2, \quad (16)$$

where $u = u(x, t)$ is a function of the variables x and t .

Taking differential transform of (15),

$$(k+1)U_{k+1}(x) = \frac{x^2}{2} \frac{\partial^2}{\partial x^2} U_k(x) + 2 \frac{\partial}{\partial x} U_k(x), \quad (17)$$

using the initial condition (16),

$$U_0(x) = x^2. \quad (18)$$

Substitution (18) into (17) and using the recurrence relation,

$$U_1(x) = x^2 + 4x, \quad U_2(x) = \frac{x^2 + 4x + 8}{2}, \quad U_3(x) = \frac{x^2 + 4x + 8}{6}, \quad U_4(x) = \frac{x^2 + 4x + 8}{24},$$

$$U_5(x) = \frac{x^2 + 4x + 8}{120}, \quad U_6(x) = \frac{x^2 + 4x + 8}{720}, \quad \dots, \quad U_k(x) = \frac{x^2 + 4x + 8}{k!}.$$

Finally, the differential inverse transform of $U_k(x)$ gives:

$$u(x, t) = \sum_{k=0}^{\infty} U_k(x) t^k = (x^2 + 4x + 8) \sum_{k=0}^{\infty} \frac{t^k}{k!}.$$

Then, the exact solution is

$$u(x, t) = (x^2 + 4x + 8)e^t.$$

Example 3

We consider the linear Klein-Gordon equation in the form

$$u_{tt}(x, t) - u_{xx}(x, t) - u(x, t) = 0, \quad (19)$$

and the initial conditions

$$u(x, 0) = 1 + \cos x, \quad u_t(x, 0) = 0, \quad (20)$$

where $u = u(x, t)$ is a function of the variables x and t .

Taking differential transform of (19),

$$(k+1)(k+2)U_{k+2}(x) = \frac{\partial^2}{\partial x^2} U_k(x) + U_k(x), \quad (21)$$

using the initial condition (20),

$$U_0(x) = 1 + \cos x, \quad U_1(x) = 0. \quad (22)$$

Substitution (22) into (21) and using the recurrence relation,

$$U_k(x) = 0, \quad k = 1, 3, 5, \dots$$

By applying the k values are $k = 2, 4, 6, \dots$,

$$U_2(x) = \frac{1}{2}, \quad U_4(x) = \frac{1}{24}, \quad U_6(x) = \frac{1}{720}, \quad \dots, \quad U_k(x) = \frac{1}{k!}.$$

Finally, the differential inverse transform of $U_k(x)$ gives:

$$u(x, t) = \sum_{k=0}^{\infty} U_k(x) t^k = (1 + \cos x) + \left(\frac{t^2}{2!} + \frac{t^4}{4!} + \frac{t^6}{6!} + \dots\right).$$

Then, the exact solution is $u(x, t) = \cos x + \cosh t$.

Example 4

We consider the one-dimensional wave equation with variable coefficients as

$$u_{tt}(x, t) + \frac{x^2}{2} u_{xx}(x, t) = 0, \tag{23}$$

and the initial conditions

$$u(x, 0) = x, u_t(x, 0) = x^2, \tag{24}$$

where $u = u(x, t)$ is a function of the variables x and t .

Taking differential transform of (23),

$$(k+1)(k+2)U_{k+2}(x) = -\frac{x^2}{2} \frac{\partial^2}{\partial x^2} U_k(x), \tag{25}$$

using the initial condition (24),

$$U_0(x) = x, U_1(x) = x^2. \tag{26}$$

Substitution (26) into (25) and using the recurrence relation,

$$U_k(x) = 0, \quad k = 2, 4, 6, \dots$$

By applying the k values are $k = 1, 3, 5, \dots$,

$$U_3(x) = -\frac{x^2}{6}, \quad U_5(x) = \frac{x^2}{120}, \quad U_7(x) = -\frac{x^2}{5040}, \quad \dots,$$

$$U_k(x) = \begin{cases} (-1)^k \frac{x^2}{k!}, & k = 3, 7, 11, \dots, \\ (-1)^{k+1} \frac{x^2}{k!}, & k = 5, 9, 13, \dots \end{cases}$$

Finally, the differential inverse transform of $U_k(x)$ gives:

$$u(x, t) = \sum_{k=0}^{\infty} U_k(x) t^k = x + x^2 \left(t - \frac{t^3}{3!} + \frac{t^5}{5!} - \frac{t^7}{7!} + \dots + \frac{t^k}{k!} \right).$$

Then, the exact solution is

$$u(x, t) = x + x^2 \sin t.$$

Example 5

We consider the one-dimensional wave equation with variable coefficients as

$$u_{tt}(x, t) - \frac{x^2}{2} u_{xx}(x, t) - u_x(x, t) = 0, \quad (27)$$

and the initial conditions

$$u(x, 0) = 1, u_t(x, 0) = x^2, \quad (28)$$

where $u = u(x, t)$ is a function of the variables x and t .

Taking differential transform of (27),

$$(k+1)(k+2)U_{k+2}(x) = \frac{x^2}{2} \frac{\partial^2}{\partial x^2} U_k(x) + \frac{\partial}{\partial x} U_k(x), \quad (29)$$

using the initial condition (28),

$$U_0(x) = 1, U_1(x) = x^2. \quad (30)$$

Substitution (30) into (29) and using the recurrence relation,

$$U_k(x) = 0, k = 2, 4, 6, \dots$$

By applying the k values are $k = 1, 3, 5, \dots$,

$$U_3(x) = \frac{x^2 + 2x}{6}, U_5(x) = \frac{x^2 + 2x + 2}{120}, U_7(x) = \frac{x^2 + 2x + 2}{5040}, \dots,$$

$$U_k(x) = \frac{x^2 + 2x + 2}{k!}.$$

Finally, the differential inverse transform of $U_k(x)$ gives:

$$u(x, t) = \sum_{k=0}^{\infty} U_k(x) t^k = 1 + (x^2 + 2x + 2) \left(t + \frac{t^3}{3!} + \frac{t^5}{5!} + \frac{t^7}{7!} + \dots + \frac{t^k}{k!} \right).$$

Then, the exact solution is

$$u(x, t) = 1 + (x^2 + 2x + 2) \sinh t.$$

Solving Initial Value Problems for Two-Dimensional Partial Differential Equations

In this section, initial value problems for two-dimensional heat equations and wave equations are solved by using one-dimensional differential transform method.

Example 6

We consider the two-dimensional heat equation with variable coefficients as

$$u_t(x, y, t) - \frac{y^2}{2} u_{xx}(x, y, t) - \frac{x^2}{2} u_{yy}(x, y, t) = 0, \tag{31}$$

and the initial condition

$$u(x, y, 0) = x^2, \tag{32}$$

where $u = u(x, t)$ is a function of the variables x and t .

Taking differential transform of (31),

$$(k + 1)U_{k+1}(x, y) = \frac{y^2}{2} \frac{\partial^2}{\partial x^2} U_k(x, y) + \frac{x^2}{2} \frac{\partial^2}{\partial y^2} U_k(x, y), \tag{33}$$

using the initial condition (32),

$$U_0(x, y) = x^2. \tag{34}$$

Substitution (34) into (33) and using the recurrence relation,

$$U_1(x, y) = y^2, \quad U_2(x, y) = \frac{x^2}{2}, \quad U_3(x, y) = \frac{y^2}{6}, \quad U_4(x, y) = \frac{x^2}{24}, \quad U_5(x, y) = \frac{y^2}{120},$$

$$U_6(x, y) = \frac{x^2}{720}, \quad U_7(x, y) = \frac{y^2}{5040}, \quad \dots, \quad U_k(x, y) = \begin{cases} \frac{x^2}{k!}, & \text{k is even,} \\ \frac{y^2}{k!}, & \text{k is odd.} \end{cases}$$

Finally, the differential inverse transform of $U_k(x, y)$ gives:

$$u(x, y, t) = \sum_{k=0}^{\infty} U_k(x, y) t^k = x^2 \sum_{k=0,2,4}^{\infty} \frac{t^k}{k!} + y^2 \sum_{k=1,3,5}^{\infty} \frac{t^k}{k!}.$$

Then, the exact solution is

$$u(x, y, t) = x^2 \left(1 + \frac{t^2}{2!} + \frac{t^4}{4!} + \dots\right) + y^2 \left(t + \frac{t^3}{3!} + \frac{t^5}{5!} + \dots\right) = x^2 \cosh t + y^2 \sinh t.$$

Example 7

We consider the two-dimensional heat equation with variable coefficients as

$$u_t(x, y, t) + \frac{y^2}{2} u_{xx}(x, y, t) + \frac{x^2}{2} u_{yy}(x, y, t) + u_x(x, y, t) + u_y(x, y, t) = 0, \tag{35}$$

and the initial condition

$$u(x, y, 0) = y^2, \tag{36}$$

where $u = u(x, t)$ is a function of the variables x and t .

Taking differential transform of (35),

$$(k+1)U_{k+1}(x, y) = -\frac{y^2}{2} \frac{\partial^2}{\partial x^2} U_k(x, y) - \frac{x^2}{2} \frac{\partial^2}{\partial y^2} U_k(x, y) - \frac{\partial}{\partial x} U_k(x, y) - \frac{\partial}{\partial y} U_k(x, y), \quad (37)$$

using the initial condition (36),

$$U_0(x, y) = y^2. \quad (38)$$

Substitution (38) into (37) and using the recurrence relation,

$$U_1(x, y) = -(x^2 + 2y), \quad U_2(x, y) = \frac{y^2 + 2x + 2}{2}, \quad U_3(x, y) = -\left(\frac{x^2 + 2y + 2}{6}\right),$$

$$U_4(x, y) = \frac{y^2 + 2x + 2}{24}, \quad U_5(x, y) = -\left(\frac{x^2 + 2y + 2}{120}\right), \quad U_6(x, y) = \frac{y^2 + 2x + 2}{720}, \dots,$$

$$U_k(x, y) = \begin{cases} \frac{y^2 + 2x + 2}{k!}, & \text{k is even,} \\ -\frac{(x^2 + 2y + 2)}{k!}, & \text{k is odd.} \end{cases}$$

Finally, the differential inverse transform of $U_k(x, y)$ gives:

$$u(x, y, t) = \sum_{k=0}^{\infty} U_k(x, y) t^k = (y^2 + 2x + 2) \sum_{k=0}^{\infty} \frac{t^k}{k!} - (x^2 + 2y + 2) \sum_{k=0}^{\infty} \frac{t^k}{k!}.$$

Then, the exact solution is

$$u(x, y, t) = (y^2 + 2x + 2) \left(1 + \frac{t^2}{2!} + \frac{t^4}{4!} + \dots\right) - (x^2 + 2y + 2) \left(t + \frac{t^3}{3!} + \frac{t^5}{5!} + \dots\right)$$

$$= (y^2 + 2x + 2) \cosh t - (x^2 + 2y + 2) \sinh t.$$

Example 8

We consider the two-dimensional wave equation with constant coefficients as

$$u_{tt}(x, y, t) - u_{xx}(x, y, t) - u_{yy}(x, y, t) - u(x, y, t) = 0, \quad (39)$$

and the initial conditions

$$u(x, y, 0) = 1 + \cos x, \quad u_t(x, y, 0) = 0, \quad (40)$$

where $u = u(x, t)$ is a function of the variables x and t .

Taking differential transform of (39),

$$(k+1)(k+2)U_{k+2}(x, y) = \frac{\partial^2}{\partial x^2} U_k(x, y) + \frac{\partial^2}{\partial y^2} U_k(x, y) + U_k(x, y), \quad (41)$$

using the initial condition (40),

$$U_0(x, y) = 1 + \cos x, \quad U_1(x, y) = 0. \quad (42)$$

Substitution (42) into (41) and using the recurrence relation,

$$U_k(x, y) = 0, k = 1, 3, 5, \dots$$

By applying the k values are k = 2, 4, 6, ...,

$$U_2(x, y) = \frac{1}{2}, \quad U_4(x, y) = \frac{1}{24}, \quad U_6(x, y) = \frac{1}{720}, \quad \dots, \quad U_k(x, y) = \frac{1}{k!}.$$

Finally, the differential inverse transform of $U_k(x)$ gives:

$$u(x, y, t) = \sum_{k=0}^{\infty} U_k(x, y) t^k = (1 + \cos x) + \left(\frac{t^2}{2!} + \frac{t^4}{4!} + \frac{t^6}{6!} + \dots\right).$$

Then, the exact solution is

$$u(x, y, t) = \cos x + \cosh t.$$

Example 9

We consider the two-dimensional wave equation with variable coefficients as

$$u_{tt}(x, y, t) - \frac{x^2}{12} u_{xx}(x, y, t) - \frac{y^2}{12} u_{yy}(x, y, t) = 0, \tag{43}$$

and the initial conditions

$$u(x, y, 0) = x^4, \quad u_t(x, y, 0) = y^4, \tag{44}$$

where $u = u(x, t)$ is a function of the variables x and t .

Taking differential transform of (43),

$$(k+1)(k+2)U_{k+2}(x, y) = \frac{x^2}{12} \frac{\partial^2}{\partial x^2} U_k(x, y) + \frac{y^2}{12} \frac{\partial^2}{\partial y^2} U_k(x, y), \tag{45}$$

using the initial condition (44),

$$U_0(x, y) = x^4, \quad U_1(x, y) = y^4. \tag{46}$$

Substitution (46) into (45) and using the recurrence relation,

$$U_2(x, y) = \frac{x^4}{2}, \quad U_3(x, y) = \frac{y^4}{6}, \quad U_4(x, y) = \frac{x^4}{24}, \quad U_5(x, y) = \frac{y^4}{120},$$

$$U_6(x, y) = \frac{x^4}{720}, \quad \dots, \quad U_k(x, y) = \begin{cases} \frac{x^4}{k!}, & k \text{ is even,} \\ \frac{y^4}{k!}, & k \text{ is odd.} \end{cases}$$

Finally, the differential inverse transform of $U_k(x, y)$ gives:

$$u(x, y, t) = \sum_{k=0}^{\infty} U_k(x, y) t^k = x^4 \sum_{k=0,2,4}^{\infty} U_k(x, y) t^k + y^4 \sum_{k=1,3,5}^{\infty} U_k(x, y) t^k.$$

Then, the exact solution is

$$u(x, y, t) = x^4 \left(1 + \frac{t^2}{2!} + \frac{t^4}{4!} + \dots\right) + y^4 \left(t + \frac{t^3}{3!} + \frac{t^5}{5!} + \dots\right) = x^4 \cosh t + y^4 \sinh t.$$

Conclusion

In this paper, we have studied one-dimensional and two-dimensional heat and wave equations with the help of differential transform method. The differential transform method has been successful, applied for solving linear and homogeneous partial differential equations with constant coefficients and variable coefficients. We conclude that differential transform method can be extended to solve many partial differential equations with constant coefficients and variable coefficients which arise in physical and engineering applications.

Acknowledgements

We would like to thank Rector Dr. Tin Tun and Pro-Rectors, University of Mandalay, for giving us their kind permission to undertake this paper. I would also like to thank Head and Professor Dr. Ko Ko Lwin, Department of Mathematics, University of Mandalay, for his permission and support concerning this research paper. I am grateful to my supervisor Dr. Khin Than Sint, Professor, Department of Mathematics, University of Mandalay, for her advice and suggestion to implement this kind of research paper.

References

- Chen, C. K. and Ho, S. H., (1999), "Solving Partial Differential Equations by Two-Dimensional Differential Transform Method", *Applied Mathematics and Computation*, Taiwan, Vol. 106, pp. 171-179.
- Hnin E. P. and Khin T. S., (2023), "Applying One-Dimensional Differential Transform Method to Nonlinear Differential Equations", *Mandalay University Research Journal*, Vol. 14, pp. 243-254.
- Khatib, A., (2016), "*Differential Transform Method for Differential Equations*", Master Thesis, Palestine Polytechnic University, Hebron, Palestine.
- Kishan, H., (2007), "*Differential Calculus*", Atlantic Publishers and Distributors (P) LTD, New Delhi.
- Priya, T. S. and Alima, N., (2016), "Differential Transform Method for Solving Linear and Homogeneous Equation with Variable Coefficients", *Journal of Emerging Technologies and Innovative Research*, Vol. 5, Issue 4, pp. 424-426.
- Raslan, K. R., Biswas, A. and Abu Sheer, Z., (2012), "Differential Transform Method for Solving Partial Differential Equations with Variable Coefficients", *International Journal of Physical Sciences*, Saudi Arabia, Vol. 7, pp. 1412-1419.
- Sutkar, P. S., (2017), "Solution of Some Differential Equations by Using Differential Transform Method", *International Journal of Scientific and Innovative Mathematical Research*, Vol. 5, Issue 5, pp. 17-20.

ANALYSIS OF TRAFFIC ACCIDENT BY USING MACHINE LEARNING

Julie Marlar¹, Wint Pa Pa Kyaw², Soe Mya Mya Aye³

Abstract

In the case of road accidents, millions of people are dead each year, and the numbers of accident rates are rising all over the world. As a result, they have a great impact on society in terms of finance and economic. In this paper, Machine Learning (ML) models are used to analyze road accident severity based on road accident dataset. The dataset was collected from Myanmar's Traffic Police Force which shares raw data on annual basis on Yangon- Naypyitaw expressway's traffic accident data in 2022. The dataset is divided into training and testing dataset. The training dataset is used to train our model, and the test dataset is utilized to evaluate the predictions. In the proposed system, the collected data is preprocessed (data cleaning, encoding, transformation) and followed by data training, testing and comparison analysis on the analysis of the ML methods. By this experiment, the road accident contributing factors is vital. By using the continuous variables, this work is predicted road accidents with different accident types and applied with ML technique like Logistic Regression (LR), Adaptive Boosting (AdaBoost), Decision Tree, Adaboost using Decision Tree and Multinomial Naive Bayes. The experimental results showed that Logistic Regression classifier achieves the best accuracy than other classifiers.

Keywords: Logistic Regression, Adaboost, Decision Tree, Multinomial Navie Bayes

Introduction

Road traffic accidents (RTAs) are increasing worldwide and a major of injuries, causing millions of deaths and fatalities, financial and economic expenses on society (S Ahmed, 2023). According to the World Health Organization (WHO), in 2019 Road traffic mortality rate is 20.94 per 100,000 of population ranks. Myanmar stands in the place of 71 in the world. The latest WHO data issued that road traffic accident Deaths in Myanmar reached 11,004 of total deaths in 2020. In recent years, road traffic accidents, especially severe vehicle crashes have increased because of the rapid growth of road traffic (J.Lil, 2023).

Machine learning techniques can be applied in road safety to improve life-threatening problems on the roads. With the advancements of information technology, machine learning becomes increasingly mature, and useful information without preconditions can be found in databases. ML is described as a method that can be used to make provisions for data analysis, decision making, and data preparation for real-life problems. The learning begins with data analysis to identify patterns within the dataset and make future decisions involving societal problems (X.Wang, 2022).

Applications of machine learning techniques in RTAs can help in the modelling for better understanding of RTAs data records and can be used to achieve numerous outcomes such as classification, prediction, and clustering analysis. Classification methods are among the most commonly used techniques in mining traffic accidents, where the goal is building classifiers that can predict the accidents. The main objectives of the proposed system are to explore the factors influencing the severity of traffic accidents on Yangon- Naypyitaw expressway road, to analyze and build the models based on the accident data which is to get a better understanding, and evaluate the causes and effects on the severity of traffic accidents. In this paper, the purpose of the methodology is to set the classification rules for prediction of the best performing five models based on machine learning algorithms are constructed.

* Special Award (2023)

¹ Department of Computer Studies, University of Yangon

² Department of Computer Studies, University of Yangon

³ Department of Computer Studies, University of Yangon

Machine Learning Methods

Machine learning involves a group of computational algorithms that can perform classification, pattern recognition and prediction. There are different types of machine learning Algorithms such as supervised learning, unsupervised learning, semi-supervised learning and reinforcement learning. ML have successfully been implemented in automated stock trading, computer vision, health care, speech recognition, and customer services. Most ML classifiers are influenced by the size of the dataset and capabilities to handle overfitting problems and are being implemented in different environments such as urban and rural settings and on freeways and expressway. ML classifiers employed during the comparative analysis are described below.

Logistic Regression

Logistic regression is one of the most popular Machine Learning algorithms, which comes under the Supervised Learning technique. It is used for predicting the categorical dependent variable using a given set of independent variables. The idea of the algorithm is to map the results of linear functions to sigmoid functions. The sigmoid function is a mathematical function used to map the predicted values to probabilities. The value must be between 0 and 1, which cannot go beyond this limit, so it forms a curve like the "S" form. Logistic function is shown in Figure 1.

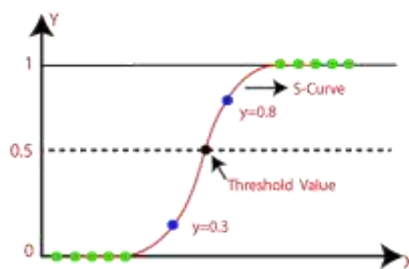


Figure 1: Logistic Regression

Adaptive boosting (AdaBoost)

AdaBoost is the simplest boosting algorithm based on an ensemble decision tree. It uses an iterative adaptive approach in which weights are adjusted at each iteration by assigning higher weights to incorrectly classified instances. Boosting is an ensemble learning method that combines a set of weak learners into strong learners to minimize training errors. This method operates iteratively, identifying misclassified data points and adjusting their weights to minimize the training error. AdaBoost function is shown in Figure 2.

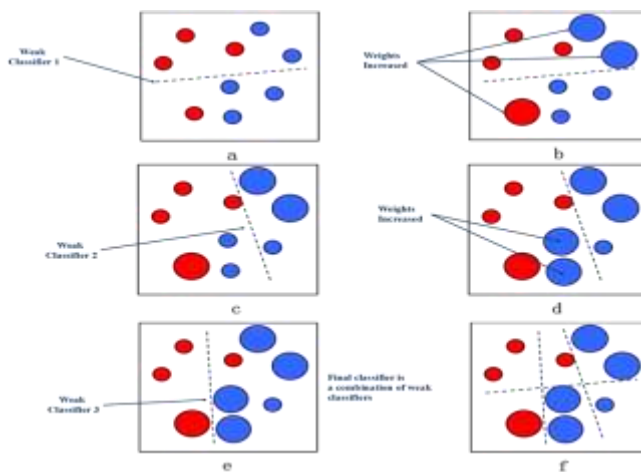


Figure 2: Adaptive Boosting (Adaboost)

Naive Bayes

The NB classifier is a simple probabilistic classifier based on applying Bayes’ theorem with strong independence assumptions among variables. Naive Bayes is one of the fast and easy simple ML algorithms to predict a class of datasets. which helps in building fast machine learning models that can make quick predictions. Since the feature set contains continuous variables, the Gaussian NB was chosen. The naive Bayes model is easy to build and particularly useful for very large data sets. Naïve Bayes function is shown in Figure 3.

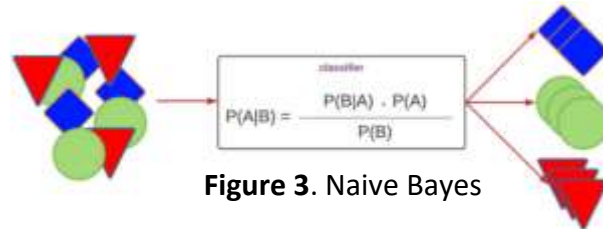


Figure 3. Naive Bayes

Decision Tree

Decision Tree is a Supervised learning technique which is also called ‘Classification and Regression Tree algorithm (CART)’ used that can be used for both classification and Regression problems. It is a tree-structured classifier, where internal nodes represent the features of a dataset, branches represent the decision rules and each leaf node represents the outcome. The goal is to create a model that predicts the value of a target variable by learning simple decision rules inferred from the data features. Decision Tree function is shown in Figure 4.

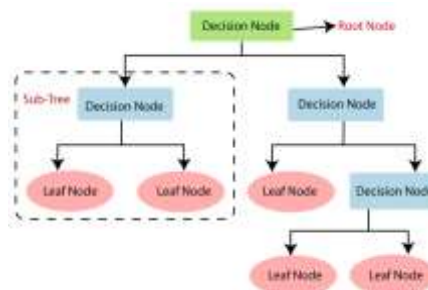


Figure 4. Decision Tree

Implementation of the Road Traffic Accident Data Set

In this study, the dataset is built information about road crashes occurred on Yangon-Naypyitaw expressway during the period from January to December in 2022. Additionally, the dataset contains traffic accident records in this year, having the total number of 165 traffic crashes. The data used is provided from the traffic accident report of Myanmar’s Traffic Police Force. This station shares raw data on annual basis on Yangon- Naypyitaw expressway’s traffic accident data. The original dataset has 165 records and 14 variables. This research utilized 165 records involving 11 selected variables. The sample dataset was shown in Table 1. Data preparation is performed before each model building.

The process includes various steps such as cleaning, encoding and data transformation. Data cleaning is conducted to correct the missing values and the erroneous values. In this study, dummy coding scheme are used, this categorical data encoding method transforms the categorical variable into a set of binary variables (also known as dummy variables). In this encoding, for each level of a categorical feature, create a new variable. Each category is mapped with a binary variable containing either 0 or 1. Here, 0 represents the absence, and 1 represents the presence of that category. Likewise, the study chose the factors which are related to the accidents that include, accident type, crash injuries, human factors, reason, season, time, weather condition, environment, road condition, road characteristics and road alignment.

Table 1: Dataset of Selected Features on Road Traffic Accidents

Accident Type	People	Human Factor	Reason	Season
Rollover	Death	No Seat-belt used	Tire puncture	Spring
Collision	Death	No Seat-belt used	Overspeed	Spring
Hit	Minor injury	Seat-belt used	Overspeed	Spring
Hit	Serious injury	No Seat-belt used	Tire puncture	Spring
Rollover	Serious injury	Motorcycle Helmet used	Not Permitted Motorcycle zone	Spring
Hit	Death	Drowsy Driver	Overspeed	Spring
Collision	Death	Seat-belt used	Overspeed	Spring
:	:	:	:	:
:	:	:	:	:
Rollover	Minor injury	Seat-belt used	Tire puncture	Spring
Rollover	Death	No Seat-belt used	Overspeed	Rainy
Hit	Serious injury	No Seat-belt used	Overspeed	Spring
Collision	Serious injury	Seat-belt used	Overspeed	Spring
Hit	Serious injury	No Motorcycle Helmet used	Not Permitted Motorcycle zone	Spring

...

Time	Weather Condition	Environment	Road Condition	Road Characteristics	Road Alignment
Daytime	Fine	Light	Dry	General Road	Flat
Daytime	Fine	Light	Dry	Junction Type	Curve
Nighttime	Mist	Dark	Snow	Barrier Type	Curve
Nighttime	Mist	Dark	Snow	General Road	Flat
Daytime	Fine	Light	Dry	General Road	Flat
Daytime	Mist	Light	Wet	General Road	Flat
Nighttime	Mist	Dark	Snow	General Road	Flat
:	:	:	:	:	:
:	:	:	:	:	:
Nighttime	Fine	Dark	Snow	General Road	Flat
Nighttime	Heavy Rain	Dark	Wet	General Road	Flat
Nighttime	Mist	Dark	Snow	Bridge	Flat
Nighttime	Mist	Dark	Wet	General Road	Flat
Nighttime	Mist	Dark	Snow	Barrier Type	Curve

In developing the system, Python programming language is used and Jupyter notebook which is an open-source IDE that allows us to create and share documents that contain live code, equations, visualizations, and narrative text. The uses include data cleaning, transformation, statistical modeling, data visualization, machine learning, and so on. In preprocessing, the dataset was encoded with dummies method and data transformation by using MinMaxScaler in Scikit-Learn. It can support various languages that are popular in data science such as Python language. In this study, the applied ML classifiers are the Logistic regression, Adaboost, Naive Bayes, Decision Tree and Adaboost with Decision Tree using Python's Scikit-Learn library (T.Bokaba.et.al, 2020).

Workflow Diagram of a Proposed System

During the construction of the RTA model, the stages of the experimental process are illustrated in Figure 5. This process consists of five steps. In the first step, the work flow of the proposed system starts with input of dataset (165 records). In the second step, handling missing data is an essential part of the pre-processing data stage that helps to ensure that absent values are

dealt with sufficiently. After data pre-processing, data training and testing was followed by third step.

In this step, the dataset is divided into training dataset and testing dataset, the system uses the train dataset to train with the model, and the test dataset is used to evaluate the predictions. 80% of the dataset is used for the training and 20% is used for the testing and will be randomly split in the same way. By the fourth step, the models are built and analyzed on two separate datasets. In this way, if we want to train another model, we will be able to accurately compare it with another one, because it will be trained on the same data set.

The comparison analysis of the ML methods and finally, the predicted RTAs model evaluated to test the accuracy of each model in the last step. Evaluation of the models show that the best results are obtained and the goal of classification methods is building models that can predict the accidents. These models are built using training sets of data in which accidents factors are known. To investigate the factors influencing the severity of traffic accidents on Yangon-Naypyitaw expressways and to analyze and model accident data to understand better and assess the causes and effects of the severity of traffic accidents. The scores of different models are measured to evaluate and compare their accuracy.

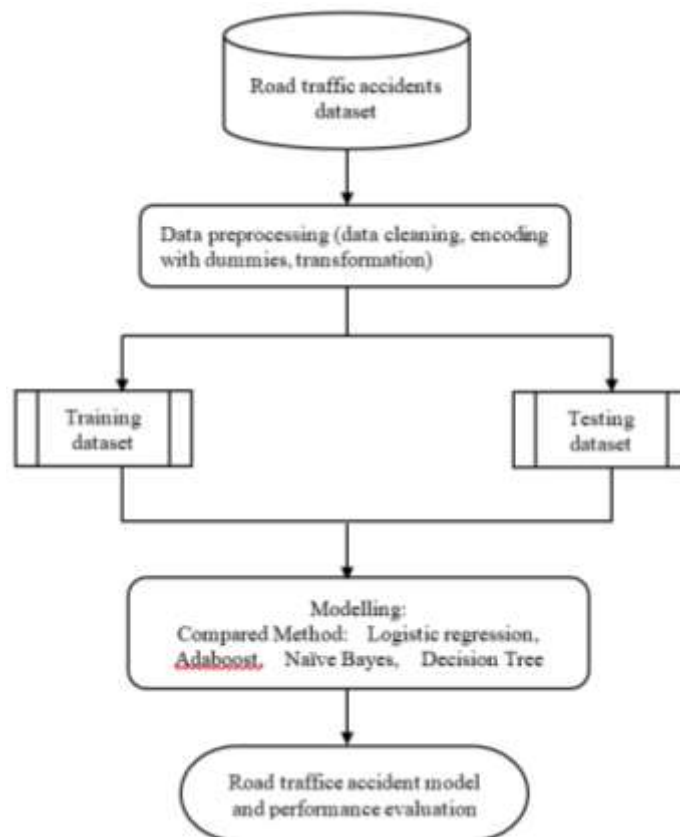


Figure 5. Work Flow Diagram of a Proposed System

Results and Discussion

Visualization of the discovered patterns is important in order to communicate information efficiently using graphs, charts and tables. The paper discusses on data visualization. The data visualization of road accidents is presented with respect to three injuries. The different machine learning algorithms are used to identify the key features of road traffic accident that leads to explore the importance of road accident contributing factors and to evaluate the performance of classification results. The investigation effort establishes the models to select a set of influential factors and to build up a model for classifying the severity of injuries.

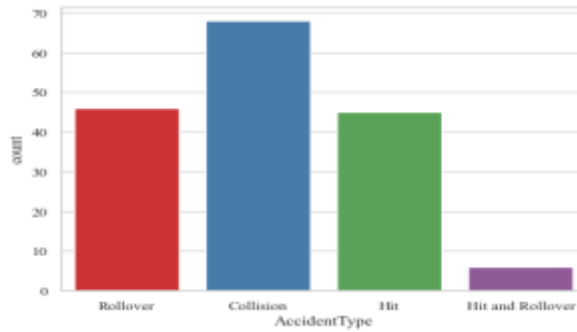


Figure 6: Accident Type

As illustrated in figure 6, it was found that collision is almost 68% - higher rate of accident type. Hit and rollover is 6% - the least accident type. The number of rollover and hit accident type were accounted with 46% and 45% as respectively.

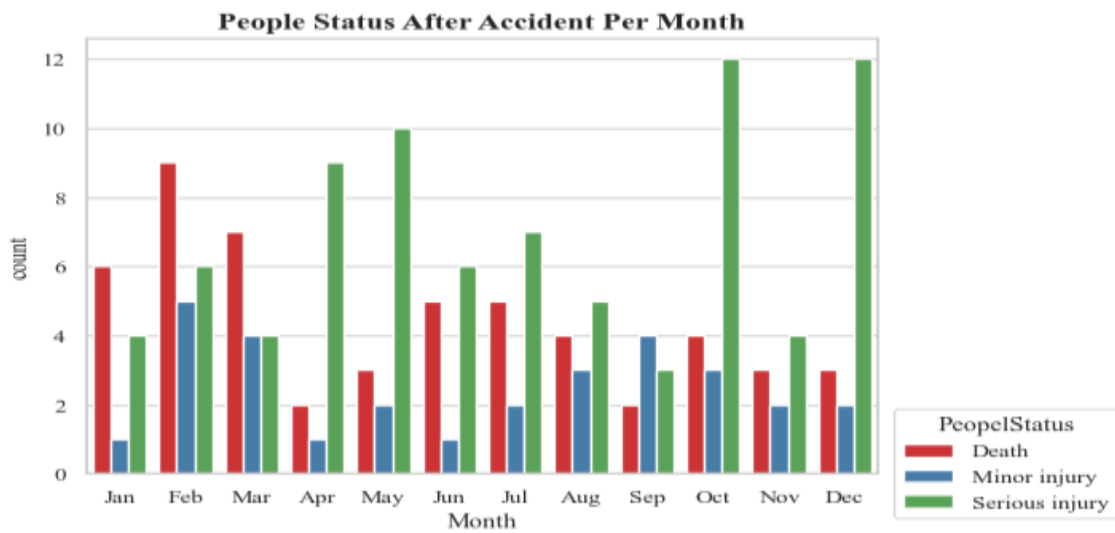


Figure 7: People Status After Accident Per Month

As illustrated in Figure 7, it was found that the serious injuries are caused by 12% in October and December. The higher rate of death case is almost 9% and also minor injury is caused with 5% in February. In Figure 8, when the collision accident occurs, the highest number of people are death by the crashes of vehicles and serious injury that describes 24% and 31%. By the hit and rollover accident type, it is the lowest rate of accident type but the percentage of serious injury and death is equal in 5%.

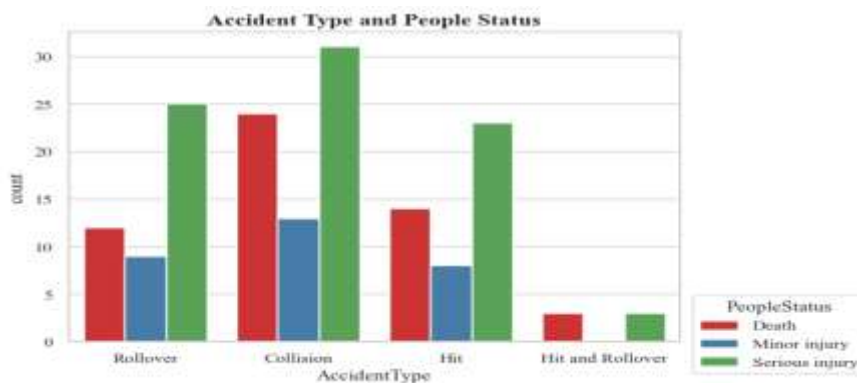


Figure 8: People Status Based on Accident Type

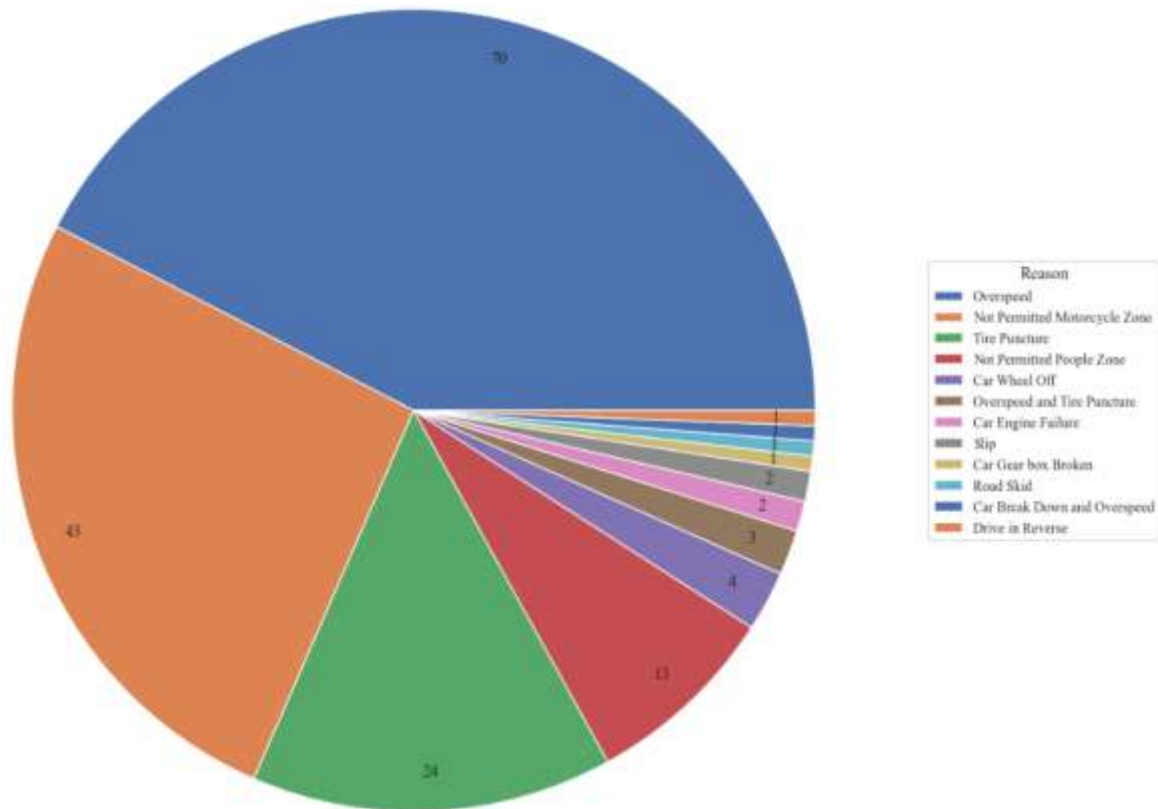


Figure 9: Reason of Accidents Occurred

According to the Figure 9, the reason of accident in which most of accident is happened by the reason of over speed.

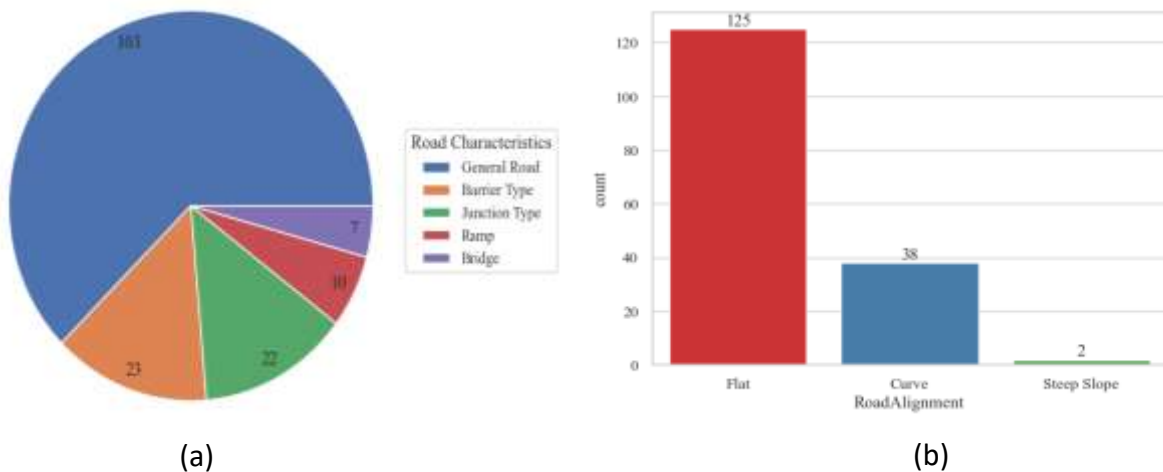


Figure 10 (a) and (b): Traffic Accident Occurred Road Characteristics and Road

According to the road characteristics in Figure 10 (a), since it is based on accidents that occur on the expressway ,most accident is caused on the general road. In Figure 10 (b), road alignment can be seen that the flat alignment is the highest number of accident cases than on the curve and steep slope alignment.

The following the Figures 11, according to the people status based on season, the percentage of serious injuries caused in rainy season significantly increased with 24% in spring and 32% in rainy season, the percentage of death was decreased with the lowest percentage of 13% in summer than in other two seasons.

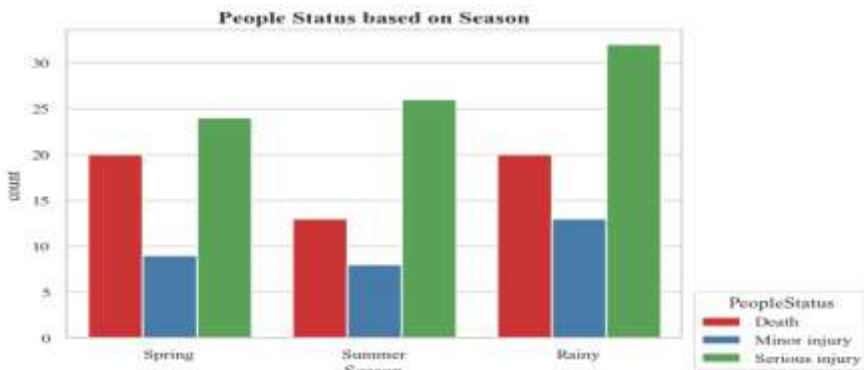


Figure 11: People status based on season

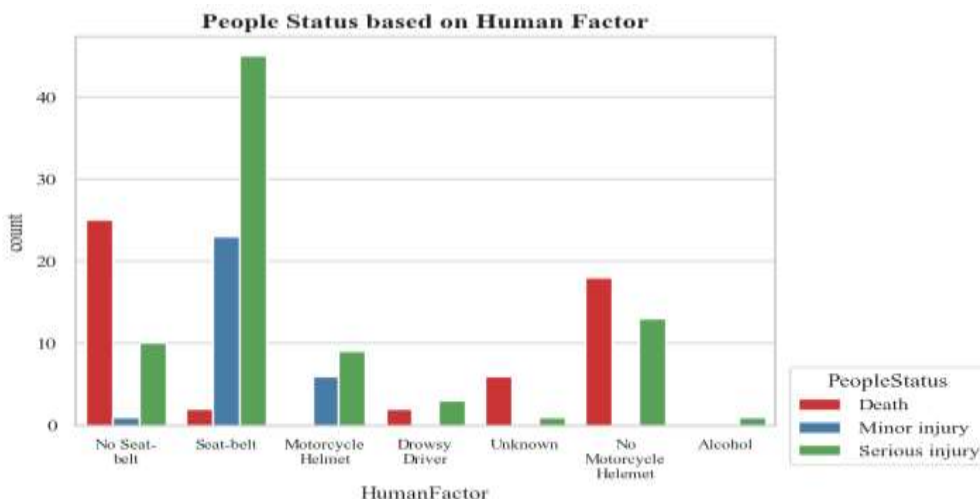


Figure 12: People Status Based on Human Factor

By Figure 12, it is apparent that although most of the drivers wear seat belts, the highest number of serious injuries and minor injuries was achieved with 45% and 23% and the highest number of deaths 25% and 18% were achieved during some drivers are driving without wearing seat belts and without using helmet when driving motorcycle.

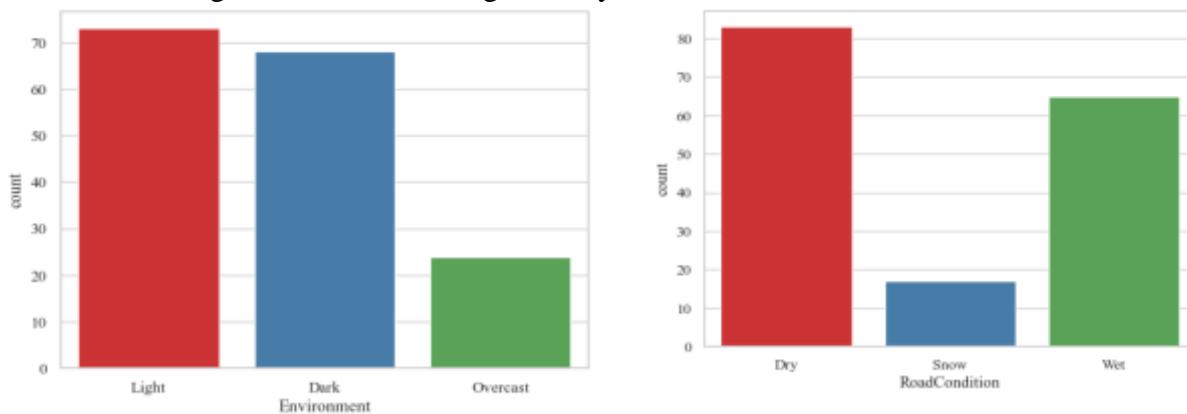


Figure 13 (a) and (b): Traffic Accident Occurred Environment and Road Condition

In the Figure 13 (a), shows that the highest rate of traffic accident causes is light environment with 73% and the lowest rate is overcast with 24 % than dark environment. According to Figure 13 (b), the most accidents cases occur in dry road condition with 83% and the fewest case occurs in snow road condition with 17%. The following Figure 14, shows the highest percentage of death and serious injuries caused in the day-time and night-time which is relatively increased while the percentage is decreased in twilight.

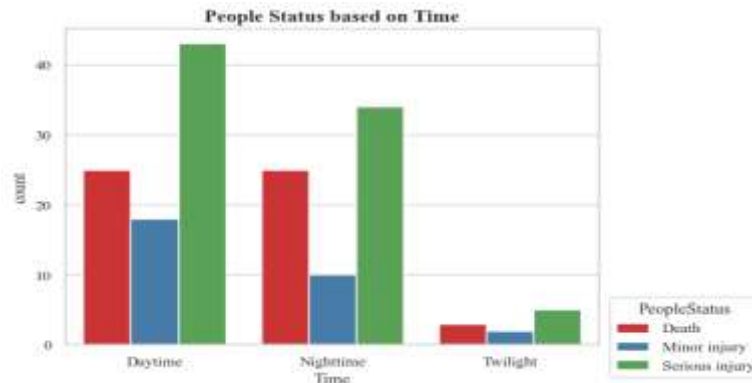


Figure 14: People Status Based on Time

Model Evaluation

The datasets are designed to train or “supervise” algorithms into classifying data or predicting outcomes accurately. Using labeled inputs and outputs, the model can measure its accuracy and learn over time. Evaluating a model is the core part of creating an effective model. After building machine learning models by using Logistic Regression, Adaboost, Multinomial Naive Bayes, Decision Tree and Adaboost using Decision Tree, the accuracy of the model is measured to make improvements and continue until achieving a desirable accuracy (J.Wen, 2009).

Table 2: Results of Evaluation Performance

Model	Training Result	Testing Result
Logistic Regression	0.8561	0.8485
AdaBoost	0.7045	0.6061
Decision Tree	0.9470	0.6061
AdaBoost using Decision Tree	0.9697	0.7273
Multinomial Naive Bayes	0.6970	0.7273

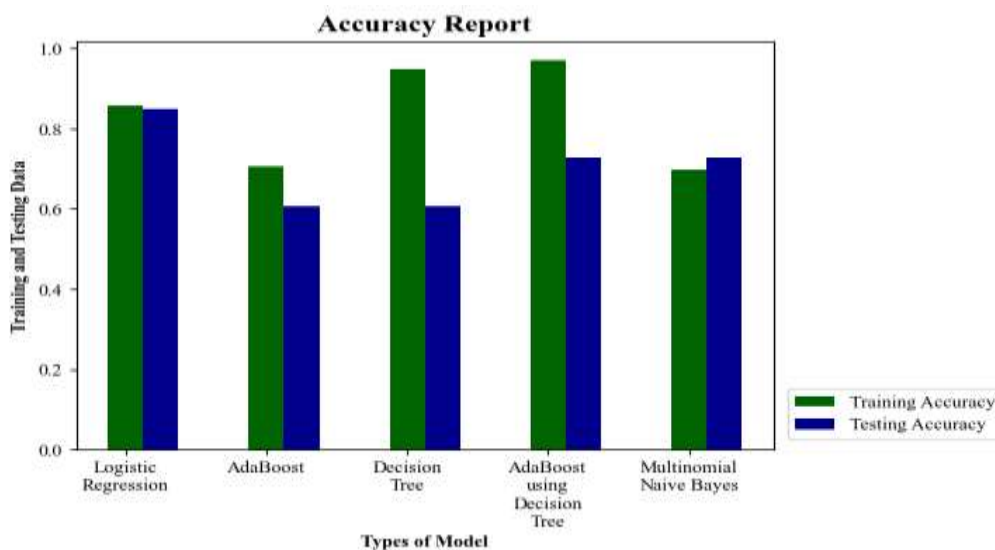


Figure 15: Comparison of Evaluation Performance

According to Table (2) and Figure (15), the experimental result shows that Logistic Regression is superior to the other four models considered. More specifically, the model accuracy for Logistic Regression was 84.85%, while Multinomial Naïve Bayes and AdaBoost

using Decision Tree achieved the second highest accuracy of 72.73%. The test results for both Decision Tree and AdaBoost were identical at 60.61%. As an obvious comparison, Logistic Regression achieved the highest accuracy at 84.85% for testing and 85.61% for training. In contrast, AdaBoost displayed the lowest accuracy, with 70.45% in training and 60.61% in testing, highlighting a notable difference in its performance between the two sets of results. The findings indicate that the most effective machine learning technique for the proposed system is Logistic Regression. This technique exhibits superior performance when compared to other classifiers.

Conclusion

Road accidents are increasing in Myanmar, resulting in 11,004 fatalities, which accounts for 3.05% of total deaths. Reducing fatality and serious injury by 50% are the main targets for most countries. In addition to road accident prevention policy and strategy, it is important to accurately understand and analyze the contributing factors of road accidents and their impacts in order to design safer roads. In this study, 11 factors influencing accident severity are selected and Machine Learning techniques to analyze road accident datasets for continuous variables. It is essential to understand these factors and their influence on a model, which is the primary focus of this research. This research utilized traffic accident data from the year 2022. The five models are used to produce optimal performance and to improve the acceptability of road accident prediction.

This research utilized the dataset of 165 records with 11 selected variables: accident type, people, human factor, reason, season, time, weather condition, environment, road condition, road characteristics, and road alignment. From this analysis, the first result is that collisions are the most common type of accident, and the highest number of deaths in February and serious injuries occurred in December and October. The second results are that most accident happened by the reason of overspeed, general road characteristics and the flat alignment is the highest number of accident cases than on the curve and steep slope alignment. The final conclusion is the highest number of deaths and serious injuries were happened during some drivers' driving without wearing seat belts and helmet and also caused both in the day and at night but the highest rate of accident caused in light environment and dry road condition than others. According to the model analysis, it indicates that Logistic Regression is better than other classifiers, with the highest accuracy in both training and testing outcomes for the proposed system. We intend to continue the analysis as a future scope to add more data to get better results. In further extension, the existing system can be extended with the feature selection process and investigated the performance of this classification problem using different artificial neural networks. For other future extensions, it is suggested to do further analysis in the most prevalent areas of traffic accidents on Naypyitaw -Yangon expressway.

Acknowledgements

I would like to give my warmest thanks to Professor Dr. Wint Pa Pa Kyaw, Department of Computer Studies, University of Yangon for guiding me through all the stages of doing my research. I would like to express my special thanks to Professor Dr. Soe Mya Mya Aye, Head of Department of Computer Studies, University of Yangon for her kind permission to carry out this research. My thanks for my gratitude to U Ye Myint Than, Principal of Co-operative College (Phaunggyi) for giving me a chance to do this research.

References

- J. Li1, et.al, (2023), “Predicting the severity of traffic accidents on mountain freeways with dynamic traffic and weather data”, *Transportation Safety and Environment*, ISSN: 2631-4428, DOI:10.1093/ tse/tdad001.
- J. Wen, (2009), “Comparison of AdaBoost and logistic regression for detecting colorectal cancer patients with synchronous liver metastasis”, *International Conference on Biomedical and Pharmaceutical Engineering, ICBPE*, DOI:10.1109/ICBPE.2009.5384087.
- J.Y. Lee, et.al, (2008), “Analysis of traffic accident size for Korean highway using structural equation models”, *Accid Anal Prev.*, 40(6), 1955-1963, DOI: 10.1016/j.aap.2008.08.006.
- N. Saxena, (2023), “ Analysis of Road Traffic Accident using Causation Theory with Traffic Safety Model and Measures”, *International Journal for Research in Applied Science & Engineering Technology (IJRASET)* , ISSN: 2321-9653; Volume 5 Issue VIII, DOI:10.22214/ijraset.2017.8179.
- S Ahmed, et.al, (2023), “A study on road accident prediction and contributing factors using explainable machine learning models: analysis and performance”, *Transportation Research Interdisciplinary Perspectives*, Volume 19, 100814, <https://doi.org/10.1016/j.trip.2023.100814>.
- T. Bokaba.et.al, (2020), “Comparative Study of Machine Learning Classifiers for Modelling Road Traffic Accidents”, *Applied Sciences*, DOI: "10.3390/app12020828, <https://doi.org/10.3390/ app12020828>.
- X. Wang, et.al, (2022), “Research on the Prediction of Traffic Accident Severity Based on BP Neural Network”, *Applied Mathematics, Modeling and Computer Simulation*, Vol 30. <https://ebooks.iospress.nl/volume/appliedmathematics-modeling-and-computer-simulation-proceedings-of-ammcs-2022>, DOI:10.3233/ATDE221138.

PREDICTING STUDENT DROPOUT SYSTEM FOR BASIC EDUCATION HIGH SCHOOL BY K-MEANS CLUSTERING

Ei Ei Thwe¹, Khin Sandar Myint², Soe Mya Mya Aye³

Abstract

The prediction of Basic Education High School students' dropout has been an important field for educational institutions. Recently, Educational Data Mining (EDM) has gained attention among educational researchers and information technology researchers. Developing a strategic plan helps every student to attend school with positive outcomes. Data mining technique called cluster can predict why students drop out. The proposed system of this study is to analyse the performance of data mining techniques and to predict students' dropout using the K-Means clustering algorithm. A pre-processing step for the student; parent; teacher survey data led to a higher level of accuracy due to data cleaning and data reduction using Principal Component Analysis. The proposed system processed the survey data of the Basic Education High School students in rural Patheingyi, Ayeyarwady Region.

Keywords: Educational data mining, K-Means clustering algorithm, Principal Component Analysis

Introduction

Education is a very important part in Human life. Education makes theory, practice, even moral. The prediction of students' dropout result has been an important field for Basic Education Institutions. Because it provides planning to support and develop any strategic programs that can improve student school attendance. In order to predict school dropouts, student achievement and failure, it is necessary to survey the factors influencing basic education. Educational Data Mining (EDM) is a developing research field, and many researchers are interested in it. The information collected by them must be collected and kept annually. The main reason for modelling this field is a large amount of spread information and it has on different platforms. The vast amount of data available from scatter information is a continuous challenge to seize value.

Predicting student outcomes after graduation is an important area for higher education institutions as they plan to expand and expand any strategic programs that may improve student academic performance. It can also affect the reputation of institutions regarding the quality of graduates.

Most completed studies use data mining or multi-attribute decision-making techniques to predict student achievement. Some techniques are C4.5, Decision Tree, Naïve Bayes, MADM and Support Vector Machine (E. Budiman et al, 2018). In their previous research, Student learning outcomes were predicted using C4.5 and Naive Bayesian methods. This study compares the performance of two methods in classifying students' graduation time into 3 classes.

K-means Clustering Algorithm

K-means algorithm is one of most important data clustering algorithms. Clustering can be understood as grouping. In this paper, K-means algorithm is used to cluster the courses into different groups according to the required learning skills. K-means algorithm was first raised by James MacQueen and Hugo Steinhaus. Generally, it can be separated into three main parts (A.Elizabeth et al, 2018).

- (1) Centroids Initialization: To initialize the centroids by randomly choosing k observations from the dataset.
- (2) Assignment Step: Allocate each observation to the nearest cluster (the distance between its mean and the observation is shortest compared with other clusters).
- (3) Update Step: Recalculate the meaning to be the centroid of each new cluster. The pseudo code of the K-means algorithm as follows:
 - (i) Randomly select two data points from students' survey dataset to serve as the initial centroids. These could be any two points in students' survey dataset.
 - (ii) Calculate the distances between each observation and each centroid.

¹ Department of Computer Studies, University of Yangon

² Department of Computer Studies, University of Yangon

³ Department of Computer Studies, University of Yangon

- (iii) Allocate each observation to the nearest centroid.
- (iv) Recalculate the meaning to be the centroid of each new cluster.
- (v) Repeat 2 to 4 until convergence happens.
- (vi) Repeat step 1 to step 5 with k from 2 to 6 and pick the best one according to the sum of distance between each observation and centroids.

K-Means is a non-hierarchical clustering method that attempts to partition data into defined clusters. Therefore, Data with similar characteristics are collected into the same cluster and others into another cluster (A. Sarker et al, 2018). The K-Means method is a prominent cluster analysis algorithm in data mining.

In the K-means method, the result obtained through some clustering test is the original cluster centre point (A. Sarker et al, 2018). Different from (C. Casuat, 2019), the advantages of K-means algorithm are faster convergence to distortion minimum and apprehending how many clusters in the dataset (M. Li et al, 2018).

Implementation of Predicting Student Dropout System

In the proposed system, methodology for data collection and techniques is firstly defined. Student Survey Dataset in the data pre-processing step includes the data cleaning and reducing the attributes using Principal Component Analysis (PCA) method. The Cluster Model Using K-Means step includes PCA to k-means algorithm and to determine the best number of clusters.

Methodology for Data Collection and Techniques

The two data mining techniques, K-means algorithm, and Principal Component Analysis (PCA) are described in this section. Figure 1 shows the steps of the proposed system to predict students' dropout.

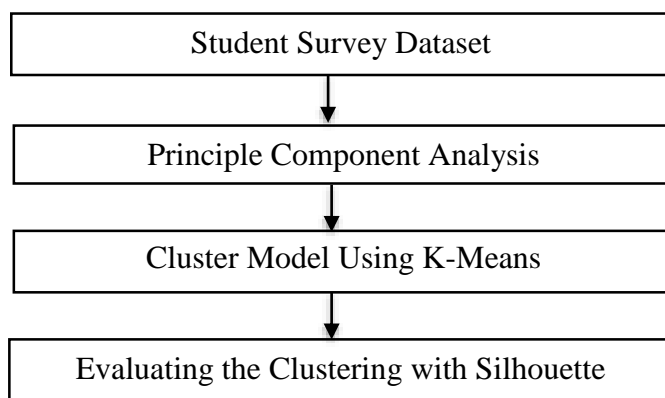


Figure 1 Proposed System Steps to Predict Students' Dropout

The 2015-2020 university entrance (10th grade) students list was gathered from the Office of the Director of Education, Patheingyi city, Ayeyarwady Region. The dataset comprises information from 4424 students across Basic Education High School in Ayeyarwady Region. Each student is represented by 20 features, including Name, Class, Age, Mother's Education, Father's Education, Mother's monthly average income, Father's monthly average income, Amount of Debt, Gender etc. Any deviations from the received data will be collected in the field in the townships. A difference between the percentage of students and the percentage of dropout students will be collected by township in the form of a questionnaire on mobile application. This difference will be analysed using MACHINE LEARNING MODEL and DROUPOUT rate.

Questionnaire format is mainly to collect information related to students, teachers, parents, and administrators. The cities that will collect data include Patheingyi city in Ayeyarwady Region. Knowledge Discovery in Databases (KDD) can help educational organizations by

turning their data into useful information. Organizations that take advantage of KDD techniques will find that they can improve education quality by using fast and better educational decision making. The data collection of the proposed system is based on cloud database and mobile android application in Figure 2.



Figure 2 Android Application of Data Collection

The android version survey apk installed on at least android 7 versions. Mobile phone applications use internet connection for data collection. Data collection mobile apk is installed on smartphones that provide a student dropout survey system. The student dropout survey app uses google cloud platform as shown in Figure 3.



Figure 3 Mobile Application

The attributes of student survey data for Predicting Student Dropout System is shown in Table 1.

Table 1 Attributes of Student Survey Data

No	Feature	Value range
၁။	အမိပညာအရည်အချင်း	Degree
၂။	အဘပညာအရည်အချင်း	Degree
၃။	အမိတစ်လဝင်ငွေ	Money amount
၄။	အဘဝင်ငွေ	Money amount
၅။	အကြွေးရှိပမာဏ	Money amount
၆။	ကျောင်းသားအသက်(နှစ်)	Age
၇။	ကျား/မ	Male/Female
၈။	ဆရာစာသင်ကြားမှုအခြေအနေ	1-5

၉။	မိသားစုမှာမိခင်ဘယ်နှစ်ယောက်ရှိလဲ	Count
၁၀။	စာလိုက်နိုင်မှုအခြေအနေ	1-5
၁၁။	မိသားစုအရေအတွက်	Count
၁၂။	သင်ယူတာနားလည်မှု	1-5
၁၃။	စာသင်ကြားရတာစိတ်ပါဝင်စားမှုရှိလား	1-5
၁၄။	မြို့/နယ်	1-2
၁၅။	ကျောင်းနှင့်အိမ်အကွာအဝေး	1-5
၁၆။	ကျန်းမာရေးအခြေအနေ	1-5
၁၇။	ကျောင်းသွားတက်ရသည့်အခြေအနေ	1-5
၁၈။	ကျောင်းသားGradeအဆင့်	A-E
၁၉။	ရို/ထွက်	0-1

Data Pre-processing

The data clean method is useful for cleaning datasets that have a missing value. It removes missing value attributes from the dataset. PCA is used to attribute reduction. Principal Component Analysis (PCA) is a feature selection method which is used to reduce missing value attributes. It is used to eliminate irrelevant attributes in predicting student’s survey data. The selecting relevant and non-correlated attributes does not affect the information in the initial data set, then the prediction is developed using the K-means method to cluster the data set (C. Casuat, 2019), (M. Z. Nasution, 2018). It used to eliminate irrelevant attributes in predicting students' dropout data.

A correlation heatmap was designed to analyse the correlations between input features and output variables. The code in Python to create the heatmap of the correlation matrix is described in Figure 4.

```
principalDataframe = pd.DataFrame(data = principalComponents, columns = ["PC1", "PC2"])
targetDataframe = df[['Target']]

newDataframe = pd.concat([principalDataframe, targetDataframe],axis = 1)
print(newDataframe)

plt.scatter(principalDataframe.PC1, principalDataframe.PC2)
plt.title('PC1 against PC2')
plt.xlabel('PC1')
plt.ylabel('PC2')
plt.show()

fig = plt.figure(figsize=(8, 8))
ax = fig.add_subplot(1, 1, 1)
ax.set_xlabel('PC1')
for i in range(1, 23):
```

Figure 4 Heatmap of the Correlation Matrix

Using the PCA method, selected relevant data and non-correlated attributes are without affecting the original information of the data set (C. Casuat, 2019), (M. Z. Nasution, 2018) as shown in Figure 5. There exists a medium correlation between important features and grade

points. Features such as Mother’s qualification, Father's qualification, Mother’s monthly average income, Father’s monthly average income and health status have a strong correlation with grade points. As a result, strongly correlated features are considered in the model building due to their highest impact on student dropout outcomes. In the last stage of data pre-processing, the dataset was normalized using a standard scalar to eliminate the mean and scale it to unit variance.

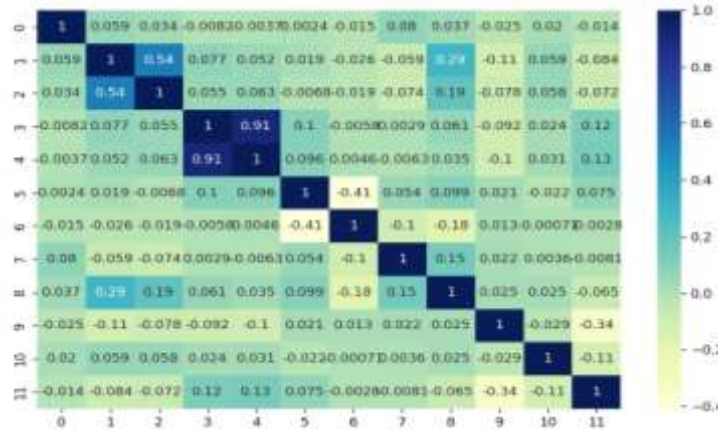


Figure 5 Value of PCA Loading Factor for Each Variable.

Modelling for Proposed System

The K-means clustering method is used to predict student dropout in this proposed system. The algorithm of the K-means clustering method is shown in Figure 6.

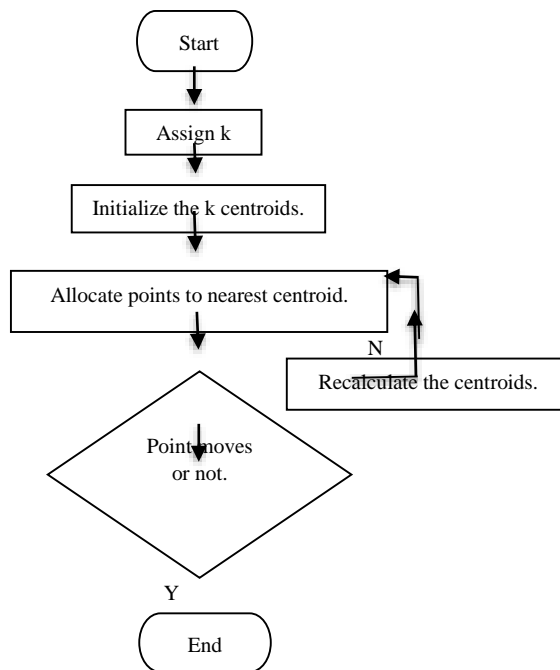


Figure 6 The Logic Flow of K-means Algorithm with a Specified K

The classification model describes these two: Naïve Bayes classifier has an accuracy rate of 60% and the Tree C4.5 method has an accuracy rate of 58.82% (M. E. Hiswati et al, 2018) over other methods. Data clustering aims to group similar data records together. Clustering is often confused as classification, but they both have different goals. Simply put, the inter-cluster distance needs to be reduced to achieve better clustering results, as in the K-means algorithm.

Evaluation

The evaluation is conducted using the Silhouette method and Principal Component Analysis (PCA) to calculate the prediction accuracy for the student survey dataset. Silhouette analysis can be used to study the separation distance between the resulting clusters. Silhouette Score is a metric to evaluate the performance of a clustering algorithm (P. Pannen et al, 2019) (Y. Pang et al, 2017). It uses compactness of individual clusters (*intra cluster distance*) and separation amongst clusters (*inter cluster distance*) to measure an overall representative score of how well our clustering algorithm has performed. The silhouette score is a valuable metric for objectively evaluating the effectiveness of K-means clustering, helping to determine the optimal number of clusters, and ensuring that the resulting clusters are meaningful and well-separated. The silhouette plot displays a measure of how close each point in one cluster is to points in the neighbouring clusters and thus provides a way to assess parameters like number of clusters visually.

The proposed system approach has four important stages namely, student survey dataset processing, Principal Component Analysis (PCA), K-Means clustering and evaluation. All steps are important for predicting a student's dropout accuracy and performance.

Result and Discussion

The data pre-processing step carried out data cleaning and reduction data with the PCA method, so we obtained the relevant attributes to clustering the dataset using the K-means algorithm. The value of each PCA loading factor variable is presented in Figure 7.



Figure 7 Exact Match Ratio (EMR) in 6 models of cluster

Silhouette Plot of K-Means Cluster for $k = 2, 3, 4, 5,$ and 6 are shown in Figure 8, 9, 10, 11, 12 respectively. Figure 13 shows Silhoutte Plot of K-Means Cluster for $k=2$ to $k=6$. For these following figures, YellowBrick-a machine learning visualization library in Python is used. Silhoutte score for clusters 2, 3, 4, 5, and 6 is shown in Figure 14 using line graph.

```
import matplotlib.pyplot as plt

def visualize_clusters(X, clusters):
    fig, axs = plt.subplots(1, len(clusters), figsize=(len(clusters) * 6, 6))
    for i, cluster in enumerate(clusters):
        km = KMeans(n_clusters=cluster, init='k-means++', n_init=10, max_iter=300, random_state=0)
        visualizer = SilhouetteVisualizer(km, colors='yellowbrick', ax=axs[i])
        visualizer.fit(X)
        visualizer.finalize()
        axs[i].set_title(f'{cluster} clusters')

    plt.tight_layout()
    plt.show()

# Load your dataset and define the features
dataset = pd.read_csv("data/e1ithwe11.csv")
features = ["Id", "Mother's qualification", "Father's qualification", "Mother's occupation", "Father's occupation", "Tuition fees up to date", "Gender", "Age at enrollment", "Unemployment rate", "Inflation rate"]
X = dataset.loc[:, features].values

# PCA transformation
pca = PCA(n_components=2)
X_pca = pca.fit_transform(X)

# Define the cluster sizes you want to visualize
cluster_sizes = [2, 3, 4, 5, 6]
```

K-means Clustering Coding

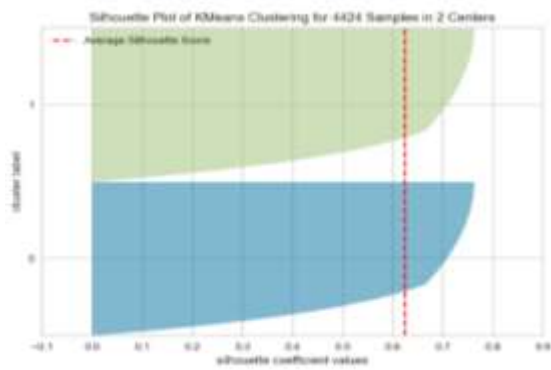


Figure 8 Silhouette Plot of K-Means Cluster for k = 2

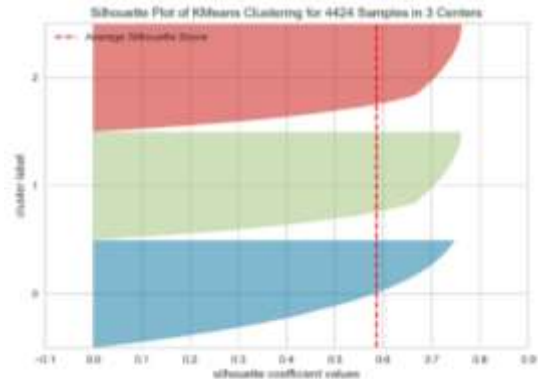


Figure 9. Silhouette Plot of KMeans Cluster for k = 3

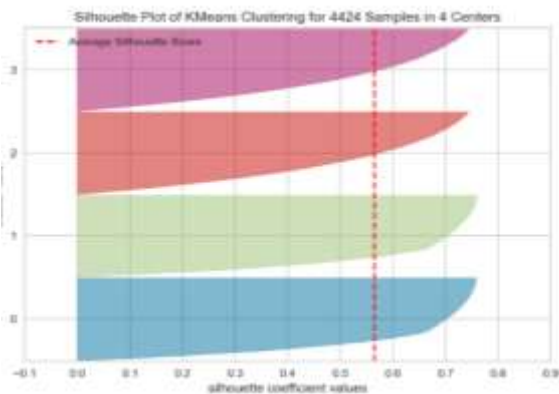


Figure 10. Silhouette Plot of K-Means Cluster for k=4

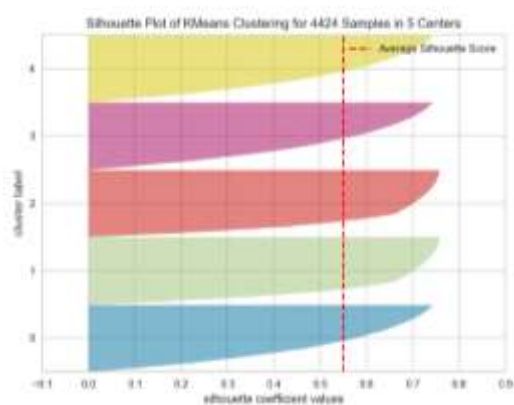


Figure 11. Silhouette Plot of K-Means Cluster for k = 5

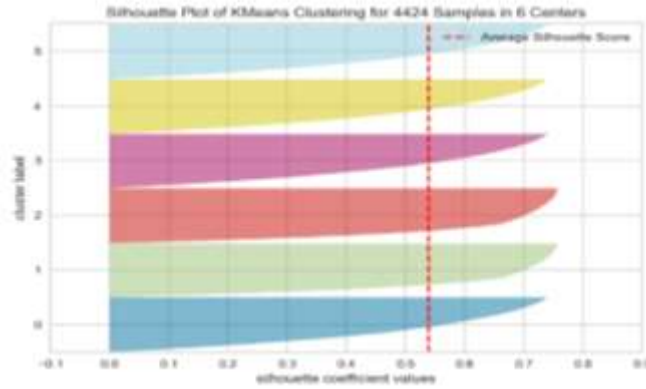


Figure 12. Silhouette Plot of K-Means Cluster for k = 6

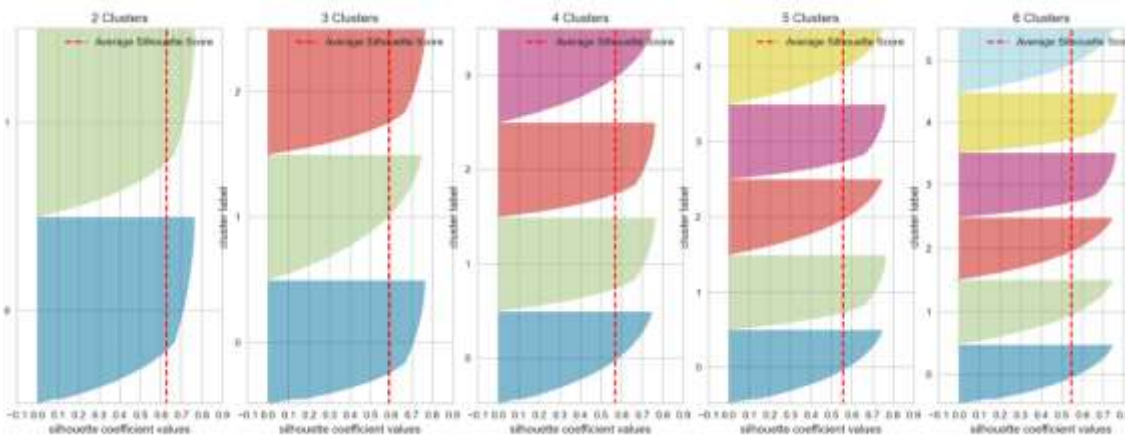


Figure 13. Silhouette Plot of K-Means Cluster for k=2 to k=6

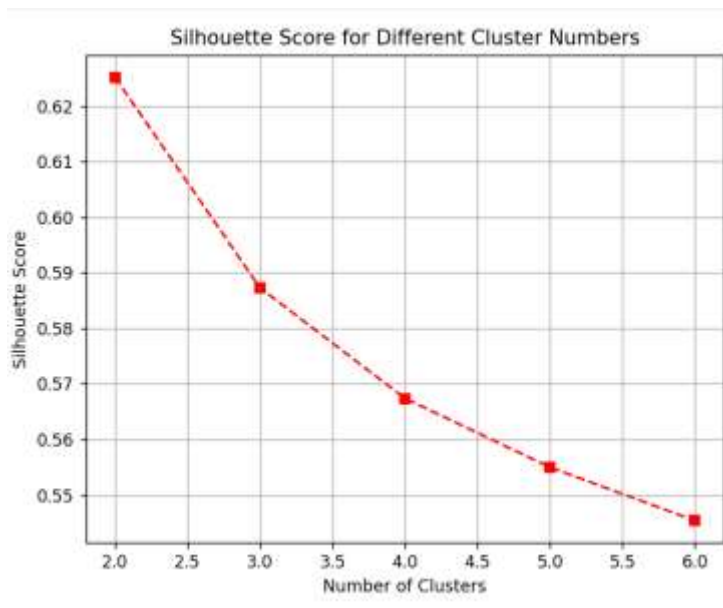


Figure 14. Silhouette Score of K-Means Cluster for k=2 to k=6

The silhouette score for k = 2 is the highest in all clusters as shown in Figure 7. It is a proposed system except for this data set as shown.

The 2-cluster model obtained an accuracy rate of 62.4%. In the 3-cluster model, the accuracy rate is 58.5%. In the 4-cluster model, the accuracy rate is 56.4%. In the 5-cluster model, the accuracy rate is 55%. In the 6-cluster model, the accuracy rate is 53.9%.

To predict student dropout prediction the highest accuracy rate of K-Means clustering modelling with 2-cluster models use the student academic survey dataset in Table 1.

This shows that the most appropriate clustering of data to predict student dropout uses a 2-cluster model. The graph can illustrate the results of the study in Figure 7.

Conclusion

As the results of this proposed system obtained, the attributes are ages, school home travel time, teacher teaching ability, guardian and number of family members all have negative loading factor value in the PCA method, which means it all has a small correlation value to the prediction of the student dropout. This paper presented a comprehensive approach to predicting student dropout in Basic Education High Schools, utilizing K-means clustering and Principal Component Analysis (PCA). The integration of these techniques provides a refined and accurate prediction system, enabling educators to implement timely interventions.

Based on 2 cluster models it is obtained that the 2-cluster model is the best clustering with an accuracy rate obtained is 62.4%. As future work, it may explore the incorporation of additional data sources and advanced machine learning techniques to further improve the accuracy and applicability of the dropout prediction system.

Acknowledgement

The authors would like to thank professor Dr. Soe Mya Mya Aye, Head of Department of Computer Studies, University of Yangon for giving a chance to do this research and for encouraging completion in time. Also, I would like to thank my respectful Daw Khin Cho Myint, Principal of Bogalay Education Degree College for her co-operation and encouragement in this research.

References

- A. Sarker et al, (2018), "Employee's Performance Analysis and Prediction using K-Means Clustering & Decision Tree Algorithm," Type Double Blind Peer Rev. Int. Res. J. Softw. Data Eng. Glob. J. Comput. Sci. Technol. C, vol. 18, no. 1.
- A. Elizabeth et al, (2018), "Groundwater quality assessment: An improved approach to K-means clustering, principal component analysis and spatial analysis: A case study," Water (Switzerland), vol. 10, no. 4, pp. 1–21, doi: 10.3390/w10040437.
- C. Casuat et al, (2019), "Predicting Students' Employability using Machine Learning Approach," ICETAS 2019 - 2019 6th IEEE Int. Conf. Eng. Technol. Appl. Sci., doi: 10.1109/ICETAS48360.2019.9117338.
- D. Konar et al, (2020), "Predicting Students' Grades Using CART, ID3, and Multiclass SVM Optimized by the Genetic Algorithm (GA): A Case Study," Recent Adv. Hybrid Metaheuristics Data Clust., pp. 85–99, doi: 10.1002/9781119551621.ch5.
- E. Budiman et al, (2018), "Performance of Decision Tree C4.5 Algorithm in Student Academic Evaluation," Lect. Notes Electr. Eng., vol. 488, pp. 380–389, doi: 10.1007/978-981-10-8276-4.
- M. E. Hiswati et al, (2018), "Minimum wage prediction based on K-Mean clustering using neural based optimized Minkowski Distance Weighting," Int. J. Eng. Technol., vol. 7, no. 2, pp. 90–93, doi: 10.14419/ijet.v7i2.2.12741.
- M. Li et al, (2018), "Application of CART decision tree combined with PCA algorithm in intrusion detection," Proc. IEEE Int. Conf. Softw. Eng. Serv. Sci. ICSESS, vol. 2017-Novem, pp. 38–41, doi: 10.1109/ICSESS.2017.8342859.
- M. Z. Nasution et al, (2018), "PCA based feature reduction to improve the accuracy of decision tree c4.5 classification," J. Phys. Conf. Ser., vol. 978, no. 1, doi: 10.1088/1742-6596/978/1/012058.
- P. Pannen et al, (2019), "Autonomous 5 higher education institutions in Indonesia," Gov. Manag. Univ. Asia Glob. Influ. local responses, p. 56.
- Y. Pang et al, (2017), "Predicting students' graduation outcomes through support vector machines," Proc. - Front. Educ. Conf. FIE, vol. 2017-October, pp. 1–8, doi: 10.1109/FIE.2017.8190666.